

Development and Fabrication of Advanced Materials for Energy and Environment Applications

Guest Editors: Ming-Guo Ma, Jie-Fang Zhu, Shao-Wen Cao, and Wen Zeng





Development and Fabrication of Advanced Materials for Energy and Environment Applications

Development and Fabrication of Advanced Materials for Energy and Environment Applications

Guest Editors: Ming-Guo Ma, Jie-Fang Zhu, Shao-Wen Cao,
and Wen Zeng



Copyright © 2013 Hindawi Publishing Corporation. All rights reserved.

This is a special issue published in “Journal of Nanomaterials.” All articles are open access articles distributed under the Creative Commons Attribution License, which permits unrestricted use, distribution, and reproduction in any medium, provided the original work is properly cited.

Editorial Board

Katerina E. Aifantis, Greece
Nageh K. Allam, USA
Margarida Amaral, Portugal
Xuedong Bai, China
Lavinia Balan, France
Enrico Bergamaschi, Italy
Theodorian Borca-Tasciuc, USA
C. Jeffrey Brinker, USA
Christian Brosseau, France
Xuebo Cao, China
Shafiul Chowdhury, USA
Kwang-Leong Choy, UK
Cui ChunXiang, China
M. A. Correa-Duarte, Spain
Shadi A. Dayeh, USA
Claude Estourns, France
Alan Fuchs, USA
Lian Gao, China
Russell E. Gorga, USA
Hongchen Chen Gu, China
Mustafa O. Guler, Turkey
John Zhanhu Guo, USA
Smrati Gupta, Germany
Michael Harris, USA
Zhongkui Hong, China
Michael Hu, USA
David Hui, USA
Y.-K. Jeong, Republic of Korea
Sheng-Rui Jian, Taiwan
Wanqin Jin, China
Rakesh K. Joshi, UK
Zhenhui Kang, China
Fathallah Karimzadeh, Iran
Alireza Khataee, Iran
Do Kyung Kim, Korea

Alan K. T. Lau, Hong Kong
Burtrand Lee, USA
Benxia Li, China
Jun Li, Singapore
Xing-Jie Liang, China
Shijun Liao, China
Gong Ru Lin, Taiwan
J. -Y. Liu, USA
Tianxi Liu, China
Songwei Lu, USA
Daniel Lu, China
Jue Lu, USA
Ed Ma, USA
Gaurav Mago, USA
Santanu K. Maiti, India
Sanjay R. Mathur, Germany
Vikas Mittal, United Arab Emirates
Weihai Ni, Germany
Sherine Obare, USA
Atsuto Okamoto, Japan
Abdelwahab Omri, Canada
Edward Andrew Payzant, USA
Kui-Qing Peng, China
Anukorn Phuruangrat, Thailand
Mahendra Rai, India
Suprakas Sinha Ray, South Africa
Ugur Serincan, Turkey
Huaiyu Shao, Japan
Donglu Shi, USA
Vladimir Sivakov, Germany
Marinella Striccoli, Italy
Bohua Sun, South Africa
Saikat Talapatra, USA
Nairong Tao, China
Titipun Thongtem, Thailand

Somchai Thongtem, Thailand
Alexander Tolmachev, Ukraine
Valeri P. Tolstoy, Russia
Tsung-Yen Tsai, Taiwan
Takuya Tsuzuki, Australia
Raquel Verdejo, Spain
Mat U. Wahit, Malaysia
Shiren Wang, USA
Yong Wang, USA
Ruibing Wang, Canada
Cheng Wang, China
Zhenbo Wang, China
Jinquan Wei, China
Ching-Ping Wong, Hong Kong
Xingcai Wu, China
Guodong Xia, Hong Kong
Zhi Li Xiao, USA
Ping Xiao, UK
Shuangxi Xing, China
Yangchuan Xing, USA
N. Xu, China
Doron Yadlovker, Israel
Yingkui Yang, China
Khaled Youssef, USA
Kui Yu, Canada
William W. Yu, USA
Haibo Zeng, China
Tianyou Zhai, Japan
Renyun Zhang, Sweden
Bin Zhang, China
Yanbao Zhao, China
Lianxi Zheng, Singapore
Chunyi Zhi, Hong Kong

Contents

Development and Fabrication of Advanced Materials for Energy and Environment Applications,
Ming-Guo Ma, Jie-Fang Zhu, Shao-Wen Cao, and Wen Zeng
Volume 2013, Article ID 279309, 2 pages

HER Catalytic Activity of Electrodeposited Ni-P Nanowires under the Influence of Magnetic Field,
Hung-Bin Lee, Jiun-Chen Tsau, and Chun-Ying Lee
Volume 2013, Article ID 191728, 9 pages

The Development of Photocatalyst with Hybrid Material CNT/TiO₂ Thin Films for Dye-Sensitized Solar Cell, Yong Woo Kim and Sang Hee Park
Volume 2013, Article ID 197276, 5 pages

Preparation of Smooth Surface TiO₂ Photoanode for High Energy Conversion Efficiency in Dye-Sensitized Solar Cells, Sasipriya Kathirvel, Huei-Siou Chen, Chaochin Su, Hsiue-Hsyang Wang, Chung-Yen Li, and Wen-Ren Li
Volume 2013, Article ID 367510, 8 pages

Synthesis of Octahedral-Shaped NiO and Approaches to an Anode Material of Manufactured Solid Oxide Fuel Cells Using the Decalcomania Method, Haeran Cho, Huryul Lee, Sun-Min Park, Byung-Hyun Choi, and Misook Kang
Volume 2013, Article ID 640146, 7 pages

Effect of Solution Spray Rate on the Properties of Chemically Sprayed ZnO:In Thin Films, Merike Kriisa, Malle Krunk, Erki Kärber, Mart Kuk, Valdek Mikli, and Arvo Mere
Volume 2013, Article ID 423632, 9 pages

Preparation of Baking-Free Brick from Manganese Residue and Its Mechanical Properties, Ping Wang and Dong-yan Liu
Volume 2013, Article ID 452854, 5 pages

Characterization of Nanoporous Ceramic Granules Made with Coal Fly Ash and Their Utilization in Phenol Removal from Water, Zhaoqian Jing
Volume 2013, Article ID 606940, 8 pages

Fabrication and Characterization of Manganese Ferrite Nanospheres as a Magnetic Adsorbent of Chromium, Li-Xia Yang, Feng Wang, Yan-Feng Meng, Qing-Hua Tang, and Zi-Qi Liu
Volume 2013, Article ID 293464, 5 pages

Pd-Doped SnO₂-Based Sensor Detecting Characteristic Fault Hydrocarbon Gases in Transformer Oil, Weigen Chen, Qu Zhou, Tuoyu Gao, Xiaoping Su, and Fu Wan
Volume 2013, Article ID 127345, 9 pages

Influence of Hydrothermal Temperature on Phosphorus Recovery Efficiency of Porous Calcium Silicate Hydrate, Wei Guan, Fangying Ji, Qingkong Chen, Peng Yan, and Weiwei Zhou
Volume 2013, Article ID 451984, 6 pages

Characterization of Porous WO₃ Electrochromic Device by Electrochemical Impedance Spectroscopy,

Chien Chon Chen

Volume 2013, Article ID 785023, 14 pages

Facile Synthesis of Fe-Doped Titanate Nanotubes with Enhanced Photocatalytic Activity for Castor Oil Oxidation,

Guozhu Fu, Gang Wei, Yanqiu Yang, WeiCheng Xiang, and Ning Qiao

Volume 2013, Article ID 621929, 4 pages

Application of Flower-Like ZnO Nanorods Gas Sensor Detecting SF₆ Decomposition Products,

Shudi Peng, Gaolin Wu, Wei Song, and Qian Wang

Volume 2013, Article ID 135147, 7 pages

Gas Sensing Properties and Mechanism of Nano-SnO₂-Based Sensor for Hydrogen and Carbon Monoxide,

Weigen Chen, Qu Zhou, Fu Wan, and Tuoyu Gao

Volume 2012, Article ID 612420, 9 pages

Mineral Phase and Physical Properties of Red Mud Calcined at Different Temperatures,

Chuan-sheng Wu and Dong-yan Liu

Volume 2012, Article ID 628592, 6 pages

Editorial

Development and Fabrication of Advanced Materials for Energy and Environment Applications

Wen Zeng,¹ Ming-Guo Ma,² Jie-Fang Zhu,³ and Shao-Wen Cao⁴

¹ College of Materials Science and Engineering, Chongqing University, Chongqing 400040, China

² Beijing Key Laboratory of Lignocellulosic Chemistry, College of Materials Science and Technology, Beijing Forestry University, Beijing 100083, China

³ Department of Materials Chemistry, The Ångström Laboratory, Uppsala University, 75121 Uppsala, Sweden

⁴ School of Materials Science and Engineering, Nanyang Technological University, Singapore 639798

Correspondence should be addressed to Wen Zeng; wenzeng@cqu.edu.cn and Ming-Guo Ma; mg_ma@bjfu.edu.cn

Received 25 July 2013; Accepted 25 July 2013

Copyright © 2013 Wen Zeng et al. This is an open access article distributed under the Creative Commons Attribution License, which permits unrestricted use, distribution, and reproduction in any medium, provided the original work is properly cited.

The increasing environmental problems and deficiencies of sustainable energy sources have become serious issues that are urgently in need of being addressed. To make up this issue, the key is of development and fabrication of advanced materials that for energy and environment applications.

The performance of materials depends critically on their microstructures, which requires the development of materials processing techniques to obtain the desired microstructures and morphologies. It is of great importance in future technological applications to understand how the materials behave at nanoscale during working and how controllably manufacture. No matter physical or chemical preparation, forward-looking theoretical guidance and characterization proof are necessary for explaining the formation mechanism so as to design devices with expected properties for nonpolluting energy generation and environmental protection. In this issue, different approaches were used to create nanostructures in several oxide materials dealing with the environmental and energy-converting problems.

The paper “Pd-doped SnO₂-based sensor detecting hydrocarbon characteristic fault/hydrocarbon gases in transformer” by W. Chen et al. synthesized Pd-doped SnO₂ nanoparticles and measured their gas-sensing properties towards methane, ethane, ethylene, and acetylene. The sensing mechanism was also addressed in detail based on a quantum chemistry calculation of molecule orbital energy. The paper “Application of flower-like ZnO nanorods gas sensor detecting SF₆

decomposition products” by S. Peng et al. proposes a novel gas sensor based on flower-like ZnO nanorods to detect typical SF₆ decompositions. This sensor shows a remarkable discrimination among SO₂, SOF₂, and SO₂F₂ with high linearity. The paper “Gas sensing properties and mechanism of nano-SnO₂ based sensor for hydrogen and carbon monoxide” by W. Chen et al. prepared nano-SnO₂ powder via a hydrothermal method and investigated the gas sensing performances of the obtained sensor against power transformer fault gases such as hydrogen and carbon monoxide. The gas sensing mechanism was qualitatively explained by the first-principles calculation. These results will present a new feasible way on exploring new metal oxide gas sensor for on-line monitoring of fault gases dissolved in power transformers.

The paper “HER catalytic activity of electrodeposited Ni-P nanowires under the influence of magnetic field” by H.-B. Lee et al. fabricated the nickel alloy electrodes both in plane and nanowires morphologies by electrodepositing in sulfamate bath. By using nanowires morphology and applying in magnetic field, the HER stability of the Ni electrode increased in more than four folds than that of its plane counterpart.

The paper “The development of photocatalyst with hybrid material CNT/TiO₂ thin films for dye-sensitized solar cell” by Y. W. Kim and S. H. Park prepared CNT/TiO₂ as a hybrid material to improve their efficiency of dye-sensitized solar cell. The higher concentration of CNT will decrease the transmission and resistance of TiO₂ thin film.

The paper “*Fabrication and characterization of manganese ferrite nanospheres as a magnetic adsorbent of chromium*” L.-X. Yang et al. synthesized the manganese ferrite nanospheres by a one-step and template-free solvothermal method. The obtained materials show an excellent ability to magnetic removal of chromium in waste water.

The paper “*Preparation of smooth surface TiO_2 photoanode for high energy conversion efficiency in dye-sensitized solar cells*” S. Kathirvel et al. fabricated the dye-sensitized solar cells by using a TiO_2 nanosol-based photoelectrode. These cells show an overall light conversion efficiency and a short-circuit current density.

The paper “*Effect of solution spray rate on the properties of chemically sprayed ZnO:In thin films*” by M. Kriisa et al. using a chemical spray method to prepare ZnO:In thin films on glass substrates and found that the solution spray rate is an important technological parameter controlling the film thickness and electrical properties of the sprayed ZnO:In films.

The paper “*Influence of hydrothermal temperature on phosphorus recovery efficiency of porous calcium silicate hydrate*” by W. Guan et al. synthesized porous calcium silicate hydrate by carbide residue and white carbon black. The influence of hydrothermal temperature on phosphorus recovery efficiency was investigated in detail.

The paper “*Preparation of baking-free brick from manganese residue and its mechanical properties*” by P. Wang and D.-y. Liu addressed a summarization of the main methods to produce building materials from manganese slag materials. It is concluded that the baking-free brick prepared from manganese residue could have excellent compressive strength performance under certain formula.

The paper “*Characterization of nanoporous ceramic granules made with coal fly ash and their utilization in phenol removal from water*” by Z. Jing Jing used the coal fly ash to produce composite ceramic granules with high porosity and specific surface area. Effects of various factors such as adsorbents dosage, contact time, and temperature were investigated and aimed to obtain optimized parameter.

The paper “*Facile synthesis of Fe-doped titanate nanotubes with enhanced photocatalytic activity for castor oil oxidation*” by G. Fu et al. reported the synthesis of the iron doped Ti nanotubes and provided a facile route to improve the photocatalytic efficiency of materials and other properties such as magnetic property.

The paper “*Mineral phase and physical properties of red mud calcined at different temperatures*” by C.-S. Wu and D.-y. Liu investigated the phase composition and structural transition of red mud from room temperature to 1200°C . The obtained results provided an important base for the further studies of comprehensive utilization of red mud.

The paper “*Synthesis of octahedral-shaped NiO and approaches to an anode material of manufactured solid oxide fuel cells using the decalcomania method*” by H. Cho et al. synthesized octahedral-shaped NiO particles by microwave thermal method. Using an octahedral NiO anode functional layer, fuel cell performance was significantly improved owing to better contact between the electrolyte and anode.

The paper “*Characterization of porous WO_3 electrochromic device by electrochemical impedance spectroscopy*” by C. C. Chen reported the microstructure of the anodic tungsten oxide and its use in an electrochromic glass device. The fabrication process can be extended to other metal oxides such as TiO_2 and Ta_2O_5 , which are electrochromic and solid charge conductive films.

By compiling these papers, we hope this issue will provide some valuable insights into our readers and researchers with respect to the field of advanced materials for energy and environment applications.

Wen Zeng
Ming-Guo Ma
Jie-Fang Zhu
Shao-Wen Cao

Research Article

HER Catalytic Activity of Electrodeposited Ni-P Nanowires under the Influence of Magnetic Field

Hung-Bin Lee,¹ Jiun-Chen Tsau,² and Chun-Ying Lee³

¹ Department of Materials Science and Engineering, Da-Yeh University, Da-Tsuen, Changhua 515, Taiwan

² Department of Electrical Engineering, Da-Yeh University, Da-Tsuen, Changhua 515, Taiwan

³ Department of Mechanical Engineering, National Taipei University of Technology, Taipei 106, Taiwan

Correspondence should be addressed to Chun-Ying Lee; leech@ntut.edu.tw

Received 23 November 2012; Accepted 26 June 2013

Academic Editor: Jie-Fang Zhu

Copyright © 2013 Hung-Bin Lee et al. This is an open access article distributed under the Creative Commons Attribution License, which permits unrestricted use, distribution, and reproduction in any medium, provided the original work is properly cited.

Nickel alloy electrodes both in plane and nanowire morphologies were fabricated by electrodeposition in sulfamate bath. With the increasing concentration of phosphorous acid in the electrolyte, the P content in the deposition increased accordingly. In the meantime, the grain refined and even became amorphous in microstructure as the P content was raised. For the nanowire electrode, vibrating sample magnetometer (VSM) measurement showed that its coercivity was anisotropic and decreased with P-content. In addition, the easy axis for magnetization of the electrode was parallel to the axial direction of nanowire. The electrocatalytic activity measurement of the electrode in 0.5 M H₂SO₄ electrolyte showed that the nanowire electrode had higher activity than the plane one, and the alloying of P in Ni electrode raised its hydrogen evolution reaction (HER) performance. The enhanced performance of nanowire electrode was attributed to the smaller and more uniform hydrogen bubbles generated in HER reaction. Finally, the applied magnetic field (3.2 T) improved significantly the HER activity of Ni but not Ni-P electrode. By using nanowire morphology and applying magnetic field, the current density at -0.75 V HER stability test of the Ni electrode increased fourfold more than its plane counterpart.

1. Introduction

Water electrolysis has been considered as one of the clean processes for producing hydrogen with less greenhouse effect, especially if the electricity is generated from renewable energy. Although the use of platinum electrode demonstrated the best electrocatalytic activity, the cost of this noble metal renders it difficult to be implemented for large scale production. Therefore, the research on the alternative electrode, which is more economic in industrial application, has been an important issue [1]. For water electrolysis, some of the control process parameters include type of electrolyte, electrode distance, temperature, and additives [2–4]. Nagai et al. reported the qualitative influences from the electrode space configuration, distance, and current density [2]. Other findings by Stojić and coworkers [3] and de Souza et al. [4] indicated that the ionic additive and shorter electrode distance improved the hydrogen evolution in KOH solution. The use of nickel-based electrode, including nickel, nickel

alloy, rare earth doped nickel, and porous nickel, has apparently raised the electrocatalytic activity in water electrolysis [5]. Another frequently studied nickel-based electrode is Ni-P alloy. Several control factors, such as phosphorus content, surface area, internal stress, hydrogen adsorption energy, and electron configuration, were identified. In basic electrolyte, Burchardt [6] reported that the electrocatalytic activity reached maximum of 17% of P and increased with the coating thickness. Among three Ni-P coatings with P content of 7, 20, and 28%, Królikowski and Wiecko [7] discovered that the crystalline Ni-7P in acidic electrolyte had better electrocatalytic property than its amorphous 20 and 28% counterparts. Sheredani and Lasia [8] proposed that the high electrocatalytic activity of amorphous Ni-P coating was indebted to its increase in surface area. A porous electrode surface was observed in the NiP₈ coating which demonstrated the best electrocatalytic activity among 8% to 23% electrodes. Associated with the increase in internal stress, the coating sometimes developed cracking and

raised the effective surface area. The electrocatalytic activity increased accordingly [9]. The increase in electrode surface area provided more space for hydrogen adsorption and, thereby, the electrocatalytic rate.

Nanomaterials, compared with its conventional bulk counterparts, possess relatively high specific surface area and surface atoms. These characteristics render them with superior electrocatalytic activity. For electrode materials in hydrogen evolution reactions, the enhancement in their activities by adopting nanomaterial fabricated from anodized aluminum oxide (AAO) has been frequently employed [10–13]. More than four-time increase in the current density of Ni electrode with nanowire configuration over its plane counterpart was reported by Lee et al. [11]. Chen and coworkers [12] studied the electrocatalytic activity of Ni nanowire exposed from the AAO template with different lengths. In 1 M Na_2SO_4 electrolyte, they found that the current density increased with longer nanowires exposed from the template. In the meantime, in 0.5 M H_2SO_4 electrolyte Hsu et al. [13] found the similar trend with Ni-P nanowires. Usually, the electrodeposited Ni-P nanowires had better HER performance than Ni nanowires.

To further enhance the HER activity, the use of magnetic field has been proposed. Iida and coworkers [14] and Matsushima et al. [15] discussed the effect of externally imposed magnetic field during hydrogen evolution reaction. Studied with different electrode distances and electrolytes, they reported that high magnetic field, small electrode distance, and low electrolyte concentration could provide better HER activity. They attributed this enhancement to the electrolyte convection caused by magnetohydrodynamics (MHD). In the KOH electrolyte with 2 mm electrode distance and 4 V overpotential, Lin and coworkers reported that the performance of ferromagnetic Ni plane electrode was better than paramagnetic platinum and graphite electrodes [16].

In nanoscale, Yu and coworkers [17] prepared a single crystalline and superparamagnetic Ni nanowire electrode with 1110 Oe coercivity, much higher than polycrystalline Ni nanowire. For Ni-P nanowire with diameter of 200 nm, Chiriac et al. [18] found the decrease in coercivity and increase in Curie temperature with phosphorus content. From the prior studies, it is understood that the HER catalytic activity is controlled by many parameters. Nevertheless, the considerations in practical application and cost should be emphasized. In this study, by combining the nanosized surface configuration of the electrode and the application of external magnetic field, both the increase in surface area and the enhancement of convection without additional constant input of energy should benefit the HER activity in water electrolysis. Therefore, the electrocatalytic activity of the electrodeposited Ni-P nanowires under the influence of magnetic field was investigated.

2. Experimental

With the same electroplating parameters, both plane and nanowire electrodes were fabricated in this study first. Subsequently, the electrochemical property and microstructure and surface morphology of the electrode were measured

TABLE 1: Plating parameters used in this study.

Parameter	Magnitude
Ni^{2+}	90 g/L
NiCl_2	3 g/L
H_3BO_3	40 g/L
H_3PO_3	0, 10, 20, 30, 40 g/L
Wetting agent	1 mL/L
Current mode	Square pulse 500 Hz
Current density	8 A/dm ²
Bath temperature	50°C

and examined. Field emission scanning electron microscope ((FESEM) JEOL 6700, Japan), X-ray diffractometer ((XRD) SHIMADZU XRD-6000, Japan), and high resolution transmission electron microscope ((HRTEM) JEOL JEM-2100F, Japan) were used for the structural examinations. The application of magnetic field with permanent magnet during HER activity measurement was employed to investigate its effect. In addition, the magnetic property of the electrode was tested using vibrating sample magnetometer ((VSM) Lake Shore 7407, USA).

2.1. Plane Electrode. The substrate used for the electroplating was 0.3 mm thick phosphor deoxidized copper plate (C1220P). Nickel pallets (S-rounds) with 25 mm diameter and 6 mm thickness were employed as anode. The substrate was cut into $1.5 \times 1.5 \text{ cm}^2$ and heat-treated at 200°C for one hour to remove the residual stress. Before electroplating, the substrate was polished with emery papers (no. 240~#1200), activated in 5% sulfuric acid solution, and rinsed with de-ionized water.

2.2. Anodized Aluminum Oxide (AAO) Template. The high purity aluminum foil (99.999%) was first annealed at 500°C in nitrogen atmosphere for 3 hours. The annealed aluminum foil was then ultrasonically cleaned for 5 min and wiped clean with alcohol. Inside an electrolyte with sulfuric acid, phosphoric acid, and deionized water in 40 wt% : 40 wt% : 20 wt% concentration, the aluminum foil was subsequently electropolished with 20 V voltage for 10 min. Following the rinse with de-ionized water, an anodizing treatment in 0.5 M oxalic acid solution at 4°C was performed. A DC power supply provided a 60 V voltage between the aluminum specimen and graphite electrodes for 3 hours. The thus formed aluminum oxide film was removed with 5 wt% NaOH solution. The specimen was then subjected to a second anodizing treatment for 4 hours. Since the oxidation was not yet complete through the thickness of the specimen, the residual aluminum substrate was dissolved away with 0.1 M $\text{CuCl}_2 \cdot \text{HCl}$ solution. After removing the barrier layer with 6 wt% phosphoric acid, the AAO template was obtained. However, for conducting current in later electrodeposition, a thin Au film was sputtered on one side of the template.

2.3. Electrodeposition of Ni Alloys in AAO Template. For the electrodeposition of Ni alloys in AAO template, a platinum plate was used as the anode. A square pulse with

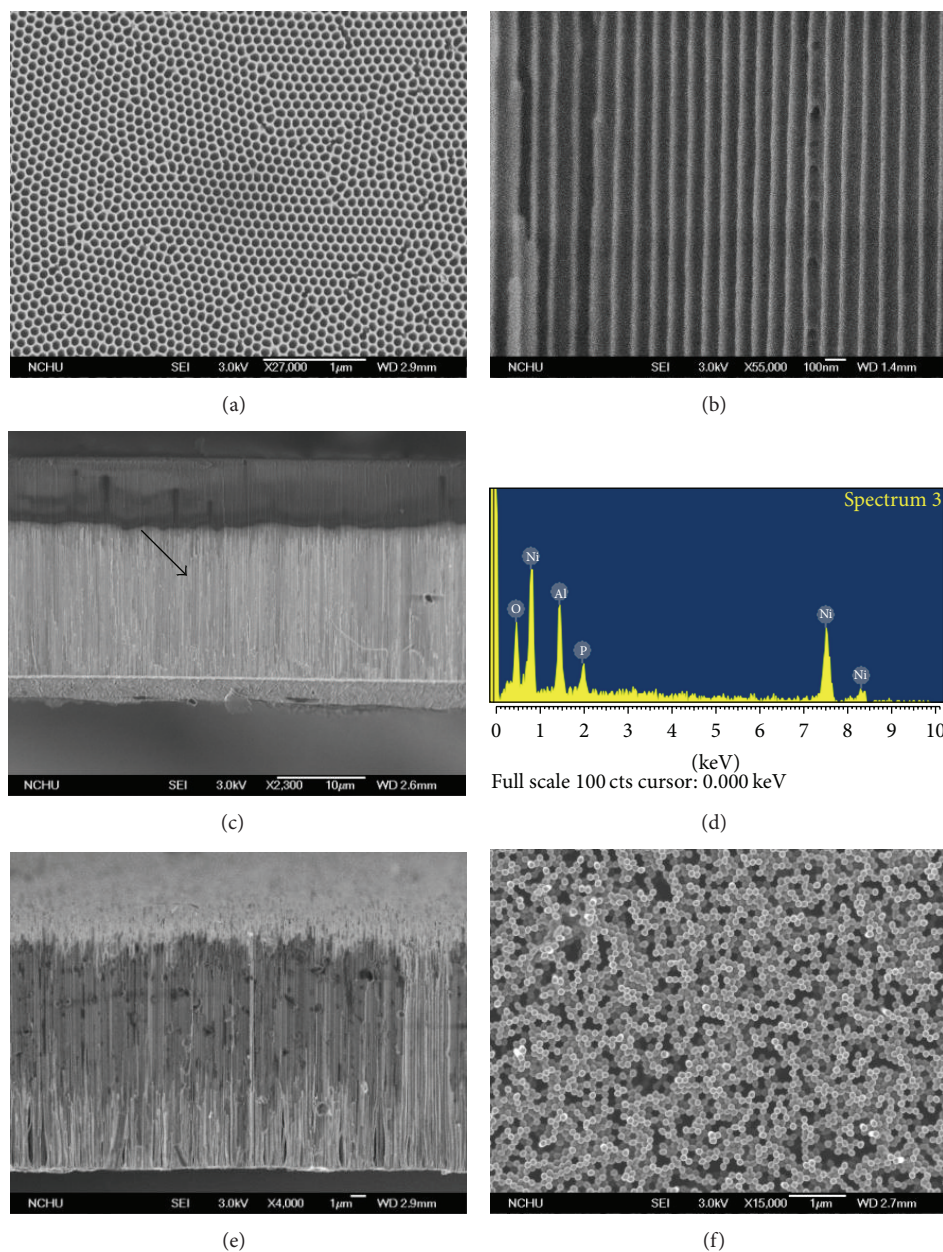


FIGURE 1: The microscopic examinations using field emission scanning electron microscope: (a) plane view of the AAO template, (b) longitudinal section of the AAO template, (c) longitudinal section of the nickel alloy nanopattern electrode, (d) EDS spectrum of nano pattern electrode, (e) longitudinal section of the nickel alloy nanowire electrode, and (f) plane view of the nickel alloy nanowire electrode.

peak current density of 8 A/dm^2 and frequency of 500 Hz was generated from a precision function generator (WAVE FACTORY WF1943, NF, Japan) and amplified through a power amplifier (NF TA-250, Japan). The nickel sulfamate electrolytes consisting of 90 g/L nickel ion, 40 g/L boric acid, 3 g/L nickel chloride, 1 ml/L wetting agent, and various (0~40 g/L) phosphorous acid concentrations for preparing different electrodes were employed, as listed in Table 1.

2.4. Electrochemical Measurement. A potentiostat (EG&G 263A, Princeton Applied Research, USA) and a three-electrode container were used in the electrochemical

measurement in this study. The prepared plane specimen or nanopatterned specimen was employed as the working electrode with 1 cm^2 exposed area in the $0.5 \text{ M H}_2\text{SO}_4$ electrolyte. A platinum wire with 0.5 mm in diameter and 25 cm in length and a saturated calomel electrode (SCE) served as the counter electrode and reference electrode, respectively. The specimen was first trimmed into 2.0 cm square and then rinsed fully with de-ionized water. The following electrochemical measurements were performed: (1) cathodic polarization curve scanned from 0 V to -0.9 V with scan rate of 1 mV/s ; (2) HER stability measurement conducted at fixed voltage of -0.75 V versus SCE for 6 hours.

TABLE 2: The P content of nanowires deposited from the bath with different H_3BO_3 concentrations.

H_3BO_3 concentration	0 g/L	10 g/L	20 g/L	30 g/L	40 g/L
P content (at%)	0%	9.76%	12.53%	15.44%	23.29%

3. Results

3.1. Morphology of AAO Template and the Fabricated Nanoelectrodes. The AAO template prepared from the aforementioned process is shown in Figure 1. It is seen that the holes were in parallel arrangement through the template thickness with 75 nm diameter, 115 nm pitch, 25 μm thickness, and $7.9 \times 10^9/\text{cm}^2$ areal density. Figure 1(c) reveals that the nanowires grew inside the nanopores from the bottom of the AAO template. The nominal dimensions of the nanowires were 75 nm in diameter and 15 μm in length, which corresponded to the approximate aspect ratio of 200. This prepared specimen was called Ni-P ($\text{Ni}_{100-x}\text{-P}_x$) alloy nanopattern electrode. The associated compositions measured from energy dispersive spectrometer (EDS) indicated four constituents—O, Al, Ni, and P, as presented in Figure 1(d). Disregarding the signals of Al and O, the P contents of the nanowires are presented in Table 2. The results show that the P content increased with the concentration of phosphorous acid used in the electrolyte. By submersing the nano pattern electrode in 5 wt% NaOH solution for sufficient duration, the AAO template was dissolved, and the nanowires were exposed. Finally, a Ni-P nanowire electrode was obtained, as presented in Figures 1(e) and 1(f).

3.2. Structural Examination on the Nanowires. The X-ray diffraction patterns of nickel alloy nanowires prepared in electrolyte with different phosphorous acid contents are shown in Figure 2. The broadening of the diffraction peaks for the electrode with increasing phosphorous acid content indicated that the grain was refined. Moreover, for the pure Ni coating the ratio between the (200) and (111) peak intensities was higher than that of powder nickel. This denoted that the prepared pure nickel coating at 8 A/dm² current density in this sulfamate bath had preferred (200) texture. However, it is apparently shown in Figure 2 that with the presence of phosphorous acid in the electrolyte the deposited coatings had nearly no (200) diffraction peak and changed their texture to (111). When the phosphorous acid content reached 40 g/L, almost no diffraction peak was detected, as shown in Figure 2(e), and the electrode became amorphous. According to the full width at half maximum of (111) diffraction peak and Scherrer formula [19], the calculated grain sizes of the electrodes were presented in Figure 3. Also shown in Figure 3 are the associated P contents in the electrodes. The results showed that the grain size decreased while the P content of the electrode increased with the addition of H_3PO_3 in the electrolyte.

The specimen for TEM examination was cut with ultramicrotome (Reichert-Jung Ultracut E, Austria) in 1 mm/s and thickness 700 Å, placed in copper grid, and air-dried.

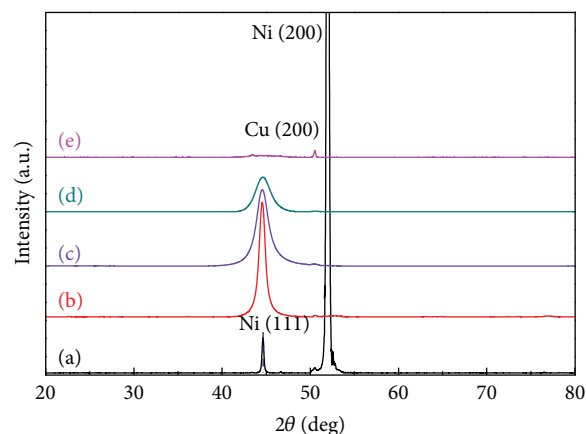


FIGURE 2: X-ray diffraction patterns of nickel alloy nanowires prepared in electrolyte with different phosphorous acid contents: (a) 0, (b) 10, (c) 20, (d) 30, and (e) 40 g/L.

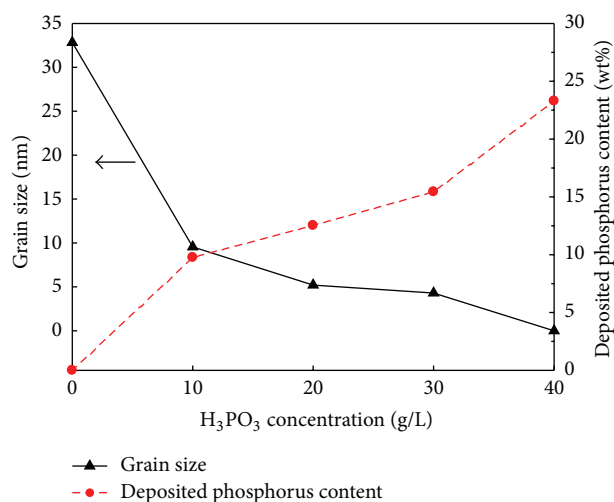


FIGURE 3: The influence of the H_3PO_3 concentration in the electrolyte on the grain size and deposited P content of the prepared electrode.

Figure 4(a) shows that electrodeposited nanowires adhered closely to the gold substrate. The line scan of the composition in Figure 4(b) revealed the traces of Au, O, Al, and Ni, which were the signals from substrate, AAO template, and nanowire, respectively. The TEM examination was also taken on the Ni-P nanowires embedded in the AAO template and was presented in Figure 4(c). The inset of this figure shows the selected area diffraction (SAED) pattern of the Ni-P nanowire. Apparently, the nanowire was amorphous in nature.

3.3. Magnetic Measurement on the Ni-P Nanowires. The magnetic characteristics of the prepared electrodes were measured by using a vibrating sample magnetometer (VSM). The specimen dimensions were 0.3 cm \times 0.3 cm \times 20 μm , and the temperature was at room temperature (300 K). To avoid the connection between nanowires due to overplating

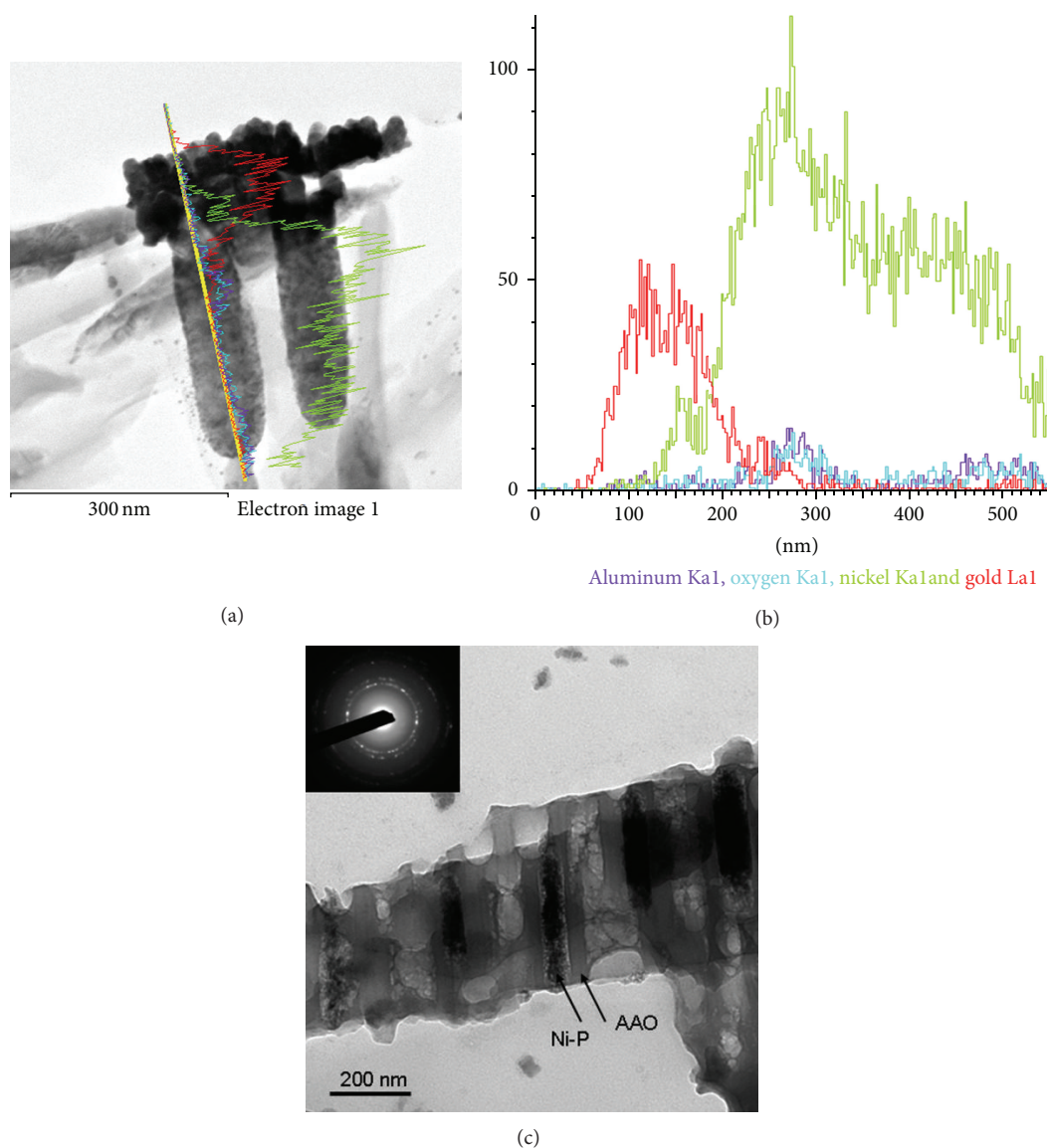


FIGURE 4: TEM micrographs of (a) Ni nanowires and (b) composition line scan in (a), (c) Ni-P nanowires in AAO template.

above the AAO template, the filled-in length of the nanowires was controlled to 15 μm nominally, as shown in Figure 2(c). For these nanopattern electrodes, the measurements were performed in H_{\perp} and H_{\parallel} directions, where H_{\perp} and H_{\parallel} denoted the directions of magnetic field in perpendicular and parallel to the plane of AAO template, respectively. In other words, H_{\perp} and H_{\parallel} were in parallel and perpendicular directions with the longitudinal axis of the nanowires, respectively. Figure 5 presents the measured hysteresis loops in H_{\perp} direction of the $\text{Ni}_{100-x}\text{P}_x$ electrodes. It is clearly seen that the hysteresis loop almost diminished and the coercivity decreased drastically with the increase of P-content in the nanowires. The nanowire with 23.29 at % P showed nearly no coercivity, and the amorphous nature of this Ni-P nanowire should be the main cause for this result. Similar measurements were also conducted in the H_{\parallel} direction, and the results are listed in Table 3. Because of the dimensional

anisotropy, the measured coercivities for pure Ni electrode in H_{\perp} and H_{\parallel} were 684.9 Oe and 117.9 Oe, respectively. Furthermore, the associated squarenesses were 0.866 and 0.068. These results revealed that the easy axis for magnetization of the electrode was parallel to the axial direction of nanowire [17]. Again, the coercivity decreased in both directions as the P content in the nanowires increased.

3.4. The Influence of Magnetic Field on the Electrocatalytic Activity. Three different morphologies of the electrodes were employed in the cathodic polarization measurements: plane, nanopattern, and nanowire. Figure 6(a) presents the polarization curves of the electrodes without the application of magnetic field. Considering the portion of the polarization curve at low potential (<0.75 V), the Ni-P electrode had higher current density, that is, higher electrocatalytic activity, than its Ni counterparts with corresponding electrode morphology.

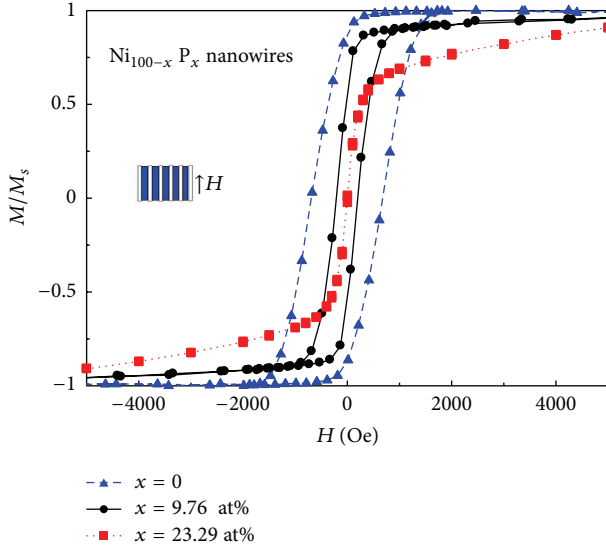


FIGURE 5: Hysteresis loops in H_{\perp} direction for Ni-P nanowires with different P contents.

Moreover, for both Ni and Ni-P electrodes the electrocatalytic activity of the electrode decreased in the following order: nanowire, nano pattern, and plane. These results should be attributed to the higher specific surface area of nanowire electrode and the more active catalytic property of the Ni-P alloy [8, 13].

Figure 6(b) presents the polarization curves of the electrodes measured under the applied magnetic field of 3.2 T. It can be seen that, although the current densities of the Ni nano pattern and nanowires were lower than their Ni-P counterparts at low potentials, they surpassed the latter at high potentials. The stronger coercivity of the Ni nanoelectrodes, as presented in Table 3, should induce higher magnetic field near the electrode. The enhanced local magnetic field could interact with the electrolyte and promote the magnetohydrodynamic motion. In this study, the direction of the applied magnetic field was set to generate Lorentz force which acted in the same direction with buoyancy. Thus, the Lorentz force facilitated the escape of hydrogen bubbles from the cathode surface and assisted the HER reaction. Consequently, the electrocatalytic activity increased under the influence of applied magnetic field accordingly [16].

4. Discussion

4.1. The Effect of Electrode Morphology on HER Activity. The better electrocatalytic performance of Ni-P alloy over its pure Ni counterpart was confirmed from the measurements presented in Figure 6(a). The electron transfer in Ni alloying with P [13, 20] and the change in crystalline texture of Ni-P with P content [21, 22] have been associated with the enhancement of this catalytic property. The grain refinement and even amorphism for the prepared Ni-P nanowires were confirmed through the XRD and TEM examinations shown in Figures 2–4. Moreover, the increase in specific surface area of the electrode by exposing longer nanowires contributes to

TABLE 3: Coercivity and squareness of Ni-P nanowires.

Nanowires $\text{Ni}_{100-x}\text{P}_x$ (at %)	Magnetization axis	Coercivity H_c (Oe)	Squareness (M_r/M_s)
$x = 0$	H_{\perp}	684.85	0.866
	$H_{//}$	117.86	0.068
$x = 9.76$	H_{\perp}	45.11	0.078
	$H_{//}$	4.36	0.0018
$x = 23.39$	H_{\perp}	7.05	0.0085
	$H_{//}$	2.63	0.0007

the improved HER activity [12]. However, based on solely the comparison the electrode surface area is not consistent with the results presented in Figure 6(a). The nano pattern electrode consists nominally of arrays of separated Ni area in 75 nm diameter, 115 nm pitch, and $7.9 \times 10^9/\text{cm}^2$ areal density. The thus calculated electrode surface area is only 36% of its plane counterpart. But the result in Figure 6(a) shows that the nanopattern electrode had better electrocatalytic property than the plane one. The mechanisms for this HER enhancement can be as follows.

It has been reported that the electric field concentration near the perimeter of the nanopatterned configuration can alter the overall current efficiency and raise HER activity of the electrode [13, 23]. In addition, a detailed examination on the evolution of hydrogen bubbles near the electrode at -0.75 V was performed with plane electrode and nanopattern electrode, respectively. Figure 7(a) shows the picture taken by a high speed CCD camera on the plane electrode. It was found that the bubbles of various sizes were elevated from the electrode surface. On the other hand, the bubbles generated from the nano pattern electrode were smaller in size and more uniform in size distribution, as shown in Figure 7(b). The smaller bubble should stay adjacent to the electrode surface in shorter duration, because it has less time to grow before escape from the electrode. The larger bubble takes more time to grow and blocks the electrode surface for longer duration. Therefore, with larger hydrogen bubbles over its surface, the plane electrode is not as active as the nano pattern electrode.

4.2. The Effect of Magnetic Field on HER Activity. As mentioned previously and shown in Figure 6(b), under the influence of applied magnetic field the paramagnetic Ni electrode enhanced its electrocatalytic activity. The stability of the electrodes in longer duration of HER reaction was further investigated. Figure 8 presents the monitored current density within 6-hour duration for electrode at constant -0.75 V potential in 0.5 M H_2SO_4 electrolyte. For plane electrode both with and without the applied magnetic field, the current density first decreased and then recovered gradually. However, under the influence of magnetic field, the electrode recovered its current density faster than under no magnetic field. After the initial stage, the applied magnetic field steadily enhanced the HER activity of the plane electrode. For the nanowire electrode, the effect of magnetic field was even more prominent. The measured current density was nearly double its magnitude with the application of magnetic field.

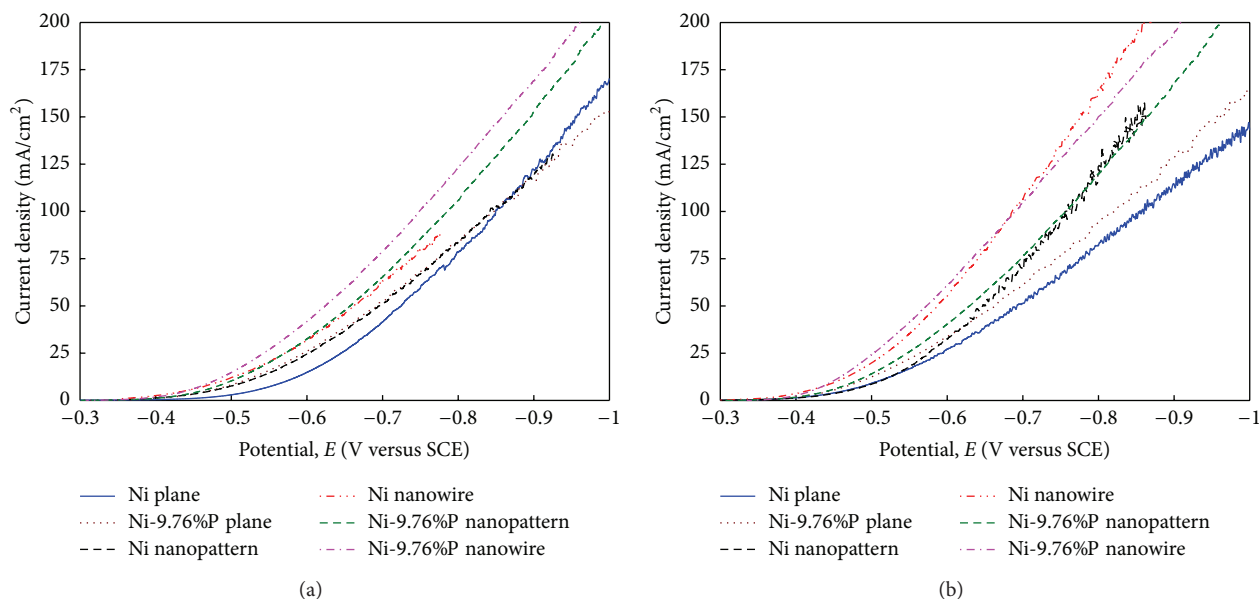


FIGURE 6: Cathodic polarization curves of Ni electrodes (a) without applied magnetic field, (b) with applied magnetic field of 3.2 T.

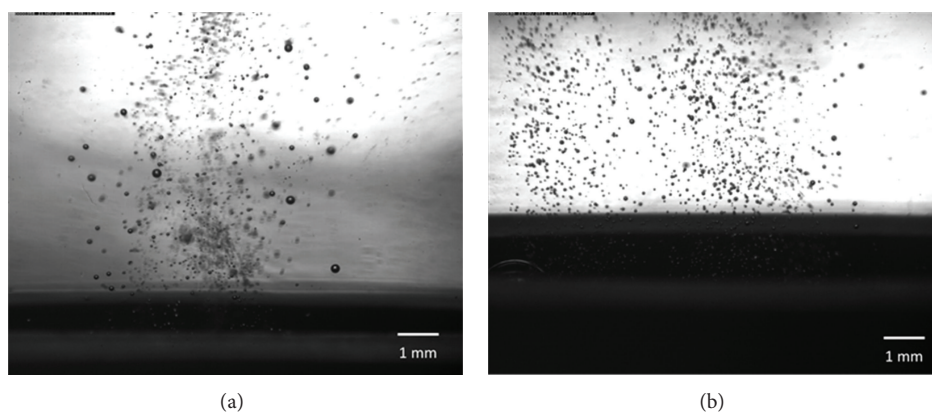


FIGURE 7: The evolution of the hydrogen bubbles over the electrode surface at constant -0.75 V potential: (a) plane electrode, (b) nanopattern electrode.

Nevertheless, the slope of i - t curves gradually decreased over time. Shown in Figure 9 are the FESEM micrographs of the specimens after this 6-hour stability test. It is obviously seen in Figure 9(a) that the remained length of the nanowires was $6\text{ }\mu\text{m}$, much shorter from its pristine length of $15\text{ }\mu\text{m}$. The top ends of the nanowires were broken which might be caused by its oxidation in acidic solution and became brittle in nature [13]. Figure 9(b) shows the aggregation of nanowires at their top ends after being dried out for SEM examination. Whether this aggregation persists when the electrode is submerged in the electrolyte is uncertain. Therefore, its effect on the HER activity is unclear. Despite this deterioration in electrode, the overall current density increased by fourfold with the introduction of nanowire morphology and magnetic field. Therefore, how to alleviate the electrode damage and prolong the electrode life should be topics for further study.

5. Summary

Different designs in electrode morphology by employing AAO template and the electrodeposition of Ni-P alloy were investigated herein along with the effect of applied magnetic field during HER reaction. The increased concentration of phosphorous acid in electrolyte during electrodeposition raised the P content and refined the grain size of the electrode. The electrocatalytic activity of the electrode was thus enhanced by the incorporation of P in the Ni substrate. Although the nanopattern electrode had less exposed electrode surface area than its plane counterpart during HER measurement, the smaller and more uniform bubbles generated by the evenly distributed reaction sites helped their quick escape from the electrode surface. Therefore, it could maintain highly active electrode surface without the blockade

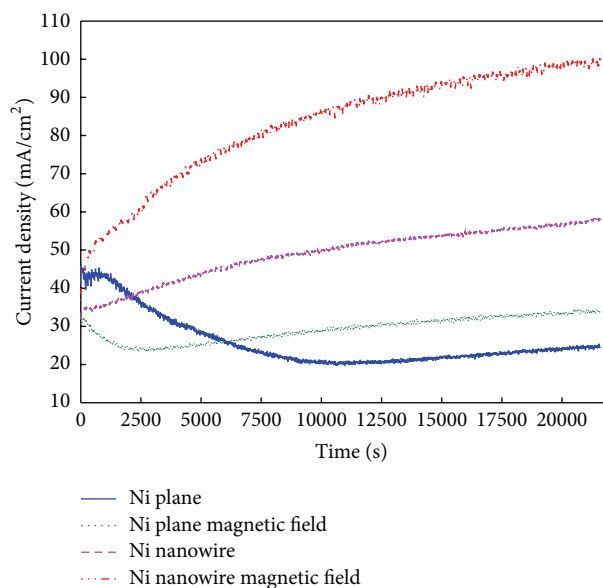


FIGURE 8: The measured i - t curves of Ni electrodes at constant -0.75 V potential.

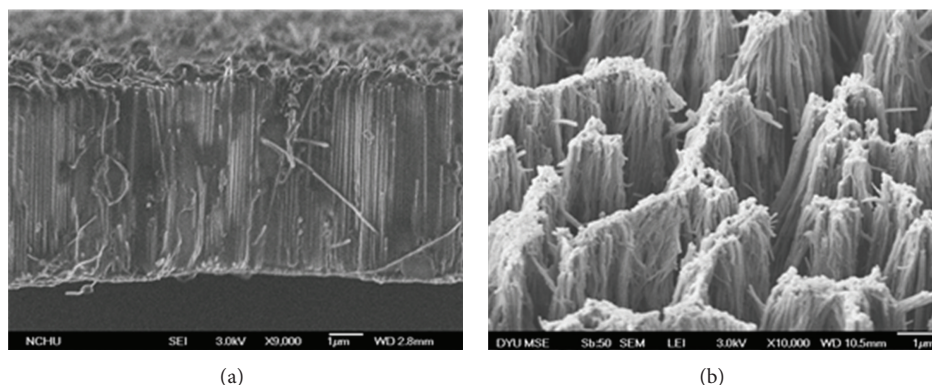


FIGURE 9: The FESEM micrographs of nanowire electrode after 6 hours of HER stability test at -0.75 V: (a) cross-sectional view, (b) top view.

of nonconducting bubbles adjacent to the electrode and show higher HER activity than the plane electrode. On the other hand, the P content decreased the coercivity of Ni-P alloy. The beneficial effect of applying magnetic field during HER reaction to increase the electrocatalytic activity was not as significant as the Ni electrode. With the use of nanowire Ni electrode and under the assistance of magnetic field, the current density of the HER reaction could be increased by fourfold over its plane electrode counterpart. Nevertheless, the damage of the nanowires over longer duration of HER reaction deteriorated the performance of the electrode. The prevention of this electrode deterioration needs further study.

Acknowledgment

The financial support provided by the National Science Council, Taiwan, under Grant no. NSC-98-2221-E-027-083-MY3 is gratefully acknowledged.

References

- [1] M. M. Jakšić, "Advances in electrocatalysis for hydrogen evolution in the light of the Brewer-Engel valence-bond theory," *International Journal of Hydrogen Energy*, vol. 12, no. 11, pp. 727–752, 1987.
- [2] N. Nagai, M. Takeuchi, T. Kimura, and T. Oka, "Existence of optimum space between electrodes on hydrogen production by water electrolysis," *International Journal of Hydrogen Energy*, vol. 28, no. 1, pp. 35–41, 2003.
- [3] D. L. Stojić, M. P. Marčeta, S. P. Sovilj, and Š. S. Miljanić, "Hydrogen generation from water electrolysis—possibilities of energy saving," *Journal of Power Sources*, vol. 118, no. 1-2, pp. 315–319, 2003.
- [4] R. F. de Souza, J. C. Padilha, R. S. Gonçalves, M. O. de Souza, and J. Rault-Berthelot, "Electrochemical hydrogen production from water electrolysis using ionic liquid as electrolytes: towards the best device," *Journal of Power Sources*, vol. 164, no. 2, pp. 792–798, 2007.

- [5] G. Lu, P. Evans, and G. Zangari, "Electrocatalytic properties of Ni-based alloys toward hydrogen evolution reaction in acid media," *Journal of the Electrochemical Society*, vol. 150, no. 5, pp. A551–A557, 2003.
- [6] T. Burchardt, "Hydrogen evolution reaction on NiPx alloys," *International Journal of Hydrogen Energy*, vol. 25, no. 7, pp. 627–634, 2000.
- [7] A. Królikowski and A. Wiecko, "Impedance studies of hydrogen evolution on Ni-P alloys," *Electrochimica Acta*, vol. 47, no. 13–14, pp. 2065–2069, 2002.
- [8] R. K. Shervedani and A. Lasia, "Studies of the hydrogen evolution reaction on Ni-P electrodes," *Journal of the Electrochemical Society*, vol. 144, no. 2, pp. 511–519, 1997.
- [9] H.-B. Lee, C.-H. Hsu, and D.-S. Wu, "A study on the hydrogen evolving activity of electroplated Ni-P coating by using the taguchi method," *Journal of New Materials for Electrochemical Systems*, vol. 14, no. 4, pp. 237–245, 2011.
- [10] H. Masuda and K. Fukuda, "Ordered metal nanohole arrays made by a two-step replication of honeycomb structures of anodic alumina," *Science*, vol. 268, no. 5216, pp. 1466–1468, 1995.
- [11] J. K. Lee, Y. Yi, H. J. Lee, S. Uhm, and J. Lee, "Electrocatalytic activity of Ni nanowires prepared by galvanic electrodeposition for hydrogen evolution reaction," *Catalysis Today*, vol. 146, no. 1–2, pp. 188–191, 2009.
- [12] P.-C. Chen, Y.-M. Chang, P.-W. Wu, and Y.-F. Chiu, "Fabrication of Ni nanowires for hydrogen evolution reaction in a neutral electrolyte," *International Journal of Hydrogen Energy*, vol. 34, no. 16, pp. 6596–6602, 2009.
- [13] C. S. Hsu, H. B. Lee, C. S. Lin, and C. Y. Lee, "Study on the electrodeposition of Ni-P nanowires and their electrocatalytic properties," *Metallurgical and Materials Transactions A*, vol. 41, no. 3, pp. 768–774, 2010.
- [14] T. Iida, H. Matsushima, and Y. Fukunaka, "Water electrolysis under a magnetic field," *Journal of the Electrochemical Society*, vol. 154, no. 8, pp. E112–E115, 2007.
- [15] H. Matsushima, D. Kiuchi, and Y. Fukunaka, "Measurement of dissolved hydrogen supersaturation during water electrolysis in a magnetic field," *Electrochimica Acta*, vol. 54, no. 24, pp. 5858–5862, 2009.
- [16] M.-Y. Lin, L.-W. Hourng, and C.-W. Kuo, "The effect of magnetic force on hydrogen production efficiency in water electrolysis," *International Journal of Hydrogen Energy*, vol. 37, no. 2, pp. 1311–1320, 2012.
- [17] C. Y. Yu, Y. L. Yu, H. Y. Sun et al., "Enhancement of the coercivity of electrodeposited nickel nanowire arrays," *Materials Letters*, vol. 61, no. 8–9, pp. 1859–1862, 2007.
- [18] H. Chiriac, A.-E. Moga, M. Urse, I. Paduraru, and N. Lupu, "Preparation and magnetic properties of amorphous NiP and CoP nanowire arrays," *Journal of Magnetism and Magnetic Materials*, vol. 272–276, pp. 1678–1680, 2004.
- [19] H. P. Klug and L. E. Alexander, *X-Ray Diffraction Procedures*, Wiley, New York, NY, USA, 2nd edition, 1974.
- [20] H. Ezaki, M. Morinaga, S. Watanabe, and J. Saito, "Hydrogen overpotential for intermetallic compounds, TiAl, FeAl and NiAl, containing 3d transition metals," *Electrochimica Acta*, vol. 39, no. 11–12, pp. 1769–1773, 1994.
- [21] I. Paseka, "Evolution of hydrogen and its sorption on remarkable active amorphous smooth NiP(x) electrodes," *Electrochimica Acta*, vol. 40, no. 11, pp. 1633–1640, 1995.
- [22] T. Burchardt, V. Hansen, and T. Vålund, "Microstructure and catalytic activity towards the hydrogen evolution reaction of electrodeposited NiPx alloys," *Electrochimica Acta*, vol. 46, no. 18, pp. 2761–2766, 2001.
- [23] C. S. Hsu, H. B. Lee, C. S. Lin, and C. Y. Lee, "The electrocatalytic activity of electrodeposited Ni-P micro-patterned structure in acidic solution," *Journal of Chinese Society of Mechanical Engineers*, vol. 32, pp. 103–109, 2011.

Research Article

The Development of Photocatalyst with Hybrid Material CNT/TiO₂ Thin Films for Dye-Sensitized Solar Cell

Yong Woo Kim¹ and Sang Hee Park²

¹ Green Energy Convergence Center, Kumoh National Institute of Technology, Daehak-ro 61, Gumi, Gyeongbuk 703-701, Republic of Korea

² Department of Mechanical Engineering, Kumoh National Institute of Technology, Gumi 703-701, Republic of Korea

Correspondence should be addressed to Sang Hee Park; parksh@kumoh.ac.kr

Received 9 November 2012; Revised 3 June 2013; Accepted 18 June 2013

Academic Editor: Jie-Fang Zhu

Copyright © 2013 Y. W. Kim and S. H. Park. This is an open access article distributed under the Creative Commons Attribution License, which permits unrestricted use, distribution, and reproduction in any medium, provided the original work is properly cited.

Dye-sensitized solar cell (DSSC) has big merits of simple manufacturing, low cost, and good applications. However, efficiency of DSSC is quite low compared with other solar cells based on silicon. Ability of electron delivery is important for improving the efficiency; therefore, CNT used as an electrode and transferring electrons and heat significantly easily can be highly expected to contribute to increase conversion efficiency of DSSC. In this paper, CNT was loaded on the photocatalyst of TiO₂ thin films in the range from 0 wt% to 0.01 wt%. CNT was treated with 60% nitric acid at 120°C for 6 hrs and performed on ball milling process for 3 hrs. Hybrid material was made of TiO₂ paste and CNT predispersed by mixing. To demonstrate the property of each sample, the analytical techniques including a spectrometer for transmission and surface resistance were used. The sample of higher concentration of CNT has low transmission but low resistance, besides we have researched a proper amount of CNT 0.001 wt% that can increase 1.5% conversion efficiency of DSSC.

1. Introduction

DSSCs based on nanostructure materials offer very low cost and relatively efficient photovoltaic energy conversion, it has attracted much attention in the last decade. The highest efficiency, to the best of our knowledge, reported on DSSCs was 11% obtained on nonporous TiO₂ by using ruthenium complex dye, containing I⁻/I₃⁻ redox couple electrolytes and platinum counter electrode [1].

There are several important aspects that need to be considered for a photocatalyst as TiO₂ in DSSC. Firstly, it must be able to transfer holes from the sensitizing dye after the dye has injected electrons into the TiO₂. Next, it must be able to be deposited within the nanocrystalline layer, and the methods used for the deposition will not dissolve and degrade the monolayer of dye on the TiO₂ nanocrystallites [2].

One of major variants of DSSC is that the dye which absorbed the light energy receives the electrons after they are transferred from ground state to excited state. The insertion of electron is done in such a short time as femtoseconds or

picooseconds, and the oxidized dyes are recycled in nanoseconds [3].

The recombination speed of the electrons that are disappeared as electrolytes through surface state is so slow as microseconds or milliseconds, resulting that most of the photoelectrons were inserted as the semiconductor does, while the rest that could not be inserted diminishes the solar cells' efficiency as it gets together again with electron holes [4]. If uses CNT, a composite which is useful for electrical and heat transmission can expect speed increase of electron injection speed than recombination speed and increase in efficiency of DSSC through more movement of electrons.

There had been lots of studies focused on carbon nanotube which is widely used in various applications such as Field Emission Display, Fuel Cell, Biosensor, and Atomic Force Microscopy [5]. In addition, nanotube has excellent electrical and mechanical properties and has larger aspect ratio than other conductive fillers which is proper structure for incorporating nanocomposites. With these superior properties, there are lots of trend to develop nanocomposites using nanotubes in and out of Korea [6–8].

The Multiwall Carbon nanotube (MWCNT) can function as a basic electrode as it can transfer electricity and heat easily. nanotube functions as an electrode that mutually penetrates through the wide surface of TiO_2 , as well as helping the electric charges to be extracted efficiently in dye layers. These electrodes are advantageous in solar light spectrum as it has very good transparency in long wavelength.

This paper is aiming at increasing moving speed of electrons that are generated in the dye using CNT/ TiO_2 thin films in the TiO_2 layers and thus generate current to enhance the efficiency of DSSC. However, though the more it has CNT's contents, the more it decreases the surface resistance, it should provide the optimum environment as it affects current generation through reducing the transmissivity. Also, measure transmissivity and surface resistance of composite film which is CNT acid treated and TiO_2 ; then, apply it to solar cell to evaluate its properties.

2. Theoretical Background

2.1. DSSC Principle and Structure. Figure 1 shows the operational principle and structure of DSSC. If visible rays are absorbed by *n*-type nanoparticles TiO_2 that dye molecules are chemically adsorbed on the surface, the dye molecules generate electron-hole pairs, and the electron were injected into the conduction band of semiconductor's oxides. These electrons that are injected into the semiconductor's oxide electrode generate current through each nanoparticles' interfaces. The holes that are made from dye molecules are deoxidized by receiving electrons, thus causing the DSSCs to begin to work [9].

2.2. CNT Dispersion. In the process of synthesis, CNT aggregation can be observed among each carbon nanotubes' particles. Also, in physical aggregation of micro level, each nanotubes as individual particles will be entangled and wound with each others, whereas chemical aggregation in nm level can be resulted from surface tension such as Vander Waals forces among molecules. As these kinds of aggregation hinder 3-dimensional network structures forming that can enhance mechanical strength and conductivity properties, it can be said CNT dispersion is a significant process [10].

The dispersion methods are mainly classified into three: chemical, physical, and solvent agent. First, chemical method uses mixed acids such as nitric acid or sulphuric acid to oxidize nanotubes' tip and surface chemically then introduces functional group that contains oxygen such as $-\text{C}=\text{O}$, $-\text{COOH}$, and $-\text{OH}$ [11]. By introducing acid functional group in nanotubes, it increases attraction with water molecules, while nanotubes are electrified negatively resulting electrostatic interaction. With this, we can get nanotube dispersion solution that shows no sedimentation and is stable. Second, there are methods in physical dispersion. The one is mechanical method that handles ultrasonic waves by mixing acetone and methanol, and the other one is ball milling that reduces length and diameter distribution. Final one is using solvent agents that melt down carbon nanotubes with SDS (sodium dodecyl sulfate) Triton X-100, LDS surfactant.

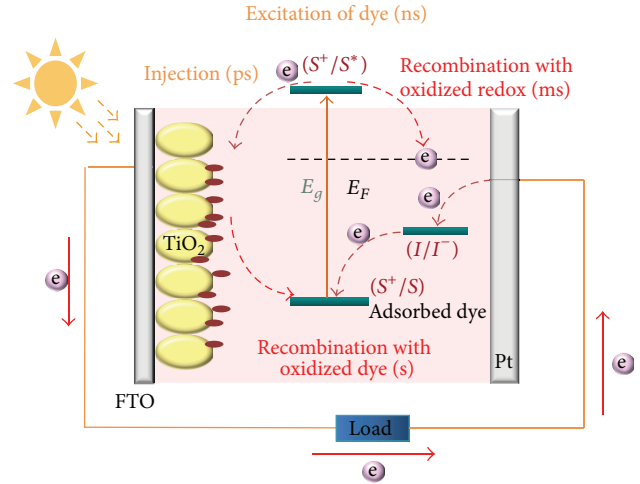


FIGURE 1: A schematic representation of the construction of a DSSC.

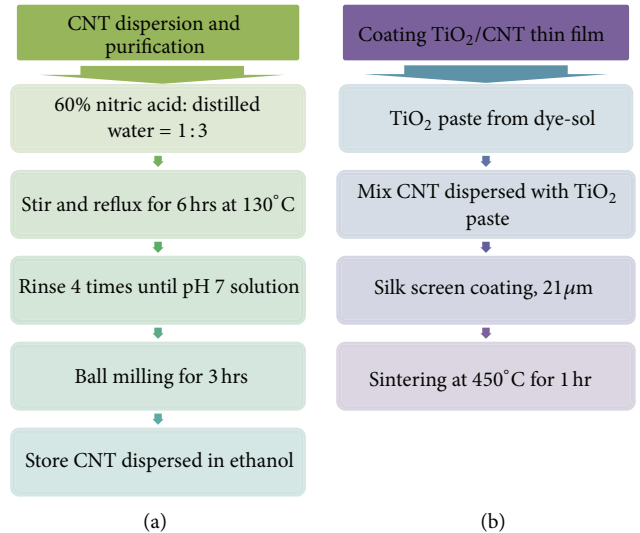


FIGURE 2: (a) Process of CNT dispersion and (b) fabricating TiO_2 thin film.

3. Experiment

3.1. CNT Dispersion. Figure 2(a) shows the dispersion process to protect CNT's aggregation. By mixing 60% nitric acid and distilled water with a proportion of 1:3, carry out reflux work intensely for an hour stirring at 130°C with an amount of 1 mg of CNT. After completion of this process, do ultrasonication about 1 hour using lots of distilled water; then, proceed to neutralization process until pH 7 of aqueous solution is reached using 1 mm diameter of PTFE thin films and vacuum pump. Acidulation with nitric acid makes multiple aggregations be released, and do 3-ball milling for 3 hours to reduce length and diameter effectively.

By filtering, get pure CNTs and follow ultrasonication process in 200 mL ethanol then store them. If CNT in ethanol does not get together and no visible particles are observed, it can be said the dispersion was successful. If CNT is not

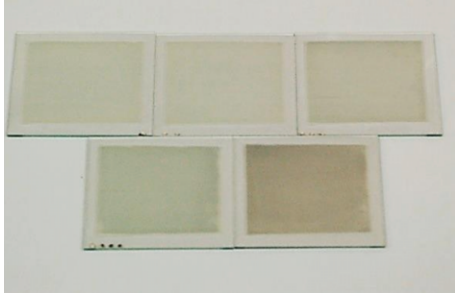


FIGURE 3: CNT/TiO₂ thin film according to each CNT wt%.

dispersed, it can cause the powder to be coagulated when it is mixed with TiO₂, which may lead to uneven coating on thin films in the process.

3.2. Manufacturing CNT/TiO₂ Thin Film. Figure 2(b) depicts composite thin films making process of CNT and TiO₂. To identify DSSC's characteristics according to CNT densities, mix 1 g of TiO₂ (dye-sol) with variable amount of dispersed CNT to make paste of 0.001%, 0.002%, 0.005%, and 0.010%. To make it have 49 mm² active area, carry out silk screening process until its thickness reaches 21 μ m. And to ensure even thickness, dry it with constant condition once coating is completed; then, sinter for 30 minutes at 250°C for 1 hour at 450°C.

Figure 3 shows coated plates by CNT concentrations, from which we can see that these plates with high content of CNT have thicker colors.

3.3. Manufacturing DSSC. Figure 4 shows a table about DSSC manufacturing process. CNT/TiO₂ board that is manufactured through sintering process is digested in N719 dyeing agent at room temperature for 12 hours. Using same process, coat Pt (Dye-sol) on FTO board; then, sinter for 1 hour at 450°C. With 40 μ m Surlyn sheet, two boards are sealed, and then inject electrolytes.

4. Results and Discussion

4.1. Change of Transmissivity of according to CNT Density. Figure 5 shows transmissivity difference of CNT/TiO₂ thin films by CNT contents. And we measured visible rays' transmissivity using UV/VIS/IR Spectrophotometer (Varian Cary 5000) in a range of 300 nm~800 nm. The more it has lots of CNT contents, it can be seen that the transmissivity is decreased steeply, and by adding small amount of CNT, there happens about 20% difference of thin films' transmissivity that has no CNT in total.

4.2. Surface Resistance Variance according to CNT Densities. Figure 6 shows electrochemical impedance spectra (EIS) using Solar Cell test station (MST-4000A). Impedances were measured under galvanostatic control of the cell. The amplitude of the sinusoidal voltage signal did not exceed 1 V. The current values were acquired by changing conditions

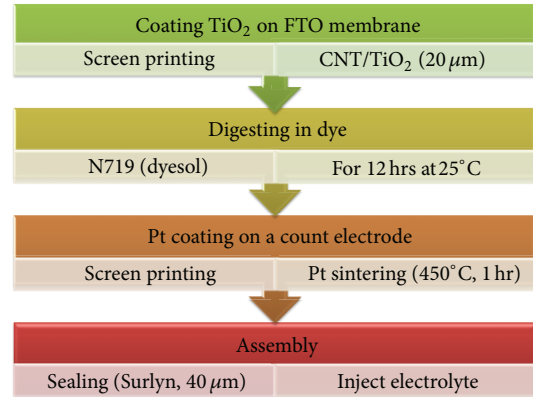


FIGURE 4: Manufacturing of dye-sensitized solar cell.

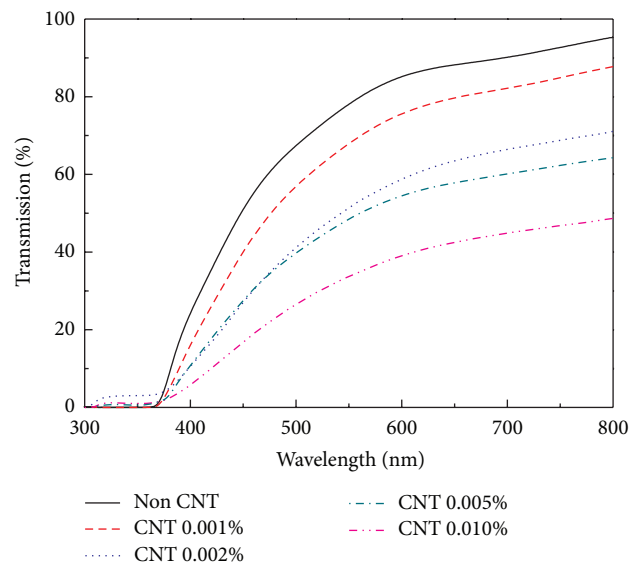


FIGURE 5: Transmission of CNT/TiO₂ thin film.

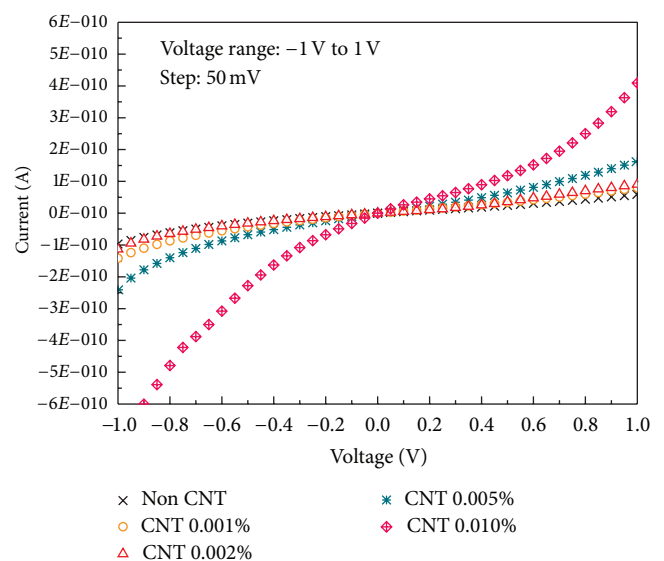


FIGURE 6: *I-V* curve for surface resistance of TiO₂ thin film.

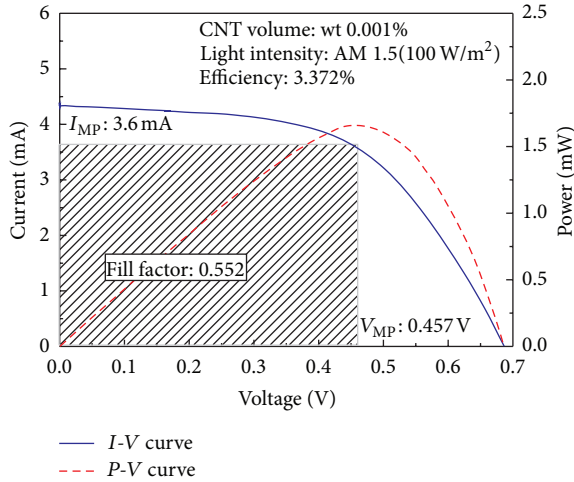


FIGURE 7: I-V/P-V curve of DSSC at CNT/TiO₂ 0.001%.

from -1 V to 1 V increasing by 50 mV intervals. The resulting impedance was analyzed based on electrical circuit element model. The value of the model elements was determined by fitting the experimental data. I - V curves for the thin films with various CNT content are displayed in Figure 4. As the density of CNT goes high, the slope of I - V curve begins to increase, whereas the resistance value goes down, and the values are almost proportional to the CNT added values. At the intermediated CNT loading of 0.01% , the maximum performance was found over whole current density regimes.

4.3. Efficiency Change according to CNT Densities. Figure 7 shows graphs of current and power according to voltage when the CNT density is 0.001% . The cell's energy transformation efficiency when the CNT is 0.001% showed the greatest efficiency (3.372%) than any other cells. We get voltage (V_{MP}) and current (I_{MP}) that can generate maximum power output, and by multiplying its values acquire power output, then calculate efficiency using ratios between incident rays energies (P_{in}) and generated electric energies (P_{out}).

4.4. Change by the Difference of I_{MP} and V_{MP} . Figure 8 shows change of I_{MP} and V_{MP} according to CNT densities. The I_{MP} value at 0.001% cell of CNT was 3.61 mA which is higher than the one (2.54 mA) of a cell that did not added CNT. However, as the density is increased more than that, the value decreases as 1.43 mA, 1.37 mA, and so forth, and the difference was found to be less than that of when it fell from 0.001% to 0.002% . This shows that CNT drops transmissivity to cause to reduce electron generation ratio whereas transfers more electrons, and when the CNT density is higher than 0.002% , the larger CNT contents reduce surface resistance, but the generated electrons becomes less as the transmissivity is very low. Furthermore, if this kind of trend assumed to be same as the one of power, we can guess that the current is more influential than that of voltage. And though V_{MP} values changes between 0.43 V~ 0.49 V by CNT densities, it cannot be said that it affects more as it may not differ significantly.

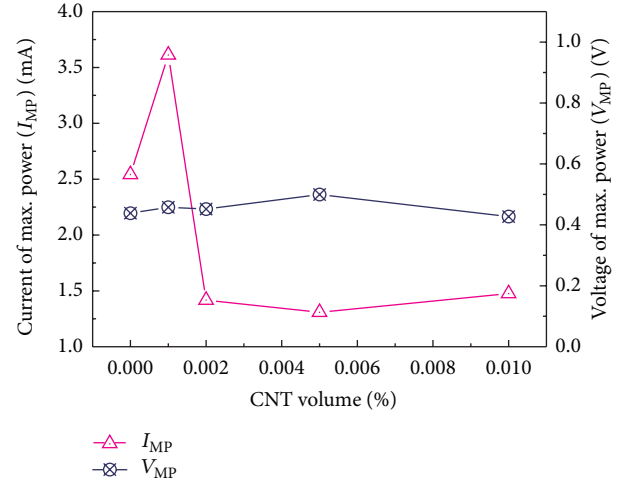


FIGURE 8: I_{MP} and V_{MP} of DSSC at each cell with different constant CNT.

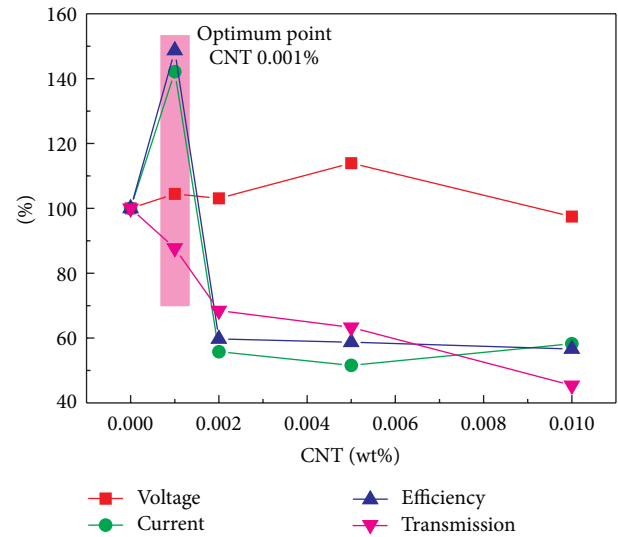


FIGURE 9: Determination of best CNT volume of DSSC.

5. Conclusion

Figure 9 shows graphs that compared transmissivity, efficiency, current, and voltage according to CNT densities when the cell that contains no CNT is to be 100% . This study tried to find out how to manufacture CNT/TiO₂ thin films that can enhance the transferring of electrons which were generated in dye as a variant that affects dye sensitized solar cell's efficiency then adopts it to cell to see the efficiency difference between transmissivity and surface resistance. Through this study, we derived conclusions as follows.

- (i) CNT/TiO₂ thin film reduces surface resistance, thus enhancing the transfer of electrons.
- (ii) As CNT decreases the transmissivity that leads to reduce the generated electric charges, it is found that wt 0.001% is most proper.

- (iii) The transforming efficiency of cells showed no significant difference among voltages, and seeing the same trend of current, it can be said that the current affects the efficiency.

References

- [1] B. Kılıc, E. Gur, and S. Tuzemen, "Nanoporous ZnO photoelectrode for dye-sensitized solar cell," *Journal of Nanomaterials*, vol. 2012, Article ID 474656, 7 pages, 2012.
- [2] M. N. Amalina, N. A. Rasheid, and M. Rusop, "The properties of sprayed nanostructured p-type CuI films for dye-sensitized solar cells application," *Journal of Nanomaterials*, vol. 2012, Article ID 637637, 6 pages, 2012.
- [3] J. Teuscher, J. D. Decoppet, A. Punzi, S. M. Zakeeruddin, J. E. Moser, and M. Gratzel, "Photoinduced interfacial electron injection dynamics in dye-sensitized solar cells under photovoltaic operating conditions," *The Journal of Physical Chemistry Letters*, vol. 3, no. 24, pp. 3786–3790, 2012.
- [4] A. Hinsch, J. M. Kroon, R. Kern et al., "Long-term stability of dye-sensitized solar cells," *Progress in Photovoltaics*, vol. 9, no. 6, pp. 425–438, 2001.
- [5] K. Tagami, N. Sasaki, and M. Tsukada, "Simulated nc-AFM images of Si(001) surface with nanotube tip," *Applied Surface Science*, vol. 172, no. 3–4, pp. 301–306, 2001.
- [6] X. Gong, J. Liu, S. Baskaran, R. D. Voise, and J. S. Young, "Surfactant-assisted processing of carbon nanotube/polymer composites," *Chemistry of Materials*, vol. 12, no. 4, pp. 1049–1052, 2000.
- [7] H. Koerner, G. Price, N. A. Pearce, M. Alexander, and R. A. Vaia, "Remotely actuated polymer nanocomposites stress-recovery of carbon-nanotube-filled thermoplastic elastomers," *Nature Materials*, vol. 3, no. 2, pp. 115–120, 2004.
- [8] J. K. W. Sandler, J. E. Kirk, I. A. Kinloch, M. S. P. Shaffer, and A. H. Windle, "Ultra-low electrical percolation threshold in carbon-nanotube-epoxy composites," *Polymer*, vol. 44, no. 19, pp. 5893–5899, 2003.
- [9] Y. Liu, J. R. Jennings, S. M. Zakeeruddin, M. Gratzel, and Q. Wang, "Heterogeneous electron transfer from dye-sensitized nanocrystalline TiO_2 to $[\text{Co}(\text{bpy})_3]^{3+}$: insights gained from impedance spectroscopy," *Journal of the American Chemical Society*, vol. 135, no. 10, pp. 3939–3952, 2013.
- [10] N. Grossiord, O. Regev, J. Loos, J. Meuldijk, and C. E. Koning, "Time-dependent study of the exfoliation process of carbon nanotubes in aqueous dispersions by using UV-visible spectroscopy," *Analytical Chemistry*, vol. 77, no. 16, pp. 5135–5139, 2005.
- [11] D. B. Mawhinney, V. Naumenko, A. Kuznetsova, J. T. Yates Jr., J. Liu, and R. E. Smalley, "Surface defect site density on single walled carbon nanotubes by titration," *Chemical Physics Letters*, vol. 324, no. 1–3, pp. 213–216, 2000.

Research Article

Preparation of Smooth Surface TiO₂ Photoanode for High Energy Conversion Efficiency in Dye-Sensitized Solar Cells

Sasipriya Kathirvel,¹ Huei-Siou Chen,¹ Chaochin Su,¹ Hsiue-Hsyan Wang,¹ Chung-Yen Li,² and Wen-Ren Li²

¹ Institute of Organic and Polymeric Materials, National Taipei University of Technology, Taipei 10608, Taiwan

² Department of Chemistry, National Central University, Chung-Li 32001, Taiwan

Correspondence should be addressed to Chaochin Su; f10913@ntut.edu.tw and Wen-Ren Li; ch01@ncu.edu.tw

Received 14 December 2012; Accepted 2 April 2013

Academic Editor: Wen Zeng

Copyright © 2013 Sasipriya Kathirvel et al. This is an open access article distributed under the Creative Commons Attribution License, which permits unrestricted use, distribution, and reproduction in any medium, provided the original work is properly cited.

Dye-sensitized solar cells (DSSCs) based on a TiO₂ photoanode have been considered as an alternative source in the field of renewable energy resources. In DSSCs, photoanode plays a key role to achieve excellent photo-to-electric conversion efficiency. The surface morphology, surface area, TiO₂ crystal phase, and the dispersion of TiO₂ nanoparticles are the most important factors influencing the properties of a photoanode. The smooth TiO₂ surface morphology of the photoanode indicates closely packed arrangement of TiO₂ particles which enhance the light harvesting efficiency of the cell. In this paper, a smooth TiO₂ photoanode has been successfully prepared using a well-dispersed anatase TiO₂ nanosol *via* a simple hydrothermal process. The above TiO₂ photoanode was then compared with the photoanode made from commercial TiO₂ nanoparticle pastes. The morphological and structural analyses of both the aforementioned photoanodes were comprehensively characterized by scanning electron microscopy and X-ray diffraction analysis. The DSSC fabricated by using a-TiO₂ nanosol-based photoelectrode exhibited an overall light conversion efficiency of 7.20% and a short-circuit current density of 13.34 mA cm⁻², which was significantly higher than those of the DSSCs with the TiO₂ nanoparticles-based electrodes.

1. Introduction

Much interest has been focused on the development of dye-sensitized solar cell (DSSC) technology, due to its low cost and easy fabrication with excellent photo-to-electric conversion efficiency [1–5]. Recently, the maximum photo-to-electric conversion efficiency of DSSCs was reported to exceed 13% at 509 W/m² simulated solar intensity [5]. Even though DSSCs have their unique advantages, further improving the efficiency is still a key challenge [6–8]. The DSSCs were composed of a photoanode, a sensitizer, a redox-coupled electrolyte, and a counter electrode [9]. Among them, the photoanode is the main component in DSSC and it significantly influences the photo-to-electric conversion efficiency of the cell, due to its dye loading, electron transportation, and electron collection characteristics [10, 11]. The photogenerated electron transport and collection are slow in the nanoparticles-based photoanode due to the

recombination of electrons [7, 12]. Hence, a well performing photoanode with desirable properties, such as high surface area, smooth surface morphology with less grain boundaries for fast electron transport, is essential for the development of a high performance solar cell [13–15].

The nanocrystalline TiO₂ film is one of the most commonly employed photoanode materials in DSSCs due to its excellent optoelectronic properties [16]. TiO₂ nanomaterials mainly exist as anatase, rutile, and brookite crystalline phase and anatase TiO₂ phase has been mostly utilized in DSSCs application [17]. Even though the rutile TiO₂ is thermodynamically stable, it possesses a smaller surface area, larger crystallite size, and lower Fermi energy level, compared to anatase TiO₂ [18, 19]. The surface morphology, particle size, surface area, porosity, crystalline phase, and dispersion of TiO₂ nanoparticles are the various influencing factors which determine the performance of a photoanode [20–22]. For instance, Park et al. investigated the effect of both

base-treated and acid-treated TiO_2 to analyze the effect of particle size, shape, film porosity, and surface structure on the performance of DSSCs [23]. For a typical photoanode, TiO_2 nanoparticle film with a thickness of 12–14 μm was utilized for highly efficient DSSCs [9]. So far, TiO_2 nanoparticle films were fabricated using the pastes prepared from TiO_2 nanopowders. Ito et al. have studied the homogenization effect of a different TiO_2 pastes by dispersing TiO_2 powders *via* both ball-milling and mortar-grinding route, in which the monodispersed particles were obtained by the former process [24]. Lee et al. studied the influence of the surface morphology of the TiO_2 film on the performance of DSSC, in which the TiO_2 paste was prepared using a poly(ethylene glycol) binder [25]. Dhungel and Park fabricated DSSCs using different TiO_2 pastes by varying the proportion of nanocrystalline particles of TiO_2 with particle size distribution in a wide range [26]. The TiO_2 film morphology, interparticle interaction, and the connection between the TiO_2 film and conductive substrate are essential for the better dye adsorption and transportation of electrons to the counter electrode with reduced charge recombination. Hence, it is very important to prepare the TiO_2 film with highly dispersed TiO_2 nanoparticles. The preparation of unagglomerated TiO_2 paste from the homogeneous TiO_2 suspension is one of the approaches to obtain a desired TiO_2 film. Jeong et al. used a TiO_2 colloidal suspension to prepare an α -terpineol-based TiO_2 paste and compared with the commercial dyesol TiO_2 paste [27]. Based on the above considerations, in order to obtain an effective TiO_2 photoanode, the preparation of different types of TiO_2 pastes using the TiO_2 nanosol and TiO_2 nanopowders was carried out.

In the present investigation, the TiO_2 nanosol was prepared by hydrothermal process using titanium (Ti) precursor and its effect on the performance of DSSCs was evaluated. The TiO_2 nanosol-based pastes were compared with the TiO_2 nanopowders-based pastes. The photovoltaic performance indicated that the anatase TiO_2 nanosol-based photoelectrode exhibited higher photocurrent density and higher efficiency than that of the photoelectrode using TiO_2 nanoparticles. This result may be attributed to the large amount of dye adsorption on the TiO_2 nanosol which has higher surface area with highly dispersed uniform a- TiO_2 particles.

2. Experimental Procedure

2.1. Materials. Titanium (IV) n-butoxide (TnB, 99%, ACROS) and acetic acid (99.8%, Scharlau, analytical grade), were used for the synthesis of TiO_2 . P25 (Degussa, Germany), ST-01 (Ishihara Sangyo, Japan), and ST-21 (Ishihara Sangyo, Japan) commercial TiO_2 nanoparticles were used for the comparison analysis. Ethyl cellulose (45 cp and 10 cp) and α -terpineol were used for the preparation of TiO_2 pastes.

2.2. Preparation of TiO_2 Nanosol. Titanium (IV) n-butoxide was added slowly into the acetic acid (2 M) solution. The solution was stirred for 4–5 days until obtaining a translucent

white solution. Then, the mixture was hydrothermally treated at 200°C for 5 h. The obtained white precipitate solution was cooled to room temperature, centrifuged, and washed once with distilled (DI) water and twice with ethanol. The centrifuged white precipitate was dispersed into 40 mL of anhydrous ethanol and kept stirring for one day. Subsequently, the centrifuged white precipitate was dispersed into 40 mL of anhydrous ethanol and kept stirring for one day. This sample is hereafter named as anatase TiO_2 (a- TiO_2) nanosol (NS) because of its anatase crystal phase.

2.3. Preparation of a- TiO_2 Nanosol-Based Paste. To prepare a- TiO_2 nanosol-based paste, the obtained precipitate after hydrothermal treatment was centrifuged/washed and dispersed into anhydrous ethanol under stirring for 24 h and sonicated further for proper homogeneous dispersion. Then, 25.96 g of α -terpineol and the mixture solution of two viscosities of ethyl cellulose (10 cp–1.8 g and 45 cp–1.4 g) in anhydrous ethanol (29 g) were added into the above solution, followed by repeated sonication for three times. The above solution was evaporated using the rotary evaporator at 40°C until to obtain a viscous paste. Finally, the paste was rolled using three-roller miller.

2.4. Preparation of TiO_2 Nanoparticles-Based Paste. Little modifications were carried out for the preparation of TiO_2 paste using TiO_2 nanoparticles, namely, P-25, ST-01, and ST-21. Briefly, 6 gram of TiO_2 nanoparticles was dispersed into the mixture of DI water, acetic acid, and anhydrous ethanol. Then the mixture was kept stirring for 24 h and sonicated for 5 min. Furthermore, the solution was sonicated 5 min followed by the addition of α -terpineol and again sonicated for 5 min after adding ethyl cellulose. The remaining procedure is the same as mentioned above in the preparation of TiO_2 nanosol paste.

2.5. Preparation of TiO_2 Photoanode and Solar Cell Assembly. Fluorine doped tin oxide (FTO, Solaronix, $8\ \Omega\text{cm}^{-2}$) conducting glass was cleaned in detergent liquid, distilled water, acetone and methanol using an ultrasonic bath each for 30 min. Then the TiO_2 paste was screen printed (Screen Printing Machine, Weger, WE-400F, Guger Industries Co., Ltd.) on cleaned FTO substrate and dried at 110°C. The process was repeated until to achieve 6 μm thick TiO_2 layer. The TiO_2 films were annealed with a programmable heating process: at 110°C for 30 min, 125°C for 15 min, 325°C for 5 min, 375°C for 5 min, 450°C for 15 min, and 500°C for 15 min. The working area of the TiO_2 films was 0.16 cm^2 . The TiO_2 electrodes were cooled to 80°C and then immersed in 0.3 mM N719 dye in acetonitrile/*tert*-butyl alcohol (1:1) for 36 h. The sensitized photoanodes and the platinum (Pt, 20 nm, ion beam sputtering E-105) sputtered FTO substrates were sandwiched together using 60 μm surlyn spacers. The ionic electrolyte consisting lithium iodide, iodide, and 4-*tert*-butylpyridine in acetonitrile was introduced into the hole predrilled on the counter electrode. Finally the hole was sealed using 30 μm surlyn and cover glass.

2.6. Characterization of Samples and Device. The particle size and the morphology of the TiO_2 nanoparticles were analyzed by transmission electron microscopy (TEM, Hitachi, H-7100). The surface morphology of TiO_2 films was studied by scanning electron microscopy (SEM, Hitachi, S-4800). X-ray diffraction (XRD, Rigaku PANalytical X'Pert PRO) measurement was carried out with $\text{Cu K}\alpha$ radiation. The surface area analysis of the TiO_2 nanoparticles was obtained using Brunauer-Emmett-Teller (BET, Micromeritics, Gemini V, ASAP-2010) surface area analyzer, in which all the samples were degassed prior to analyzes. The reflectance UV-visible spectrum was obtained using a Shimadzu UV-3600 spectrometer with an integrating sphere. The amount of adsorbed dye was determined by desorbing the dye from a- TiO_2 surface into a solution of 0.1M NaOH. The concentration of the adsorbed dye was analyzed by UV-visible spectrophotometer (JASCO, V-630). The current-voltage (I - V) characteristics of the cell under one sun irradiation (AM 1.5 filter-Oriel, #81094) using solar simulator with 300 W Xenon lamp (Oriel #91160) were obtained by applying external bias to the cell, and the generated photocurrent was measured by a Keithley model 2400 digital source meter. The incident photon-to-current efficiency (IPCE) was obtained by Model SR830 DSP Lock-In Amplifier and a Model SR540 Optical Chopper (Stanford Research Corporation, USA), a 150 W Xenon lamp and power supply (Oriel, #66902), and a monochromator (Oriel CornerstoneTM 130).

3. Results and Discussions

3.1. Structural Characterization of TiO_2 Nanoparticles and TiO_2 Films. The anatase TiO_2 (a- TiO_2) nanosol prepared by hydrothermal process was used to prepare TiO_2 paste (nanosol-based TiO_2 paste). The commercially available TiO_2 nanoparticles (P-25, ST-01, and ST-21) were concomitantly utilized to prepare TiO_2 pastes (nanoparticle-based TiO_2 pastes) by similar procedure (Section 2.4). Both types of TiO_2 pastes were screen-printed on FTO substrate and annealed with stepwise heating process in order to compare the effect of TiO_2 photoanodes prepared from nanosol-based TiO_2 paste and nanoparticle-based TiO_2 pastes in DSSCs. Figure 1 shows the typical SEM photographs of nanosol-based TiO_2 film (NS film) and nanoparticle-based TiO_2 films (P-25 film, ST-01 film, and ST-21 film) with two kinds of magnifications. The noteworthy difference in the morphology of NS film (Figure 1(a)) and nanoparticle-based TiO_2 films (Figures 1(b)–1(d)) could be observed instantaneously from the SEM images with lower magnifications ($\times 5,000$). The NS film (Figure 1(a)) is extremely smooth and uniform. This result indicates that the highly dense TiO_2 particles formed are homogeneously dispersed throughout the NS film.

It can be further confirmed by the higher resolution SEM image (Figure 1(e), $\times 50,000$). Comparatively, all the nanoparticle-based TiO_2 films show rough surface morphology which is evident in the higher magnification images (Figures 1(f)–1(h)). For P-25 film (Figures 1(b) and 1(f)), some voids between the closely packed TiO_2 nanoparticles were observed on the porous TiO_2 layers. The ST-21 film (Figures

1(d) and 1(h)) surface is rough with TiO_2 aggregates of about 300 nm. In the case of ST-01 film, a completely clumpy and nonuniform surface morphology was observed. The clumpy structure is formed by aggregation of TiO_2 particles of size from submicron to several microns. The observation of individual TiO_2 nanoparticles is hardly distinguishable.

This result is consistent with the surface-profiling measurement (results not shown here) in which the screen printed TiO_2 film made from nanosol-based TiO_2 paste is relatively flat compared with that made from nanoparticle-based TiO_2 pastes. For comparison, the thickness of TiO_2 films from nanosol-based TiO_2 paste and nanoparticle-based TiO_2 pastes were all controlled at about 6 μm .

It is concluded from the aforementioned SEM analysis that the nanosol-based TiO_2 electrode reveals smoother surface morphology characteristics in comparison with the nanoparticle-based TiO_2 electrodes. This can be insight by investigation of the size and surface morphology of TiO_2 nanoparticles. Figure 2 shows the TEM micrographs of (a) TiO_2 nanosol, (b) P-25, (c) ST-01, and (d) ST-21 samples. The TiO_2 particles in TiO_2 nanosol are well-dispersed irregular polyhedron which is typical for anatase phase TiO_2 . Similar TEM morphologies are observed for commercial TiO_2 nanoparticles except for ST-01, where severe agglomeration occurs presumably due to the extremely small TiO_2 particle size. The average particle size of P-25, ST-01, and ST-21 samples is ~ 35 nm, 5 nm, and 27 nm, respectively. The size of TiO_2 nanoparticles (TiO_2 -NP, TEM not shown) worked out (just drying) from TiO_2 nanosol is ~ 20 nm. The particle size of TiO_2 can also be estimated from BET surface area measurement. The TiO_2 -NP, P-25, ST-01, and ST-21 nanoparticles possess specific surface area of 108.5, 51.6, 247.9, and 65.1 m^2/g , respectively, which is consistent with the TEM size measurement. The results of TiO_2 particle size calculated from TEM and BET are also summarized in Table 1 and compared with the crystalline size obtained from XRD.

The TEM particle size analysis was also performed for TiO_2 samples after sintering at 500°C in order to imitate the annealing process after screen-printing the TiO_2 pastes onto FTO substrate. The particle size is marginally enlarged. The average particle size of TiO_2 -NP, P-25, ST-01, and ST-21 samples after sintering is ~ 35 nm, 42 nm, 27 nm, and 39 nm, respectively (Table 1).

Consistent with TEM analysis, the surface area from BET measurement decreased to 82.3, 51.3, 99.5, and 58.6 m^2/g . The ST-01 TiO_2 is more dispersed. It is expected that the growth of TiO_2 nanoparticles upon high temperature heat treatment may lead to the clumpy surface morphology of TiO_2 electrodes as seen from SEM images (Figure 1) for P-25 film, ST-01 film, and ST-21 film. As for the NS-film, the as-synthesized TiO_2 nanoparticles in a- TiO_2 nanosol were evenly well dispersed with unique morphological configuration on FTO. Although the heat-induced aggregation may occur to some extent after annealing, it does not significantly affect the surface morphology. Both TEM characterization and BET analysis reveal that the utilization of TiO_2 nanosol is more desirable than the TiO_2 nanoparticles for the fabrication of TiO_2 films.

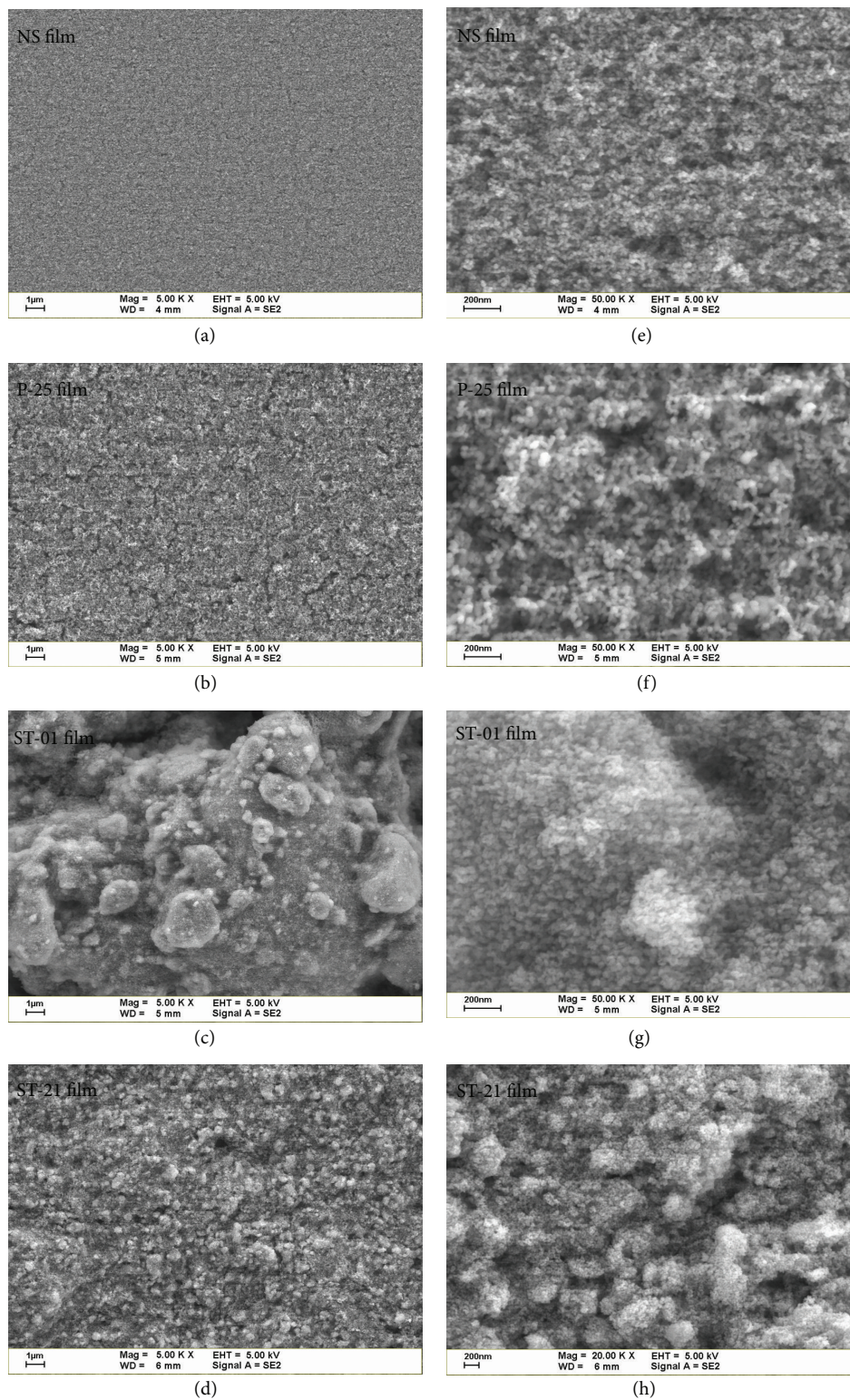


FIGURE 1: SEM images of (a) a- TiO_2 nansol film, (b) P-25 TiO_2 film, (c) ST-01 film, and (d) ST-21 film, ((e), (f), (g), and (h)) SEM images at higher magnification ($\times 20,000$) of samples (a), (b), (c), and (d), respectively.

TABLE 1: Crystallite size, particle size, and specific surface area of various TiO₂ nanoparticles.

Sample	Crystallite size (nm) * film	Particle size (nm) (before sintering) TEM	Particle size (nm) (after sintering) TEM	BET (m ² /g) (before sintering)	BET (m ² /g) (after sintering)
TiO ₂ -NP	20	20 (NS)	35	108.5	82.3
P-25	21 (anatase) 70 (rutile)	35	42	51.6	51.3
ST-01	7	5	27	247.9	99.5
ST-21	21	27	39	65.1	58.6

* Represents for film, NS indicates for TiO₂ nanosol.

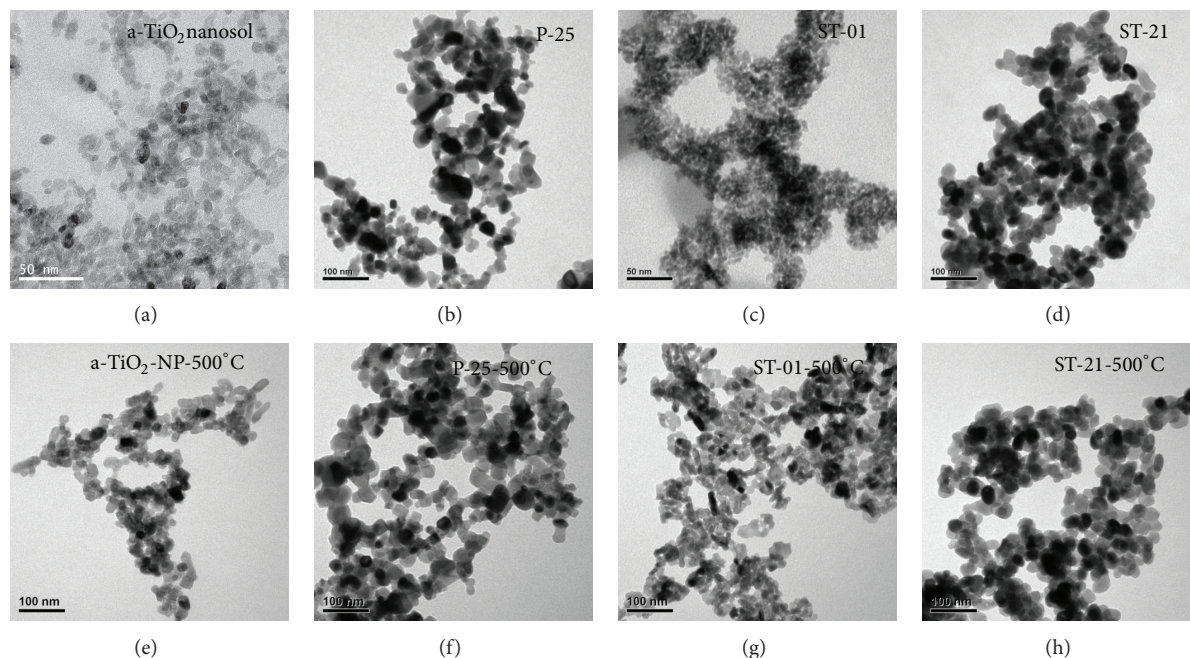
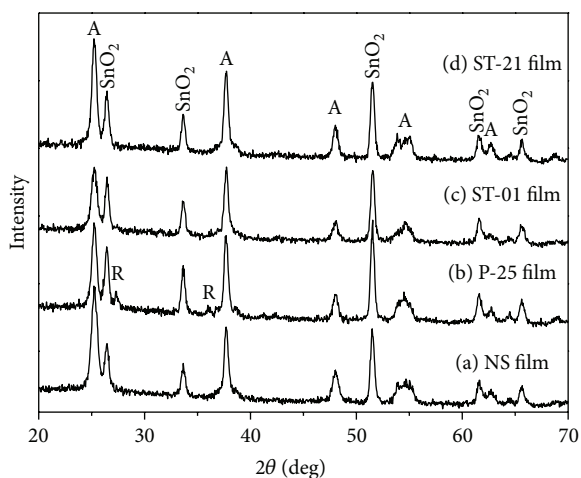


FIGURE 2: TEM image (a) a-TiO₂ nanosol (b) P-25, (c) ST-01, (d) ST-21 ((a)–(d)) before sintering ((e)–(h)) after sintering at 500°C.



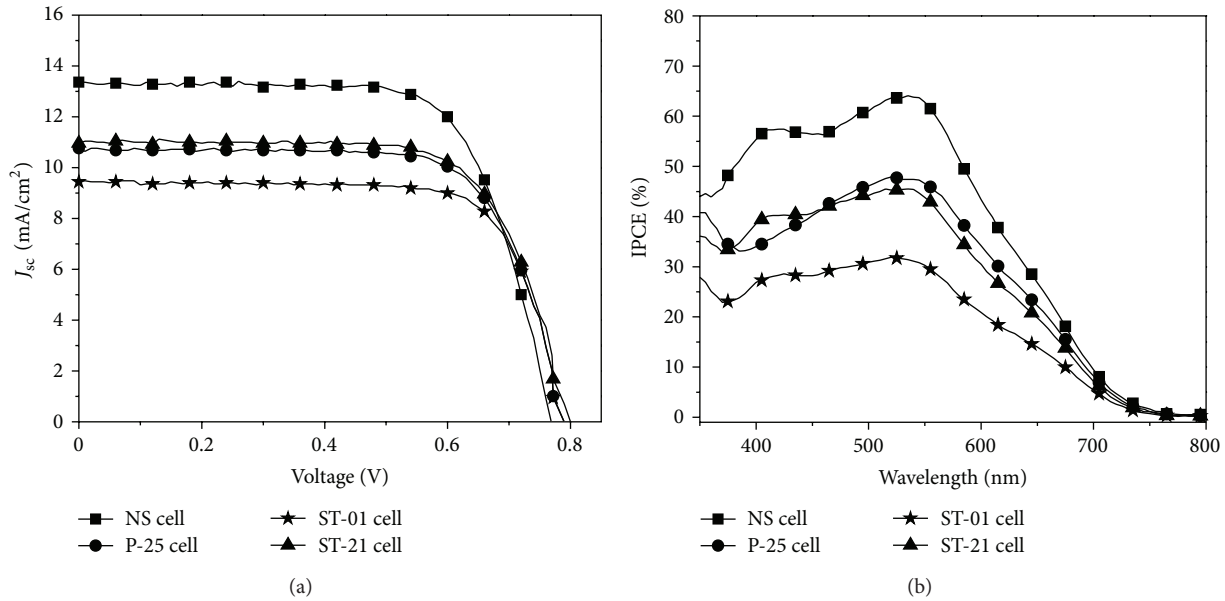
A: Anatase
R: Rutile

FIGURE 3: XRD pattern of various TiO₂ electrodes.

The crystal phase of TiO₂ films was determined by XRD. Figure 3 illustrates the XRD patterns of (a) NS films, (b) P-25 film, (c) ST-01 film, and (d) ST-21 film deposited on FTO substrate. The XRD patterns mainly indexed to anatase phase (A: anatase) with diffraction angle of 2θ at 25.23°, 37.67°, 48.05°, 53.90°, 55.03°, and 62.68° corresponding to the characteristic anatase peaks. Several peaks appearing at 26.6°, 33.9°, and 51.8° in Figure 3 are due to the SnO₂ from FTO substrate. These results indicate that the TiO₂ films exhibit a stable anatase phase even after annealing at higher temperature of 500°C. No phase transformation was detected. Only P-25 film shows some rutile (R: rutile) characteristics diffraction peaks corresponding to about 20% of rutile TiO₂. This is consistent with the crystal phase of original P-25 TiO₂ nanoparticles (XRD not shown). The average crystallite size of NS film, P-25 film, ST-01 film, and ST-21 film was estimated from the (101) peak according to the Scherrer equation, $D = 0.89\lambda / \beta \cos \theta$, where λ , β , and θ refer to X-ray wavelength (nm), the full width at half-maximum, and the diffraction

TABLE 2: Photovoltaic properties of the DSSCs made from a-TiO₂ sol and commercial DP-25, ST-01, and ST-21 TiO₂ photoanode.

DSSCs	Thickness (μm)	N719 _{ads} ($\mu\text{mol}/\text{cm}^2$)	J_{sc} (mA/cm^2)	V_{oc} (V)	FF	η (%)
NS cell	6	0.132	13.34	0.77	0.70	7.20
P-25 cell	6	0.088	10.76	0.79	0.71	6.04
ST-01 cell	6	0.110	9.45	0.79	0.74	5.53
ST-21 cell	6	0.092	10.96	0.80	0.70	6.21

FIGURE 4: (a) Current-voltage curve (b) Incident photon-to-current conversion efficiency (IPCE) curves of various TiO₂ photoelectrodes.

angle, respectively. The crystallite sizes listed in Table 1 are in good agreement with the TEM data.

3.2. Photovoltaic Properties. The photovoltaic performance of DSSCs (NS cell, P-25 cell, ST-01 cell, and ST-21 cell) fabricated using the above prepared TiO₂ photoelectrodes (NS film, P-25 film, ST-01 film, and ST-21 film) was characterized by evaluating the current-voltage behaviour under one sun AM 1.5 irradiation from a solar simulator. Figure 4(a) shows the photocurrent-voltage characteristics (I - V) curves. Table 2 summarizes the TiO₂ film thickness, the amount of dye adsorption (N719_{ads}), and the photoelectric data of the DSSCs in Figure 4(a), including, the short-circuit photocurrent density (J_{sc}), an open circuit voltage (V_{oc}), fill factor (FF), and photo-to-electric conversion efficiency (η). It is apparent that the a-TiO₂ nanosol based photoelectrode achieved the highest photo-to-electric conversion efficiency of 7.20% with a short circuit current density of 13.3 mA/cm^2 , N719_{ads} of 0.132 $\mu\text{mol}/\text{cm}^2$, V_{oc} of 0.77 V, and FF of 0.70. In contrast to the DSSCs made from TiO₂ nanoparticle-based photoelectrode, the photo-to-electric conversion performance was significantly enhanced by using the TiO₂ nanosol-based photoelectrode. The efficiency and short-circuit current density of DSSCs are mainly affected by the dye adsorption on the TiO₂ electrode. As expected, from

the SEM analysis, the amount of dye adsorbed on TiO₂ nanosol based-photoelectrode was higher than that on the TiO₂ nanoparticles-based photoelectrodes (Table 2).

Even though, the dye adsorption is higher for ST-01 nanoparticle based-photoelectrode than P-25 and ST-21 photoelectrode, the J_{sc} (mA/cm^2) and η (%) are lower. This might be attributed to the large aggregation of the TiO₂ nanoparticles. Inhomogeneous film configuration creates electron traps that hinders the electron transportation and leads to the lower DSSCs efficiency. The TiO₂ nanosol-based photoelectrode exhibits 19%, 30%, and 16% increase in the photo-to-electric conversion efficiency compared to the P-25, ST-01, and ST-21 photoelectrode, respectively.

Higher photo-to-electric conversion efficiency and short-circuit density of a-TiO₂ nanosol-based photoelectrode are attributed to higher amount of dye adsorption owing to larger surface area and more compact smooth surface morphology of TiO₂ photoanode. The higher dye adsorption value reveals that a-TiO₂ nanosol-based paste is well interconnected and the electrons are efficiently transported through the film which is consistent with the work reported by Jeong et al. [27]. The incident photon-to-current conversion efficiency (IPCE) spectra were further measured for the above prepared DSSCs. From Figure 4(b), we can observe that the IPCE% efficiency for all the samples was maximum at the wavelength of 550 nm. Again, the NS cell shows a significant increase

in IPCE percentage value over the long-wavelength range (530–700 nm) compared with other cells made from TiO₂ nanoparticles. This improvement in the long-wavelength range could be attributed to the enhancement of dye adsorption of the smooth TiO₂ film surface, leading to higher J_{sc} . Further studies are required to analyze the properties of charge transport and electron recombination process in DSSCs.

4. Conclusion

The present work has demonstrated the effect of a-TiO₂ nanosol on the performance of DSSCs in comparison with the TiO₂ nanoparticles. The well dispersed oval shaped a-TiO₂ nanosol-based TiO₂ film (6 μ m thickness) with larger surface area results in higher dye adsorption, compared to the commercial TiO₂ nanoparticles film. Hence, a-TiO₂ nanosol-based photoanode exhibits a short-circuit current density (J_{sc}) of 13.3 mA cm⁻², an open-circuit voltage (V_{oc}) of 0.77 V, and a fill factor (FF) of 0.70 and achieves an overall light conversion efficiency (η) of 7.2%. The performance of the above photoelectrode was significantly higher than the commercial P-25, ST-01, and ST-21 nanoparticle-based electrodes, owing to the higher dye loading. In addition, the NS cell shows higher IPCE efficiency than that of TiO₂ nanoparticles based DSSCs.

Authors' Contribution

S. Kathirvel and Huei-Siou Chen have equally contributed.

Acknowledgments

The authors gratefully acknowledge the National Science Council of Taiwan (Project no. NSC 98-2113-M-027-003-MY3 and 100-2113-M-008-004-MY3) for the financial support to carry out this research project.

References

- [1] B. O'Regan and M. Grätzel, "A low-cost, high-efficiency solar cell based on dye-sensitized colloidal TiO₂ films," *Nature*, vol. 353, no. 6346, pp. 737–740, 1991.
- [2] M. Grätzel, "Photoelectrochemical cells," *Nature*, vol. 414, no. 6861, pp. 338–344, 2001.
- [3] A. Hagfeldt, G. Boschloo, L. Sun, L. Kloo, and H. Pettersson, "Dye-sensitized solar cells," *Chemical Reviews*, vol. 110, no. 11, pp. 6595–6663, 2010.
- [4] J. Nelson and R. E. Chandler, "Random walk models of charge transfer and transport in dye sensitized systems," *Coordination Chemistry Reviews*, vol. 248, no. 13-14, pp. 1181–1194, 2004.
- [5] A. Yella, H.-W. Lee, H. N. Tsao et al., "Porphyrin-sensitized solar cells with cobalt (II/III)-based redox electrolyte exceed 12 percent efficiency," *Science*, vol. 334, no. 6056, pp. 629–634, 2011.
- [6] M. Grätzel, "Conversion of sunlight to electric power by nanocrystalline dye-sensitized solar cells," *Journal of Photochemistry and Photobiology A*, vol. 164, no. 1–3, pp. 3–14, 2004.
- [7] B. E. Hardin, H. J. Snaith, and M. D. McGehee, "The renaissance of dye-sensitized solar cells," *Nature Photonics*, vol. 6, no. 3, pp. 162–169, 2012.
- [8] Y.-D. Zhang, X.-M. Huang, D.-M. Li, Y.-H. Luo, and Q.-B. Meng, "How to improve the performance of dye-sensitized solar cell modules by light collection," *Solar Energy Materials and Solar Cells*, vol. 98, pp. 417–423, 2012.
- [9] T. W. Hamann, R. A. Jensen, A. B. F. Martinson, H. Van Ryswyk, and J. T. Hupp, "Advancing beyond current generation dye-sensitized solar cells," *Energy and Environmental Science*, vol. 1, no. 1, pp. 66–78, 2008.
- [10] J. van de Lagemaat, N. G. Park, and A. J. Frank, "Influence of electrical potential distribution, charge transport, and recombination on the photopotential and photocurrent conversion efficiency of dye-sensitized nanocrystalline TiO₂ solar cells: a study by electrical impedance and optical modulation techniques," *Journal of Physical Chemistry B*, vol. 104, no. 9, pp. 2044–2052, 2000.
- [11] L. Vesce, R. Riccitelli, G. Soscia, T. M. Brown, A. Di Carlo, and A. Reale, "Optimization of nanostructured titania photoanodes for dye-sensitized solar cells: study and experimentation of TiCl₄ treatment," *Journal of Non-Crystalline Solids*, vol. 356, no. 37–40, pp. 1958–1961, 2010.
- [12] A. B. F. Martinson, J. W. Elam, J. Liu, M. J. Pellin, T. J. Marks, and J. T. Hupp, "Radial electron collection in dye-sensitized solar cells," *Nano Letters*, vol. 8, no. 9, pp. 2862–2866, 2008.
- [13] U. Opara Krašovec, M. Berginc, M. Hočevár, and M. Topič, "Unique TiO₂ paste for high efficiency dye-sensitized solar cells," *Solar Energy Materials and Solar Cells*, vol. 93, no. 3, pp. 379–381, 2009.
- [14] H. Xu, X. Tao, D. T. Wang, Y. Z. Zheng, and J. F. Chen, "Enhanced efficiency in dye-sensitized solar cells based on TiO₂ nanocrystal/nanotube double-layered films," *Electrochimica Acta*, vol. 55, no. 7, pp. 2280–2285, 2010.
- [15] Q. Zhang and G. Cao, "Nanostructured photoelectrodes for dye-sensitized solar cells," *Nano Today*, vol. 6, no. 1, pp. 91–109, 2011.
- [16] Y. Duan, N. Fu, Q. Liu et al., "Sn-doped TiO₂ photoanode for dye-sensitized solar cells," *The Journal of Physical Chemistry C*, vol. 116, no. 16, pp. 8888–8893, 2012.
- [17] I. C. Baek, M. Vithal, J. A. Chang et al., "Facile preparation of large aspect ratio ellipsoidal anatase TiO₂ nanoparticles and their application to dye-sensitized solar cell," *Electrochemistry Communications*, vol. 11, no. 4, pp. 909–912, 2009.
- [18] G. Liu, X. Wang, Z. Chen, H. M. Cheng, and G. Q. Lu, "The role of crystal phase in determining photocatalytic activity of nitrogen doped TiO₂," *Journal of Colloid and Interface Science*, vol. 329, no. 2, pp. 331–338, 2009.
- [19] M. Lv, D. Zheng, M. Ye et al., "Densely aligned rutile TiO₂ nanorod arrays with high surface area for efficient dye-sensitized solar cells," *Nanoscale*, vol. 4, no. 19, pp. 5872–5879, 2012.
- [20] Z.-S. Wang, H. Kawauchi, T. Kashima, and H. Arakawa, "Significant influence of TiO₂ photoelectrode morphology on the energy conversion efficiency of N719 dye-sensitized solar cell," *Coordination Chemistry Reviews*, vol. 248, no. 13-14, pp. 1381–1389, 2004.
- [21] K. Suttiponpanit, J. Jiang, M. Sahu, S. Suvachittanont, T. Charinpanitkul, and P. Biswas, "Role of surface area, primary particle size, and crystal phase on titanium dioxide nanoparticle dispersion properties," *Nanoscale Research Letters*, vol. 6, no. 1, pp. 1–8, 2011.

- [22] J.-Y. Liao, J.-W. He, H. Xu, D.-B. Kuang, and C.-Y. Su, "Effect of TiO_2 morphology on photovoltaic performance of dye-sensitized solar cells: nanoparticles, nanofibers, hierarchical spheres and ellipsoid spheres," *Journal of Materials Chemistry*, vol. 22, no. 16, pp. 7910–7918, 2012.
- [23] D.-W. Park, Y.-K. Choi, K.-J. Hwang et al., "Nanocrystalline TiO_2 films treated with acid and base catalysts for dye-sensitized solar cells," *Advanced Powder Technology*, vol. 22, no. 6, pp. 771–776, 2011.
- [24] S. Ito, K. Takahashi, S. I. Yusa, T. Imamura, and K. Tanimoto, "Effects of homogenization scheme of TiO_2 screen-printing paste for dye-sensitized solar cells," *International Journal of Photoenergy*, vol. 2012, Article ID 405642, 7 pages, 2012.
- [25] K.-M. Lee, V. Suryanarayanan, and K.-C. Ho, "The influence of surface morphology of TiO_2 coating on the performance of dye-sensitized solar cells," *Solar Energy Materials and Solar Cells*, vol. 90, no. 15, pp. 2398–2404, 2006.
- [26] S. K. Dhungel and J. G. Park, "Optimization of paste formulation for TiO_2 nanoparticles with wide range of size distribution for its application in dye sensitized solar cells," *Renewable Energy*, vol. 35, no. 12, pp. 2776–2780, 2010.
- [27] N. C. Jeong, O. K. Farha, and J. T. Hupp, "A convenient route to high area, nanoparticulate TiO_2 photoelectrodes suitable for high-efficiency energy conversion in dye-sensitized solar cells," *Langmuir*, vol. 27, no. 5, pp. 1996–1999, 2011.

Research Article

Synthesis of Octahedral-Shaped NiO and Approaches to an Anode Material of Manufactured Solid Oxide Fuel Cells Using the Decalcomania Method

Haeran Cho,¹ Huryul Lee,² Sun-Min Park,¹ Byung-Hyun Choi,¹ and Misook Kang²

¹ Korean Institutes of Ceramic Engineering & Technology (KICET), Geumcheon-gu, Seoul 153-801, Republic of Korea

² Department of Chemistry, College of Science, Yeungnam University, Gyeongsan, Gyeongbuk 712-749, Republic of Korea

Correspondence should be addressed to Misook Kang; mskang@ynu.ac.kr

Received 30 November 2012; Revised 25 February 2013; Accepted 17 March 2013

Academic Editor: Jie-Fang Zhu

Copyright © 2013 Haeran Cho et al. This is an open access article distributed under the Creative Commons Attribution License, which permits unrestricted use, distribution, and reproduction in any medium, provided the original work is properly cited.

Micrometer-sized and octahedral-shaped NiO particles were synthesized by microwave thermal treatment at 300 watt power for 15 min in a microwave chamber to be used as an anode material in solid oxide fuel cells. SEM image and particle size distribution revealed near-perfect octahedral NiO microparticle with sizes ranging from 4.0~11.0 μm . The anode functional layer (AFL, 60 wt% NiO synthesized: commercial 40 wt% YSZ), electrolyte (commercial Yttria-stabilized zirconia, YSZ), and cathode (commercial $\text{La}_{0.8}\text{Sr}_{0.2}\text{MnO}_3$, LSM) layers were manufactured using the decalcomania method on a porous anode support, sequentially. The sintered electrolyte at 1450°C for 2 h using the decalcomania method was dense and had a thickness of about 10 μm . The cathode was sintered at 1250°C for 2 h, and it was porous. Using humidified hydrogen as a fuel, a coin cell with a 15 μm thick anode functional layer exhibited maximum power densities of 0.28, 0.38, and 0.65 W/cm² at 700, 750, and 800°C, respectively. Otherwise, when a commercial YSZ anode functional layer was used, the maximum power density was 0.55 W/cm² at 800°C.

1. Introduction

Solid oxide fuel cells (SOFCs) consist entirely of metal oxides, NiO, YSZ, and LSM and have advantages of high efficiency and durability without expensive catalysts. However, it is difficult to control the size and shape of the ceramics produced because of many restrictions and complex geometries. In order to solve these problems, many researchers have studied means of maximizing reaction areas by changing stack sizes and developing new materials [1–5]. In many of these areas, SOFC fabrication methods are generally considered to be limiting factors based on considerations of automation and scalability [6]. Some SOFC structures are produced using traditional ceramic preparation methods, such as powder pressing, tape casting, screen printing, or conventional spray methods [7]. Other more sophisticated methods, such as plasma spraying [8, 9], vacuum deposition [10], and extrusion-based direct-write methods [11], have also been reported. Here, the decalcomania printing method is introduced. This method involves the transfer of designs

from specially prepared paper to a wood or glass or metal surface. This method is expected to have some advantages because it is easy to prepare materials of the desired shape and size; manufacturing is straightforward. On the other hand, NiO/YSZ is widely used as an anode material for SOFCs because it has sufficient electronic conductivity and a good catalytic reaction for fuel gas at its operating temperature. Generally, anode materials for SOFCs also should be thermally and chemically compatible compared with other component materials at operating and higher temperatures, because SOFCs operate in the temperature range 800~1000°C. However, commercial NiO-loaded YSZ anode materials have a serious problem, because they are strongly deactivated during the operations of SOFCs, because of NiO aggregation at high temperature. Research into the synthesis of NiO nanoparticles has increased during the past decade and methods such as, sol-gel [12], microemulsion precipitation [13], chemical vapor deposition [14], and sputtering [15] have been designed. Recently, some researchers [16] have attempted to use advanced microwave treatments

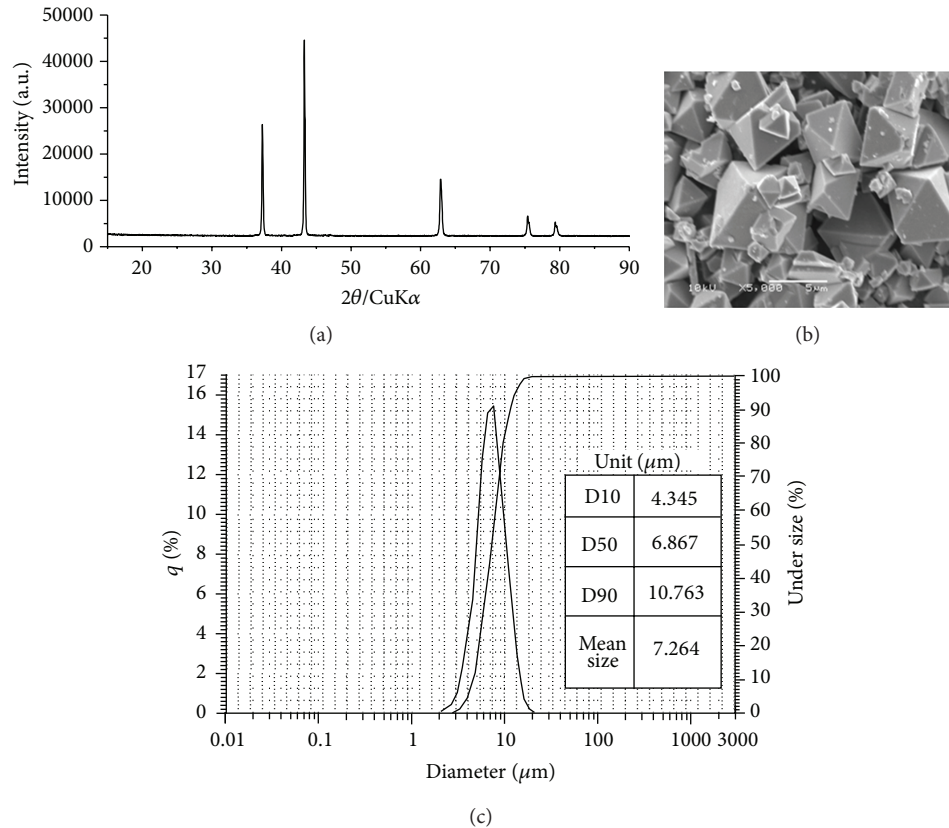


FIGURE 1: XRD pattern (a), SEM image (b), and particle size distribution (c) of the NiO powder synthesized using the microwave thermal treatment.

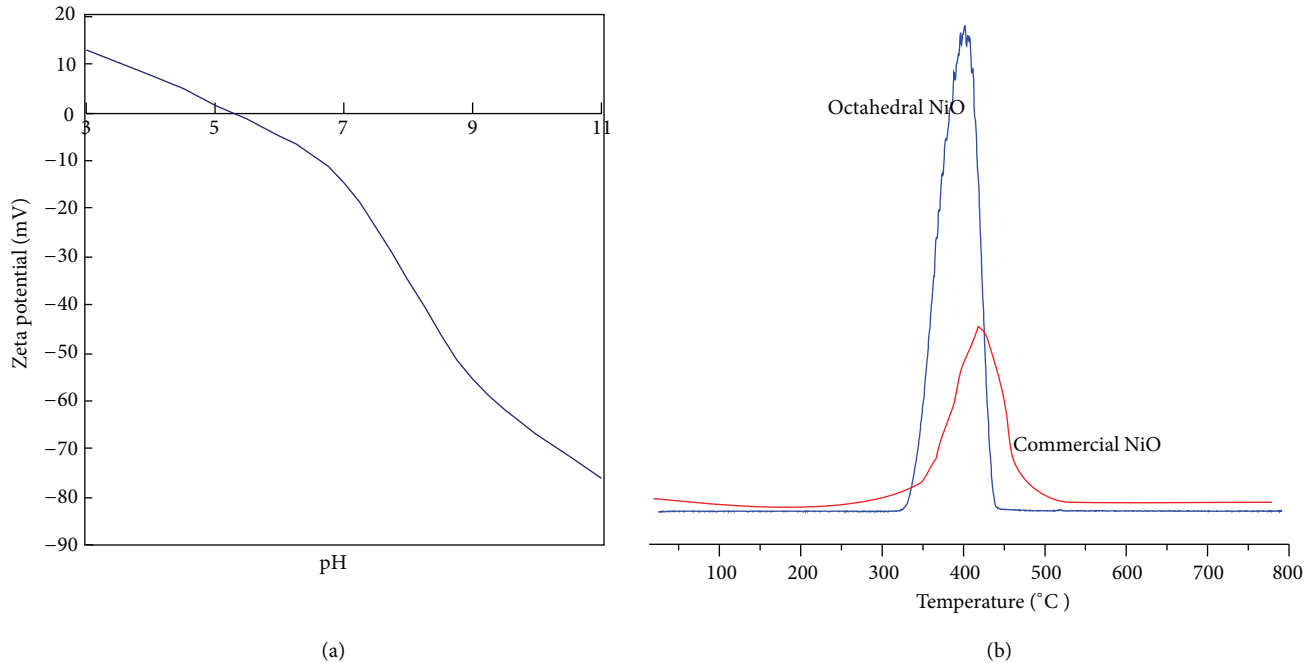
using various polymeric or surfactant additives to synthesize various metal materials with special morphologies. However, few studies have addressed the morphology for NiO as an anode material for SOFCs [17, 18]. In this study, we examined the preparation of micro-sized octahedral NiO particles using a microwave thermal treatment. Microwave heating was found to increase densification and shortened sintering time as compared with conventional heating. The synthesized NiO was characterized by X-ray diffraction (XRD), transmission electron microscopy (SEM), particle size, and zeta potentials. In order to explore the applicability of decalcomania printing to SOFC materials, a traditional set of SOFC electrolytes were synthesized during this study. An anode of commercial Ytria-stabilized zirconia and a cathode of commercial $\text{La}_{0.8}\text{Sr}_{0.2}\text{MnO}_3$ ($1.0\text{ }\mu\text{m}$, Tosho, Japan) were selected. The top and cross-section morphologies of a single cell were evaluated, and the electrochemical properties and the output of an SOFC single cell were measured under optimum conditions.

2. Experimental

2.1. Synthesis of Octahedral-Shaped Ni. The NiO was synthesized by the microwave thermal treatment method. The process used was as follows. First, after the addition of polystyrene (molecular weight = 10,000, Aldrich, USA) and

Ni source ($\text{NiCl}_2 \cdot \text{H}_2\text{O}$, 99.95%, Junsei Chemical, Japan) into ethanol, the solution was stirred homogeneously. The mixed solution was then placed in a quartz liner and the solution was microwave heated at 300 W for 15 min. The product like a lump so obtained was then thermally treated at 450°C for 3 h to allow crystallization and remove polymer components. To prepare anode functional layers, we purchased a commercially available YSZ powder (TZ8Y, D50 = $3\text{ }\mu\text{m}$, Tosoh, Japan). To prepare the synthesized NiO (60 wt%)/YSZ (40 wt%) material, a physically mixing technique was used.

2.2. Characterization of Octahedral-Shaped NiO. The prepared NiO was subjected to powder XRD analysis (model MPD from PANalytical) using nickel-filtered $\text{CuK}\alpha$ radiation (30 kV, 30 mA) at 2-theta angles of $10\text{--}90^\circ$. The scan speed was $10^\circ/\text{min}$, and the time constant was 1 s. The sizes and shapes of microparticles were determined by FE-SEM (field emission scanning electron microscopy, SEM-S-4100, Hitachi) at 120 kV. The morphologies were observed using a scanning electron microscope. Particle sizes were determined using a particle size analyzer (LA-950V2, Horiba, Japan). Zeta potentials were determined by measuring electrophoretic mobility using an electrophoresis measurement apparatus (ELS 8000, Otsuka Electronics, Japan). Electrophoretic light scattering (ELS) determinations were performed in reference beam mode using a laser light source wavelength of 670 nm,



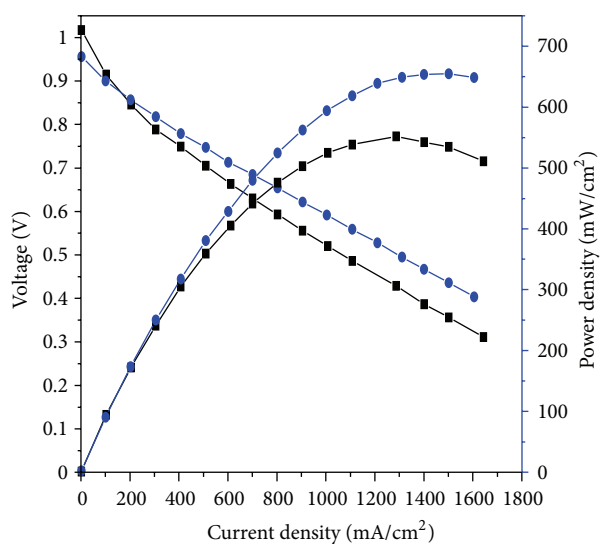
Characteristics/pHs	pH = 3	pH = 5	pH = 7	pH = 9	pH = 11
Zeta potential (mV)	12.91	1.44	-14.56	-55.7	-76.04
Particle size (nm)	8142.8	4996	14220.4	17595	25584.4

FIGURE 2: The zeta potential distribution (a) and H_2 -TPR profile (b) of the octahedral NiO sample.

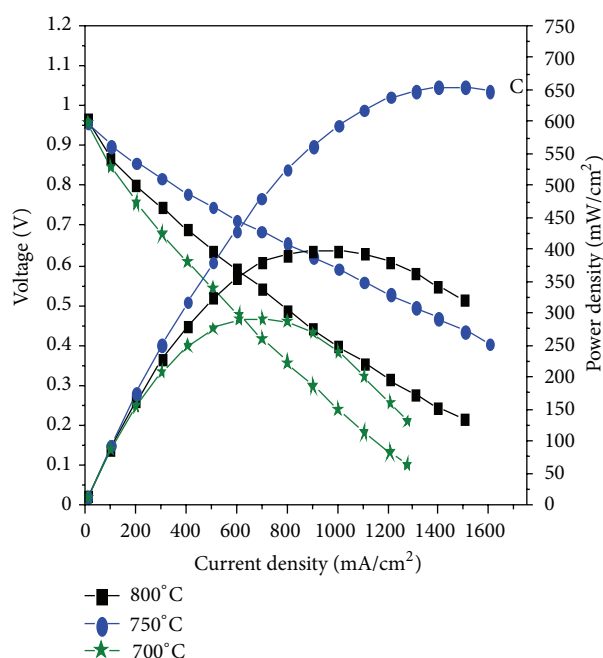
a modular frequency of 250 Hz, and a scattering angle of 15° . The standard errors of the zeta potentials, converted from experimentally determined electrophoretic mobility, were typically $<1.5\%$ and percent errors were $<5\%$. To measure zeta potentials, 0.1 wt% NiO was dispersed in deionized water and the pH of the solution was adjusted 3, 5, 7, 9, and 11 with HCl or NaOH. The relative molecular diameter size distributions of the various solutions were also measured using this equipment. Zeta potential distributions were obtained by averaging 2 or 3 runs. H_2 -temperature-programmed reduction (TPR) was conducted as follows. About 0.3 g of NiO was pretreated under helium flow (30 mL/min) at 700°C for 2 h and then cooled to room temperature. The analysis was carried out using a thermal gravimetric analyzer at H_2 (10 vol%)/ N_2 flow rate of 30 mL/min and by raising the temperature from room temperature to 800°C at $5^\circ\text{C}/\text{min}$.

2.3. Fabrication of Solid Oxide Fuel Cells Using Decalcomania Method. The decalcomania paper was prepared next. Briefly, two types of commercial and synthesized NiO were each mixed with YSZ powders at a weight ratio 6 : 4 in a mortar for 1 h to obtain anode functional layer (AFL) precursor powder. Mixtures were reduced to unique and fine particles ($5\sim 10\ \mu\text{m}$) using a 3-roll ball mill (EXAKT50, German) and a high speed mixer (Thinky centrifugal mixer, Japan), and then a binder (benzene oil) was dropped into the powder mixture (the weight ratio of powder to benzene oil in paste was 58~66 : 42~

34). The prepared pastes were assembled onto decalcomania sheets (Tullis Russell Coaters, Republic of Korea) using screen printing equipment (DSP-380VS, Nsys, Republic of Korea). Papers were dried at 40°C for 24 h and then detached from decalcomania sheets to use anode functional layer. First, the AFL layer was fabricated onto a ceramic support ($\Phi 20\ \text{mm}$ disk) using the decalcomania coating method and then an electrolyte (YSZ) layer paper was attached to the AFL layer. The layers were pretreated at 400°C for 1 h to remove the organic binder and then cotreated at 1400°C for 10 h at a heating rate of $3^\circ\text{C}/\text{min}$. $\text{La}_{0.7}\text{Sr}_{0.3}\text{MnO}_3/\text{YSZ}$ paper cathode was fabricated on the YSZ films using the decalcomania method. Finally, the assembled cell was sintered by heating at 1200°C for 2 h. Cell 1 was based on commercial NiO anodes (particle size $0.6\ \mu\text{m}$, Sumitomo, Japan) and NiO anode in cell 2 was synthesized in this study; cell efficiencies were compared. Pt paste (DAD-87, China) was employed as a current collector and a sealing material. After being sealed, cells were tested for power density in an electrical furnace using the four-probe method. The NiO/YSZ anode was reduced in situ at 800°C . The anode was fed with hydrogen at a flow rate of $500\ \text{mL min}^{-1}$ and the cathode was exposed to an oxygen flow of $1,000\ \text{mL min}^{-1}$. I - V characteristics and EIS impedance spectra were measured using an SOFC Button Cell Test Station (Nara Cell Tech., Republic of Korea) and an impedance analyzer SI 1260 (Solatron, England) at a frequency range of 1 Hz to 100,000 Hz and at an AC voltage of 20 mV.



(a)



(b)

FIGURE 3: The I - V and power density curves of single cells based on commercial NiO and synthesized octahedral NiO anode functional layers (a) at different temperatures (b).

3. Results and Discussion

Figures 1(a), 1(b), and 1(c) show the XRD pattern, SEM image, and particle size distribution of an NiO powder synthesized by microwave treatment. We believe in the microwave chamber that ROR or H_2O elimination rapidly induces a combination between each Ni alkoxide or hydroxide. During this reaction, the condensation reaction continues in the absence

of any blocking molecules, and the resulting nucleated NiO can grow in all directions to produce a spherical-shaped NiO. However, the presence of polystyrene induces a selective and competitive condensation reaction at the six terminals of the Ni hydroxide complexes, resulting in an octahedral shape. These results revealed that microwave pretreatment had a significant effect on crystal growth, presumably because microwave treatment processing induces rapid hydrolysis of Ni-OH or Ni-OR and polycondensation of these. Initial growth leads to a linear chain of Ni-OH and the high concentration of OH ions present leads to crystallization of NiO possibly because the intermolecular reaction between each Ni-OH is higher than the intra-molecular reaction. Due to the complexity of the NiO synthetic method, perfect octahedral NiO has not been synthesized for SOFCs. Fortunately, we were able to obtain the octahedral NiO by using the microwave thermal treatment method, as shown in Figure 1(a). The NiO structure showed peaks at $2\theta = 38.0, 43.5, 63.0, 70.0,$ and 78.58 , which were assigned to the (d111), (d200), (d220), (d311), and (d222) planes, respectively [19]. Line broadening of the peak of the main 200 plane is related to crystallite size. The full width at half maximum (FWHM) of the peak at $2\theta = 43.58$ was estimated using Scherrer's equation [20] ($t = 0.9\lambda/\beta \cos \theta$, where λ is the wavelength of incident X-rays, β the FWHM height in radians, and θ the diffraction angle). From this calculation, the crystalline domain size was calculated as $7.2 \mu\text{m}$. Figure 1(b) shows FE-SEM images of the particle shapes of NiO. A relatively uniform octahedral shape and particle sizes in the range $4\sim 10 \mu\text{m}$ (average size $7.2 \mu\text{m}$ by the particle size analyzer in Figure 1(c)) were observed.

Figures 2(a) and 2(b) depict the influence of pH on the position of the zeta potential distribution and H_2 -TPR profile of the octahedral NiO sample. Aggregated particle sizes in aqueous solution are summarized in the table in Figure 2. The zeta potentials of octahedral NiO suspensions significantly decreased on increasing pH (Figure 2(a)). Surface charges changed from positive in acidic solution to negative in alkali solution. The isoelectric point was at pH 5.4 and at this value a large amount of aggregation occurred. Absolute surface charge peaked at -76.04 mV at pH 11, indicating that the octahedral colloidal NiO is stable [21]. At this level, it exhibited little aggregation, indicating that reaction sites were present over the surface of the anode material. In addition, we compared the H_2 -TPR profiles of the two NiO samples (octahedral and commercial), as shown in Figure 2(b). One H_2 -TPR peak corresponding to the reduction of the NiO component was observed. In general, H_2 -TPR results indicated that (1) the peak area corresponded to hydrogen uptake and (2) the peak at high temperatures corresponded to the chemical reduction. The reduction peaks of the octahedral NiO sample were gradually shifted more so to lower temperatures than those of the commercial NiO. Ni^{2+} ions were reduced to Ni^0 at a comparatively low temperature of $330\sim 430^\circ\text{C}$ in octahedral NiO.

Figures 3(a) and 2(b) compare the I - V and power density curves of a single cell based on commercial NiO (cell 1) and the cell assembled by synthesized octahedral NiO anode functional layers (cell 2). Maximum power densities

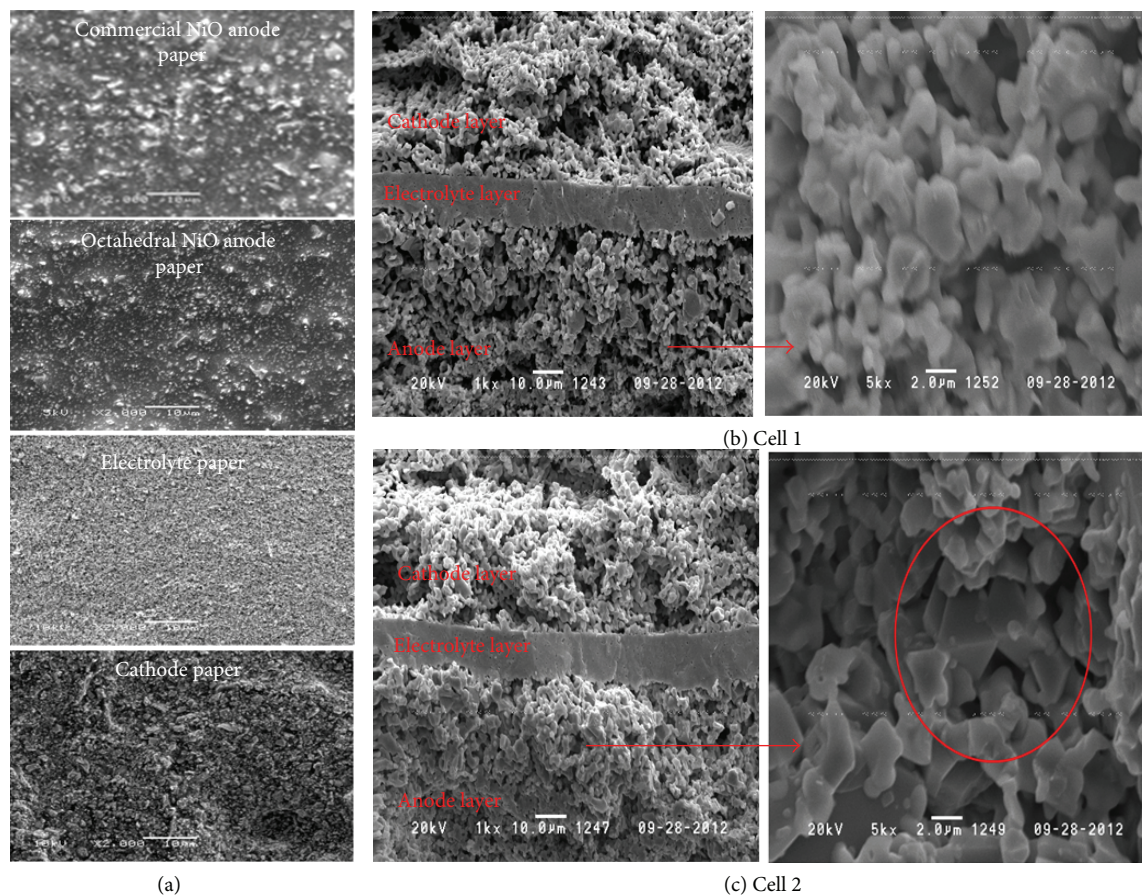


FIGURE 4: FE-SEM micrographs of cells with different anode functional layers after SOFC testing.

in cells 1 and 2 were measured at 551 and 654 mWcm^{-2} at 800°C, respectively (Figure 3(b)). Cell performance was significantly improved by the addition of the octahedral NiO anode functional layer. In Figure 3(b), according to operating temperatures, the maximum power densities on a single type of cell were increased up to 293, 401, and 654 mW cm^{-2} at 700, 750, and 800°C, respectively.

We considered that fuel cell performance differences could be due to different interfacial microstructures.

Figures 4(a) and 4(b) show the SEM micrographs of the cells with different anode functional layers after SOFC testing. The pores in the commercial NiO-AFL (cell 1) are submicron in diameter and the large pores are 2~5 micrometers in diameter. The estimated porosity of the commercial AFL is about 35%. However, the pores in the octahedral NiO-AFL (cell 2) were smaller than those in commercial NiO-AFL. Large cracks were clearly discernible at the interface between the AFL and the electrolyte layer in the commercial NiO cell, but no crack was observed in the octahedral NiO cell. The development of cracks at the AFL/electrolyte layer interface was probably caused by the differential sintering shrinkages of the multiple layers, and thus, the octahedral NiO particles perhaps better matched the YSZ electrolyte particles in this respect. Additionally the grains between octahedral NiO particles were well connected in octahedral NiO-AFL cells.

Fewer cracks at the AFL/electrolyte interface result in a lower ohmic cell ASR. Electrochemical impedance spectroscopy (EIS) measurements in open-circuit conditions were used to evaluate the resistance values with respect to operating temperature for the octahedral NiO-AFL cell. Figure 5 shows typical Nyquist plots of cells with an octahedral NiO anode functional layer, measured at 700, 750, and 800°C. The intercept with the real axis at high frequency represents the ohmic resistance of a cell (R_{ohmic}), which includes its electrolyte and lead wire resistances and some contact resistance associated with interfaces. The low-frequency intercept corresponds to the total resistance of the cell. Therefore, the difference between the high frequency and low frequency represents the total interfacial polarization resistance (R_p) of the cell [22]. The R_{ohmic} of the cell was almost the same ($0.78 \Omega \text{ cm}^{-2}$) at all temperatures, but R_p was significantly lower at 800°C than at 700 and 750°C. R_p reduced from 2.85 to $1.21 \Omega \text{ cm}^{-2}$, respectively, with increasing temperature from 700 to 850°C. Generally, these different resistance values are ascribed to the addition of the anode functional layer, since other parameters, such as electrolyte thickness, cathode material, anode substrate, and sintering temperature, were kept constant. As mentioned above, R_p is mainly due to electrolyte and contact resistance. Therefore, a better contact between electrolyte and anode can decrease contact resistance and

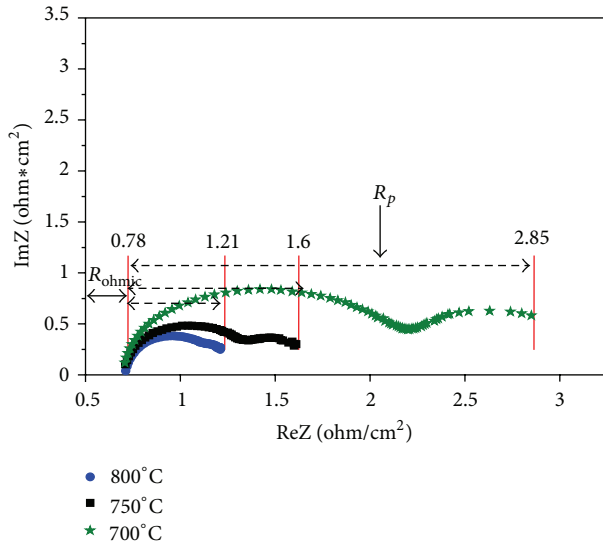


FIGURE 5: Typical Nyquist plots of cells with an octahedral NiO anode functional layer at 700, 750, and 800°C.

reduce total R_p for a given electrolyte thickness. At the anode/electrolyte interface for the cell with anode functional layer, the elimination of macropores led to a better contact between electrolyte and the anode, which reduced contact resistance at the anode/electrolyte interface. In this study, the octahedral NiO-AFL cell provided lower R_p values due to faster electrochemical reactions at the anode/electrolyte interface.

4. Conclusions

This study described the effect of anode functional layer on SOFC performance. Identical single cells, differing only in terms of anode functional layer morphology, were fabricated and tested. Using an octahedral NiO anode functional layer, fuel cell performance was significantly improved by up to a power output of 100 mWcm^{-2} at 850°C , due to better contact between the electrolyte and anode. These findings demonstrate cell performance is critically dependent on anode microstructure and that microwave thermal treatment provides an effective means of octahedral NiO anode materials.

Acknowledgments

This work was supported by the New & Renewable Energy of the Korea Institute of Energy Technology Evaluation and Planning (KETEP) Grant funded by the Korea Government Ministry of Knowledge Economy (no. 2010T100100622).

References

- [1] T. Suzuki, Y. Funahashi, T. Yamaguchi, Y. Fujishiro, and M. Awano, "Development of cube-type SOFC stacks using anode-supported tubular cells," *Journal of Power Sources*, vol. 175, no. 1, pp. 68–74, 2008.
- [2] T. Yamaguchi, S. Shimizu, T. Suzuki, Y. Fujishiro, and M. Awano, "Fabrication and evaluation of a novel cathode-supported honeycomb SOFC stack," *Materials Letters*, vol. 63, no. 29, pp. 2577–2580, 2009.
- [3] Y. Yang, G. Wang, H. Zhang, and W. Xia, "Computational analysis of thermo-fluid and electrochemical characteristics of MOLB-type SOFC stacks," *Journal of Power Sources*, vol. 173, no. 1, pp. 233–239, 2007.
- [4] F. Smeacetto, M. Salvo, M. Santarelli et al., "Performance of a glass-ceramic sealant in a SOFC short stack," *International Journal of Hydrogen Energy*, vol. 38, no. 1, pp. 588–596, 2013.
- [5] M. Lockett, M. J. H. Simmons, and K. Kendall, "CFD to predict temperature profile for scale up of micro-tubular SOFC stacks," *Journal of Power Sources*, vol. 131, no. 1-2, pp. 243–246, 2004.
- [6] F. Tietz, H. P. Buchkremer, and D. Stöver, "Components manufacturing for solid oxide fuel cells," *Solid State Ionics*, vol. 152-153, pp. 373–381, 2002.
- [7] J. Will, A. Mitterdorfer, C. Kleinlogel, D. Perednis, and L. J. Gauckler, "Fabrication of thin electrolytes for second-generation solid oxide fuel cells," *Solid State Ionics*, vol. 131, no. 1, pp. 79–96, 2000.
- [8] D. Rui, H. Zhang, G. Wang, F. Xiong, and B. Hu, "Fabrication of finely structured silicon-supported SOFC with anode deposited by multi-phase plasma spraying," *Journal of Materials Processing Technology*, vol. 212, pp. 2193–2199, 2012.
- [9] Y. C. Yang, T. H. Chang, Y. C. Wu, and S. F. Wang, "Porous Ni/8YSZ anode of SOFC fabricated by the plasma sprayed method," *International Journal of Hydrogen Energy*, vol. 37, pp. 13746–13754, 2012.
- [10] L. R. Pederson, P. Singh, and X. D. Zhou, "Application of vacuum deposition methods to solid oxide fuel cells," *Vacuum*, vol. 80, no. 10, pp. 1066–1083, 2006.
- [11] Y. Du, N. M. Sammes, and G. A. Tompsett, "Optimisation parameters for the extrusion of thin YSZ tubes for SOFC electrolytes," *Journal of the European Ceramic Society*, vol. 20, no. 7, pp. 959–965, 2000.
- [12] Q. Yang, J. Sha, X. Ma, and D. Yang, "Synthesis of NiO nanowires by a sol-gel process," *Materials Letters*, vol. 59, no. 14-15, pp. 1967–1970, 2005.
- [13] C. Zhang, J. Zhan, J. Wu, X. Guo, and M. Okido, "Preparation of fibrous nickel oxide particles," *Transactions of Nonferrous Metals Society of China*, vol. 13, pp. 1441–1445, 2003.
- [14] S. M. Tan, S. P. Chai, W. W. Liu, and A. R. Mohamed, "Effects of FeO_x , CoO_x , and NiO catalysts and calcination temperatures on the synthesis of single-walled carbon nanotubes through chemical vapor deposition of methane," *Journal of Alloys and Compounds*, vol. 477, no. 1-2, pp. 785–788, 2009.
- [15] A. M. Reddy, A. S. Reddy, K. S. Lee, and P. S. Reddy, "Growth and characterization of NiO thin films prepared by dc reactive magnetron sputtering," *Solid State Sciences*, vol. 13, no. 2, pp. 314–320, 2011.
- [16] C. H. Jung, S. Jalota, and S. B. Bhaduri, "Quantitative effects of fuel on the synthesis of Ni/NiO particles using a microwave-induced solution combustion synthesis in air atmosphere," *Materials Letters*, vol. 59, no. 19-20, pp. 2426–2432, 2005.
- [17] F. Rousseau, S. Awamat, M. Nikravec, D. Morvan, and J. Amouroux, "Deposit of dense YSZ electrolyte and porous NiO-YSZ anode for SOFC device by a low pressure plasma process," *Surface and Coatings Technology*, vol. 202, no. 4–7, pp. 1226–1230, 2007.

- [18] S. Biswas, T. Nithyanantham, S. N. Thangavel, and S. Bandopadhyay, "High-temperature mechanical properties of reduced NiO-8YSZ anode-supported bi-layer SOFC structures in ambient air and reducing environments," *Ceramics International*, vol. 39, no. 3, pp. 3103–3111, 2013.
- [19] D. Y. Han, H. Y. Yang, C. B. Shen, X. Zhou, and F. H. Wang, "Synthesis and size control of NiO nanoparticles by water-in-oil microemulsion," *Powder Technology*, vol. 147, no. 1–3, pp. 113–116, 2004.
- [20] N. M. Deraz, M. M. Selim, and M. Ramadan, "Processing and properties of nanocrystalline Ni and NiO catalysts," *Materials Chemistry and Physics*, vol. 113, no. 1, pp. 269–275, 2009.
- [21] L. Zhang, S. P. Jiang, W. Wang, and Y. Zhang, "NiO/YSZ, anode-supported, thin-electrolyte, solid oxide fuel cells fabricated by gel casting," *Journal of Power Sources*, vol. 170, no. 1, pp. 55–60, 2007.
- [22] Q. L. Liu, K. A. Khor, and S. H. Chan, "High-performance low-temperature solid oxide fuel cell with novel BSCF cathode," *Journal of Power Sources*, vol. 161, no. 1, pp. 123–128, 2006.

Research Article

Effect of Solution Spray Rate on the Properties of Chemically Sprayed ZnO:In Thin Films

Merike Kriisa,¹ Malle Krunks,¹ Erki Kärber,¹ Mart Kukk,¹ Valdek Mikli,² and Arvo Mere¹

¹ Department of Materials Science, Tallinn University of Technology, Ehitajate Tee 5, 19086 Tallinn, Estonia

² Centre for Materials Research, Tallinn University of Technology, Ehitajate Tee 5, 19086 Tallinn, Estonia

Correspondence should be addressed to Malle Krunks; malle.krunks@ttu.ee

Received 14 December 2012; Accepted 1 March 2013

Academic Editor: Jie-Fang Zhu

Copyright © 2013 Merike Kriisa et al. This is an open access article distributed under the Creative Commons Attribution License, which permits unrestricted use, distribution, and reproduction in any medium, provided the original work is properly cited.

ZnO:In thin films were grown from 100 mL of spray solution on glass substrates by chemical spray at $T_s = 400^\circ\text{C}$ using solution spray rates of 0.5–6.7 mL/min. Zinc acetate and indium(III)chloride were used as Zn and In sources, respectively, with $[\text{In}]/[\text{Zn}] = 3$ at.%. Independent of solution spray rate, the crystallites in ZnO:In films grow preferentially in the (101) plane parallel to the substrate. The solution spray rate influences the surface morphology, grain size, film thickness, and electrical and optical properties. According to SEM and AFM studies, sharp-edged pyramidal grains and canvas-resembling surfaces are characteristic of films grown at spray rates of 0.5 and 3.3 mL/min, respectively. To obtain films with comparable film thickness and grain size, more spray solution should be used at low spray rates. The electrical resistivity of sprayed ZnO:In films is controlled by the solution spray rate. The carrier concentration increases from $2 \cdot 10^{19} \text{ cm}^{-3}$ to $1 \cdot 10^{20} \text{ cm}^{-3}$ when spray rate is increased from 0.5 mL/min to 3.3 mL/min independent of the film thickness; the carrier mobilities are always lower in slowly grown films. Sprayed ZnO:In films transmit 75–80% of the visible light while the increase in solution spray rate from 0.5 mL/min to 3.3 mL/min decreases the transmittance in the NIR region and increases the band gap in accordance with the increase in carrier concentration. Lower carrier concentration in slowly sprayed films is likely due to the indium oxidation.

1. Introduction

The wide band gap zinc oxide can be used in many applications, for example, in piezoelectric transducers, as transparent conductive layers (TCO-s), and as window layers in photovoltaic devices [1]. Various methods such as atomic layer deposition (ALD) [2], pulsed laser deposition (PLD) [3], chemical bath deposition (CBD) [4], RF magnetron sputtering [5], and chemical spray pyrolysis (CSP) [3, 6–16] have been used to deposit ZnO thin films. Among these methods, the spray pyrolysis is a versatile and cost-effective method for the rapid production of large-area metal oxide thin films.

Up to date, the effect of several technological parameters (zinc source and concentration, dopant type and concentration, solvent, growth temperature, etc.) on the properties of sprayed ZnO films have been studied [6–16] to determine the optimal deposition conditions to obtain as high electrical conductivity and optical transparency as possible. Earlier

studies have shown that the preferred crystallite orientation of intrinsic ZnO and gallium- and aluminium-doped ZnO is along *c*-axis [8, 9, 15] while the preferred crystallite orientation of indium-doped ZnO film is (101) plane parallel to the substrate [7–9, 12, 15]. The use of Ga or Al as the dopant leads to smaller grains than the use of In as a dopant [6, 7, 9]. Additionally, the density and the optical transmittance of sprayed ZnO film is controlled by the dopant type and concentration [7]. It has been reported that an optimal growth temperature for sprayed ZnO films is in the range of 350–500°C. Independent of dopant, the optical transmittance is ca. 85% [7, 9, 17–19] while the lowest resistivities of sprayed indium-doped and gallium-doped ZnO thin films are in the order of 10^{-4} – $10^{-3} \Omega\text{cm}$ [17, 18] and in the order of 10^{-3} – $10^{-2} \Omega\text{cm}$ for aluminium-doped ZnO [19].

Sprayed ZnO:In thin films have been used successfully as front electrodes in thin film silicon solar cells [20] and as window layer in Cu(In,Ga)(S,Se) solar cells [21]. Our long-term goal is to study the feasibility of ITO substitution with

ZnO:In, for use as the front electrode in the CSP-prepared extremely thin inorganic absorber (ETA) solar cell [22].

Among mentioned technological parameters, the solution spray rate (or solution flow rate) and its effect on ZnO thin films have received little attention. Ebothé et al. [16] studied the effect of the solution flow rate on the growth of undoped ZnO films prepared from ZnCl_2 solution and reported that the solution flow rate influences the surface topology. Dedova et al. [10] concluded that the solution spray rate affects the surface morphology and roughness of undoped ZnO thin films produced by spraying Zn acetate solutions.

Recently, we showed that the electrical resistivity of chemically sprayed In-doped ZnO thin films grown at 400°C can be altered within an interval of 10^2 – 10^{-3} Ωcm by varying the solution spray rate [12]. In this study we will not focus on obtaining the highest electrical conductivity or optical transmittance; we study the effect of the solution spray rate on the structural, morphological, optical, and electrical properties of ZnO:In thin films deposited by chemical spray. The aim is to find the optimal solution spray rate to deposit transparent and conductive ZnO:In thin films.

2. Experimental

ZnO thin films were grown from 100 mL of spray solution that was pneumatically sprayed onto preheated soda-lime glass substrate ($25 \times 25 \times 1 \text{ mm}^3$). The chemical spray pyrolysis (CSP) setup is described elsewhere [23]. The spray solution consisted of $\text{Zn}(\text{CH}_3\text{COO})_2 \cdot 2\text{H}_2\text{O}$ (Merck, analytical grade, 99.5%), dissolved in a mixture of deionised water and isopropyl alcohol (2:3 by volume) with $\text{Zn}(\text{CH}_3\text{COO})_2$ concentration of 0.2 mol/L. To avoid the precipitation of zinc hydroxide, a few drops of acetic acid were added to the spray solution. As a doping agent, indium(III)chloride (InCl_3) was added to the spray solution with an indium to zinc atomic ratio of 3 ($[\text{In}^{3+}]/[\text{Zn}^{2+}] = 3 \text{ at.}\%$). Compressed air (flow rate 8 L/min) was used as the carrier gas. The glass substrate was washed with soapy water, rinsed with deionised water, and cleaned ultrasonically in ethanol. After cleaning, the substrate was dried using compressed air and placed onto a hot plate. According to the results of our previous study [12], a film growth temperature of 400°C was chosen as optimal and kept constant within $\pm 5^\circ\text{C}$ throughout the experiments using a feedback control system for the heater. The solution spray rate was varied from 0.5 mL/min to 6.7 mL/min. We verified that the solution spray rate has no effect on the growth temperature.

For a comparison, films with spray rates of 0.35 mL/min, 0.5 mL/min, and 1.5 mL/min were grown from 150 mL of spray solution on a soda-lime glass substrate to obtain films with comparable thicknesses throughout the solution spray rate range.

The structure of the films was characterised by X-ray diffraction (XRD) using a Rigaku Ultima IV diffractometer with monochromatic $\text{Cu K}\alpha$ radiation ($\lambda = 1.5406 \text{ \AA}$), a tube voltage of 40 kV, and a current of 40 mA using a D/teX Ultra silicon strip detector. The crystallite size was

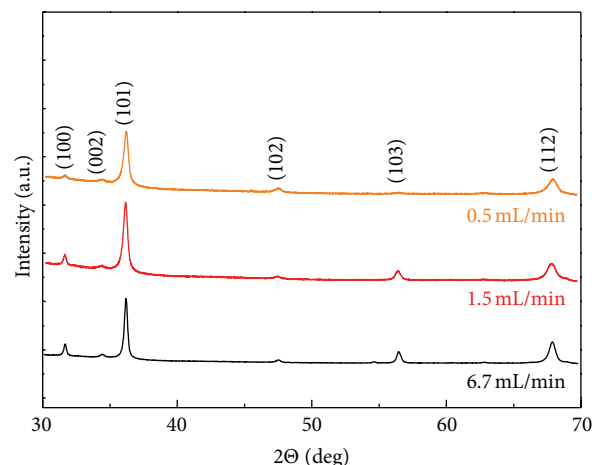


FIGURE 1: X-ray diffraction patterns of ZnO:In thin films deposited from 100 mL of spray solution at solution spray rates of 0.5 mL/min, 1.5 mL/min, and 6.7 mL/min.

calculated by the Debye-Scherrer method from the FWHM (full width at half maximum) of the (101) reflection of ZnO. The surface morphology of the films was characterised by scanning electron microscopy (SEM) and atomic force microscopy (AFM). SEM was performed with a Zeiss EVO-MA15 microscope at magnifications of 25000x and 50000x. AFM was performed on NT-MDT Solver 47 Pro system in tapping mode. The samples were studied over a $2 \times 2 \mu\text{m}^2$ area. The grain sizes estimated from the SEM images were comparable to those measured with the AFM. The surface roughness analysis was performed according to the ISO 4287/1 standard. The root mean square (RMS) roughness was calculated over a $3 \times 3 \mu\text{m}^2$ scanned surface area with an accuracy of $\pm 0.5 \text{ nm}$. Image analysis (IA) was achieved using the Media Cybernetics Image-Pro 7 analysing system. The specular UV-VIS-NIR transmittance was recorded in the wavelength range of 350–2500 nm with Jasco V-670 spectrophotometer. The film thickness was calculated using the Spectra Manager software (version 2.02.00) by analysing the interference in the transmittance spectra. The film thickness calculated from the optical spectra is in good agreement (less than $\pm 10\%$ variance) with that obtained from the SEM images. The elemental composition of the thin films was evaluated from four different $20 \times 20 \mu\text{m}^2$ areas on the film using energy dispersive X-ray (EDX) analysis with an Oxford Instruments INCA at an accelerating voltage of 7 kV. The electrical properties of the thin films (resistivity, charge carrier concentration, and mobility) were measured at room temperature using MMR's Variable Temperature Hall System supplied with Hall, Van der Pauw Controller H-50. The contact material used for the Van der Pauw and Hall measurements was graphite.

3. Results and Discussion

3.1. Structural Properties. The X-ray diffraction patterns of ZnO:In thin films deposited at various solution spray rates at 400°C are presented in Figure 1. All of the determined

TABLE 1: The effect of the solution spray rate on the sprayed ZnO:In film thickness (t), crystallite size (d), average grain size (D), electrical resistivity (ρ), main carrier mobility (μ), carrier concentration (n), and optical band gap (E_g). Soda-lime and borosilicate glasses are designated as Na-gl and B-gl, respectively.

Spray rate, mL/min	V, mL	Substrate	t , nm	d , nm	D , nm	ρ , Ωcm	μ , cm^2/Vs	n , cm^{-3}	E_g , eV
0.5	100	Na-gl	700	22	~ 100	$6.3 \cdot 10^{-2}$	4.4	$2.3 \cdot 10^{19}$	3.28
0.5	150	Na-gl	1400	26	~ 250	$3.3 \cdot 10^{-2}$	9.2	$2.1 \cdot 10^{19}$	3.24
0.5	150	B-gl	1350	26	*n.m.	$7.8 \cdot 10^{-2}$	3.9	$2.0 \cdot 10^{19}$	3.24
1.5	100	Na-gl	900	21	~ 120	$1.2 \cdot 10^{-2}$	7.7	$6.9 \cdot 10^{19}$	3.31
1.5	150	Na-gl	1400	29	~ 250	$7.3 \cdot 10^{-3}$	11	$7.6 \cdot 10^{19}$	3.27
3.3	100	Na-gl	1100	34	~ 250	$3.7 \cdot 10^{-3}$	16	$1.1 \cdot 10^{20}$	3.34
4.7	100	Na-gl	1100	35	~ 250	$3.2 \cdot 10^{-3}$	15	$1.4 \cdot 10^{20}$	3.36
6.7	100	Na-gl	1350	36	~ 250	$4.6 \cdot 10^{-3}$	12	$1.2 \cdot 10^{20}$	3.32

*n.m.: not measured.

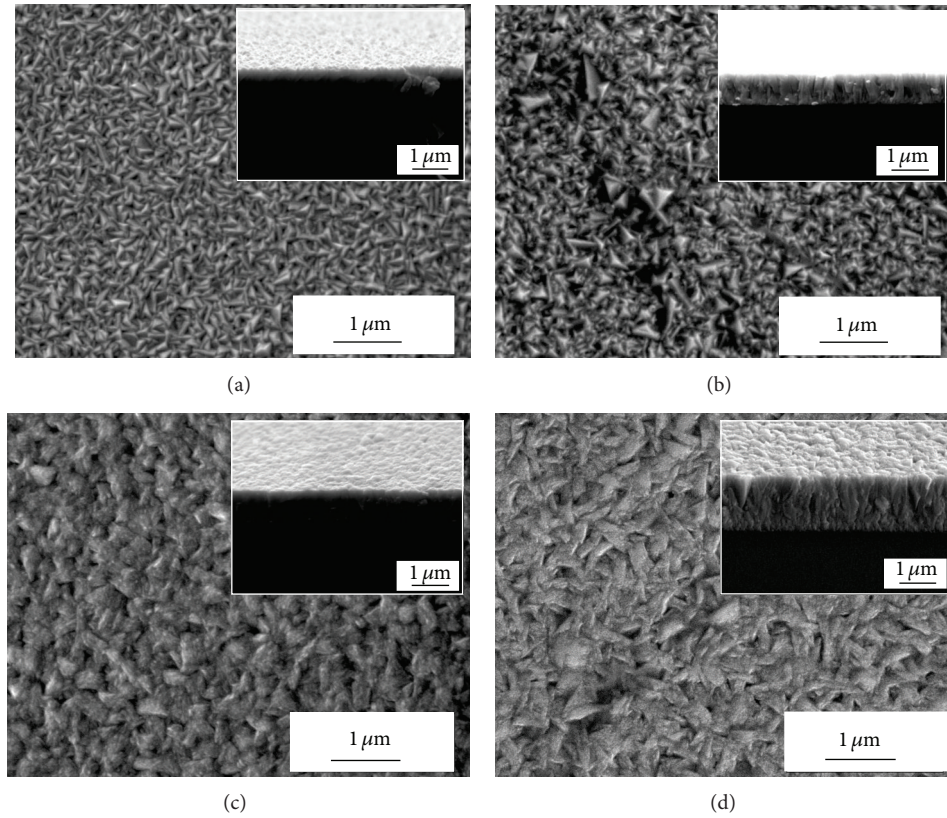


FIGURE 2: SEM images of ZnO:In thin films deposited from 100 mL of spray solution at solution spray rates of (a) 0.5 mL/min, (b) 1.5 mL/min, (c) 3.3 mL/min, and (d) 6.7 mL/min. The cross-sectional views are presented as insets on the surface images.

peaks belong to zincite (PDF card number 01-079-0208) [24]. According to Figure 1, ZnO:In film is preferably orientated in the (101) plane parallel to the substrate irrespective of the solution spray rate. Solution spray rates below 3 mL/min lead to smaller crystallites (average size of 20 nm), whereas solution spray rates above 3 mL/min result in crystallite sizes of ca. 35 nm (Table 1).

The microstructure of ZnO:In films was studied using SEM and AFM. According to the SEM study, sprayed ZnO:In

films exhibit a dense inner structure and relatively smooth surface with no cracks or pinholes. The SEM surface and cross-sectional images of ZnO:In films obtained at various solution spray rates are presented in Figure 2. The surface of the film deposited at the solution spray rate of 0.5 mL/min has well-shaped prismatic grains with similar sizes of ca. 100 nm (Figure 2(a)). The surface of the film grown with the solution flow rate of 1.5 mL/min consists of grains that vary in size from 50 nm to 500 nm (Figure 2(b)). The surface

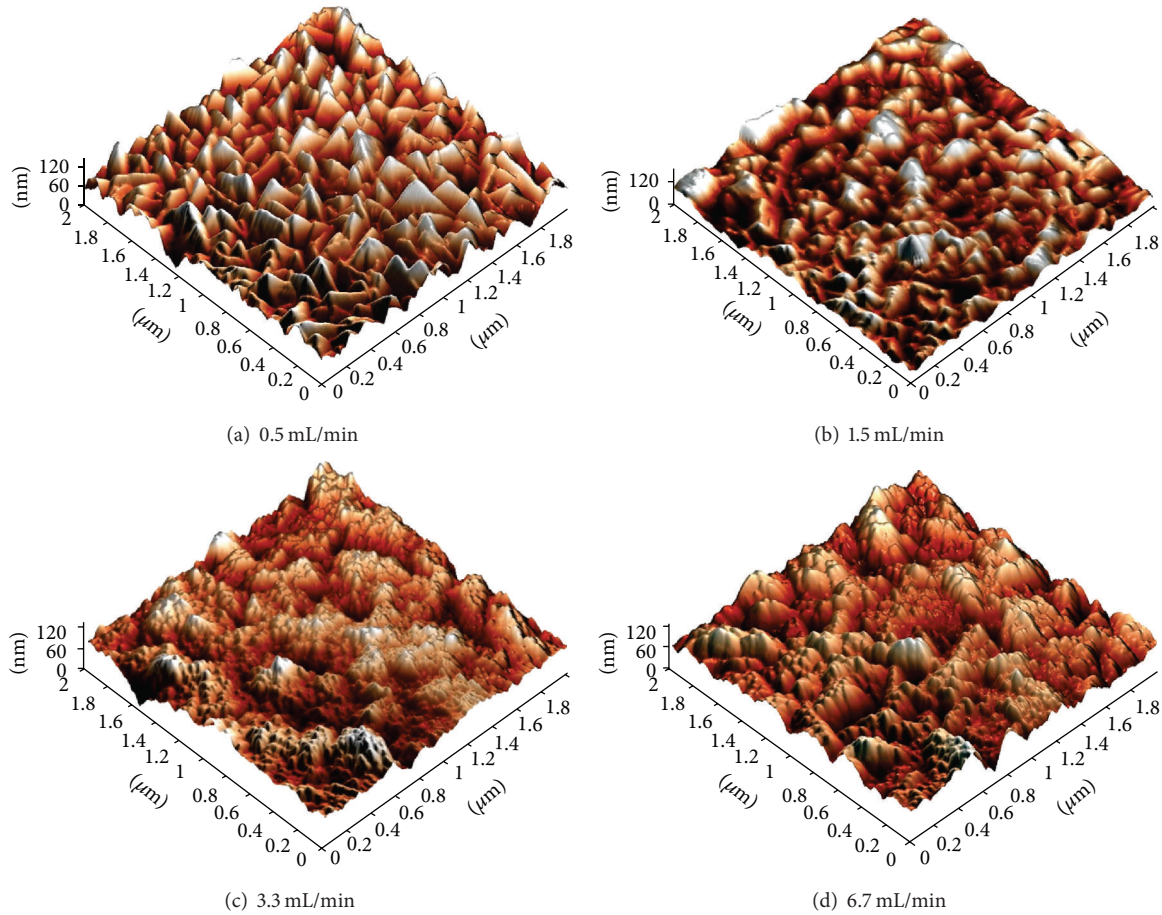


FIGURE 3: AFM 3D images of ZnO:In films deposited from 100 mL of spray solution with solution flow rates of (a) 0.5 mL/min, (b) 1.5 mL/min, (c) 3.3 mL/min, and 6.7 mL/min (d). AFM images are of a $2 \times 2 \mu\text{m}^2$ area.

structure of the film deposited with the solution spray rate of 3.3 mL/min is a network of interweaving grains (size of ca. 250 nm) resembling canvas or burlap (see Figure 2(c)). Further increase in the solution spray rate to 6.7 mL/min has a minor effect on the surface of ZnO:In thin film (Figure 2(d)).

The surface morphology of the ZnO:In films deposited at different solution spray rates was also characterised by AFM using images acquired over a $2 \times 2 \mu\text{m}^2$ area (Figure 3). The AFM images reveal that the solution spray rate has a strong effect on the surface morphology. The surface of the ZnO:In film obtained at a solution spray rate of 0.5 mL/min (Figure 3(a)) consists of well-shaped pyramidal grains with sharp edges and tip. The mean grain size is ca. 100 nm and the grain aspect ratio (the ratio of the major axis length to the minor axis length of an equiareal ellipse) is ca. 2.0. For the ZnO:In film with solution spray rate of 1.5 mL/min, the peaks and edges of the grains are rounded (Figure 3(b)), and the grain size varied from 70 nm to 200 nm (Figure 3(b)). According to the SEM image (Figure 2(b)), some of the grains had a diameter of ca. 500 nm. According to the AFM study, the mean grain size is ca. 120 nm and the aspect ratio of the grains is ca. 1.7. In contrast, the ZnO:In films prepared at solution spray rates of 3.3 mL/min and above have more complex surface structure (Figures 3(c) and 3(d)).

Using the solution spray rate of 3.3 mL/min, the film surface (Figure 3(c)) shows a fine-grain structure on top of grains with the size of ca. 200–250 nm and an aspect ratio of ca. 1.6, forming a double-layer surface. The fine-grain layer is composed of particles with an average diameter of ca. 40 nm. The surface structure of the film deposited at a solution spray rate of 6.7 mL/min (Figure 3(d)) is similar to that prepared at 3.3 mL/min (Figure 3(c)). The ca. 200–300 nm sized grains are covered by individually distinct particles with an average diameter of ca. 50 nm (Figure 3(d)).

Interestingly, the RMS roughness was ca. 20 nm for all sprayed ZnO:In films independent of solution spray rate and surface morphology. This RMS is similar to that reported by Dedova et al. [10] for sprayed ZnO:In films.

AFM study showed that the grain size increases with increasing solution spray rate. It is generally recognised that large grains are formed due to the recrystallisation of smaller grains. An extra phase on the grain boundaries may inhibit the growth of grains. This problem will be discussed in more detail in Section 3.2.

3.2. Electrical Properties. The resistivity, carrier concentration, and mobility of ZnO:In thin films dependent on the solution spray rate are presented in Figure 4. The films

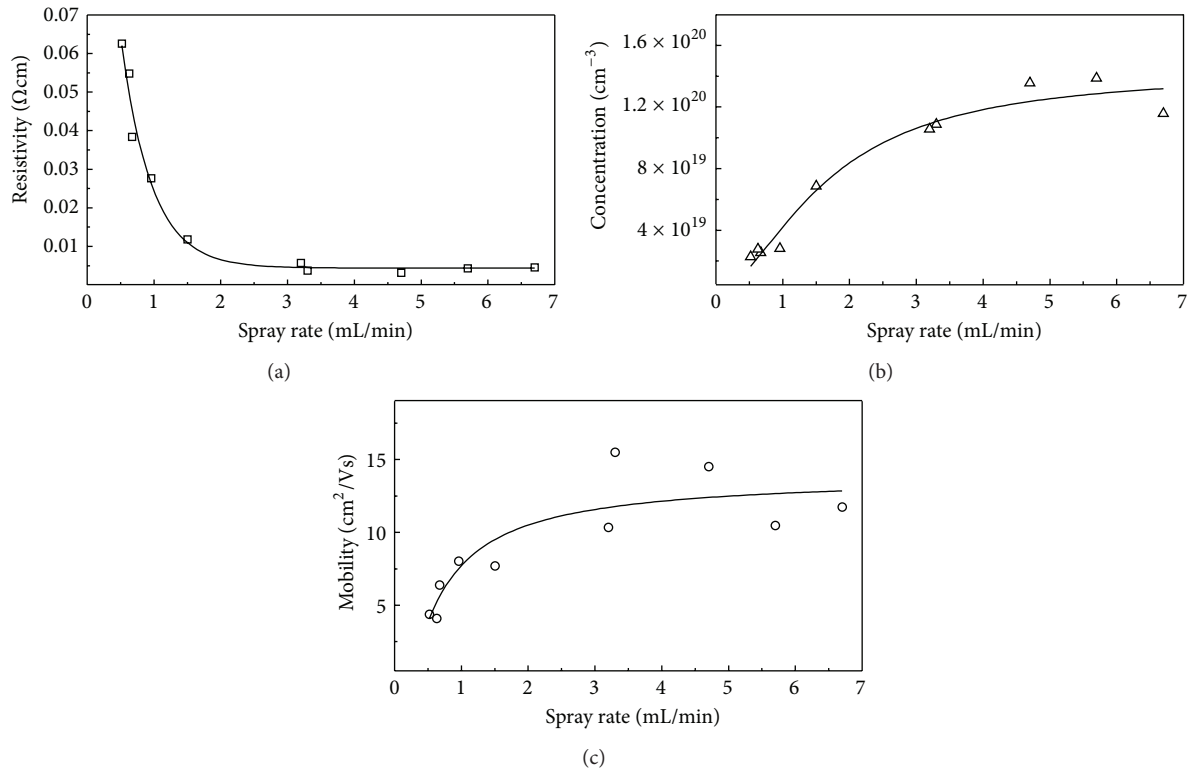


FIGURE 4: Resistivity (\square), carrier concentration (Δ), and carrier mobility (\circ) of ZnO:In thin films deposited from 100 mL of spray solution at solution spray rates of 0.5–6.7 mL/min.

presented in Figure 4 are sprayed from 100 mL of spray solution. The resistivity of the sprayed ZnO:In films decreases from ca. $6.3 \cdot 10^{-2} \Omega\text{cm}$ to $3.7 \cdot 10^{-3} \Omega\text{cm}$ while increasing the solution spray rate from 0.5 mL/min to 3.3 mL/min, respectively (Figure 4 and Table 1). Increasing the solution spray rate from 0.5 mL/min to 3.3 mL/min increases the carrier concentration from $2.3 \cdot 10^{19} \text{ cm}^{-3}$ to $1.1 \cdot 10^{20} \text{ cm}^{-3}$ and mobility from $4.4 \text{ cm}^2/\text{Vs}$ to $16 \text{ cm}^2/\text{Vs}$, respectively. The increase in the carrier mobility with increasing solution spray rate can be ascribed to the increased grain size from 100 to 250 nm as shown by AFM (Figure 3 and Table 1). This hypothesis is further supported by the following. The positive correlation between the carrier concentration and carrier mobility observed in our films is presented in Figure 5. A similar relation has been noted for ZnO:Al films grown by PLD [25], indicating that the conduction mechanism is driven by grain boundary scattering. Further increase in spray rate from 3.3 mL/min to 6.7 mL/min has minor effect on the electrical properties of ZnO:In thin films. The films prepared with spray rates above 3 mL/min show carrier concentrations around $1 \cdot 10^{20} \text{ cm}^{-3}$ and carrier mobilities in the range of 12–16 cm^2/Vs . A minor rise in resistivity (to $4.6 \cdot 10^{-3} \Omega\text{cm}$) in the film deposited at spray rate of 6.7 mL/min is attributed to lower carrier mobility of $12 \text{ cm}^2/\text{Vs}$. Wienke and Booi [15] reported similar carrier mobility of ca. $14 \text{ cm}^2/\text{Vs}$ and concentration of $1.4 \cdot 10^{20} \text{ cm}^{-3}$ for ultrasonically sprayed ZnO:In film.

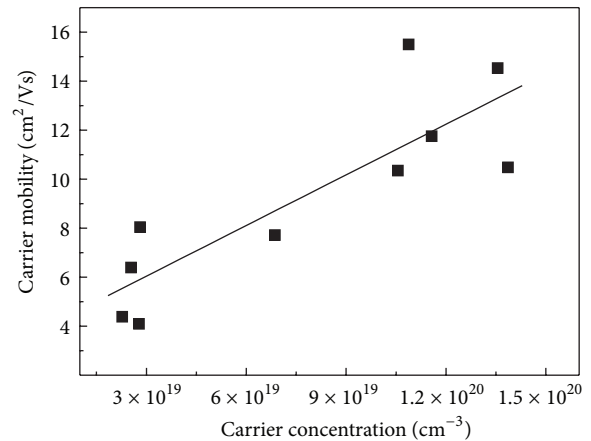


FIGURE 5: Carrier mobility versus carrier concentration of ZnO:In thin films deposited from 100 mL of spray solution at solution spray rates of 0.5–6.7 mL/min.

The films grown with the spray rates of 0.5–1.5 mL/min show carrier mobilities of 4.4–7.7 cm^2/Vs that is up to three times lower than recorded for the films grown with the spray rates above 3 mL/min (Figure 4, Table 1). It is known that the carrier mobility in the film is thickness and grain size dependent [26]. To prepare films with comparable thicknesses, the ZnO:In films with spray rates of 0.5 mL/min and 1.5 mL/min were deposited from 150 mL of spray solution and as a result,

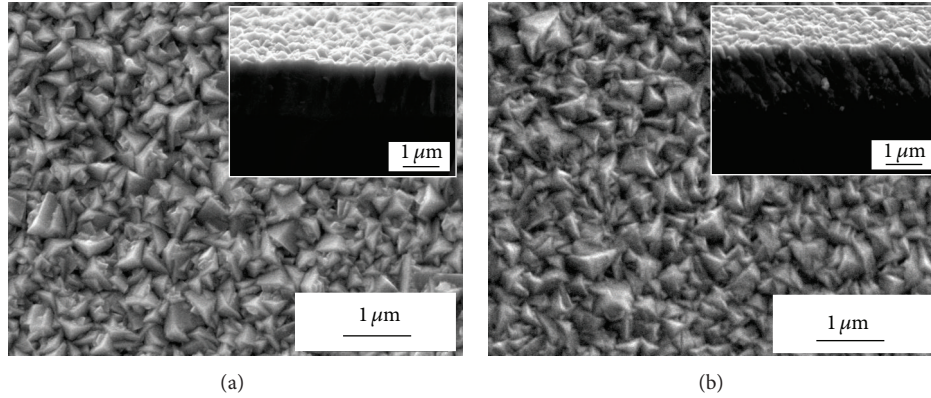


FIGURE 6: SEM images of ZnO:In thin films deposited from 150 mL of spray solution at solution spray rates of (a) 0.5 mL/min, and (b) 1.5 mL/min. The cross-sectional views are presented as insets on the surface images.

films with thicknesses of ca. 1400 nm were grown (Table 1). According to SEM images in Figure 6, the shape of the grains in the thicker films is similar to that reported for the thinner films with spray rates of 0.5 mL/min and 1.5 mL/min in Section 3.1 (Figures 2(a) and 2(b)). The grain sizes of the thicker films with spray rates of 0.5–1.5 mL/min were estimated from SEM images (Figure 6). The grain size of the thicker films is ca. 2 times higher when compared to the thinner films (Figures 2(a) and 2(b)). Thus, larger grains (size of ca. 250 nm) were obtained in thicker films and that is in accordance with the literature [9, 27, 28]. The carrier mobilities increased with the film thickness from $4.4 \text{ cm}^2/\text{Vs}$ to $9.2 \text{ cm}^2/\text{Vs}$ and from $7.7 \text{ cm}^2/\text{Vs}$ to $11 \text{ cm}^2/\text{Vs}$ for films deposited at 0.5 mL/min and 1.5 mL/min, respectively. Still, the mobilities in the films deposited at spray rates of 0.5–1.5 mL/min are slightly lower than in the films grown with solution spray rates above 3 mL/min regardless of comparable thicknesses (Table 1). The decrease could be due to the larger grain size distribution (75–700 nm) in the film with spray rate of 0.5 mL/min (Figure 6(a)) compared to the film with spray rate of 3.3 mL/min (200–300 nm) (Figure 2(c)).

It can be seen from Table 1 that carrier concentration depends on the solution spray rate independent of the film thickness. The carrier concentration of ca. $2 \cdot 10^{19} \text{ cm}^{-3}$ in film grown at 0.5 mL/min is ca. 10 times lower than in films with solution spray rate above 3 mL/min (ca. $1 \cdot 10^{20} \text{ cm}^{-3}$). Moreover, a ZnO:In film with thickness of 1400 nm was grown with solution spray rate of 0.35 mL/min and the carrier concentration of the mentioned film was $6 \cdot 10^{18} \text{ cm}^{-3}$. As the carrier concentration depends on the doping level [6, 8, 15] then it is possible that part of the indium was not incorporated into the ZnO lattice at lower solution spray rates.

It could be speculated that part of the dopant source might have left the system at slow spray rates due to relatively high InCl_3 vapour pressure of ca. 1.0 kPa at 400°C [29]. For this reason, the elemental composition of the films obtained with different spray rates was studied. According to EDX, the films deposited at different solution spray rates have similar elemental compositions (Table 2). Thus, the $[\text{In}]/[\text{Zn}]$ ratio in the film is constant at varied spray rates. As the EDX measurements were performed using factory-defined

TABLE 2: Elemental composition (in at.%) of ZnO:In thin films deposited at solution spray rates of 0.5 mL/min and 3.2 mL/min according to EDX.

Solution spray rate, mL/min	Zn	O	In
0.5	43.4	54.4	2.2
3.2	43.3	54.7	2.0

standards only, the atomic percentages of the elements are not absolute values. However, EDX confirms that there is no loss of the dopant source or that the loss is similar at all solution spray rates used.

Another cause for lower electron concentration while using low solution spray rates can be the diffusion of Na to the ZnO film from the soda-lime glass substrate at 400°C during long spray process [30]. In that case, Na could create defects that reduce the concentration of free electrons. Unfortunately, EDX cannot be used to detect Na due to the overlapping peaks of Zn and Na. To overcome this problem, a thicker ZnO:In film (from 150 mL) with thickness comparable to that on a soda-lime glass was deposited onto a borosilicate substrate at 0.5 mL/min. Film with thickness of ca. 1350 nm has a resistivity of $7.8 \cdot 10^{-2} \Omega\text{cm}$, carrier mobility of $3.9 \text{ cm}^2/\text{Vs}$, and concentration of $2.0 \cdot 10^{19} \text{ cm}^{-3}$ (see Table 1). The carrier concentrations of ZnO:In films on soda-lime and borosilicate glass substrate are comparable and thus the diffusion of Na is not responsible for the lower concentration of electrons in the films with low spray rates.

As there is no difference in the dopant concentration in the films deposited at different solution spray rates and the diffusion of sodium is not the case, the lower carrier concentration in the films with lower solution spray rates could be due to the failing of In incorporation into the ZnO lattice due to the oxidation of indium source. The study of ZnO:In films structural properties supports this hypothesis, as an extra phase on the grain boundaries inhibited the grain growth at low solution spray rates (see Section 3.1).

3.3. Optical Properties. The optical transmittance spectra of the ZnO:In films grown from 100 mL of spray solution using

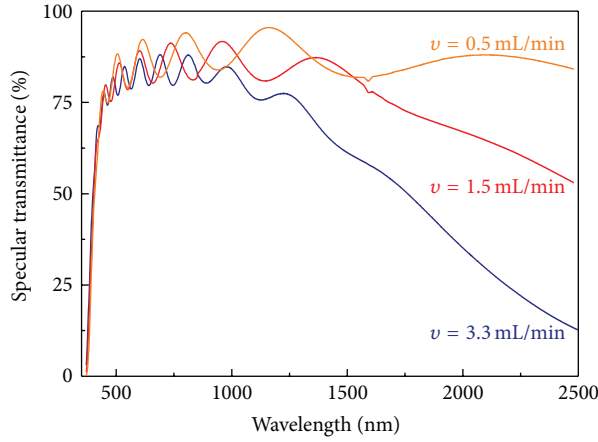


FIGURE 7: Specular transmittance of ZnO:In thin films deposited from 100 mL of spray solution at solution spray rates of 0.5 mL/min, 1.5 mL/min, and 3.3 mL/min.

various solution spray rates are presented in Figure 7. In the visible light region, the ZnO:In thin films show specular transmittance above 75% irrespective of the solution spray rate.

For the film prepared at 0.5 mL/min or lower, the transmittance in the near infrared region (NIR) is comparable to that in UV-VIS region. The increase in solution spray rate decreases film transmittance in the NIR region and the lowest transmittance is recorded for the film with solution spray rate of 3.3 mL/min. The decrease in the optical transmittance in the NIR spectral region corresponds to the increased concentration of carriers in the films sprayed at higher solution spray rates (Table 1). According to the literature, the decrease in the transmittance of TCO films in NIR spectral region is caused by the free carrier absorption [31–33]. This has been recorded for conductive ZnO films with electron concentrations of $3 \cdot 10^{20} \text{ cm}^{-3}$ and $6 \cdot 10^{20} \text{ cm}^{-3}$ deposited by ion-layer gas reaction spray [31] and PLD [32], respectively.

The optical band gap of the films is determined from the transmittance spectra. The optical band gap values were determined from the commonly used equation

$$\alpha h\nu = A \cdot (h\nu - E_g)^{1/n}, \quad (1)$$

where A is the parameter that does not depend on the photon energy, h is the Planck constant, E_g is the band gap energy, $h\nu$ is the incident photon energy, and $1/n$ is an exponent that depends on the nature of the optical transition ($n = 0.5$ for direct transition). The determination of E_g from $(\alpha h\nu)^2$ versus the $h\nu$ plot is shown in Figure 8 and the E_g values of ZnO:In films depending on the solution spray rate are given in Table 1. The ZnO:In film band gap increases from 3.24 eV to 3.36 eV as the solution spray rate increases from 0.5 mL/min to 4.7 mL/min, respectively. The increase in the band gap is in accordance with the increase in the carrier concentration (Table 1) and can be explained by the Burstein-Moss effect [33]. Thus, we have achieved a good agreement with the results of similar studies on ZnO [11, 13, 15, 25, 33].

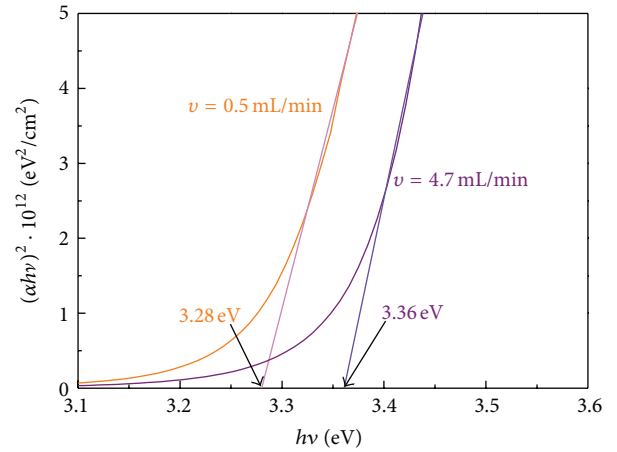


FIGURE 8: Graphical determination of direct optical band gap of ZnO:In thin films deposited from 100 mL of spray solution with solution spray rates of 0.5 mL/min and 4.7 mL/min.

4. Conclusions

At constant spray solution volume, an increase in the solution spray rate results in thicker ZnO:In films with larger crystallites and grains; also the surface morphology and electrical conductivity are affected. The grains in the film with spray rate of 1.5 mL/min are roundish when compared to the sharp-edged grains in the film with spray rate of 0.5 mL/min. The surface of the films with spray rate above 3 mL/min is composed of canvas-resembling grains (size ca. 250 nm) covered with particles with the size of ca. 40–50 nm. Increasing the spray rate from 0.5 mL/min to 3.3 mL/min decreases the electrical resistivity from $6.3 \cdot 10^{-2} \Omega\text{cm}$ to $3.7 \cdot 10^{-3} \Omega\text{cm}$ as the carrier concentration increases from $2.3 \cdot 10^{19} \text{ cm}^{-3}$ to $1.1 \cdot 10^{20} \text{ cm}^{-3}$ and mobility from $4.4 \text{ cm}^2/\text{Vs}$ to $16 \text{ cm}^2/\text{Vs}$, respectively.

To obtain films with comparable thicknesses throughout the solution spray rate range, more spray solution has to be used for films deposited at 1.5 mL/min and below. An increase in film thickness from 700 nm to 1400 nm and in grain size from 100 nm to ca. 250 nm increases the carrier mobility from $4.4 \text{ cm}^2/\text{Vs}$ to $9.2 \text{ cm}^2/\text{Vs}$ and from $7.7 \text{ cm}^2/\text{Vs}$ to $11 \text{ cm}^2/\text{Vs}$ for films deposited at 0.5 mL/min and 1.5 mL/min, respectively. Independent of the similar film thicknesses and the mean grain sizes, the mobilities in the slowly grown films are lower than in films with spray rate above 3 mL/min. Higher spray rates lead to higher carrier concentrations: spray rates of 0.5, 1.5, and 3.3 mL/min result in carrier concentrations of ca. $2 \cdot 10^{19}$, $7 \cdot 10^{19}$, and $1 \cdot 10^{20} \text{ cm}^{-3}$, respectively. The decreased carrier concentrations characteristic of the films with lower spray rates could be due to the oxidation of indium source that prevents indium from acting as the dopant in ZnO. Sprayed ZnO:In films with thickness of 1.1–1.4 μm transmit 75–80% of visible light. A decrease of the transmittance in NIR spectral region and an increase in band gap is characteristic of films with higher spray rate and corresponds to the increased carrier concentration in these films.

This study shows that the solution spray rate is an important technological parameter controlling the film thickness, morphology, grain size, optical properties, and electrical conductivity of the sprayed ZnO:In films. Still, the optimal spray rate should be determined for every setup to obtain films with properties required for a transparent and conductive material.

Conflict of Interests

The authors declare that they have no conflict of interests in the submitted paper.

Acknowledgments

Financing by the Estonian Ministry of Education and Research under Project SF0140092s08, the Estonian Science Foundation (ETF9081), and the European Regional Development Fund (Centre of Excellence “Mesosystems: Theory and Applications” TK114 and Project 3.2.1101.12-0023) is gratefully acknowledged. This work has been partially supported by the graduate school “Functional materials and technologies” receiving funding from the European Social Fund under Project 1.2.0401.09-0079 in Estonia.

References

- [1] N. H. Nickel and E. Terukov, *Zinc Oxide—A Material For Micro- and Optoelectronic Applications*, Springer, Dordrecht, The Netherlands, 2005.
- [2] L. Niinistö, J. Päiväsaari, J. Niinistö, M. Putkonen, and M. Nieminen, “Advanced electronic and optoelectronic materials by Atomic Layer Deposition: an overview with special emphasis on recent progress in processing of high- k dielectrics and other oxide materials,” *Physica Status Solidi A*, vol. 201, pp. 1443–1452, 2004.
- [3] X. M. Li, J. L. Zhao, J. M. Bian, W. D. Yu, and C. Y. Zhang, “Comparison of structural and photoluminescence properties of ZnO thin films grown by pulsed laser deposition and ultrasonic spray pyrolysis,” *Thin Solid Films*, vol. 515, no. 4, pp. 1763–1766, 2006.
- [4] A. Drici, G. Djeteli, G. Tchangbedji et al., “Structured ZnO thin films grown by chemical bath deposition for photovoltaic applications,” *Physica Status Solidi A*, vol. 201, no. 7, pp. 1528–1536, 2004.
- [5] M. K. Jayaraj, A. Antony, and M. Ramachandran, “Transparent conducting zinc oxide thin film prepared by off-axis rf magnetron sputtering,” *Bulletin of Materials Science*, vol. 25, no. 3, pp. 227–230, 2002.
- [6] A. Hafdallah, F. Yanineb, M. S. Aida, and N. Attaf, “In doped ZnO thin films,” *Journal of Alloys and Compounds*, vol. 509, no. 26, pp. 7267–7270, 2011.
- [7] A. R. Babar, P. R. Deshamukh, R. J. Deokate, D. Haranath, C. H. Bhosale, and K. Y. Rajpure, “Gallium doping in transparent conductive ZnO thin films prepared by chemical spray pyrolysis,” *Journal of Physics D*, vol. 41, no. 13, Article ID 135404, 2008.
- [8] M. Krunk, O. Bijakina, V. Mikli, T. Varema, and E. Mellikov, “Zinc oxide thin films by spray pyrolysis method,” *Physica Scripta*, vol. 79, pp. 209–212, 1999.
- [9] M. L. Olvera, H. Gómez, and A. Maldonado, “Doping, vacuum annealing, and thickness effect on the physical properties of zinc oxide films deposited by spray pyrolysis,” *Solar Energy Materials and Solar Cells*, vol. 91, no. 15–16, pp. 1449–1453, 2007.
- [10] T. Dedova, J. Klauson, C. Badre et al., “Chemical spray deposition of zinc oxide nanostructured layers from zinc acetate solutions,” *Physica Status Solidi A*, vol. 205, no. 10, pp. 2355–2359, 2008.
- [11] T. V. Vimalkumar, N. Poornima, C. Sudha Kartha, and K. P. Vijayakumar, “On tuning the orientation of grains of spray pyrolysed ZnO thin films,” *Applied Surface Science*, vol. 256, no. 20, pp. 6025–6028, 2010.
- [12] M. Vent, E. Kärber, T. Unt, A. Mere, and M. Krunk, “The effect of growth temperature and spraying rate on the properties of ZnO:In films,” *Physica Status Solidi C*, vol. 9, pp. 1604–1606, 2012.
- [13] A. Maldonado, J. Rodríguez-Baez, and M. L. Olvera, “Physical properties of indium and fluorine codoped zinc oxide thin films deposited by chemical spray,” *Materials Chemistry and Physics*, vol. 129, no. 1–2, pp. 109–115, 2011.
- [14] R. Biswal, L. Castañeda, R. Moctezuma, J. Vega-Pérez, M. L. Olvera, and A. Maldonado, “Formation of indium-doped zinc oxide thin films using ultrasonic spray pyrolysis: the importance of the water content in the aerosol solution and the substrate temperature for enhancing electrical transport,” *Materials*, vol. 5, pp. 432–442, 2012.
- [15] J. Wienke and A. S. Booi, “ZnO:In deposition by spray pyrolysis—influence of the growth conditions on the electrical and optical properties,” *Thin Solid Films*, vol. 516, no. 14, pp. 4508–4512, 2008.
- [16] J. Ebothe, A. El Hichou, P. Vautrot, and M. Addou, “Flow rate and interface roughness of zinc oxide thin films deposited by spray pyrolysis technique,” *Journal of Applied Physics*, vol. 93, no. 1, pp. 632–640, 2003.
- [17] S. Major, A. Banerjee, and K. L. Chopra, “Highly transparent and conducting indium-doped zinc oxide films by spray pyrolysis,” *Thin Solid Films*, vol. 108, no. 3, pp. 333–340, 1983.
- [18] K. T. R. Reddy, T. B. S. Reddy, I. Forbes, and R. W. Miles, “Highly oriented and conducting ZnO:Ga layers grown by chemical spray pyrolysis,” *Surface and Coatings Technology*, vol. 151–152, pp. 110–113, 2002.
- [19] M. L. Olvera, A. Maldonado, R. Asomoza, R. Castanedo-Pérez, G. Torres-Delgado, and J. Cañetas-Ortega, “Conductive and transparent ZnO:Al thin films obtained by chemical spray,” *Journal of Materials Science*, vol. 11, no. 5, pp. 383–387, 2000.
- [20] J. Wienke, B. van der Zanden, M. Tijssen, and M. Zeman, “Performance of spray-deposited ZnO:In layers as front electrodes in thin-film silicon solar cells,” *Solar Energy Materials and Solar Cells*, vol. 92, no. 8, pp. 884–890, 2008.
- [21] C. H. Fischer, N. A. Allsop, S. E. Gledhill et al., “The spray-ILGAR (ion layer gas reaction) method for the deposition of thin semiconductor layers: process and applications for thin film solar cells,” *Solar Energy Materials and Solar Cells*, vol. 95, no. 6, pp. 1518–1526, 2011.
- [22] M. Krunk, E. Kärber, A. Katerski et al., “Extremely thin absorber layer solar cells on zinc oxide nanorods by chemical spray,” *Solar Energy Materials and Solar Cells*, vol. 94, no. 7, pp. 1191–1195, 2010.
- [23] K. Otto, A. Katerski, A. Mere, O. Volobujeva, and M. Krunk, “Spray pyrolysis deposition of indium sulphide thin films,” *Thin Solid Films*, vol. 519, no. 10, pp. 3055–3060, 2011.
- [24] “International Centre for Diffraction Data (ICDD),” PDF-2 Release 2008.

- [25] T. Minami, "Transparent conducting oxide semiconductors for transparent electrodes," *Semiconductor Science and Technology*, vol. 20, no. 4, pp. S35–S44, 2005.
- [26] C. E. Benouis, M. Benhaliliba, A. Sanchez Juarez, M. S. Aida, F. Chami, and F. Yakuphanoglu, "The effect of indium doping on structural, electrical conductivity, photoconductivity and density of states properties of ZnO films," *Journal of Alloys and Compounds*, vol. 490, no. 1-2, pp. 62–67, 2010.
- [27] R. Venkatraman and J. C. Bravman, "Separation of film thickness and grain boundary strengthening effects in Al thin films on Si," *Journal of Materials Research*, vol. 7, no. 8, pp. 2040–2048, 1992.
- [28] R. M. Keller, S. P. Baker, and E. Arzt, "Quantitative analysis of strengthening mechanisms in thin Cu films: effects of film thickness, grain size, and passivation," *Journal of Materials Research*, vol. 13, no. 5, pp. 1307–1317, 1998.
- [29] B. Brunetti, V. Piacente, and P. Scardala, "Torsion study on the sublimation process of InCl_3 ," *Journal of Chemical and Engineering Data*, vol. 43, no. 1, pp. 101–104, 1998.
- [30] A. Katerski, A. Mere, V. Kazlauskienė et al., "Surface analysis of spray deposited copper indium disulfide films," *Thin Solid Films*, vol. 516, no. 20, pp. 7110–7115, 2008.
- [31] S. Gledhill, A. Grimm, D. Greiner, W. Bohne, M. Lux-Steiner, and C. H. Fischer, "Doping induced structural and compositional changes in ZnO spray pyrolysed films and the effects on optical and electrical properties," *Thin Solid Films*, vol. 519, no. 13, pp. 4293–4298, 2011.
- [32] L. Gong, Z. Ye, J. Lu et al., "Highly transparent conductive and near-infrared reflective ZnO:Al thin films," *Vacuum*, vol. 84, no. 7, pp. 947–952, 2010.
- [33] V. Bhosle, A. Tiwari, and J. Narayan, "Electrical properties of transparent and conducting Ga doped ZnO," *Journal of Applied Physics*, vol. 100, no. 3, Article ID 033713, 6 pages, 2006.

Research Article

Preparation of Baking-Free Brick from Manganese Residue and Its Mechanical Properties

Ping Wang^{1,2} and Dong-yan Liu¹

¹ Department of Civil Engineering, Chongqing University, Chongqing 401300, China

² Department of Architecture & Civil Engineering, Logistical Engineering University, Chongqing 401331, China

Correspondence should be addressed to Dong-yan Liu; cqudyliu@yahoo.com.cn

Received 12 December 2012; Revised 21 February 2013; Accepted 3 March 2013

Academic Editor: Wen Zeng

Copyright © 2013 P. Wang and D.-y. Liu. This is an open access article distributed under the Creative Commons Attribution License, which permits unrestricted use, distribution, and reproduction in any medium, provided the original work is properly cited.

The increasing amount of waste residue produced during the electrolytic preparation process of manganese has nowadays brought about serious environmental problems. The research on utilization of manganese slag has been a hot spot around the world. The utilization of manganese slag is not only environment friendly, but also economically feasible. In the current work, a summarization of the main methods to produced building materials from manganese slag materials was given. Baking-free brick, a promising building material, was produced from manganese slag with the addition of quicklime and cement. The physical properties, chemical composition, and mechanical performances of the obtained samples were measured by several analyses and characterization methods. Then the influence of adding materials and molding pressure during the preparation of baking-free brick samples on their compressive strength properties was researched. It is concluded that the baking-free brick prepared from manganese residue could have excellent compressive strength performance under certain formula.

1. Introduction

China has the largest amount of electrolytic manganese in production, consummation, and exportation. The total quantity of electrolytic manganese can be as huge as millions of tons every year, which account for up to 95% of that of the world [1–3]. It is also reported that Chinese electrolytic manganese production enterprises are mainly located in provinces like Hunan, Chongqing, Sichuan, Guizhou, and Yunnan. The production capacity and production amount of Chinese electrolytic manganese industry have a significant increase from 0.210 million tons in 2002 to 1.411 million tons in 2011, which can be seen in Table 1 [4, 5]. The production of manganese metal is finical to our life. But, with the continuous increase production amount, the grade of available manganese ore has been decreased to only 15%~20%. This means that there will be 5~7 t of acid residue prepared per 1 t of electrolytic manganese, resulting in the formation of a great deal of electrolytic manganese residue.

Electrolytic manganese residue (EMR) can be defined as the acid residue obtained during the preparation of

electrolytic manganese, which is a process of adding mineral powders containing manganese carbonate into the sulfuric acid. It is also an inert salic material, more than 80% of whose particle size is below 80 μm . On the other hand, EMR is full of sulfate, for the content of SO_3 can be up to 15%~25% [6]. However, EMR has a complicated composition due to its production process. The heavy metal ions in EMR would introduce terrible environmental pollution to the around soil and water after a long time of stockpiling and weathering. These soil and water rich of heavy metal ions could be a threat to human health. So for the purpose of reuse of manganese residue and reduction of its negative influences, research on the comprehensive utilization is an extremely interesting subject.

As a promising active material, EMR can be widely use in the production of building materials like cement, concrete, and brick [7–12]. The prepared cement and concrete could have excellent performance of corrosion resistance and mechanical properties [13, 14]. As to the according research [15, 16], industrial residues such as EMR, slag can be used to produce the sintered brick, ceramic brick, steam-pressing

TABLE 1: Production capacity and amount of the Chinese electrolytic manganese industry (million tons).

Year	2002	2003	2004	2005	2006	2007	2008	2009	2010	2011
Production capacity	0.300	0.450	0.550	0.921	1.049	1.570	1.879	2.110	2.200	2.230
Production amount	0.210	0.325	0.494	0.566	0.733	1.024	1.139	1.317	1.376	1.411

TABLE 2: The physical properties of EMR.

Physical properties	Fineness (%)	Density (g/cm ³)	Moisture content (%)	Dry density (g/cm ³)	Cohesion (kPa)	Internal friction angle (°)
EMR	31.1	1.72	52.6	1.13	11.5	22.2

brick, and baking-free brick. The method is to produce brick from the mixture of these industrial residues with shale and deposited mud. It is not only economically feasible, but also environmental friendly. Recently, many attempts have been made to prepare these kinds of bricks with better mechanical properties. Both Peng et al. [17] and Gao [18] have prepared sintered bricks using EMR, shale, and fly ash as raw materials. Their compressive strength can be up to 22.64 MPa. Zhang et al. [19] have done the research on the preparation of cameral brick materials from manganese slag. The mixing amount can be up to as much as 40%. Wang et al. [20] obtained the steam-pressing brick from EMR with 10%~20% of cement and 5%~10% of quicklime. And the compressive strength can be about 20~30 MPa.

As to the preparation of baking-free brick, Jiang et al. [21] have found a new preparation method to obtain the compressive strength reaching up to 10 MPa. They mixed the EMR with fly ash, lime, and binding materials like lime cement followed by the addition of aggregate. Then the baking-free brick is obtained after the process of compression moulding. This process can dramatically enhance the strength and decrease the use of water. Generally, it is an effective way of resource utilization of EMR to obtain baking-free brick by the process of compression moulding [22]. In this paper, we have produced baking free brick from manganese slag with the addition of quicklime and cement and have measured the physical properties, chemical compositions, and mechanical performances of the obtained samples.

2. The Preparation of EMR Brick

2.1. Materials. The status of EMR is loose when it was first poured into the slag stocking site and will change into half flow conditions under the action of rainwater which is as shown in Figure 1(a). Then the manganese slag will solidify after a long time of evaporation. The surface can turn into a hardened state which is illustrated in Figure 1(b). And it is harder than the part under the surface.

Figure 2(a) reveals the vertical distribution pattern of the manganese residue. The sampling site is 30 m far from the slag dam and 0.8~1.2 m below the hardened surface. EMR in this site is black dope in the state of half flow as shown in Figure 2(b).

The physical performances and chemical composition of the taken samples are separately illustrated in Tables 2 and 3. From Table 2, it can be known that the density is 1.72 g/cm³,

and the moisture content can be around 52.6%. And from Table 3 it can be seen that the main composition is SiO₂ which is the main composition of brick. On the other hand, the cement used in these experiments is 42.5 ordinary Portland cement. The fineness modulus of sand is separately 3.1 and 1.1. The experimental quicklime containing 76.5% of active calcium oxide is sieved at a 0.8% residue. Its fineness is referring to the standard of cement.

2.2. Preparation of the Samples. The proportion of materials in this experimental is in dry status. As shown in Table 2, the moisture content of the taken EMR is 52.6%. What is more the contents of MnSO₄ and (NH₄)₂SO₄ are separately 3.75% and 2.47%. As to the fabrication of EMR brick, the forming process is was semidry pressing process. The size of the performing tool was Φ100 mm × 100 mm. The samples after forming were maintained by watering in the air. The strength is referring to the Mortar Strength Testing Method of Cement (GB/T17671-1999), performances testing to the Chinese National Standard of Wall Bricks Testing Methods (GB/T2542-2003), and the Detection Technological Standards of Building Structure (GB/T 50344-2004).

3. Testing Properties of EMR Baking-Free Brick

3.1. Raw Materials Systems. The low strength of brick from EMR-sand-lime system cannot afford the requirement of building materials. But the properties can be enhanced through adding ~15% content of cement into the system [23]. As a building material, the fabrication process of baking-free brick is simple and becomes a hot spot of the researchers globally. In the previous studies, fly ash often acts as cementing materials [24]. However, due to the widely use of fly ash rather than cement and low production quantity of electrolytic manganese enterprise, it is critically important and low cost to produce the brick with the utilization of cement. The purpose of this paper is to investigate the influence of ratio and kinds of the raw materials on the mechanical properties of obtained bricks. According to the previous paper and the comparing experiments, it was proved that the system of EMR-sand-lime-cement is the best.

3.2. Forming Pressure. The early strength of EMR baking-free brick obtained in the process of forming pressure is due to the

TABLE 3: The chemical composition of the EMR.

Composition (%)	SiO ₂	Al ₂ O ₃	Fe ₂ O ₃	CaO	MgO	MnO	SO ₃	Loss
EMR	38.4	14.3	6.78	9.45	—	3.75	19.2	10.12



(a)



(b)

FIGURE 1: (a) Half flow conditions; (b) hardened state of surface.

TABLE 4: Compressive strength of bricks under different forming pressures.

Forming pressure (MPa)	Compressive strength (MPa)	
	7d	28d
20	10.6	16.3
25	13.5	17.4
30	14.7	21.3
35	15.3	21.7
40	16.2	22.3

close contact of the raw particle materials [25]. It is beneficial to the physical and chemical reaction between these particles and simultaneously provides base for the later strength. The compressive strength of the bricks prepared under different forming pressures is shown in Table 4. From Table 4, it can be known that the 7d and 28d compressive strengths increase gradually along with the value of forming pressure. The rate of increase is low. But it is said that the larger the forming pressure is, the higher cost and the lower production efficiency is. Comprehensively considering these factors, we conclude that the forming force of 25~30 MPa can meet the requirement of architectural design. So it is believed to be the optimum range of moulding pressure.

3.3. Properties of EMR. Compressive strength testing was carried out on the baking-free brick fabricated by binding materials base on the previous forming pressure experiment. The binding material was obtained under different ratios of EMR-sand-lime-cement system. In the process, the ratio of water to solid is an important factor. Its value was determined in the range of 0.10~0.20, according to case if the slurry would overflow from the forming mold. What is more the result also will differ under different ratio of cement to sand. The 7d and 24d compressive strengths under different formulas are stated

in Table 5. It can also be seen that the average compressive strength of the as-obtained samples is over 10 MPa, which is up to the standard of building materials.

Table 5 illustrates that an optimum formula is 50% of EMR, 20% of river sand, 15% of quicklime, and 15% of cement, and ideal ratio of water to solid materials is 13%. On the other hand, the result of test for heavy metal extraction meets the environmental criterion. The concentration of leaching Mn²⁺ is about 1.3 mg/L, while that of the national discharged standard of sewage is 1.8 mg/L. Consequently, the preparation of baking-free brick with excellent properties can be achieved using EMR as the main raw material.

The addition of aggregate can improve the particle size of mixture, reduce the contraction of the fabricated bricks, and enhance the mechanical behavior and durability of the samples. Due to the high proportion of aggregate and low proportion of cementing materials in Formula 1 and Formula 2, only when reducing the ratio of water to cement can it meet the conditions of compression moulding. Even though it has a large value of 28d strength, products from these two formulas have no practical applications because of the lacking of binding materials, tendency to loose, complex corporation of production process, and bad durability. While as to Formula 4 and Formula 5, the samples have more binding materials and less aggregate, leading to low strength. Shortage of framework materials and high demand of water are the main reasons. Above all, it can be concluded that the as-fabricated samples can have the largest 7d and 28d strength at a cement aggregate ratio of 1:1. It can be used in actual production using the formula of 50% EMR, 25% river sand, 10% quicklime, and 15% cement.

4. Conclusion

From the experiments and discussions in this paper, we can know that, in the production of EMR baking-free brick, 25~30 MPa of molding force is economically feasible,



FIGURE 2: (a) Vertical distribution pattern of the manganese residue; (b) samples taken from 1.0 m below.

TABLE 5: Compressive strength under different ratios of cement to sand.

Formula	Cement-sand ratio	Water-solid ratio	Compressive strength (MPa)	
			7d	28d
1	1 : 2.0	0.11	10.4	12.4
2	1 : 1.5	0.12	11.9	15.3
3	1 : 1.0	0.15	14.7	19.0
4	1 : 0.6	0.18	14.3	18.1
5	1 : 0	0.22	7.9	16.5

and the pressure during forming process is beneficial to obtainment of the brick strength. Furthermore, when the cement aggregate ratio is 1 : 1 water solid ratio is 0.15, and the moulding pressure is 30 MPa, the produced EMR baking-free bricks have excellent mechanical properties like compressive strength. What is more is EMR-sand-lime-cement production system is the optimum one with 50% of EMR, 25% of river sand, 10% of quicklime, and 15% of cement.

References

- [1] A. Veyseyre, K. van de Velde, C. Ferrari, and C. Boutron, "Searching for manganese pollution from MMT anti-knock gasoline additives in snow from central Greenland," *Science of the Total Environment*, vol. 221, no. 2-3, pp. 149–158, 1998.
- [2] N. Duan, W. Fan, Z. Changbo, Z. Chunlei, and Y. Hongbing, "Analysis of pollution materials generated from electrolytic manganese industries in China," *Resources, Conservation and Recycling*, vol. 54, no. 8, pp. 506–511, 2010.
- [3] J. J. Jing and J. M. Xie, "Hazards of manganese pollution to health," *Guangdong Trace Elements Science*, vol. 15, no. 2, pp. 6–9, 2008.
- [4] Z. Z. Tan, "The development of "11.5 plan" and the forecast of "12.5 plan" in Chinese EMM industry's," *China's Manganese Industry*, vol. 29, no. 1, pp. 1–4, 2011.
- [5] J. Yang and Z. M. Zeng, "The situation analysis of EMM of China market in 2010," *China's Manganese Industry*, vol. 29, pp. 6–9, 2011.
- [6] J. S. Qian, K. P. Hou, and Z. Wang, "Properties of electrolytic manganese slag used as building materials," *Materials Review*, vol. 23, pp. 59–61, 2009.
- [7] T. P. Li, H. L. Xie, X. M. He, and X. Z. Zhou, "Experimental study of calcined electrolysis manganese residue and fly ash complex admixture," *Bulletin of the Chinese Ceramic Society*, vol. 26, pp. 567–573, 2007.
- [8] Y. Z. Ouyang, X. W. Peng, J. B. Cao, Z. P. Li, and X. D. Deng, "Ultrasonic leaching of electrolytic manganese residue with additive," *Environmental Protection of Chemical Industry*, vol. 27, pp. 257–259, 2007.
- [9] J. S. Qian, P. K. Hou, Z. Wang, and Y. Z. Qu, "Qu. Crystallization characteristic of glass-ceramic made from electrolytic manganese residue," *Journal of Wuhan University of Technology—Materials Science Edition*, vol. 27, pp. 45–49, 2012.
- [10] P. K. Hou, J. S. Qian, Z. Wang, and C. Deng, "Production of quasi-sulfoaluminate cementitious materials with electrolytic manganese residue," *Cement and Concrete Composites*, vol. 34, pp. 248–254, 2012.
- [11] Y. Wang, W. H. Ye, and J. Wan, "Method for manufacturing aerated concrete from electrolysis manganese slag," CN, 101698586 [P], 2010.
- [12] Y. Wang, Y. S. Gao, L. Hengbo et al., "Water quenching manganese slag high performance concrete and preparation method," CN, 101844905 [P], 2010.
- [13] Kh. S. A. E. Sherbini, "Simultaneous extraction of manganese from low grade manganese dioxide ore and beneficiation of sulphur slag," *Separation and Purification Technology*, vol. 27, no. 1, pp. 67–75, 2002.
- [14] R. J. Liu, P. Chen, and Y. J. Wang, "Manufacture of light weight heat-insulating wall materials from water-quenched manganese slags," CN, 101774208 [P], 2010.
- [15] S. D. Li, H. Xiao, and R. Liu, "Recycling of fly ash, reservoir sludge and metallurgical tailings in manufacture of sintered decorative brick for dry walls," CN, 101666148 [P], 2010.
- [16] K. Y. Chiang, K. L. Chien, and S. J. Hwang, "Study on the characteristics of building bricks produced from reservoir sediment," *Journal of Hazardous Materials*, vol. 159, no. 2-3, pp. 499–504, 2008.

- [17] B. Peng, L. Y. Chai, and J. Wang, "Method for treating industrial wastes, through sintering and solidifying, for the production of bricks," CN, 101775868 [P], 2010.
- [18] H. L. Gao, "Production and consumption of manganese ore in and out of China," *China Metal Bulletin*, vol. 7, pp. 33–36, 2006.
- [19] J. Zhang, Q. Lian, J. R. Wang, and F. Chen, "The experimental study on making use of manganese dregs to prepare ceramic wall and floor tile," *China Ceramic Industry*, vol. 16, no. 3, pp. 16–19, 2009.
- [20] Y. Wang, N. C. Zhang, and W. H. Ye, "Method for the manufacture of bricks from electrolytic manganese-production slag, suitable for reducing environmental pollution and energy consumption," CN, 01644089 [P], 2010.
- [21] X. H. Jiang, Z. Wang, P. K. Hou, J. S. Qian, and J. P. Cao, "Experimental study on preparation of non-burnt brick from electrolytic manganese residue," *Non-Metallic Mines*, vol. 33, no. 1, pp. 14–17, 2010.
- [22] C. S. Poon, S. C. Kou, and L. Lam, "Use of recycled aggregates in molded concrete bricks and blocks," *Construction and Building Materials*, vol. 16, no. 5, pp. 281–289, 2002.
- [23] P. Chen, Z. J. Wang, and R. J. Liu, "Experimental study on concrete of manganese slag in different dosage," *Concrete*, vol. 2, pp. 71–73, 2010.
- [24] J. Xie and H. M. Bao, "Study on service test of cement mortar and concrete mixed with manganic sinter," *Subgrade Engineering*, no. 5, pp. 156–158, 2007.
- [25] Y. L. Wang, P. Chen, T. Liu, and J. R. Liu, "Experimental research of admixtures prepared with ferromanganese slag," *Journal of Guilin University of Electronic Technology*, vol. 29, no. 6, pp. 507–510, 2009.

Research Article

Characterization of Nanoporous Ceramic Granules Made with Coal Fly Ash and Their Utilization in Phenol Removal from Water

Zhaoqian Jing

College of Civil Engineering, Nanjing Forestry University, Nanjing 210037, China

Correspondence should be addressed to Zhaoqian Jing; zqjing@yahoo.com

Received 1 December 2012; Accepted 13 February 2013

Academic Editor: Shao-Wen Cao

Copyright © 2013 Zhaoqian Jing. This is an open access article distributed under the Creative Commons Attribution License, which permits unrestricted use, distribution, and reproduction in any medium, provided the original work is properly cited.

Coal fly ash has been evaluated as low-cost material for pollutants adsorption. But powdered fly ash is difficult to be separated from the adsorbate and solution after saturation. When it is made into granules, this problem can be solved. Granules with uniform diameter of 6 mm were prepared and used as adsorbents for phenol removal from aqueous solution. The physical and chemical characteristics of the granules were investigated. The data indicated that the granules were abundant with nanosize pores of 9.8 nm on average. The specific surface area and porosity reached $130.5 \text{ m}^2/\text{g}$ and 60.1%, respectively. The main components in the granules were SiO_2 , Al_2O_3 , MgO , Fe_2O_3 , CaO , K_2O , and unburned carbon. The adsorption batch experiments showed that this granular material was an efficient adsorbent for phenol removal. Phenol adsorption on the granules was mainly influenced by dosage and contact time. Increase in the dosage could enhance phenol adsorption effectively. More than 90% phenol could be removed under normal temperature and neutral pH with initial concentration of 100 mg/L, contact time of 90 min, and dosage of 140 g/L. The adsorption of phenol on the granules was spontaneous and complied well with the pseudo-second-order model and Langmuir isotherm model.

1. Introduction

Coal fly ash is byproduct from the burning process of coal in fired burning plants and other industries with coal as fuel. It is usually taken as solid industrial waste in many countries and places. The annual production of coal fly ash has continued to increase in recent years. Disposal of it usually consumes large quantities of land and water [1]. Coal fly ash is generally composed of SiO_2 , Al_2O_3 , CaO , Fe_2O_3 , MgO , and unburned carbon. It can be used not only as an additive in construction industry [2] but also as cheap media for soil amelioration [3] and adsorbents for pollutants removal [4].

Phenol is an important raw material or product of some industries such as coal tar, gasoline, plastic, pesticide, and steel production. It can be combined with other pollutants as phenolic compounds. Moreover, phenol is always dissolved in water with high solubility, but lesser amount of it can produce unpleasant odor and cause chronic toxic effects to human being, animals, and plants [5]. Many countries have listed

phenol as one kind of priority pollutants and set strict limits for it in surface water and wastewater discharge [6]. Complete removal or in some cases reduction of it to an acceptable concentration has become a major challenge for environment protection.

Because of the toxic characteristics, it is very difficult for phenol to be biodegraded directly. The regular treatment methods for water containing phenol are flocculation, solvent extraction, adsorption, advanced oxidation, and so forth. Among these processes, adsorption has been taken as an effective separation process for phenol. Although activated carbon is widely used as adsorbent for phenol removal from water, it has the disadvantage of high-cost and complex regeneration. The development of potential low-cost adsorbents with high adsorption capacity is essential for phenol removal. In recent years, many materials such as synthetic resin [7], green macro alga [8], and bagasse fly ash [9] have been used in phenol removal from aqueous solution. Some researchers have studied the removal of phenol and its analogs from water

TABLE 1: Physical indexes of the granules acquired by mercury porosimeter.

Index	V_{ti} (mL/g)	A_t (m ² /g)	R_{mv} (nm)	R_{ma} (nm)	R_a (nm)	D_a (g/mL)	Porosity (%)
Value	0.33	66.8	14.7	6.0	9.8	4.63	60.1

with coal fly ash [10]. But powdered fly ash is difficult to be separated from the adsorbed phenol and solution. When it is used to remove phenol from water, additional coagulation and sedimentation measures are usually needed.

In this study, coal fly ash was used to produce composite ceramic granules with high porosity and specific surface area. The physical characteristics and chemical composition of the granules were studied. The granules were used as adsorbents for phenol removal from water. Effects of various parameters such as adsorbents dosage, contact time, and temperature were studied to optimize the adsorption parameters. Kinetics, thermodynamics, and isotherm studies were also carried out to illustrate the adsorption process of phenol onto the ceramic granules.

2. Material and Methods

2.1. Granules Preparation. Coal fly ash was taken from a fired burning power plant utilizing coal as fuel in Huludao, Liaoning Province of China. 51% fly ash, 39% clay, and 10% diatomite (in weight) were mixed after crushing and screening. The mixture was used to produce spherical granules of certain diameter with the aid of sodium silicate in a granulator. After being dried at 383 K with a baking furnace, the raw granules were calcined for 2 hours at 723 K in an incinerator [11]. The finished granules were finally produced. In the preparation process, the diameter of the granules could be accurately controlled. Granules with uniform diameter of 6 mm were used as adsorbent to remove phenol from aqueous solution in this study.

2.2. Characterization of the Granules. Since adsorption is an interface phenomenon, pore area and distribution in the granules are vital for the adsorption process. This material was studied firstly with scanning electron microscope (SEM, Quanta 200, FEI, Holland) to ascertain the external and sectional structure of the granules. A mercury porosimeter (Autopore 9500, Micromeritics, USA) was used to characterize the granules in terms of porosity, total pore area, pore radius, and so on. It is capable of generating a pressure up to 60,000 psi to detect the main indexes of meso- to macropores [12]. The granules were also analyzed with energy dispersive X-ray spectrometry (EDS, GENESIS, EDAX, USA) to investigate the main compositions [13].

2.3. Adsorption Experiments. The batch studies were conducted by dosing the granules into aqueous solution with certain initial phenol concentration prepared in the laboratory. The pH of the solutions was controlled around 7.0 with 1 mol/L solutions of HCl or NaOH. The samples were stirred in a temperature-controlled oscillator at a constant speed of 180 rpm. After some time, the supernatant was

withdrawn and filtered through 0.45 μ m membrane filter. Residual phenol concentration was analyzed with the method of spectrophotometry [14]. The effect of operation parameters such as dosage, contact time, and temperature on phenol removal was investigated. The adsorption kinetics, thermodynamics parameters, and isotherm model were also studied.

The removal percentage of phenol (η) and adsorption capacity q (mg/g) were calculated using the following equations:

$$\eta(\%) = \frac{C_0 - C}{C_0} \times 100, \quad (1)$$

$$q = \frac{(C_0 - C)V}{w},$$

where C_0 is the initial phenol concentration (mg/L), C is phenol concentration (mg/L) after adsorption, V is the volume of the solution (L), and w is the mass of the granules (g).

3. Results and Discussion

3.1. SEM Characterization. The shape of materials, surface texture, and even particle distribution can be observed and analyzed by scanning electron microscope [15, 16]. SEM pictures of the external and sectional view of the composite granules are shown in Figure 1. It can be seen that this kind of ceramic granules had many drapes and pores in the surface. Some pores even penetrated into the internal part. The section plane showed typical laminated and layered structure in the granules, which amplified the specific surface area of this material and favored pollutants adsorption into the inner positions of this material.

3.2. Porous Characterization. Table 1 contains the data for the granules with the mercury intrusion method in terms of the total intrusion volume (V_{ti}), total pore area (A_t), median pore radius (volume, R_{mv}), median pore radius (area, R_{ma}), average pore radius ($2V/A$, R_a), apparent (skeletal) density (D_a), and porosity. The average pore radius in the granules was 9.8 nm. The total pore area, porosity, and apparent (skeletal) density of the granules reached 66.8 m²/g, 60.1%, and 4.63 g/mL, respectively. The relationship between pore radius and incremental pore volume is shown in Figure 2. The data indicated that the radius of meso- to macropores was in the wide range of 1.5 nm to 45300 nm. The peak of nanopores distribution was located at 10.5 nm with the incremental pore volume of 0.03289 mL/g, amounting to about 10% of the total intrusion volume. The pores with radius under 10 nm, 50 nm, and 100 nm accounted for 35.1%, 79.2%, and 91.4%, respectively. The proportion of pores with radius above 100 nm was only 8.6%. These data indicated that the granular material was a kind of nanosize porous media

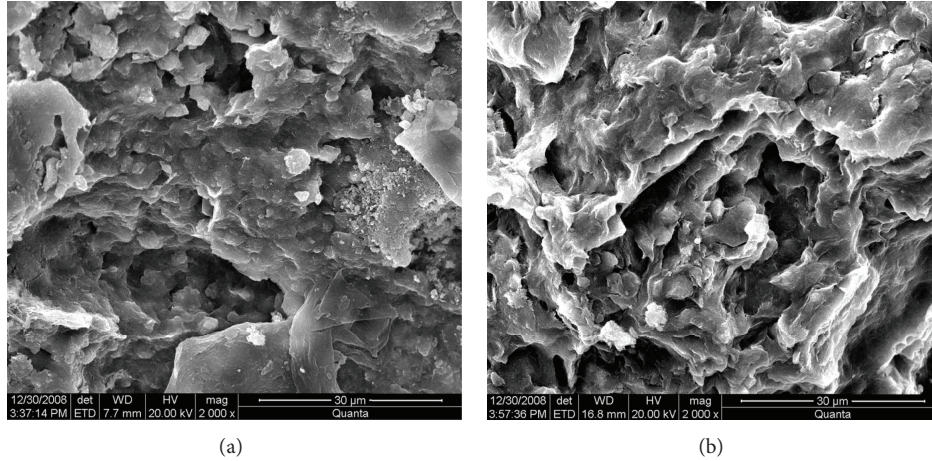


FIGURE 1: Typical SEM photographs of the ceramic granules: (a) external; (b) sectional.

TABLE 2: Main elements composition of the granules.

Main elements	O	Si	C	Al	Mg	Fe	Ca	K
Mass (%)	55.94	17.51	9.97	4.83	3.2	2.69	2.04	1.06
Trace elements composition of the granules.								
Trace elements	Cl	Na	S	Ti	Se	Zn	Mn	Cu
Mass (%)	0.89	0.67	0.4	0.35	0.3	0.07	0.05	0.03

with high porosity and specific surface area, which were vital parameters in the utilization as adsorbent.

3.3. Chemical Composition. As determined by EDS (Table 2), the predominant elements were O, Si, C, Al, Mg, Fe, Ca, and K, which amounted to 97.24% in total. There were also other minor elements of Cl, Na, S, Ti, Se, Zn, Mn, and Cu. Element composition of carbon accounted for 9.97% (mass fraction). This is significant since it has been shown that carbon and its compounds can significantly increase the porosity and total pore area of ceramic granules made of fly ash [17, 18]. According to the elements composition, the chemical oxides' components in the granules were calculated. The main oxides were SiO_2 (37.47%), Al_2O_3 (9.13%), MgO (5.31%), Fe_2O_3 (3.46%), CaO (2.86%), and K_2O (1.28%).

3.4. Effect of Dosage on Phenol Adsorption. The effect of granules dosage on phenol adsorption percentage (η) and adsorption capacity (q) was investigated by varying the dosage from 20 g/L to 300 g/L at pH 7.0 and 288 K with initial phenol concentration of 100 mg/L and contact time of 60 min. The increase in dosage supplied more active sites at the surface and the internal structures of the granules and resulted in obvious rise in the phenol adsorption. As shown in Figure 3, with the dosage increasing from 20 g/L to 300 g/L, the removal percentage of phenol with initial concentration of 100 mg/L increased obviously from 51.4% to 100%. So it was feasible to remove phenol completely with sufficient granules dosage. At 140 g/L dosage, nearly 90% of phenol was removed from water.

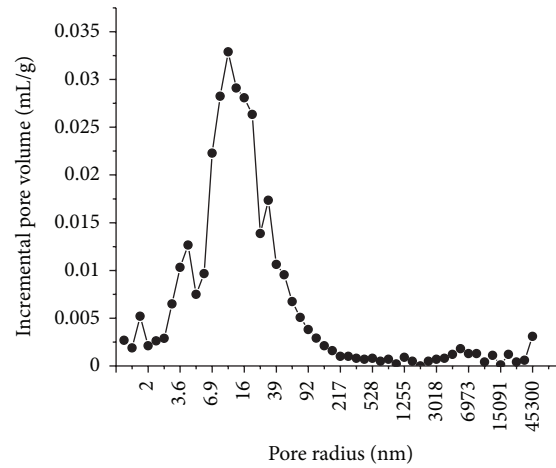


FIGURE 2: Distribution of pore size in the granules.

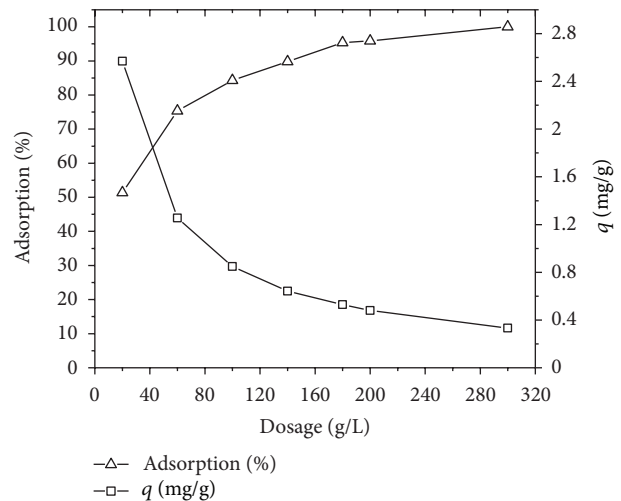


FIGURE 3: Effect of dosage on phenol removal. pH: 7.0; temperature: 288 K; initial concentration: 100 mg/L; contact time: 60 min.

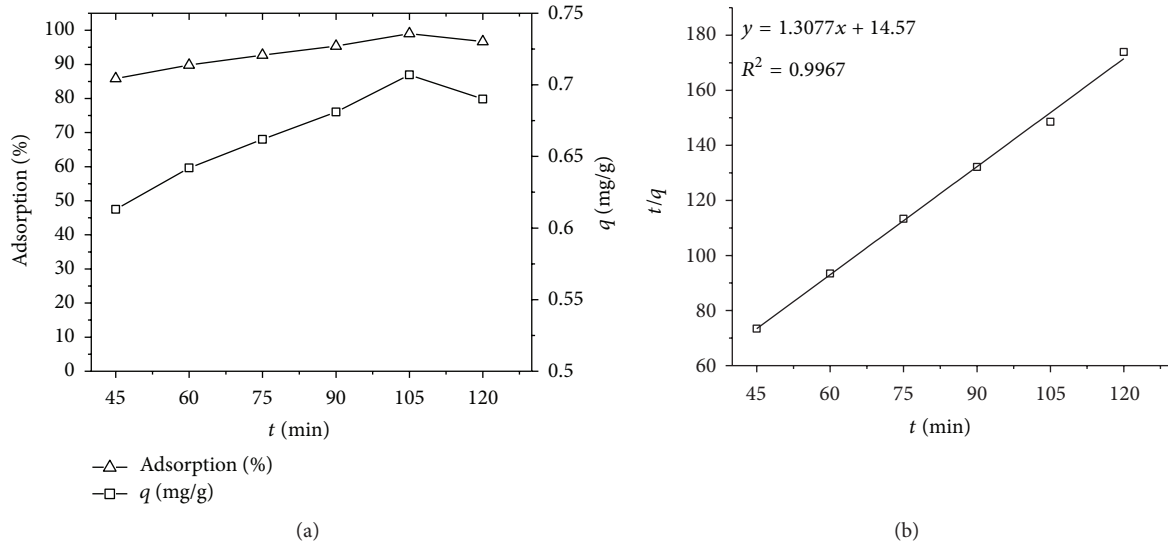


FIGURE 4: Effect of contact time on phenol adsorption: (a) adsorption percentage and capacity variation with time; (b) pseudo-second-order kinetic model. pH: 7.0; dosage: 140 g/L; temperature: 303 K; initial concentration: 100 mg/L.

It can also be seen that the adsorption capacity declined obviously with dosage increase. The adsorption capacity at 300 g/L dosage was only 13.0% of that at 20 g/L dosage. This indicated that the adsorption capacity could not be fully utilized at high-dosage operations. Consequently the granules after adsorption at high dosage could be reused at low-dosage operations.

3.5. Effect of Contact Time and Adsorption Kinetics. The effect of contact time on phenol adsorption was carried out to ascertain the equilibrium point and adsorption kinetics at pH 7 and 303 K with the granules dosage of 140 mg/L. Figure 4(a) shows phenol adsorption variation versus contact time. Before 105 min, there were enough vacant adsorption sites on the granules, and phenol adsorption almost increased linearly with contact time. Phenol removal rose from 85.9% to 99.0% with contact time increasing from 45 min to 105 min, indicating that contact time was a vital parameter for phenol adsorption on the granular material. But it can also be noticed that overlong contact time was not helpful when the adsorption of phenol attained equilibrium between the solution and the granules after 105 min [19]. Phenol removal percentage was maintained above 95% with contact time in the range 90–105 min. Subsequent experiments were done with adsorption time of 90 min, which was considered as approximately sufficient for phenol removal from water with the granules.

There are several kinetics models for substances adsorption such as the first-order kinetic model, pseudo-second-order kinetic model, and an intraparticle diffusion kinetic model [20]. The adsorption of phenol on the granular material had the characteristics of both physisorption and chemisorption [21]. Consequently, the pseudo-second-order model might be more suitable for phenol adsorption on the granules [22].

TABLE 3: Main thermodynamic parameters variation at different temperatures.

T (K)	ΔG° (kJ/mol)	ΔH° (kJ/mol)	ΔS° (J/mol K)
288	−9.93		
298	−10.78		
303	−11.20	14.42	84.56
308	−11.62		
318	−12.47		

The pseudo-second-order model can be expressed using

$$\frac{t}{q_t} = \frac{1}{k_2 q_e^2} + \frac{1}{q_e} t, \quad (2)$$

where q_e is the equilibrium adsorption capacity (mg/g), q_t is the amount of phenol adsorbed at time t (min), and k_2 is the rate constant of pseudo-second-order adsorption (g/(mg min)).

t/q_t against t for the pseudo-second-order model is shown in Figure 4(b). The correlation coefficient value (R^2) reached 0.9967, implying that the pseudo-second-order model was appropriate for phenol adsorption onto the granular material.

3.6. Effect of Temperature on Phenol Adsorption. The effect of temperature on phenol adsorption was investigated with the operation temperature ranging from 288 K to 318 K with initial phenol concentration of 100 mg/L, contact time of 90 min and solution pH of 7.0. Figure 5(a) shows the changes of equilibrium concentration (C_e) and adsorption capacity (q_e) under different temperatures. With the increase in temperature from 288 K to 318 K, C_e decreased from 10.18 mg/L to 5.97 mg/L, whereas q_e increased slightly from 0.642 mg/g to 0.672 mg/g. Phenol removal percentage and adsorption

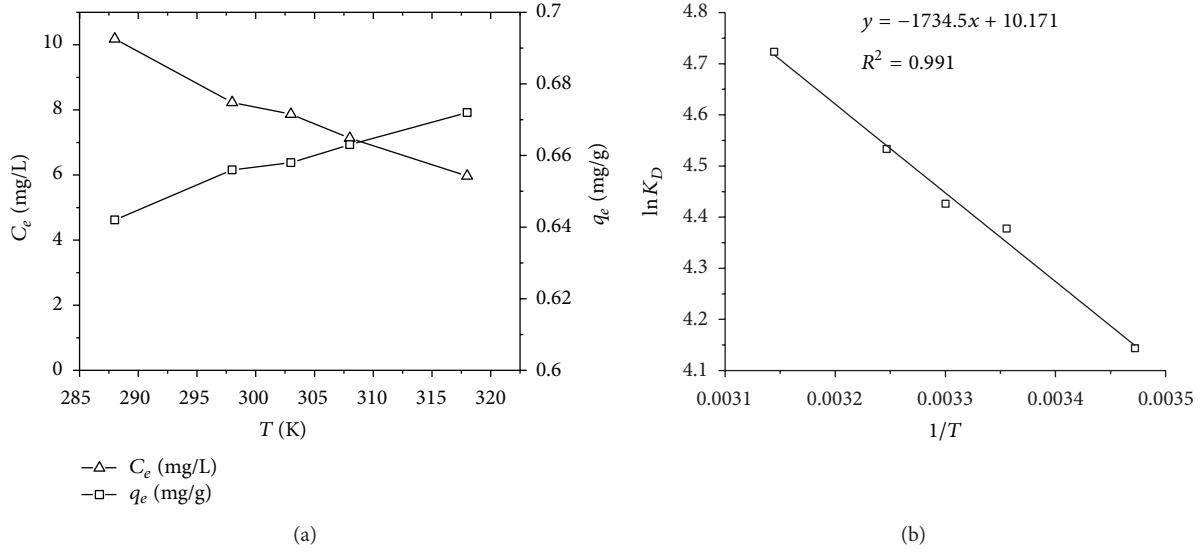


FIGURE 5: Effect of temperature on phenol adsorption: (a) the equilibrium concentration (C_e) and equilibrium adsorption capacity (q_e) variation; (b) distribution coefficient (K_D) variation.

capacity obviously increased with temperature rise, which indicated that the adsorption of phenol on the granules was not exothermic but endothermic [23]. The increase in temperature supplied more energy to the phenol molecules and more chances for phenol interaction with the active sites at the surface and internal structure of the granules [24]; consequently more phenol was adsorbed. The increase in phenol adsorption capacity of the granules with the increase in temperature was similar to some carbonaceous adsorbents [25].

The influence of temperature on phenol adsorption onto the ceramic granules can be analyzed with thermodynamic parameters including free energy change (ΔG°), enthalpy (ΔH°), and entropy (ΔS°). The relation among the three parameters can be expressed with (3), and ΔG° can be calculated with thermodynamic distribution coefficient (K_D) ((4) and (5)) [26, 27]:

$$\Delta G^\circ = \Delta H^\circ - T\Delta S^\circ, \quad (3)$$

where T is the temperature,

$$\Delta G^\circ = -RT \ln K_D, \quad (4)$$

where R is the universal gas constant (8.314 J/(mol K)), and

$$K_D = \frac{q_e}{C_e}, \quad (5)$$

where C_e and q_e are the equilibrium concentration and the equilibrium adsorption capacity with units of mg/mL and mg/g, respectively.

Consequently, (6) can be obtained with the combination of (3) and (4). With the data in Figure 5(a), the thermodynamic parameters of ΔH° and ΔS° were acquired with the slope and intercept of Figure 5(b); then ΔG° was calculated

using (3). The values of ΔG° , ΔH° , and ΔS° for the adsorption of phenol on the ceramic granules are shown in Table 3:

$$\ln K_D = \frac{\Delta S^\circ}{R} - \frac{\Delta H^\circ}{RT}. \quad (6)$$

The positive value of ΔH° indicated that the adsorption of phenol was endothermic, which was also supported by the slightly increase of the equilibrium adsorption capacity with temperature rise. The positive value of ΔS° suggested the increase of randomness at liquid/solid interface during phenol adsorption, which was mainly caused by the substitution of water by phenol with larger molecular weight at the interface [28]. The faster move of water molecules from the solid interface to liquid face resulted in the increase of the entropy. The negative free energy changes (ΔG°) indicated that the adsorption of phenol on the ceramic granules was spontaneous. Moreover, the decrease of ΔG° with temperature showed that the adsorption was more favorable at higher temperatures. As shown in Figure 5(a), the adsorption was more complete at higher temperatures. However, ΔG° only changed from -9.93 kJ/mol to -12.47 kJ/mol with temperature ranging from 288 K to 318 K, and adsorption capacity also varied slightly with temperature variation. Therefore, the influence of temperature on phenol adsorption was minor compared with that of dosage and contact time. Phenol adsorption on the ceramic granules can be accomplished at normal temperatures.

3.7. Adsorption Isotherm. Adsorption isotherm is usually used to describe the relationship between the equilibrium adsorption capacity and equilibrium concentration under a constant temperature. Langmuir isotherm model (7) and Freundlich isotherm model (8) are usually used to describe the distribution of adsorbates between the liquid phase and the solid phase [29]. The adsorption isotherm of phenol on

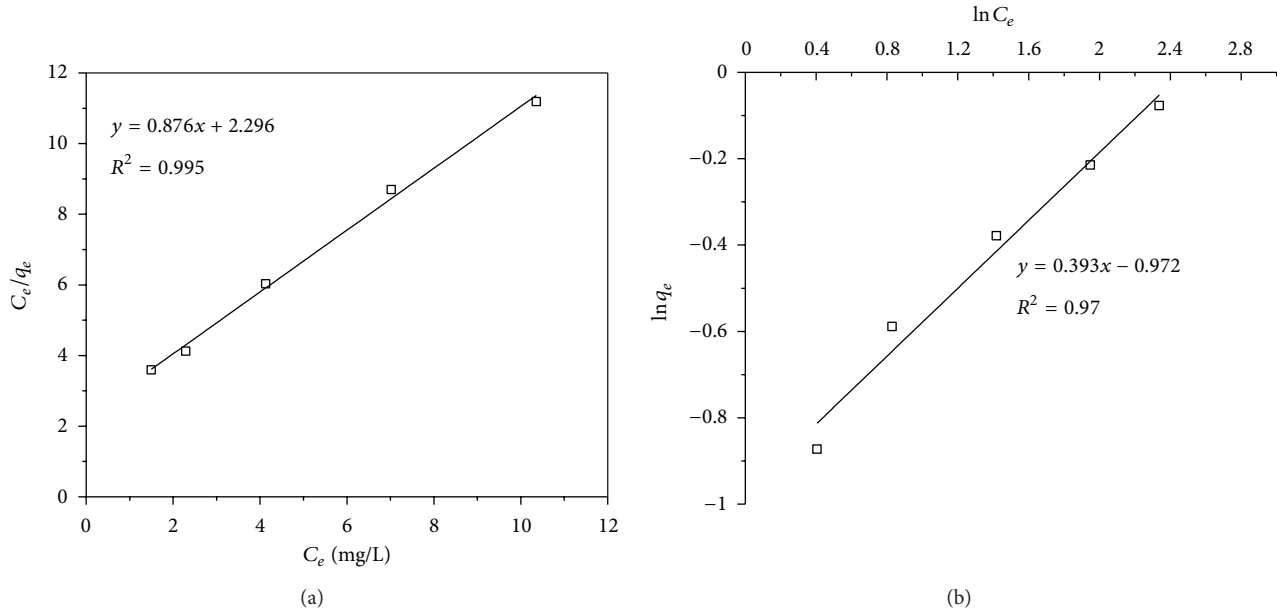


FIGURE 6: Adsorption isotherm of phenol onto the granules: (a) Langmuir model; (b) Freundlich model.

the ceramic granules was obtained with initial phenol concentration varying from 60 mg/L to 140 mg/L and granules dosage of 140 g/L at 303 K. The adsorption time and initial pH value were controlled at 90 min and 7.0, respectively:

$$\frac{C_e}{q_e} = \frac{1}{Q_m b} + \frac{C_e}{Q_m}, \quad (7)$$

$$q_e = k_f C_e^{1/n}, \quad (8)$$

where Q_m is the adsorption capacity (mg/g), and b , k_f , and n are characteristic constants of adsorption. For linearization of the data, the Freundlich equation can be written in the following logarithmic form:

$$\ln q_e = \ln k_f + \frac{1}{n} \ln C_e. \quad (9)$$

The linearization of equilibrium data under different initial concentrations showed that the adsorption of phenol on the ceramic granules complied with both Langmuir and Freundlich isotherm model (Figure 6). Q_m and b in Langmuir model were calculated to be 1.142 mg/g and 0.381 L/mg. k_f and n in Freundlich model were estimated to be 0.378 and 2.545, respectively. Nevertheless, the R^2 value of Langmuir model was higher than that of Freundlich model, so the Langmuir isotherm model was more appropriate for phenol adsorption on the granules.

3.8. Overall Evaluation and Comparison with Other Adsorbents. This kind of ceramic granules is efficient and convenient to be used in phenol removal from water. After saturation, the granules are easily to be separated from the aqueous solution. There are many studies on phenol removal with powder-activated carbon, fly ash [10], and organobentonite [30]. However, such materials can only work

efficiently with the integration of coagulation [31]. In this study, with the ceramic granules' application, there is no need for other disposal steps of coagulation or sedimentation. The adsorption with the granules can be operated under normal temperature and neutral pH with high efficiency. In the study of Parida and Pradhan [29] with manganese nodule leached residue as adsorbent, the adsorption was almost doubled with temperature increased from 298 K to 338 K, and phenol was only adsorbed completely at low pH. Alzaydien and Manasreh [32] found that phenol adsorption onto activated phosphate rock was also affected obviously by pH and temperature. The adsorption capacity reached the highest value at pH 8.0, whereas it decreased greatly with temperature increase. In this study, the adsorption of phenol onto the ceramic granules is also very fast, and it can reach equilibrium at around 90 min. In the study of Srivastava et al. [9] with bagasse fly ash and activated carbon to remove phenol, the optimum equilibrium time was around 5 h, whereas in a study with zeolitic material made from bagasse fly ash as adsorbent, the adsorption equilibrium time was as long as 10 h [33].

4. Conclusions

The granules mainly made of coal fly ash were abundant with nanosize pores. The specific surface area and porosity reached 130.5 m²/g and 60.1%, respectively. SiO₂, Al₂O₃, MgO, Fe₂O₃, CaO, K₂O, and unburned carbon were the main compositions in the granules. The granules showed high efficiency in phenol adsorption. From solution with initial phenol concentration of 100 mg/L, more than 90% phenol could be removed with contact time of 90 min and dosage of 140 g/L. Although the adsorption of phenol on the granules was endothermic, phenol adsorption on the granules could

be operated under normal temperature efficiently. Phenol adsorption on the granules complied well with the pseudo-second-order kinetic model and Langmuir isotherm model.

Acknowledgment

This study is supported by the project of the Priority Academic Program Development of Jiangsu Higher Education Institutions (PAPD).

References

- [1] S. Wang, M. Soudi, L. Li, and Z. H. Zhu, "Coal ash conversion into effective adsorbents for removal of heavy metals and dyes from wastewater," *Journal of Hazardous Materials*, vol. 133, no. 1–3, pp. 243–251, 2006.
- [2] A. Olgun, Y. Erdogan, Y. Ayhan, and B. Zeybek, "Development of ceramic tiles from coal fly ash and tincal ore waste," *Ceramics International*, vol. 31, no. 1, pp. 153–158, 2005.
- [3] A. Singh, R. K. Sharma, and S. B. Agrawal, "Effects of fly ash incorporation on heavy metal accumulation, growth and yield responses of Beta vulgaris plants," *Bioresource Technology*, vol. 99, no. 15, pp. 7200–7207, 2008.
- [4] S. Wang, Q. Ma, and Z. H. Zhu, "Characteristics of coal fly ash and adsorption application," *Fuel*, vol. 87, no. 15–16, pp. 3469–3473, 2008.
- [5] A. H. Norzilah, A. Fakhru'l-Razi, S. Y. Thomas Choong, and A. Luqman Chuah, "Surface modification effects on CNTs adsorption of methylene blue and phenol," *Journal of Nanomaterials*, vol. 2011, Article ID 495676, 18 pages, 2011.
- [6] M. Sarkar, P. K. Acharya, and B. Bhattacharya, "Modeling the adsorption kinetics of some priority organic pollutants in water from diffusion and activation energy parameters," *Journal of Colloid and Interface Science*, vol. 266, no. 1, pp. 28–32, 2003.
- [7] S. H. Lin and R. S. Juang, "Adsorption of phenol and its derivatives from water using synthetic resins and low-cost natural adsorbents: a review," *Journal of Environmental Management*, vol. 90, no. 3, pp. 1336–1349, 2009.
- [8] R. Aravindhan, J. R. Rao, and B. U. Nair, "Application of a chemically modified green macro alga as a biosorbent for phenol removal," *Journal of Environmental Management*, vol. 90, no. 5, pp. 1877–1883, 2009.
- [9] V. C. Srivastava, M. M. Swamy, I. D. Mall, B. Prasad, and I. M. Mishra, "Adsorptive removal of phenol by bagasse fly ash and activated carbon: equilibrium, kinetics and thermodynamics," *Colloids and Surfaces A*, vol. 272, no. 1–2, pp. 89–104, 2006.
- [10] M. Sarkar and P. K. Acharya, "Use of fly ash for the removal of phenol and its analogues from contaminated water," *Waste Management*, vol. 26, no. 6, pp. 559–570, 2006.
- [11] Z. Jing, Y. Y. Li, S. Cao, and Y. Liu, "Performance of double-layer biofilter packed with coal fly ash ceramic granules in treating highly polluted river water," *Bioresource Technology*, vol. 120, pp. 212–217, 2012.
- [12] G. Lu, G. Q. Lu, and Z. M. Xiao, "Mechanical properties of porous materials," *Journal of Porous Materials*, vol. 6, no. 4, pp. 359–368, 1999.
- [13] Y. Liu, L. Zheng, X. Li, and S. Xie, "SEM/EDS and XRD characterization of raw and washed MSWI fly ash sintered at different temperatures," *Journal of Hazardous Materials*, vol. 162, no. 1, pp. 161–173, 2009.
- [14] C. Kang, Y. Wang, R. Li et al., "A modified spectrophotometric method for the determination of trace amounts of phenol in water," *Microchemical Journal*, vol. 64, no. 2, pp. 161–171, 2000.
- [15] Y. Xue, S. Wu, H. Hou, and J. Zha, "Experimental investigation of basic oxygen furnace slag used as aggregate in asphalt mixture," *Journal of Hazardous Materials*, vol. 138, no. 2, pp. 261–268, 2006.
- [16] B. G. Kutchko and A. G. Kim, "Fly ash characterization by SEM-EDS," *Fuel*, vol. 85, no. 17–18, pp. 2537–2544, 2006.
- [17] M. Inagaki, S. Kobayashi, F. Kojin, N. Tanaka, T. Morishita, and B. Tryba, "Pore structure of carbons coated on ceramic particles," *Carbon*, vol. 42, no. 15, pp. 3153–3158, 2004.
- [18] R. M. Prasad, G. Mera, K. Morita et al., "Thermal decomposition of carbon-rich polymer-derived silicon carbonitrides leading to ceramics with high specific surface area and tunable micro- and mesoporosity," *Journal of the European Ceramic Society*, vol. 32, no. 2, pp. 477–484, 2012.
- [19] R. Tailor, B. Shah, and A. Shah, "Sorption removal of phenol by zeolitic bagasse fly ash: equilibrium, kinetics, and column studies," *Journal of Chemical & Engineering Data*, vol. 57, no. 5, pp. 1437–1448, 2012.
- [20] R. L. Tseng, K. T. Wu, F. C. Wu, and R. S. Juang, "Kinetic studies on the adsorption of phenol, 4-chlorophenol, and 2,4-dichlorophenol from water using activated carbons," *Journal of Environmental Management*, vol. 91, no. 11, pp. 2208–2214, 2010.
- [21] A. Bhatnagar and M. Sillanpää, "Utilization of agro-industrial and municipal waste materials as potential adsorbents for water treatment-A review," *Chemical Engineering Journal*, vol. 157, no. 2–3, pp. 277–296, 2010.
- [22] S. Wang and H. Wu, "Environmental-benign utilisation of fly ash as low-cost adsorbents," *Journal of Hazardous Materials*, vol. 136, no. 3, pp. 482–501, 2006.
- [23] H. L. Wang and W. F. Jiang, "Adsorption of Dinitro Butyl Phenol (DNBP) from aqueous solutions by fly ash," *Industrial and Engineering Chemistry Research*, vol. 46, no. 16, pp. 5405–5411, 2007.
- [24] M. A. Hararah, K. A. Ibrahim, A. H. Al-Muhtaseb, R. I. Yousef, A. Abu-Surrah, and A. Qatatsheh, "Removal of phenol from aqueous solutions by adsorption onto polymeric adsorbents," *Journal of Applied Polymer Science*, vol. 117, no. 4, pp. 1908–1913, 2010.
- [25] F. Banat, S. Al-Asheh, and L. Al-Makhadmeh, "Utilization of raw and activated date pits for the removal of phenol from aqueous solutions," *Chemical Engineering and Technology*, vol. 27, no. 1, pp. 80–86, 2004.
- [26] A. A. Khan and R. P. Singh, "Adsorption thermodynamics of carbofuran on Sn (IV) arsenosilicate in H⁺, Na⁺ and Ca²⁺ forms," *Colloids and Surfaces*, vol. 24, no. 1, pp. 33–42, 1987.
- [27] H. B. Senturk, D. Ozdes, A. Gundogdu, C. Duran, and M. Soy-lak, "Removal of phenol from aqueous solutions by adsorption onto organomodified Tirebolu bentonite: equilibrium, kinetic and thermodynamic study," *Journal of Hazardous Materials*, vol. 172, no. 1, pp. 353–362, 2009.
- [28] V. Gökmen and A. Serpen, "Equilibrium and kinetic studies on the adsorption of dark colored compounds from apple juice using adsorbent resin," *Journal of Food Engineering*, vol. 53, no. 3, pp. 221–227, 2002.
- [29] K. M. Parida and A. C. Pradhan, "Removal of phenolic compounds from aqueous solutions by adsorption onto manganese nodule leached residue," *Journal of Hazardous Materials*, vol. 173, no. 1–3, pp. 758–764, 2010.

- [30] Y. H. Shen, "Removal of phenol from water by adsorption-flocculation using organobentonite," *Water Research*, vol. 36, no. 5, pp. 1107–1114, 2002.
- [31] M. Tomaszewska, S. Mozia, and A. W. Morawski, "Removal of organic matter by coagulation enhanced with adsorption on PAC," *Desalination*, vol. 161, no. 1, pp. 79–87, 2004.
- [32] A. S. Alzaydien and W. Manasreh, "Equilibrium, kinetic and thermodynamic studies on the adsorption of phenol onto activated phosphate rock," *International Journal of Physical Sciences*, vol. 4, no. 4, pp. 172–181, 2009.
- [33] B. Shah, R. Tailor, and A. Shah, "Adaptation of bagasse fly ash, a sugar industry solid waste into zeolitic material for the uptake of phenol," *Environmental Progress & Sustainable Energy*, vol. 30, no. 3, pp. 358–367, 2011.

Research Article

Fabrication and Characterization of Manganese Ferrite Nanospheres as a Magnetic Adsorbent of Chromium

Li-Xia Yang,¹ Feng Wang,¹ Yan-Feng Meng,¹ Qing-Hua Tang,¹ and Zi-Qi Liu²

¹ School of Chemistry and Materials Science, Ludong University, Yantai 264025, China

² College of Materials Science and Engineering, Qingdao University of Science and Technology, Qingdao 266042, China

Correspondence should be addressed to Li-Xia Yang; yanglx2003@163.com

Received 13 December 2012; Accepted 30 January 2013

Academic Editor: Shao-Wen Cao

Copyright © 2013 Li-Xia Yang et al. This is an open access article distributed under the Creative Commons Attribution License, which permits unrestricted use, distribution, and reproduction in any medium, provided the original work is properly cited.

Manganese ferrite nanospheres constructed by nanoparticles were synthesized in high yield via a general, one-step, and template-free solvothermal method. The product was characterized by X-ray diffraction (XRD), scanning electron microscope (SEM), and transmission electron microscopy (TEM). BJH pore-size distribution shows that the sphere-like manganese ferrite particle was a porous structure with a narrow pore-size distribution. The investigation of magnetic property of manganese ferrite nanospheres reveals that the saturation magnetization is high, which shows an excellent ability for magnetic removal of chromium in wastewater.

1. Introduction

Manganese ferrite is a kind of magnetic materials with cubic spinel structure which have been extensively used in various technological applications. The properties of manganese ferrite highly depend on the composition, morphology, and size, which are strongly connected with the preparation conditions. Up to now, various morphologies and sizes of manganese ferrite have been synthesized. For example, nanoparticles of MFe_2O_4 ($M = Mn, Co, \text{ and } Ni$) with diameters ranging from 5 to 10 nm have been obtained through a solvothermal method [1]. Zhang et al. reported the preparation of octahedral-like $MnFe_2O_4$ crystallites fabricated using a TEA-assisted route under mild conditions [2]. A large number of high-purity $Mn_{1-x}Zn_xFe_2O_4$ nanocrystallites were synthesized and these nanocrystallites oriented aggregation to nanospheres [3]. Hollow spheres and colloidal nanocrystal clusters of $MnFe_2O_4$ with similar submicron scales have been synthesized controllably by a solvothermal method through simply adjusting the synthesis microenvironment [4].

Chromium (Cr(VI)), one of the most toxic heavy metals, is usually generated by the electroplating, metal finishing, leather tanning, dye, and textile industries. Trivalent chromium is less toxic than hexavalent chromium which is carcinogenic to living organism [5, 6]. Therefore, Cr(VI)

should be removed from aqueous solution in order to protect human health. Adsorption is a simple and effective method in the removal of Cr(VI). Several kinds of materials were used as adsorbents for heavy metal ions, such as zeolite [6], active carbon [7, 8], boehmite [9], activated alumina [10], aluminum magnesium mixed hydroxide [11] and, chitosan [12]. These materials showed good performance for the removal of Cr(VI) from aqueous solutions. However, these kinds of adsorbents suffer from a common problem that it needs a next separation process from the solution, which will increase the operation cost. In order to avoid this problem, some researchers have found that magnetic materials can be a promising candidate to be easily separated from solution through a magnetic field [13, 14], which is convenient for the separation of adsorbents from aqueous solution.

Magnetic adsorbent can provide a quick and effective route for magnetic separation from an aqueous solution. Various applications have been carried out by using magnetic materials in environmental protection [15], catalytic chemistry [16], and drug delivery [17]. In this paper, the application of magnetic separation technology was employed to solve environmental problem. Although nanoparticles usually showed a high surface area, the magnetic response was low. In this case, nanospheres constructed by nanoparticles have a high surface area; at the same time, magnetization is high

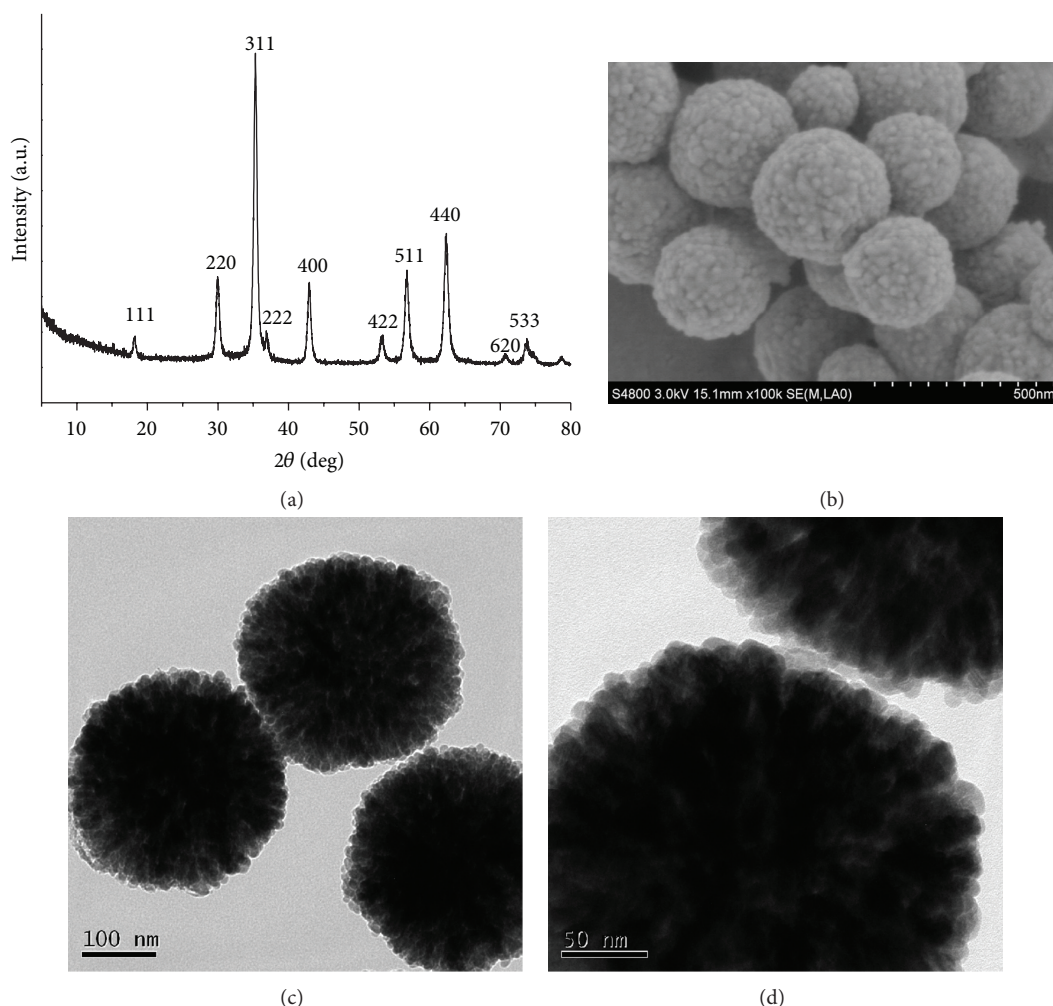


FIGURE 1: (a) XRD pattern, (b) SEM image, and (c)-(d) TEM images of manganese ferrite product prepared at 200°C for 24 h.

enough for separating the adsorbent from aqueous solution in a few seconds.

2. Experimental

2.1. Preparation of Manganese Ferrite Nanospheres. All reagents are analytically pure and used as-received without further purification. In a typical experiment, 4 mmol $\text{FeCl}_3 \cdot 6\text{H}_2\text{O}$ and 2 mmol $\text{MnCl}_2 \cdot 4\text{H}_2\text{O}$ were dissolved in 50 mL of ethylene glycol using magnetic stirring under room temperature. 5 mL ethanolamine was added to the above solution and followed by magnetic stirring to form a homogeneous solution. Then, this solution was transferred into a Teflon-lined stainless steel autoclave for hydrothermal treatment at 200°C for 24 h. After the autoclave was allowed to cool down to room temperature naturally, the solid products were collected by centrifugation, washed separately with distilled water and ethanol for several times, and then dried in an oven at 60°C before characterization and application.

2.2. Characterization. X-ray diffraction (XRD, Rigaku D/max 2500 VPC, Japan) was used to analyze the composition

and crystal structure of the prepared products. The shapes of the products were characterized by transmission electron microscopy (TEM, JEM-1230, Japan) and scanning electron microscope (SEM, Hitachi S4800, Japan). N_2 adsorption and desorption isotherm was measured on a Micromeritics ASAP-2020 nitrogen adsorption apparatus (USA). Magnetic property data were collected with a quantum design physical property measurement system (PPMS). The absorption spectra of the solutions were obtained on a UNIC 7200 spectrophotometer (China).

2.3. Adsorption of Cr^{6+} . Adsorption experiments were carried out with a desk-type constant temperature oscillator (SHA-CA, China) at 25°C at a rate of 200 r/min. 0.1 g Mn ferrite adsorbent was added in 50 mL chromium(VI) solution (100 mg/L) prepared by dissolving required amount of potassium dichromate ($\text{K}_2\text{Cr}_2\text{O}_7$) in distilled water. Chromium(VI) concentrations were measured by 1,5-diphenylcarbazide spectrophotometric method. The sorption kinetics was investigated. After shaking for various time intervals, the suspensions were separated with a magnet in a few seconds. The equilibrium concentrations of chromium

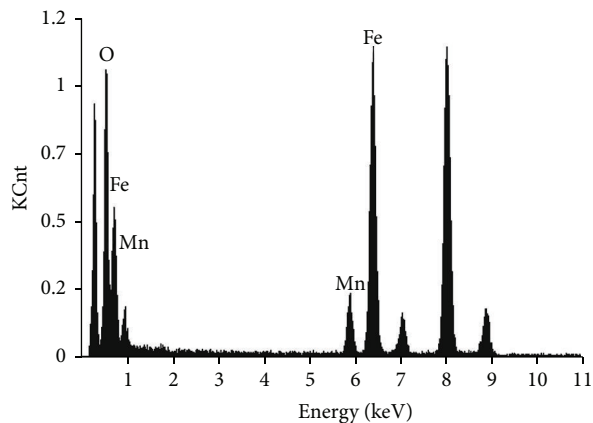


FIGURE 2: EDAX spectrum of manganese ferrite sample.

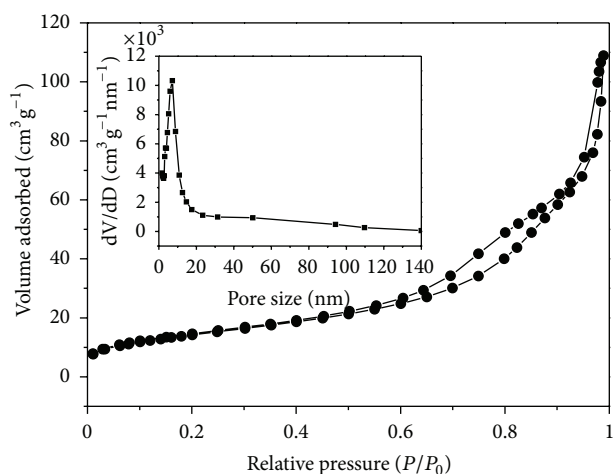


FIGURE 3: Nitrogen adsorption-desorption isotherms and the inset—the BJH pore-size distribution of manganese ferrite product prepared at 200°C for 24 h.

were determined at 540 nm using a 7200 spectrophotometer.

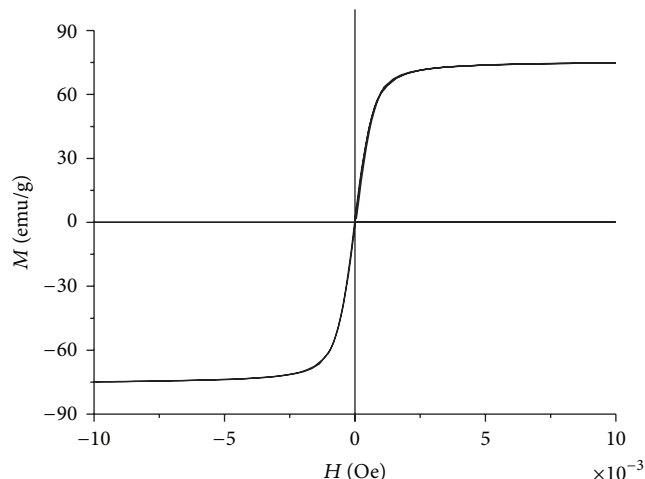
The removal percentage ($R\%$) of chromium was calculated using the following equation:

$$(R\%) = \frac{C_i - C_e}{C_i} \times 100, \quad (1)$$

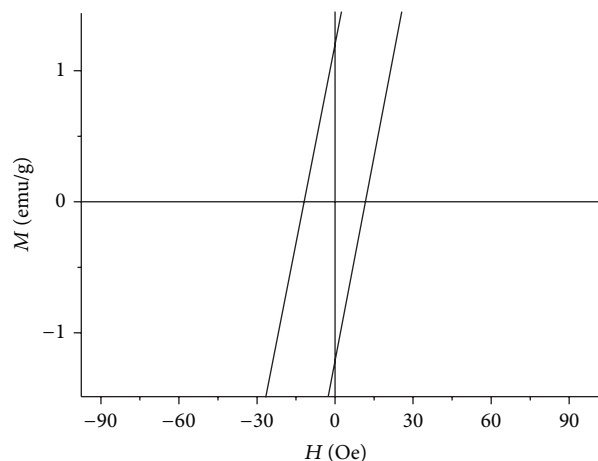
where C_i and C_e are the initial and equilibrium concentrations of chromium.

3. Results and Discussion

The powder XRD pattern of the product synthesized at 200°C for 24 h using 5 mL ethanolamine is depicted in Figure 1(a). Crystalline nature can be derived from the appearance of sharp diffraction peaks in the XRD pattern prepared by the solvothermal method, which can be well indexed to a pure cubic phase of spinel manganese ferrite (JCPDS Card no. 38-0430). Morphology of the sample is studied by TEM and SEM. The SEM image of sample shows that the diameters of



(a)



(b)

FIGURE 4: The magnetization hysteresis of manganese ferrite nanospheres at room temperature.

most of the spheres are in the range of 200–400 nm. The surface roughness demonstrates the formation of a ferrite sphere via the construction of nanoparticles (Figures 1(b) and 1(c)). Careful observation from an enlarged spheres, as shown in Figure 1(d), can further confirm the assembly of nanoparticles.

Figure 2 was the EDAX spectrum of the obtained manganese ferrite sample. The result shows that the as-prepared manganese ferrite nanospheres contained Fe, O and Mn, and no contamination element is detected. The atomic ratio of Fe:Mn is about 5.5, indicating that the chemical formula of the as-synthesized Mn ferrite is nonstoichiometric in nature.

Figure 3 shows the nitrogen adsorption-desorption isotherm and pore-size distribution curve of manganese ferrite nanospheres. Manganese ferrite nanospheres exhibit a type IV isotherm with an H3 type hysteresis loop, namely, typical hysteresis loops of mesoporous materials. Moreover, a sharp peak at 7 nm can be observed in the Barrett-Joyner-Halenda (BJH) pore-size distribution curve (the inset of Figure 3), which further demonstrates the existence of

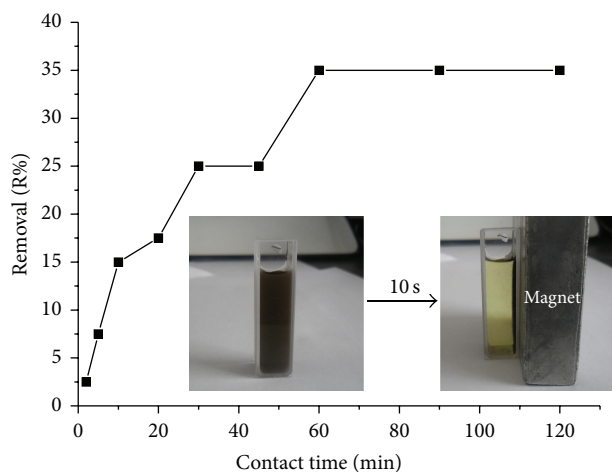


FIGURE 5: Effect of contact time on adsorption of chromium(VI). The inset is the photograph of separation of manganese ferrite nanospheres from solution under an external magnetic field.

mesopores with a relatively narrow pore-size distribution. The Brunauer-Emmett-Teller-(BET-) specific surface area of manganese ferrite spheres is $52.39 \text{ m}^2/\text{g}$.

Figure 4 represents the magnetization curves measured at 300 K. As-prepared manganese ferrite nanospheres showed high magnetization performance. The magnetic saturation values reached 75 emu/g . As depicted in Figure 4(a), it is hard to see an obvious hysteresis loop at the full scale. In the close-up view (Figure 4(b)), the curve presents a very small hysteresis loop with a remnant M_r of 1.2 emu/g and a coercivity H_c of 12 Oe , denoting the ferromagnetic behaviour of the sample. This structural particle with high magnetization performance is supposed to be of great potential in magnetic separation of chromium in wastewater.

The relationship between contact time and chromium adsorption onto Mn ferrite is shown in Figure 5. The adsorption increased from the beginning to 60 min, and the removal percentage increased to 35% at a contact time of 60 min. With a further increase in time, the adsorption approached to equilibrium in all the cases. The fast adsorption at the initial stage is probably due to the increased concentration gradient between the adsorbate in solution and adsorbate in adsorbent as there must be increased number of vacant sites available in the beginning. The attainment of equilibrium adsorption may be due to limited mass transfer of the adsorbate molecules from the bulk liquid to the external surface of ferrite. As shown in the inset of Figure 5, manganese ferrite nanospheres were attracted toward the magnet within 10 s, demonstrating directly that manganese ferrite nanospheres could be easily separated from wastewater by applying a magnetic field.

4. Conclusion

In summary, the solvothermal method has been used to successfully synthesize manganese ferrite nanospheres with high magnetization. This approach developed a simple and efficient route to fabricate manganese ferrite nanospheres in large scale. The maximum saturation magnetization value of

the product is 75 emu/g , which showed a magnetic manipulation of chromium in wastewater.

Acknowledgments

The authors are grateful for the financial support by National Natural Science Foundation of China (no. 51102128 and no. 20904018), the Applied Project of Yantai City (no. 2008308), the Foundation of Innovation Team Building of Ludong University (08-CXB001), and Shandong Province Natural Science Foundation (ZR2011EL005).

References

- [1] S. Yáñez-Vilar, M. Sánchez-Andújar, C. Gómez-Aguirre, J. Mira, M. A. Señaís-Rodríguez, and S. Castro-García, "A simple solvothermal synthesis of MFe_2O_4 ($\text{M} = \text{Mn}, \text{Co}$ and Ni) nanoparticles," *Journal of Solid State Chemistry*, vol. 182, no. 10, pp. 2685–2690, 2009.
- [2] D. Zhang, X. Zhang, X. Ni, J. Song, and H. Zheng, "Low-temperature fabrication of MnFe_2O_4 octahedrons: magnetic and electrochemical properties," *Chemical Physics Letters*, vol. 426, no. 1–3, pp. 120–123, 2006.
- [3] Q. Zhang, M. Zhu, Q. Zhang, Y. Li, and H. Wang, "Fabrication and magnetic property analysis of monodisperse manganese-zinc ferrite nanospheres," *Journal of Magnetism and Magnetic Materials*, vol. 321, no. 19, pp. 3203–3206, 2009.
- [4] P. Guo, G. Zhang, J. Yu, H. Li, and Zhao, "Controlled synthesis, magnetic and photocatalytic properties of hollow spheres and colloidal nanocrystal clusters of manganese ferrite," *Colloids and Surfaces A*, vol. 395, pp. 168–174, 2012.
- [5] S. A. Katz and H. Salem, "The toxicology of chromium with respect to its chemical speciation: a review," *Journal of Applied Toxicology*, vol. 13, no. 3, pp. 217–224, 1993.
- [6] A. M. Yusof and N. A. N. N. Malek, "Removal of Cr(VI) and As(V) from aqueous solutions by HDTMA-modified zeolite Y," *Journal of Hazardous Materials*, vol. 162, no. 2–3, pp. 1019–1024, 2009.
- [7] R. M. Schneider, C. F. Cavalin, M. A. S. D. Barros, and C. R. G. Tavares, "Adsorption of chromium ions in activated carbon," *Chemical Engineering Journal*, vol. 132, no. 1–3, pp. 355–362, 2007.
- [8] H. Demiral, I. Demiral, F. Tümsel, and B. Karabacakoglu, "Adsorption of chromium(VI) from aqueous solution by activated carbon derived from olive bagasse and applicability of different adsorption models," *Chemical Engineering Journal*, vol. 144, no. 2, pp. 188–196, 2008.
- [9] F. Granados-Correa and J. Jiménez-Becerril, "Chromium (VI) adsorption on boehmite," *Journal of Hazardous Materials*, vol. 162, no. 2–3, pp. 1178–1184, 2009.
- [10] S. Mor, K. Ravindra, and Bishnoi, "Adsorption of chromium from aqueous solution by activated alumina and activated charcoal," *Bioresource Technology*, vol. 98, no. 4, pp. 954–957, 2007.
- [11] Y. Li, B. Gao, T. Wu et al., "Hexavalent chromium removal from aqueous solution by adsorption on aluminum magnesium mixed hydroxide," *Water Research*, vol. 43, no. 12, pp. 3067–3075, 2009.
- [12] N. Sankaramakrishnan, A. Dixit, L. Iyengar, and R. Sanghi, "Removal of hexavalent chromium using a novel cross linked

- xanthated chitosan,” *Bioresource Technology*, vol. 97, no. 18, pp. 2377–2382, 2006.
- [13] V. K. Gupta, S. Agarwal, and T. A. Saleh, “Chromium removal by combining the magnetic properties of iron oxide with adsorption properties of carbon nanotubes,” *Water Research*, vol. 45, no. 6, pp. 2207–2212, 2011.
- [14] L. Wei, G. Yang, R. Wang, and W. Ma, “Selective adsorption and separation of chromium (VI) on the magnetic iron-nickel oxide from waste nickel liquid,” *Journal of Hazardous Materials*, vol. 164, no. 2-3, pp. 1159–1163, 2009.
- [15] L. Ai, H. Huang, Z. Chen, X. Wei, and Jiang, “Activated carbon/CoFe₂O₄ composites: facile synthesis, magnetic performance and their potential application for the removal of malachite green from water,” *Chemical Engineering Journal*, vol. 156, no. 2, pp. 243–249, 2010.
- [16] L. Kong, X. Lu, X. Bian, W. Zhang, and C. Wang, “Constructing carbon-coated Fe₃O₄ microspheres as antiacid and magnetic support for palladium nanoparticles for catalytic applications,” *ACS Applied Materials and Interfaces*, vol. 3, no. 1, pp. 35–42, 2011.
- [17] X. Liu, Q. Hu, Z. Fang, Q. Wu, and Q. Xie, “Carboxyl enriched monodisperse porous Fe₃O₄ nanoparticles with extraordinary sustained-release property,” *Langmuir*, vol. 25, no. 13, pp. 7244–7248, 2009.

Research Article

Pd-Doped SnO_2 -Based Sensor Detecting Characteristic Fault Hydrocarbon Gases in Transformer Oil

Weigen Chen,¹ Qu Zhou,¹ Tuoyu Gao,¹ Xiaoping Su,² and Fu Wan¹

¹ State Key Laboratory of Power Transmission Equipment & System Security and New Technology, Chongqing University, Chongqing 400030, China

² Electric Operations and Control Centers, Chengdu Power Supply Company, Chengdu 610017, China

Correspondence should be addressed to Qu Zhou; zhouqupsd@yahoo.cn

Received 7 December 2012; Revised 11 January 2013; Accepted 14 January 2013

Academic Editor: Ming-Guo Ma

Copyright © 2013 Weigen Chen et al. This is an open access article distributed under the Creative Commons Attribution License, which permits unrestricted use, distribution, and reproduction in any medium, provided the original work is properly cited.

Methane (CH_4), ethane (C_2H_6), ethylene (C_2H_4), and acetylene (C_2H_2) are important fault characteristic hydrocarbon gases dissolved in power transformer oil. Online monitoring these gaseous components and their generation rates can present the operational state of power transformer timely and effectively. Gas sensing technology is the most sticky and tricky point in online monitoring system. In this paper, pure and Pd-doped SnO_2 nanoparticles were synthesized by hydrothermal method and characterized by X-ray powder diffraction, field-emission scanning electron microscopy, and energy dispersive X-ray spectroscopy, respectively. The gas sensors were fabricated by side-heated preparation, and their gas sensing properties against CH_4 , C_2H_6 , C_2H_4 , and C_2H_2 were measured. Pd doping increases the electric conductance of the prepared SnO_2 sensors and improves their gas sensing performances to hydrocarbon gases. In addition based on the frontier molecular orbital theory, the highest occupied molecular orbital energy and the lowest unoccupied molecular orbital energy were calculated. Calculation results demonstrate that C_2H_4 has the highest occupied molecular orbital energy among CH_4 , C_2H_6 , C_2H_4 , and C_2H_2 , which promotes charge transfer in gas sensing process, and SnO_2 surfaces capture a relatively larger amount of electric charge from adsorbed C_2H_4 .

1. Introduction

With the development of ultra-high voltage and extra-high voltage electricity transmission and transformation project [1, 2], the quantity and capacity of power transformers with various voltage levels sharply increase. Power transformers are essential electrical apparatus, and their operating conditions directly affect the safety and reliability of the power system [3–5]. Faults happened in power transformers bring huge economic losses to our national economy [6]. Now, most of the large power transformers are in oil-paper insulation structures. When internal insulation faults occur in a transformer, the transformer generates some low molecular hydrocarbon gases [7–9], such as methane (CH_4), ethane (C_2H_6), ethylene (C_2H_4), and acetylene (C_2H_2), and most of these gaseous components are dissolved in transformer oil. Online monitoring the component contents of these dissolved hydrocarbon gases and their generation rates is one

of the most effective and convenient methods for diagnosing transformer incipient faults. This method can distinguish different types of faults which happened in power transformer, such as overheating, partial discharge, spark discharge, and arcing discharge [10–13].

Gas sensing technology is the core of online monitoring. At present, semiconductor gas sensors [14, 15], palladium gate field effect transistors [16], catalytic combustion sensors [17, 18], fuel cell sensors [19], and optical sensors [20, 21] are mainly methods utilized to detect characteristic fault gases. Given remarkable advantages of simple fabrication process, low maintenance cost, rapid response and recovery time, long service life [22], metal oxide semiconductor materials like SnO_2 [22], ZnO [23], TiO_2 [24], and In_2O_3 [25] have been receiving scientific and technological importance for many years [26, 27] and widely used to detect flammable, explosive, and poisonous gases. However, when used to detect hydrocarbon gases traditional SnO_2 -based gas sensor

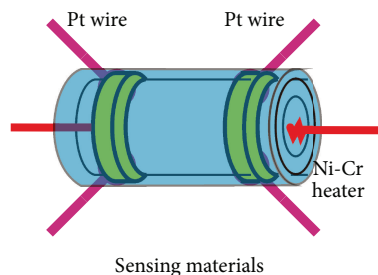


FIGURE 1: The structure of a side-heated gas sensor.

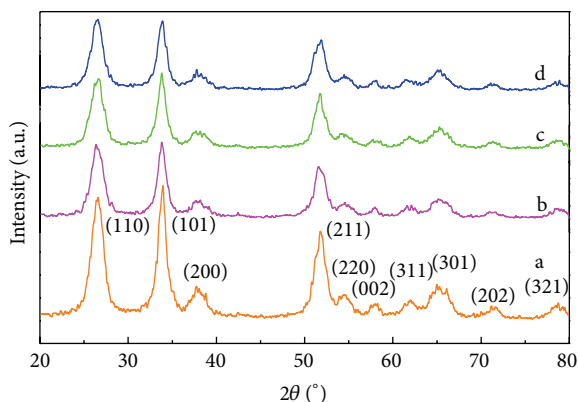


FIGURE 2: XRD patterns of (a) pure, (b) 1 wt%, (c) 3 wt%, and (d) 5 wt% Pd-doped SnO_2 nanoparticles.

presents some limitations such as low gas response and high operating temperature [28]. Many relevant studies have been conducted to enhance the sensing performances of SnO_2 [29–31]. Doping noble metal is an effective method to improve the gas sensing properties of conventional thick or thin film gas sensor [32, 33]. However, due to the same composition and similar structure for the four hydrocarbons, the gas sensing mechanism is still unclear and lack detail understandings.

In this work, SnO_2 samples doped with metallic ions Pd^{2+} (1, 3, and 5 wt%) were prepared using a simple hydrothermal synthesis route. The crystalline structures, chemical compositions, and surface morphologies of the prepared samples were performed by X-ray powder diffraction (XRD), field-emission scanning electron microscopy (FESEM), and energy dispersive X-ray spectroscopy (EDS), respectively; as well as their gas sensing properties to CH_4 , C_2H_6 , C_2H_4 , and C_2H_2 were measured. Furthermore, the highest occupied molecular orbital (HOMO) and the lowest unoccupied molecular orbital (LOMO) of hydrocarbon gases and the density of states (DOS) of SnO_2 (110) surface were calculated.

2. Experimental

2.1. Preparation and Characterization of Materials. Pure and Pd-doped SnO_2 powders were prepared by hydrothermal method using $\text{SnCl}_4 \cdot 5\text{H}_2\text{O}$, $\text{Na}_2\text{SO}_4 \cdot 5\text{H}_2\text{O}$, $\text{PdCl}_2 \cdot 2\text{H}_2\text{O}$,

NaOH , absolute ethanol, and distilled water as precursors. All chemical reagents were of analytical grade and purchased from Beijing Chemicals Co. Ltd. In this study, 0.903 g of NaOH , 1.262 g of $\text{SnCl}_4 \cdot 5\text{H}_2\text{O}$, 0.3 g of $\text{Na}_2\text{SO}_4 \cdot 5\text{H}_2\text{O}$, 30 mL of absolute ethanol, and 30 mL of distilled water were mixed together. Then, the compound metal salt $\text{PdCl}_2 \cdot 2\text{H}_2\text{O}$ was added drop by drop to the mixed solution with intense magnetic stirring. The mass ratio of the total metallic ions added was estimated in a molar ratio of 1, 3, and 5 wt%, respectively. The reaction mixtures were magnetically stirred for about 30 min and then transferred into a 100 mL Teflon autoclave. The vessel was sealed and heated at 180°C for 24 h in an electric furnace. The prepared products were centrifuged and then washed several times with distilled water and absolute ethanol until Cl^- could not be detected by 0.1 mol/L AgNO_3 aqueous solutions. Finally, the products were further air-dried for further characterization.

The crystalline structures of the products were investigated using X-ray powder diffraction. The surface morphologies of both pure and Pd-doped SnO_2 samples were characterized by field-emission scanning electron microscopy. An energy dispersive X-ray spectroscopy analysis was utilized to confirm the chemical compositions of the prepared samples.

2.2. Fabrication and Measurement of Sensors. To fabricate the sensors, the synthesized samples were mixed with absolute ethanol and distilled water at a weight ratio of 80:10:10 to form a paste. The paste was then screen-printed on an Al_2O_3 ceramic tube, in which a pair of gold electrodes was previously printed. And an Ni-Cr heating wire was inserted into the tube to form a side-heated gas sensor. Figure 1 shows the structure of a side-heated gas sensor.

Its gas sensing properties were measured by a chemical gas sensor-8 (CGS-8) intelligent gas sensing analysis system (Beijing Elite Tech Co., Ltd., China). The sensors were preheated at different operating temperatures for about 30 min. When electric resistances of all the sensors were stable, a targeted gas was injected into the test chamber (20 L in volume) by a microinjector through a rubber plug. The targeted gas was mixed with air by using two fans in the analysis system. After the sensor resistance values reached a new constant value, the test chamber was opened to recover the sensors. All measurements were performed in a laboratory fume hood. Sensor electric resistance and gas response values were automatically acquired by the analysis system. The whole

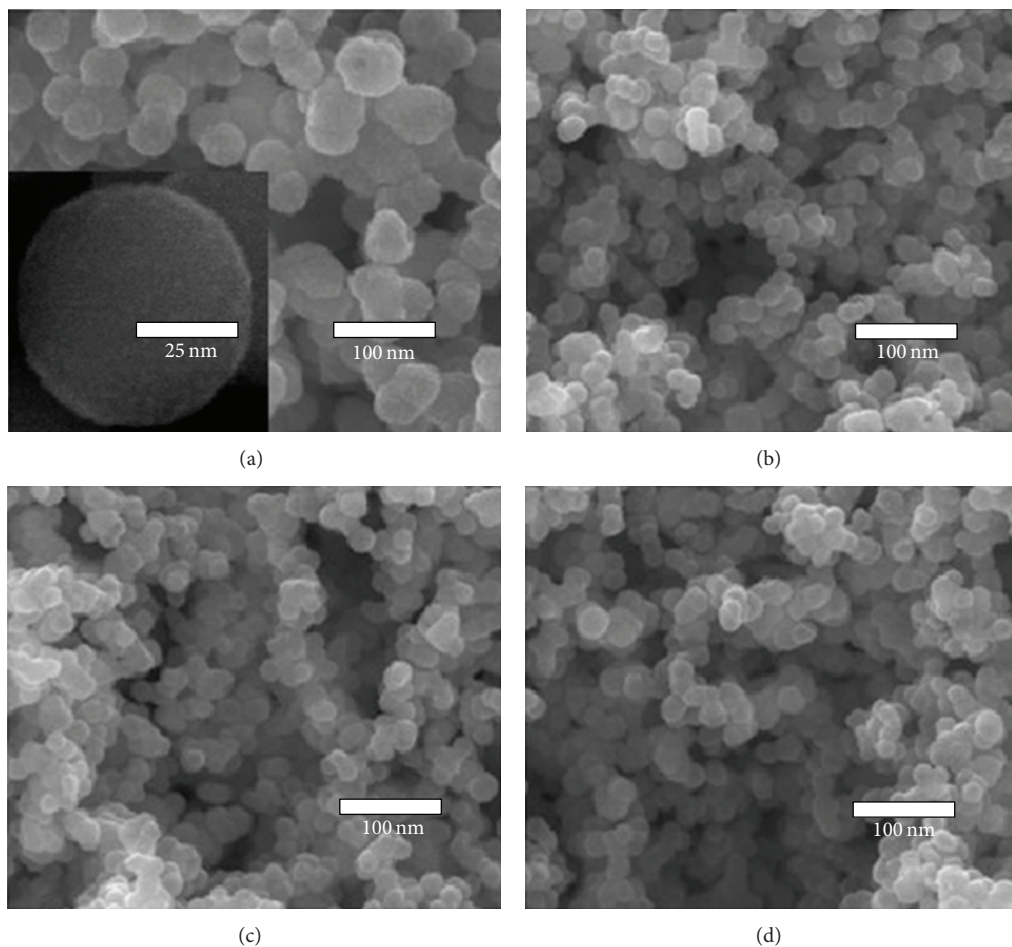


FIGURE 3: FESEM images of (a) pure, (b) 1 wt%, (c) 3 wt%, and (d) 5 wt% Pd-doped SnO_2 nanoparticles.

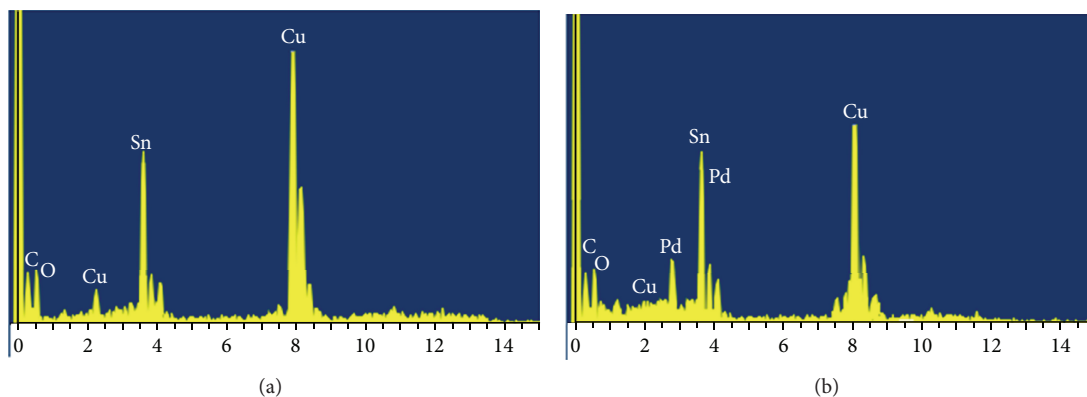


FIGURE 4: EDS spectra of (a) pure and (b) 3 wt% Pd-doped SnO_2 nanoparticles.

experiment process was performed in a clean room with constant humidity and temperature, which were monitored by the analysis system.

The relative variation of the gas response was defined as $S = (R_0 - R)/R_0$, where R_0 and R represent the resistance of the sensor in air and in targeted gas, respectively. Response time and recovery time were defined as the time taken by the

sensor to reach 90% of the total resistance change when gas in and 10% when gas out, respectively. All measurements were repeated several times in order to ensure the reproducibility of the gas sensing response.

2.3. Theoretical Calculation Method. The orbital energy was calculated with the DMol³ module, which is based on the

linear combination of the atomic orbits. The exchange-correlation function between electrons is described by the revised Perdew-Burke-Ernzerh form of the generalized gradient approximation [34–36]. The orbital cutoff quality was set as 4.3 Å, and the maximum root-mean-square convergent tolerance is 1.0×10^{-6} eV/atom. The basis set was approximated with a double numerical orbit base group and an orbit polarization function to handle the p orbit polarization of hydrogen atom.

3. Results and Discussions

3.1. Structural Characterization. X-ray powder diffraction patterns of the synthesized pure and Pd-doped (1, 3, and 5 wt%) SnO_2 samples were shown in Figure 2. It is obvious that the prominent peaks of (110), (101), (211), and other smaller peaks are corresponding to the standard data file of rutile SnO_2 (JCPDS 41-1445). As the amount of metallic ions doped in SnO_2 is small, no other metal-oxide diffraction features were observed in the patterns. With the amount of metallic ions doped in SnO_2 increasing, the relative intensity of the diffraction peaks decreases, and the full width at half maximum increases. Based on the Scherrer equation $D = 0.89\lambda/(\beta \cos \theta)$, where γ presents the X-ray wavelength, β means the half peak width, and θ is the Bragg angle, the calculated average particle size of pure SnO_2 samples is about 50 nm, and it is about 35–40 nm for Pd-doped SnO_2 samples.

Field-emission scanning electron microscopy was used for characteristic surface morphologies of the prepared samples. One can clearly see in Figure 3 that the crystal particles of prepared samples are uniform in size and have a nearly spherical shape. As shown in Figure 3(a), the average size of pure SnO_2 nanospheres is about 50 nm, and the image inset in Figure 3(a) presents a high-resolution image of a single nanosphere. As seen in Figures 3(b)–3(d), the diameters of the sphere-like Pd-doped SnO_2 samples are ranging from 25 to 30 nm. From these images, it is clearly seen that doping a moderate amount of noble metallic ions Pd^{2+} affects the shapes of SnO_2 slightly but inhibits the crystalline growth of the samples evidently.

In order to further check whether metallic ions Pd^{2+} were successfully doped into the SnO_2 particles, energy dispersive X-ray spectroscopy was used to confirm the elemental chemical compositions of the prepared samples. Figure 4 shows the EDS spectra of pure and 3 wt% Pd-doped SnO_2 nanoparticles. As shown in Figure 4(a), the EDS spectra reveal the elemental compositions of Sn, O, C, and Cu, and no other peaks have been found. Nevertheless, the presence of Pd element is confirmed in the EDS date of Figure 4(b), and the atomic percentage of Pd in the samples is calculated to be about 3 wt%.

3.2. Gas Sensing Properties. Figure 5 shows the electric resistance properties of the prepared SnO_2 -based sensors at different temperatures in pure air. As seen in Figure 5, the resistance values of all the sensors decrease when the working temperature increases from 200 to 500°C, which is the intrinsic characteristic of a semiconductor gas sensor. It is

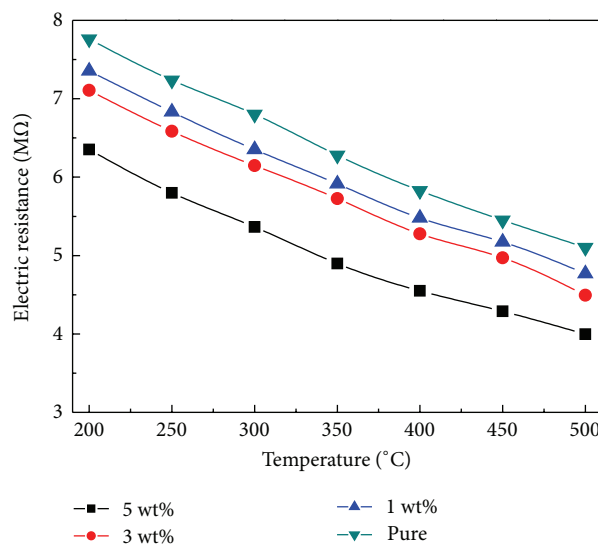


FIGURE 5: The electric resistance properties of the prepared sensors to different temperatures in air (room temperature at 25°C and relative humidity as 60%).

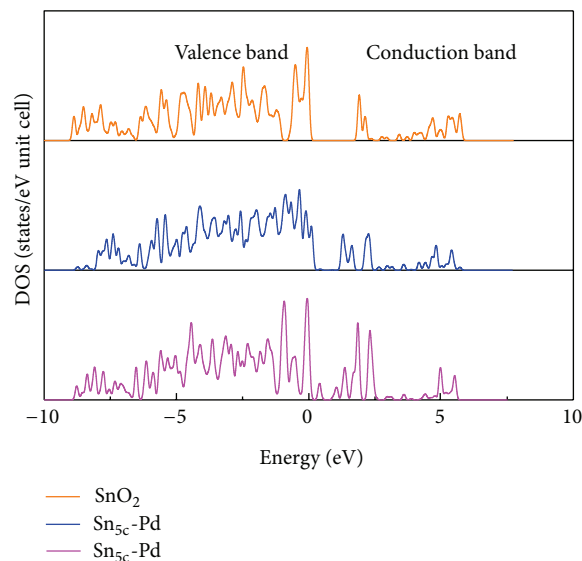


FIGURE 6: DOS of SnO_2 (110) surface before and after Pd^{2+} -doping.

also observed that the resistance of the SnO_2 sensor decreases somewhat after Pd^{2+} ions doping. When worked at a same temperature, the electric resistance value decreases in the order of pure 1, 3, and 5 wt% Pd-doped SnO_2 sensors, which means doping a moderate amount of noble metal can improve the electric conductivity of our prepared sensor, and 5 wt% is the optimum doping content among our samples.

It is well known that gas sensing performances of metal oxide semiconductor gas sensor are attributed to the changes of electric conductance and particularly dominantly controlled by band structure, conduction band, and valence band near the Fermi level.

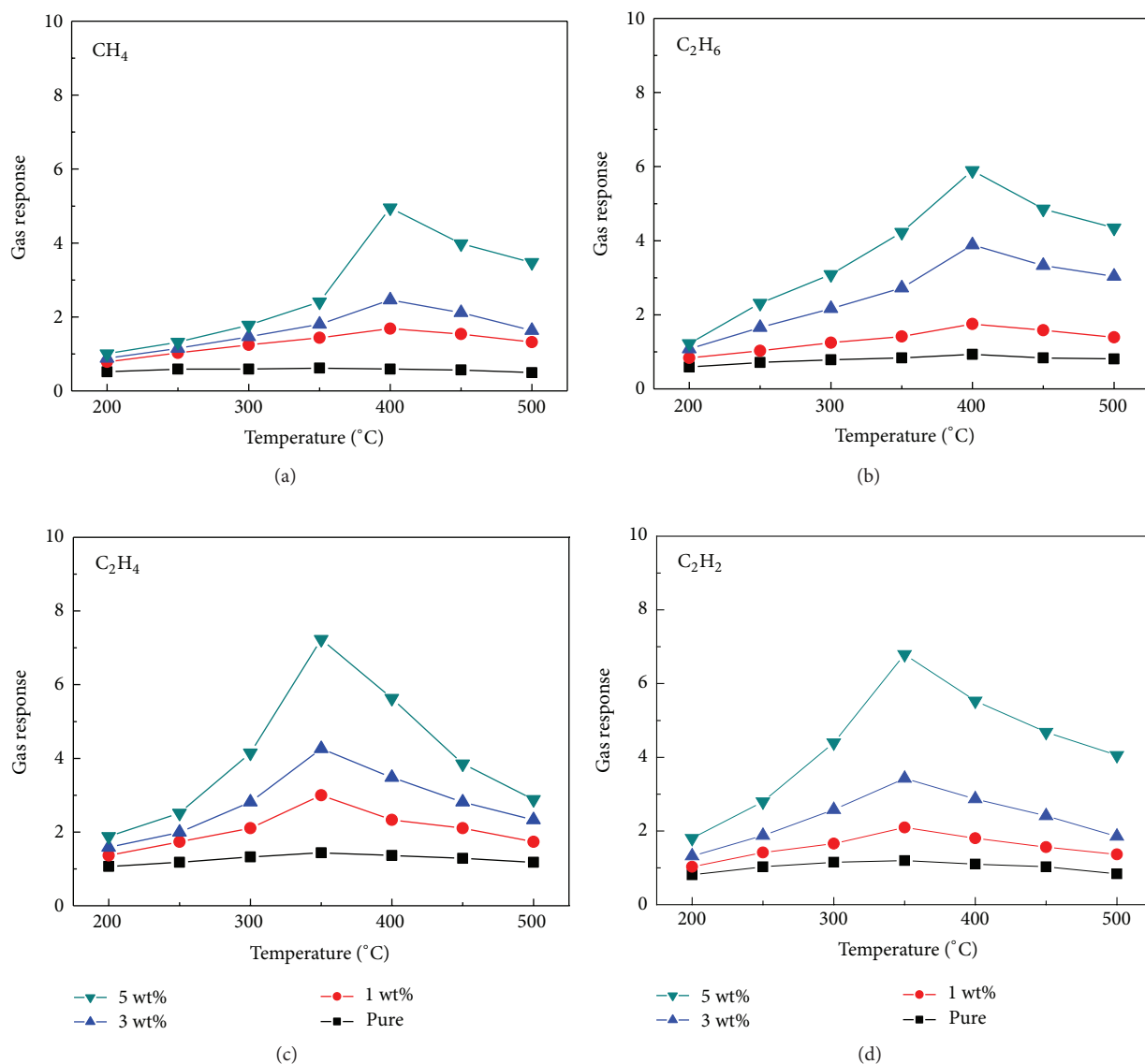


FIGURE 7: Gas responses of the sensors to 100 $\mu\text{L/L}$ of CH_4 , C_2H_6 , C_2H_4 , and C_2H_2 at different operating temperatures (room temperature at 25°C and relative humidity as 60%).

Rutile SnO_2 crystal has four major low-index surfaces (110), (101), (100), and (001) [37, 38]. The (110) surface is the most thermodynamically stable surface and has been widely used to investigate the surface properties of SnO_2 . Thus, the density of states (DOS) of SnO_2 (110) surface before and after Pd^{2+} -doping were calculated by replacing partial Sn atoms on the (110) surface ($\text{Sn}:\text{Pd} = 4:1$). As shown in Figure 6 after Pd^{2+} -doping the DOS of SnO_2 (110) surface shifted downward somewhat, the band gap narrowed and new doping levels appeared near the Fermi level. Pd^{2+} -doping promotes electron transfer between conduction band and valence band and improves the electric conductance properties of the sensor.

The gas responses of these sensors against CH_4 , C_2H_6 , C_2H_4 , and C_2H_2 were measured at different operating temperatures to find out their optimum operating temperatures.

The gas responses of the sensors to 100 $\mu\text{L/L}$ of CH_4 , C_2H_6 , C_2H_4 , and C_2H_2 at different operating temperatures were indicated in Figure 7, respectively. For each gas, the gas response values of the sensor increase at different degrees firstly and reach its maximum value at the optimum operating temperature and then decrease rapidly with the operating temperature rising. This tendency is commonly observed in pure and Pd^{2+} -doped SnO_2 sensors. As shown in Figure 7, the optimum operating temperature of the prepared sensor to 100 $\mu\text{L/L}$ of CH_4 , C_2H_6 , C_2H_4 and C_2H_2 are about 400, 400, 350 and 350°C, respectively, which is attributed to the sensor showing the maximum gas response at the corresponding operating temperature. It is also noted that for each hydrocarbon gas the sensor doped with 5 wt% Pd^{2+} exhibits the highest sensitivity among the four prepared sensors. Correspondingly, when worked at optimum operating

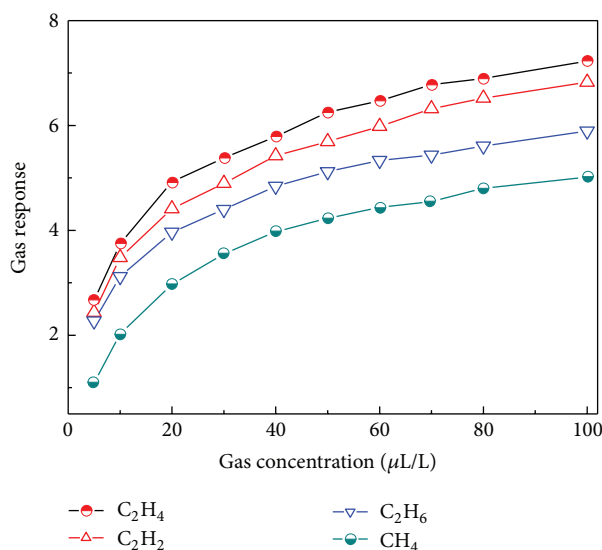


FIGURE 8: Gas response of the 5 wt% Pd²⁺-doped sensor to different concentrations of CH₄, C₂H₆, C₂H₄, and C₂H₂ (room temperature at 25°C and relative humidity as 60%).

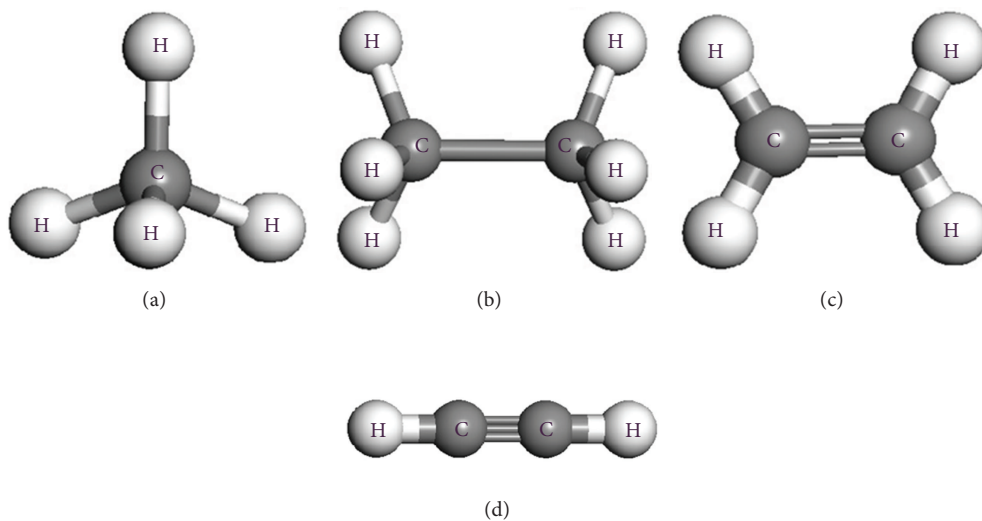


FIGURE 9: The gas molecule models of CH₄, C₂H₆, C₂H₄, and C₂H₂.

temperatures, the gas responses of the 5 wt% Pd²⁺-doped sensor against 100 μL/L of CH₄, C₂H₆, C₂H₄, and C₂H₂ are about 4.95, 5.89, 6.78, and 7.22, respectively, which are obviously larger than those of pure 1 and 3 wt% Pd²⁺-doped sensors.

The gas response of the 5 wt% Pd²⁺-doped SnO₂ sensor to different gas concentrations of CH₄, C₂H₆, C₂H₄, and C₂H₂ is shown in Figure 8, where the sensor worked at its own optimum operating temperatures as mentioned above. One can clearly see in Figure 8 that with the gas concentration increasing, the gas response of the sensor has an increasing trend in different degrees. Among the four characteristic

hydrocarbons, the sensor exhibits maximum response to C₂H₄, followed by C₂H₂, C₂H₆, and CH₄ with a descending order. The relationship between gas response and concentration is quasilinear, which indicates that our prepared sensor can be used to online monitor and detect characteristic hydrocarbon gases dissolved in transformer oil.

Based on the molecular frontier orbital theory, a large number of gas molecular properties are decided by the orbits, particularly HOMO orbits and LOMO orbits [36], which determine the ability of atoms to gain or loss electrons and perform electronic transfer. It is considered that HOMO orbits occupied with the highest energetic electrons are

easy to lose electrons, whereas LUMO orbits occupied with the lowest unoccupied electrons are demonstrated to easily capture electrons during the gas sensing process.

Tin oxide is a typical n-type semiconductor material, and characteristic fault hydrocarbons like CH_4 , C_2H_6 , C_2H_4 , and C_2H_2 are reducing gases. During the gas sensing process, reducing gas molecules manifest to lose electrons, and SnO_2 -based gas sensor would capture the same number of electrons lost by adsorbed gas molecules. The electrons received by sensing materials increase the number of carriers and decrease the height of the barrier in the depletion region. In order to further understand the difference of the 5 wt% Pd^{2+} -doped SnO_2 sensor exhibiting various gas responses to hydrocarbon gases, orbital energies of CH_4 , C_2H_6 , C_2H_4 , and C_2H_2 were calculated through the quantum mechanics program. The models of built hydrocarbon gases are shown in Figure 9. After geometry optimization, orbital energy calculations were performed using the DMol³ module.

As shown in Figure 10, the HOMO energy values of CH_4 , C_2H_4 , C_2H_2 , and C_2H_6 are -0.3441 , -0.2401 , -0.2542 , and -0.2995 eV, respectively, and the LUMO energy values for CH_4 , C_2H_4 , C_2H_2 , and C_2H_6 are 0.0834 , -0.0272 , 0.0121 , and 0.0702 eV. Based on the molecular frontier orbital theory, gas molecules easily lose electrons with a higher HOMO. Thus, the ability of losing electron weakens in the following order of C_2H_4 , C_2H_2 , C_2H_6 , and CH_4 . The possibility of electron transfer between adsorbed gas molecules and adsorption surface diminishes with the sequence of C_2H_4 , C_2H_2 , C_2H_6 and CH_4 . Because C_2H_4 has the highest HOMO among the four hydrocarbon gases, a relatively higher gas response of the prepared sensor to C_2H_4 is observed. On the contrary, a relatively lower gas response was measured to CH_4 . Theoretical calculation results highly agree with our experimental data as mentioned in Figure 8. This finding provides a qualitative understanding for the 5 wt% Pd^{2+} -doped SnO_2 sensor, which indicates different gas responses to CH_4 , C_2H_6 , C_2H_4 , and C_2H_2 with the same gas concentration.

Figure 11 presents the voltage responses of the 5 wt% Pd^{2+} -doped SnO_2 gas sensor to $50 \mu\text{L/L}$ of CH_4 , C_2H_6 , C_2H_4 , and C_2H_2 , where the sensor worked at the optimum operating temperature. It is an intrinsic characteristic of the prepared SnO_2 -based sensor that voltage response sharply increased when gas in and dramatically decreased when gas out. As seen in Figure 11, the prepared sensor shows rapid response and recovery to CH_4 , C_2H_6 , C_2H_4 , and C_2H_2 , and for each gas, the recovery time is somewhat longer than the response time. Such a rapid response and recovery property could be attributed to the doping effect of the doped metallic ions, which provide some new activity points and catalyze the gas sensing process [29, 33, 34].

4. Conclusions

Pure and Pd-doped nano- SnO_2 particles were successfully prepared and characterized by XRD, FESEM, and EDS, respectively. The sensor doped with 5 wt% Pd^{2+} ions shows a higher electric conductance and gas sensing properties to characteristic fault hydrocarbons with rapid response and

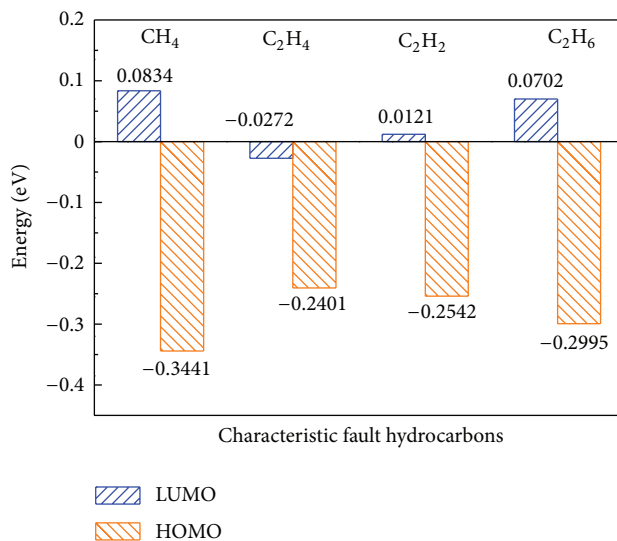


FIGURE 10: The HOMO and LUMO values of CH_4 , C_2H_4 , C_2H_2 , and C_2H_6 .

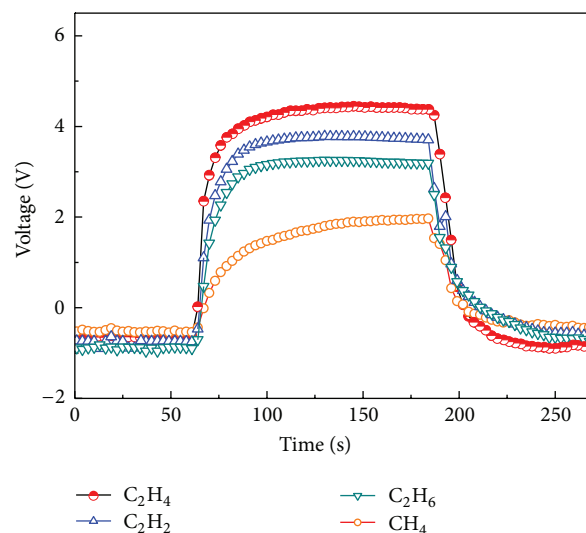


FIGURE 11: Response and recovery property of the 5 wt% Pd^{2+} -doped sensor to $50 \mu\text{L/L}$ of CH_4 , C_2H_6 , C_2H_4 , and C_2H_2 (room temperature at 25°C and relative humidity as 60%).

recovery property. The optimum operating temperatures of the 5 wt% Pd-doped sensor are about 400 , 400 , 350 , and 350°C for $100 \mu\text{L/L}$ of CH_4 , C_2H_6 , C_2H_4 , and C_2H_2 with gas responses of 4.95 , 5.89 , 6.78 , and 7.22 , respectively. Based on the molecular frontier orbital theory calculations, the HOMO energy values of CH_4 , C_2H_6 , C_2H_4 , and C_2H_2 are -0.2401 , -0.2542 , -0.3441 , and -0.2995 eV, separately. The ability of lose electrons weakens in the following order: C_2H_4 , C_2H_2 , C_2H_6 , and CH_4 . Therefore, the sensor exhibits a larger gas response to C_2H_4 among the four characteristic hydrocarbon gases. These findings provide a further insight to understand different gas sensing properties of the prepared sensors to CH_4 , C_2H_6 , C_2H_4 , and C_2H_2 .

Acknowledgments

This work was supported in part by the National Natural Science Foundation of China (no. 51277185), China Postdoctoral Science Foundation (no. 2012M511904), and National Basic Research Program of China (973 Program: 2012CB215205).

References

- [1] J. Suonan, K. Liu, and G. Song, "A novel UHV/EHV transmission-line pilot protection based on fault component integrated impedance," *IEEE Transactions on Power Delivery*, vol. 26, no. 1, pp. 127–134, 2011.
- [2] J. W. Liu, Y. H. Xiong, and Y. Ji, "The research of the status quo and development of UHV transmission lines construction in China," *Advanced Materials Research*, vol. 516–517, no. 1, pp. 1555–1559, 2012.
- [3] I. Villar, U. Viscarret, I. Etxeberria-Otadui, and A. Rufer, "Global loss evaluation methods for nonsinusoidally fed medium-frequency power transformers," *IEEE Transactions on Industrial Electronics*, vol. 56, no. 10, pp. 4132–4140, 2009.
- [4] S. M. Markalous, S. Tenbohlen, and K. Feser, "Detection and location of partial discharges in power transformers using acoustic and electromagnetic signals," *IEEE Transactions on Dielectrics and Electrical Insulation*, vol. 15, no. 6, pp. 1576–1583, 2008.
- [5] Z. Yang, W. H. Tang, A. Shintemirov, and Q. H. Wu, "Association rule mining-based dissolved gas analysis for fault diagnosis of power transformers," *IEEE Transactions on Systems, Man and Cybernetics Part C*, vol. 39, no. 6, pp. 597–610, 2009.
- [6] R. J. Liao, H. B. Zheng, S. Grzybowski, L. Yang, Y. Zhang, and Y. Liao, "An integrated decision-making model for condition assessment of power transformers using fuzzy approach and evidential reasoning," *IEEE Transactions on Power Delivery*, vol. 26, no. 2, pp. 1111–1118, 2011.
- [7] A. Akbari, A. Setayeshmehr, H. Borsi, E. Gockenbach, and I. Fofana, "Intelligent agent-based system using dissolved gas analysis to detect incipient faults in power transformers," *IEEE Electrical Insulation Magazine*, vol. 26, no. 6, pp. 27–40, 2010.
- [8] H. Xiong, C. X. Sun, R. J. Liao, J. Li, and L. Du, "Study on kernel-based possibilistic clustering and dissolved gas analysis for fault diagnosis of power transformer," *Proceedings of the Chinese Society of Electrical Engineering*, vol. 25, no. 20, pp. 162–166, 2005.
- [9] W. G. Chen, Y. X. Yun, C. Pan, and C. X. Sun, "Analysis of infrared absorption properties of dissolved gases in transformer oil," *Proceedings of the Chinese Society of Electrical Engineering*, vol. 28, no. 16, pp. 148–153, 2008.
- [10] H. C. Sun, Y. C. Huang, and C. M. Huang, "A review of dissolved gas analysis in power transformers," in *2nd International Conference on Advances in Energy Engineering (ICAEE '12)*, vol. 14, pp. 1220–1225, 2012.
- [11] S. Singh and M. Bandyopadhyay, "Dissolved gas analysis technique for incipient fault diagnosis in power transformers: a bibliographic survey," *IEEE Electrical Insulation Magazine*, vol. 26, no. 6, pp. 41–46, 2010.
- [12] R. J. Liao, H. B. Zheng, G. Stanislaw, and L. J. Yang, "Particle swarm optimization-least squares support vector regression based forecasting model on dissolved gases in oil-filled power transformers," *Electric Power Systems Research*, vol. 81, no. 12, pp. 2074–2080, 2011.
- [13] W. G. Chen, C. Pan, Y. X. Yun, Y. Y. Wang, and C. X. Sun, "Fault diagnosis method of power transformers based on wavelet networks and dissolved gas analysis," *Proceedings of the Chinese Society of Electrical Engineering*, vol. 28, no. 7, pp. 121–126, 2008.
- [14] S. Nakata and K. Kashima, "Distinction between alcohols and hydrocarbons with a semiconductor gas sensor depending on the range and frequency of a cyclic temperature," *Analytical Methods*, vol. 4, no. 4, pp. 1126–1131, 2012.
- [15] H. T. Giang, H. T. Duy, P. Q. Ngan et al., "Hydrocarbon gas sensing of nano-crystalline perovskite oxides LnFeO_3 ($\text{Ln} = \text{La}$, Nd and Sm)," *Sensors and Actuators B*, vol. 158, no. 1, pp. 246–251, 2011.
- [16] D. Braga and G. Horowitz, "High-Performance organic field-effect transistors," *Advanced Materials*, vol. 21, no. 14–15, pp. 1473–1486, 2009.
- [17] F. M. Liu, Y. Q. Zhang, Y. S. Yu, and J. B. Sun, "Enhanced sensing performance of catalytic combustion methane sensor by using Pd nanorod/ $\gamma\text{-Al}_2\text{O}_3$," *Sensors and Actuators B*, vol. 160, no. 1, pp. 1091–1097, 2011.
- [18] L. Xu, T. Li, X. Gao et al., "Behaviour of a catalytic combustion methane gas sensor working on pulse mode," in *Proceedings of the 9th IEEE Sensors Conference (SENSORS '10)*, pp. 391–394, November 2010.
- [19] C. Pijolat, G. Tournier, and J. P. Viricelle, "Detection of CO in H_2 -rich gases with a samarium doped ceria (SDC) sensor for fuel cell applications," *Sensors and Actuators B*, vol. 141, no. 1, pp. 7–12, 2009.
- [20] Y. Yun, W. Chen, Y. Wang, and C. Pan, "Photoacoustic detection of dissolved gases in transformer oil," *European Transactions on Electrical Power*, vol. 18, no. 6, pp. 562–576, 2008.
- [21] W. G. Chen, B. J. Liu, and H. X. Huang, "Photoacoustic sensor signal transmission line model for gas detection in transformer oil," *Sensor Letters*, vol. 9, no. 4, pp. 1511–1514, 2011.
- [22] W. Zeng, T. M. Liu, and D. J. Liu, "Hydrogen sensing and mechanism of M-doped SnO_2 ($\text{M} = \text{Cr}^{3+}$, Cu^{2+} and Pd^{2+}) nanocomposite," *Sensors and Actuators B*, vol. 160, no. 1, pp. 455–462, 2011.
- [23] J. Zhang, S. Wang, M. Xu et al., "Hierarchically porous ZnO architectures for gas sensor application," *Crystal Growth and Design*, vol. 9, no. 8, pp. 3532–3537, 2009.
- [24] J. Gong, Y. Li, Z. Hu, Z. Zhou, and Y. Deng, "Ultrasensitive NH_3 gas sensor from polyaniline nanograin enched TiO_2 fibers," *Journal of Physical Chemistry C*, vol. 114, no. 21, pp. 9970–9974, 2010.
- [25] T. Waitz, T. Wagner, T. Sauerwald, C. D. Kohl, and M. Tiemann, "Ordered mesoporous In_2O_3 : synthesis by structure replication and application as a methane gas sensor," *Advanced Functional Materials*, vol. 19, no. 4, pp. 653–661, 2009.
- [26] Y. Wang, Q. Mu, G. Wang, and Z. Zhou, "Sensing characterization to NH_3 of nanocrystalline Sb-doped SnO_2 synthesized by a nonaqueous sol-gel route," *Sensors and Actuators B*, vol. 145, no. 2, pp. 847–853, 2010.
- [27] C. Wang, L. Yin, L. Zhang, D. Xiang, and R. Gao, "Metal oxide gas sensors: sensitivity and influencing factors," *Sensors*, vol. 10, no. 3, pp. 2088–2106, 2010.
- [28] Q. Qi, T. Zhang, L. Liu, and X. Zheng, "Synthesis and toluene sensing properties of SnO_2 nanofibers," *Sensors and Actuators B*, vol. 137, no. 2, pp. 471–475, 2009.
- [29] T. Zhang, L. Liu, Q. Qi, S. Li, and G. Lu, "Development of micro-structure In/Pd-doped SnO_2 sensor for low-level CO detection," *Sensors and Actuators B*, vol. 139, no. 2, pp. 287–291, 2009.
- [30] X. Song, Q. Qi, T. Zhang, and C. Wang, "A humidity sensor based on KCl-doped SnO_2 nanofibers," *Sensors and Actuators B*, vol. 138, no. 1, pp. 368–373, 2009.

- [31] Y. Shen, T. Yamazaki, Z. Liu, D. Meng, and T. Kikuta, "Hydrogen sensors made of undoped and Pt-doped SnO_2 nanowires," *Journal of Alloys and Compounds*, vol. 488, no. 1, pp. L21–L25, 2009.
- [32] Y. C. Lee, H. Huang, O. K. Tan, and M. S. Tse, "Semiconductor gas sensor based on Pd-doped SnO_2 nanorod thin films," *Sensors and Actuators B*, vol. 132, no. 1, pp. 239–242, 2008.
- [33] S. Wang, Y. Zhao, J. Huang et al., "Low-temperature CO gas sensors based on Au/ SnO_2 thick film," *Applied Surface Science*, vol. 253, no. 6, pp. 3057–3061, 2007.
- [34] Y. B. Xue and Z. A. Tang, "Density functional study of the interaction of CO with undoped and Pd doped SnO_2 (110) surface," *Sensors and Actuators B*, vol. 138, no. 1, pp. 108–112, 2009.
- [35] F. Trani, M. Causà, D. Ninno, G. Cantele, and V. Barone, "Density functional study of oxygen vacancies at the SnO_2 surface and subsurface sites," *Physical Review B*, vol. 77, no. 24, Article ID 245410, 8 pages, 2008.
- [36] Z. Wen and L. Tian-mo, "Gas-sensing properties of SnO_2 - TiO_2 -based sensor for volatile organic compound gas and its sensing mechanism," *Physica B*, vol. 405, no. 5, pp. 1345–1348, 2010.
- [37] Z. Wen, L. Tian-Mo, and L. Xiao-Fei, "Hydrogen sensing properties of low-index surfaces of SnO_2 from first-principles," *Physica B*, vol. 405, no. 16, pp. 3458–3462, 2010.
- [38] J. Oviedo and M. J. Gillan, "Energetics and structure of stoichiometric SnO_2 surfaces studied by first-principles calculations," *Surface Science*, vol. 463, no. 2, pp. 93–101, 2000.

Research Article

Influence of Hydrothermal Temperature on Phosphorus Recovery Efficiency of Porous Calcium Silicate Hydrate

Wei Guan, Fangying Ji, Qingkong Chen, Peng Yan, and Weiwei Zhou

Key Laboratory of Three Gorges Reservoir Region's Eco-Environment of Ministry of Education, Chongqing University, Chongqing 400045, China

Correspondence should be addressed to Fangying Ji; jfy@cqu.edu.cn

Received 2 November 2012; Revised 20 December 2012; Accepted 3 January 2013

Academic Editor: Wen Zeng

Copyright © 2013 Wei Guan et al. This is an open access article distributed under the Creative Commons Attribution License, which permits unrestricted use, distribution, and reproduction in any medium, provided the original work is properly cited.

Porous calcium silicate hydrate (PCSH) was synthesized by carbide residue and white carbon black. The influence of hydrothermal temperature on phosphorus recovery efficiency was investigated by Field Emission Scanning Electron Microscopy (FESEM), Brunauer-Emmett-Teller (BET), and X-Ray Diffraction (XRD). Hydrothermal temperature exerted significant influence on phosphorus recovery performance of PCSH. Hydrothermal temperature 170°C for PCSH was more proper to recover phosphorus. PCSH could recover phosphorus with content of 18.51%. The law of Ca^{2+} and OH^- release was the key of phosphorus recovery efficiency, and this law depended upon the microstructure of PCSH. When the temperature of synthesis reached to 170°C, the reactions between CaO and amorphous SiO_2 were more efficient. Solubility of SiO_2 was a limiting factor.

1. Introduction

Phosphorus recovery from wastewater in the form of hydroxyapatite is an effective method [1]. However, the optimal pH value for the formation of hydroxyapatite is in the range of 10.5~12.5 [2]. But this pH value is too high to biochemical treatment system where the pH value is located between 6.0 and 9.0 [3].

Phosphorus recovery on the condition of alkalescency not only decreased the significant competition between carbonate and calcium, but also decreased the cost of chemical treatment and increased the effective phosphorus composition of the final products [4]. To address these issues, calcium silicate hydrate was introduced [5]. The existing researches showed that calcium silicate hydrate could be considered as a very attractive and promising material to remove phosphorus from wastewater when compared with the common natural materials [6]. Because calcium silicate hydrate could release Ca^{2+} and OH^- [7], Ca^{2+} , OH^- and PO_4^{3-} in the solution form a condition locally for the growth of HAP, which could grow with pH = 8.0-9.0. In order to achieve this goal, it is necessary to find a process condition to prepare calcium silicate hydrate.

From a theoretical and practical point of view, the synthesis, properties, and structure of calcium silicate hydrate

have been analyzed in detail [8–11]. Dynamic hydrothermal synthesis is a common method to prepare calcium silicate hydrate [12, 13]. Hydrothermal temperature is one of the most important factors, which determine the microstructure of calcium silicate hydrate [14]. Prophase researches showed that the difference of microstructure has an effect on the phosphorus recovery performance of calcium silicate hydrate. However, the bottleneck problem was that it was hard to determine the appropriate hydrothermal temperature for the preparation of the calcium silicate hydrate which possesses the phosphorus recovery performance.

The main aim of the research is to find a proper hydrothermal temperature for calcium silicate hydrate to recover phosphorus. The originality and importance of this paper are highlighted by the following three points.

- (1) PCSH was synthesized by carbide residue and white carbon black with a dynamic hydrothermal method. The influence of hydrothermal temperature on phosphorus recovery performance was investigated.
- (2) The relationship between pore structure and the law of Ca^{2+} and OH^- release was established by Avrami kinetic model.

TABLE 1: Chemical components of carbide residue and white carbon black.

	Chemical components (contents)/%									
	CaO	SiO ₂	Al ₂ O ₃	SO ₂	MgO	Fe ₂ O ₃	SrO	NaOH	CuO	H ₂ O
Carbide residue	79.34	3.57	2.14	1.22	0.62	0.21	0.26	—	—	12.64
White carbon black	0.08	97.46	0.16	1.82	—	0.03	—	0.29	0.02	0.14

- (3) The mechanism of phosphorus recovery was studied by FESEM, BET, and XRD on the basis of an in-depth critical investigation.

2. Materials and Methods

2.1. Preparation of PCSH. PCSH was synthesized with carbide residue (providing Ca) and white carbon black (providing Si). Carbide residue (calcareous, hoar, and powdery) was obtained from Chongqing Changshou Chemical Co. Ltd. and calcined at 700°C for 2 h. White carbon black (particles present spherical with homogeneous diameter) was purchased from Chongqing Jianfeng chemical Co. Ltd. Chemical constituents of carbide residue and white carbon black are shown in Table 1. The phosphorus solution was adjusted by adding KH₂PO₄ (Analytical reagent, Chongqing Boyi Chemical reagent Co. Ltd.) to prepare solution with initial phosphorus concentration of 100 mg/L. The above materials and chemicals were placed into sealed bottles for storage.

Carbide residue and white carbon black were mixed, and the Ca/Si molar ratios were controlled at 1.6:1. The mixture was then added to prepared slurries. The slurry was hydrothermally reacted at 110°C, 140°C, 170°C, and 200°C, respectively, and the reaction time was 6 h. The samples were taken out when the temperature was reduced to the natural condition. The hydrothermal reaction was carried out with a liquid/solid ratio of 30. The obtained products were dried at 105°C for 2 h, and then were ground through a sieve of 200 meshes. The prepared samples that were hydrothermally reacted at 110°C, 140°C, 170°C, and 200°C were denoted as PCSH: 110°C, PCSH: 140°C, PCSH: 170°C, and PCSH: 200°C, respectively.

2.2. Evaluation of Phosphorus Recovery Performance. Firstly, synthetic solution (1 L) was added into several bottles. 4 g of samples were added to these bottles, respectively, and shaken at 40 r/min under controlled temperature conditions (20°C). Phosphorus concentration of supernatant was measured according to the molybdenum blue ascorbic acid method (the relative error of data is 0.3%) with a Unico spectrophotometer (UV-2012PCS, Shanghai Unico Instruments Co., Ltd., China). The solid samples were then separated from the removed synthetic solution with the addition of samples after reaction. Finally, the produced sediments were separated from removed synthetic solution, dried, and weighted. Phosphorus was contented by

$$P = \frac{(C_0 - C_t) \times v}{w} \times 100\%, \quad (1)$$

where C_t is the restrained phosphorus concentration in synthetic solution (mg/L), v is the volume of the solution (L), w is the mass of produced sediment after phosphorus recovery (mg), and C_0 is the initial phosphorus concentration (mg/L).

4 g of samples (PCSH: 110°C, PCSH: 140°C, PCSH: 170°C, and PCSH: 200°C) were immersed in 1 L of demonized water, respectively, contained in a glass bottle, generating samples with a solution concentration of 4 g/L. The bottle was placed on an agitation table and shaken at 40 r/min under controlled temperature conditions (20°C). Samples of solution were taken after 5, 10, 15, 20, 40, 60, and 80 mins of agitation. Ca²⁺ concentration of the samples was determined by EDTA titration (the relative error of data is 0.05%).

2.3. Characterization Methods. XRD patterns were collected in an XD-2 instrument (Persee, China) using Cu K α radiation. FESEM images were collected on an S-4800 field emission scanning electron microscope (Hitachi, Japan). BET surface areas were measured by nitrogen adsorption at 77.35 K on an ASAP-2010 adsorption apparatus (Micromeritics, USA).

3. Results and Discussion

3.1. Phosphorus Recovery Performance of PCSH. The PCSH samples were separated from the removed synthetic solution after phosphorus removal, and these samples were added into synthetic solution with initial phosphorus concentration 100 mg/L again. This process was repeated for several times in order to explore the phosphorus recovery performance of PCSH. Changes of restrained phosphorus concentration are shown in Figure 1. There were great differences among the phosphorus recovery performance of these samples. Phosphorus content of PCSH: 110°C was only 6.49% after 7 times of phosphorus removal. Phosphorus content of PCSH: 140°C was 9.07% after 9 times of phosphorus removal. PCSH: 170°C could remove phosphorus repeated for 15 times, and phosphorus content of this sample reached 18.51%. Phosphorus content of PCSH: 200°C was 12.92% after 11 times of phosphorus removal. Generally speaking, the material could be used as a high grade phosphorus ore when the phosphorus content of this material exceeds 15% [15]. Therefore, the hydrothermal temperature 170°C was beneficial for the PCSH to phosphorus removal. As seen in Figure 2, these samples reflected good phosphorus removal efficiency when pH values maintained 8.0~9.0. But with the times of phosphorus removal increased, pH values and the phosphorus removal efficiency of PCSH samples declined. The concentration of restrained phosphorus kept unchanged when pH values

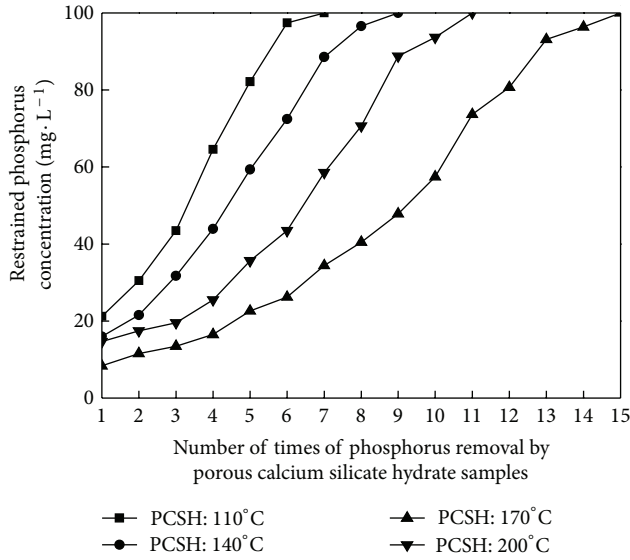


FIGURE 1: Changes of restrained phosphorus concentration by circulation of phosphorus removal.

declined to 7.0. This phenomenon showed that these samples had no phosphorus recovery performance on the condition of neutral. In contrast, PCSH: 170°C could maintain pH values at a range of 8.0~9.0 more effectively.

3.2. The Pore Structure and Ca^{2+} Release of PCSH. Specific surface area and pore size distribution were calculated by BET equation and Barrett-Joyner-Halenda method, respectively (Figure 3). The nitrogen sorption analysis was conducted to reveal the pore structure of calcium silicate hydrate. All three samples showed similar adsorption-desorption isotherms, which could be classified as type IV according to IUPAC nomenclature [16]. The results suggested the phenomenon of adsorption hysteresis loop. That mean mesopore or narrow gap pore existed on sample. Adsorption in mesopore occurred mainly in medium pressure region ($0.4 < P/P_0 < 0.9$). When the hydrothermal temperature was lower than 170°C, with the increase of hydrothermal temperature, the phenomenon of adsorption hysteresis loop became obvious and the adsorption curve increased. While the adsorption curve of PCSH: 200°C declined slightly, specific surface areas of PCSH: 110°C, PCSH: 140°C, PCSH: 170°C, and PCSH: 200°C were 11.91, 49.85, 113.36, and 59.67 m^2/g , respectively. Pore volumes of these samples were 0.07, 0.15, 0.53, and 0.30 cm^3/g , respectively.

The morphology of PCSH: 110°C, PCSH: 140°C, PCSH: 170°C, and PCSH: 200°C was examined by FESEM observations (Figure 4). It could be indicated from the photographs that the surface structure of PCSH: 110°C seems dense with pore size inhomogeneous distribution. The surface structure of PCSH: 140°C and PCSH: 200°C seems dense with pore size homogeneous distribution. In contrast, PCSH: 170°C possesses obverse fibrous-network structure with a large number of mesopores, and the particle size of spherical particle distributed from 25 to 30 μm uniformly.

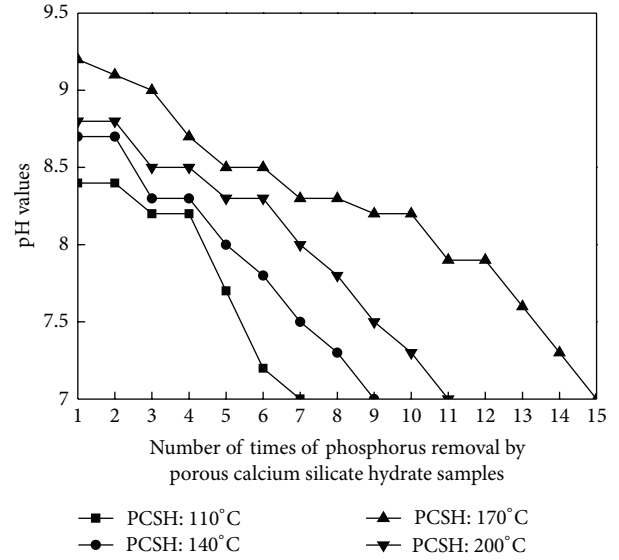


FIGURE 2: Changes of pH values by circulation of phosphorus removal.

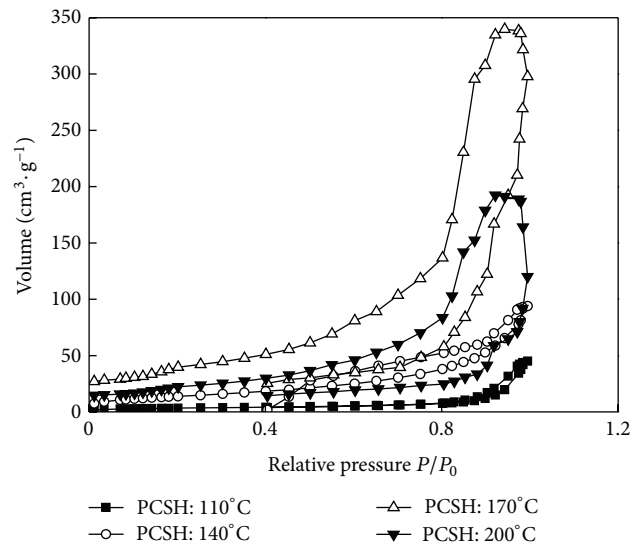


FIGURE 3: Nitrogen adsorption-desorption isotherms on samples.

The experiments showed that Ca^{2+} concentration dissolved from PCSH: 110°C, PCSH: 140°C, PCSH: 170°C, and PCSH: 200°C was 2.70, 3.11, 4.91, and 3.76 mg/g , respectively (Figure 5). This result showed that PCSH: 170°C reflected better performance of Ca^{2+} release. The experimental capacities of Ca^{2+} release were potted according to Avrami kinetic model as follows [17]:

$$-\ln(1-x) = kt^n, \quad (2)$$

where k is the kinetic constant, n is the characteristic constant of solid, t is the reaction time (min) and x ($x = C_t/C_{\max}$, C_t is concentration of time t (mg/L), and C_{\max} is concentration of the maximum (mg/L) is the fraction conversion. The characteristic constant n was 0.947. The kinetic constants

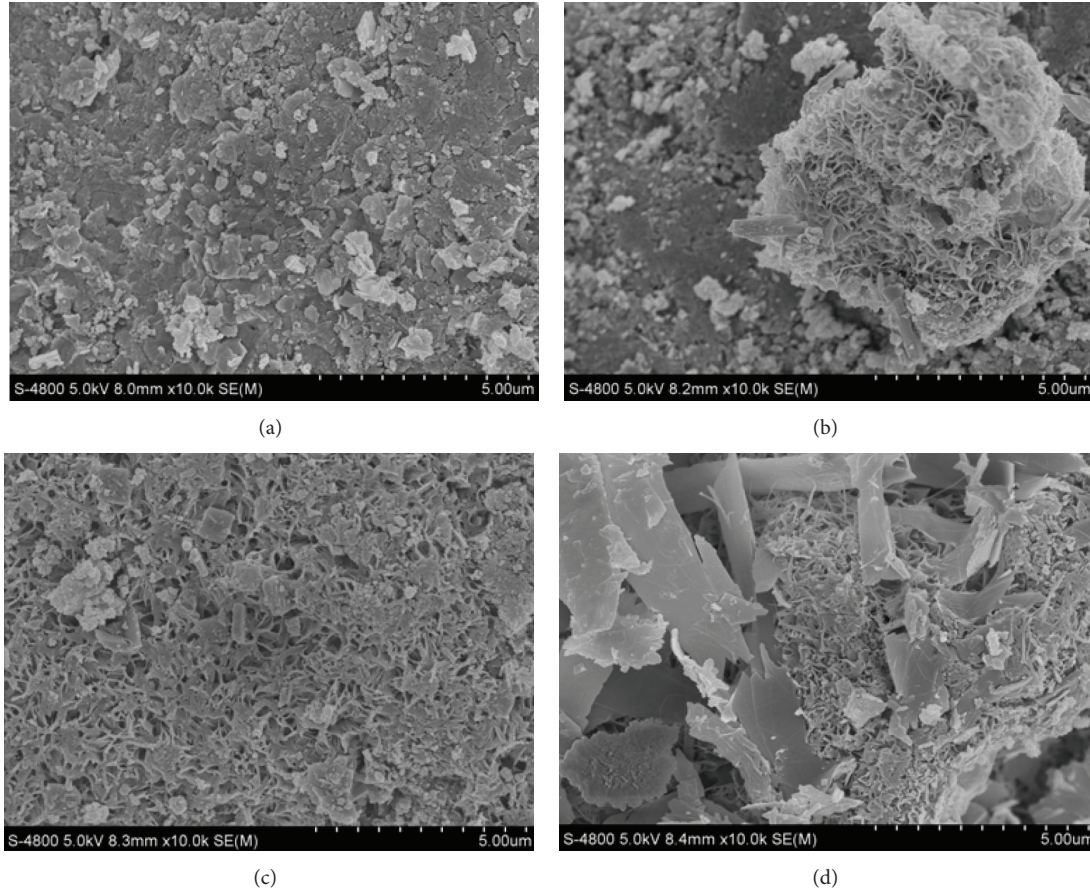


FIGURE 4: FESEM photographs of samples. (a) PCSH: 110°C; (b) PCSH: 140°C; (c) PCSH: 170°C; (d) PCSH: 200°C.

were determined by fitting the Avrami kinetic model to the experimental data obtained from Table 2. The high correlation coefficients ($R^2 > 0.9$) indicated that this model could describe the law of Ca^{2+} release well. Combined with specific surface area (S) of samples, a relationship between k and S could be established as follows:

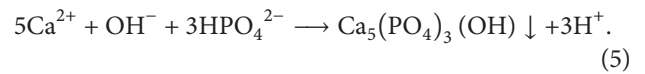
$$k = 0.018S^{0.315}. \quad (3)$$

According to (3), specific surface area of samples and the rate of Ca^{2+} release were in good agreement with each other. The relationship between specific surface area and dissolved concentration of Ca^{2+} was obtained by substituting (3) into (2) as follows:

$$-\ln(1-x) = 0.018S^{0.315}t^{0.947}. \quad (4)$$

According to (4), concentration of Ca^{2+} release was related to specific surface area. This result demonstrated the influence of hydrothermal temperature on phosphorus recovery performance. Hydrothermal temperature affected the pore structure and the performance of Ca^{2+} release. Ca^{2+} was released faster due to the larger specific surface area. Comparatively speaking, PCSH: 170°C possesses larger specific surface area. Porous structure provided a local condition to maintain a high concentration of Ca^{2+} release. PCSH:

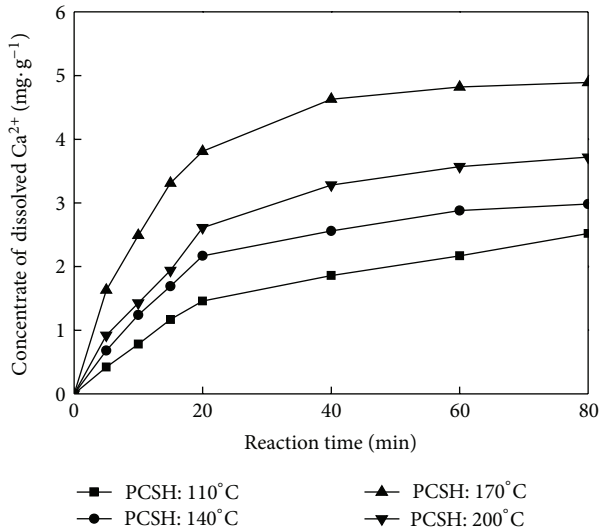
170°C could release a suitable concentration of Ca^{2+} and OH^- to maintain the pH values during 8.0~9.0. Phosphate existed in the form of HPO_4^{2-} in the range of these pH values [18]. Ca^{2+} , OH^- , and HPO_4^{2-} formed a local condition with high concentration. This condition was beneficial to the formation of hydroxyapatite with pH = 8.0~9.0. The major reaction of the hydroxyapatite crystallization on PCSH crystal seed was as follows:



3.3. Mechanism of Hydrothermal Temperature Effect on Phosphorus Recovery Performance. The mechanism of hydrothermal temperature effect on phosphorus recovery performance could be further investigated by XRD. The XRD patterns of PCSH samples were compared (Figure 6). The main phase of PCSH: 110°C was SiO_2 (PDF card 18-1169), and this result indicated that carbide residue and white carbon black had not reacted completely. When the hydrothermal temperature increased to 140°C, the main phase included Jennite (PDF card 18-1206, chemical formula $\text{Ca}_9\text{Si}_6\text{O}_{18}(\text{OH})_6 \cdot 8\text{H}_2\text{O}$) and SiO_2 , but the principal peaks of Jennite were not obvious. In this stage, a part of SiO_2 had involved in the formation of Jennite, but the reaction was not completely, so

TABLE 2: Correlation equations and rate constants for the Avrami kinetic model describing Ca^{2+} release.

Samples	Avrami kinetic equations	Kinetic constant (k)	Correlation coefficient (R^2)
PCSH: 110°C	$-\ln(1-x) = 0.039t^{0.947}$	0.039	0.973
PCSH: 140°C	$-\ln(1-x) = 0.052t^{0.947}$	0.052	0.985
PCSH: 170°C	$-\ln(1-x) = 0.085t^{0.947}$	0.085	0.998
PCSH: 200°C	$-\ln(1-x) = 0.066t^{0.947}$	0.066	0.988

FIGURE 5: Concentrate of Ca^{2+} dissolved from samples.

the content of Jennite was low. When the hydrothermal temperature reached to 170°C, the principal peaks of Jennite appeared instead of the principal peaks of SiO_2 in the XRD patterns. This result indicated that the main component of PCSH: 170°C was Jennite. As the hydrothermal temperature heated to 200°C, the production included jennite, xonotlite (PDF card 23-0125, chemical formula $\text{Ca}_6\text{Si}_6\text{O}_{17}(\text{OH})_2$), and $\text{Ca}_3\text{Si}_2\text{O}_7$ (PDF card 11-0317).

As the siliceous material, white carbon black exhibited high activity [19]. Therefore, the hydrothermal reaction in the high-pressure reactor belonged to controlling solution reaction. The reaction process depended on the dissolution of SiO_2 , and the dissolution rate depended on the solubility of SiO_2 in the white carbon black. Based on the above analysis, when the hydrothermal reaction was too low, SiO_2 was difficult to dissolve, and formed a layer of rich silicon on the surface of samples. This condition made the pore structure of samples became dense. Rising the hydrothermal temperature could increase the solubility of SiO_2 . The solubility of white carbon black was low at atmospheric temperature and pressure, but the solubility increased with the increasing of hydrothermal temperature. Jennite formed when the hydrothermal temperature reached to 170°C, and this material could dissolve a proper concentration of Ca^{2+} and OH^- due to loose and porous structure. So PCSH: 170°C has better phosphorus recovery performance. The system of PCSH became instable due to a too high hydrothermal temperature, and multiple impurities appeared in this

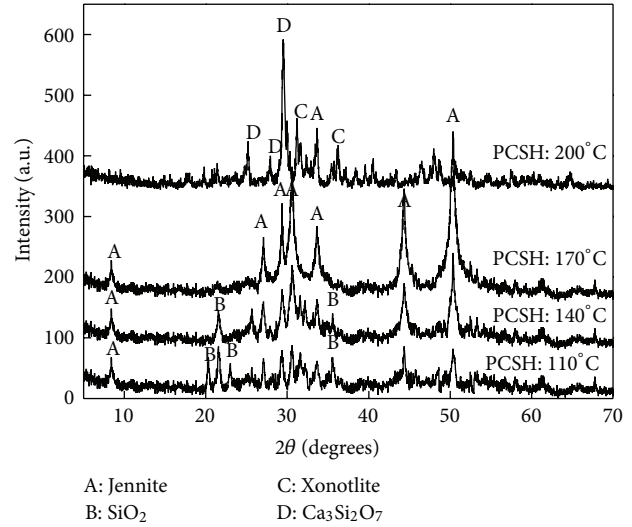


FIGURE 6: XRD patterns of samples.

system. The phosphorus recovery performance of the sample declined because the efficiency of Ca^{2+} and OH^- release of the impurities was too low.

4. Conclusions

Porous calcium silicate hydrate was synthesized by carbide residue and white carbon black with a dynamic hydrothermal method. This material could be considered a tenable material for phosphorus removal and recovery from wastewater. Hydrothermal temperature showed significant influence on phosphorus recovery performance of PCSH. Hydrothermal temperature 170°C for PCSH was more proper to recover phosphorus. PCSH could recover phosphorus with content of 18.51%.

The law of Ca^{2+} and OH^- release was the key of phosphorus recovery efficiency. Changes of hydrothermal temperature led to the different pore structures. The increase of specific surface area and the increase in concentration of Ca^{2+} release were in good agreement with each other.

Further analysis by XRD indicated that hydrothermal reaction process depended on the dissolution of SiO_2 . And hydrothermal temperature affected the solubility of SiO_2 .

References

- [1] E. H. Kim, S. B. Yim, H. C. Jung, and E. J. Lee, "Hydroxyapatite crystallization from a highly concentrated phosphate solution

- using powdered converter slag as a seed material," *Journal of Hazardous Materials B*, vol. 136, no. 3, pp. 690–697, 2006.
- [2] J. Z. Zhou, L. L. Feng, J. Zhao et al., "Efficient and controllable phosphate removal on hydrocalumite by multi-step treatment based on pH-dependent precipitation," *Chemical Engineering Journal*, vol. 185, pp. 219–225, 2012.
 - [3] P. Battistoni, P. Pavan, M. Prisciandaro, and F. Cecchi, "Struvite crystallization: a feasible and reliable way to fix phosphorus in anaerobic supernatants," *Water Research*, vol. 34, no. 11, pp. 3033–3041, 2000.
 - [4] P. Battistoni, A. de Angelis, P. Pavan, M. Prisciandaro, and F. Cecchi, "Phosphorus removal from a real anaerobic supernatant by struvite crystallization," *Water Research*, vol. 35, no. 9, pp. 2167–2178, 2001.
 - [5] D. Sugiyama and T. Fujita, "A thermodynamic model of dissolution and precipitation of calcium silicate hydrates," *Cement and Concrete Research*, vol. 36, no. 2, pp. 227–237, 2006.
 - [6] X. C. Chen, H. N. Kong, D. Y. Wu, X. Z. Wang, and Y. Lin, "Phosphate removal and recovery through crystallization of hydroxyapatite using xonotlite as seed crystal," *Journal of Environmental Sciences*, vol. 21, no. 5, pp. 575–580, 2009.
 - [7] J. J. Chen, J. J. Thomas, H. F. W. Taylor, and H. M. Jennings, "Solubility and structure of calcium silicate hydrate," *Cement and Concrete Research*, vol. 34, no. 9, pp. 1499–1519, 2004.
 - [8] F. Tariq, R. Haswell, P. D. Lee, and D. W. McComb, "Characterization of hierarchical pore structures in ceramics using multiscale tomography," *Acta Materialia*, vol. 59, no. 5, pp. 2109–2120, 2011.
 - [9] S. Sánchez-Salcedo, J. Werner, and M. Vallet-Regí, "Hierarchical pore structure of calcium phosphate scaffolds by a combination of gel-casting and multiple tape-casting methods," *Acta Biomaterialia*, vol. 4, no. 4, pp. 913–922, 2008.
 - [10] R. Siauciunas and K. Baltakys, "Formation of gyrolite during hydrothermal synthesis in the mixtures of CaO and amorphous SiO₂ or quartz," *Cement and Concrete Research*, vol. 34, no. 11, pp. 2029–2036, 2004.
 - [11] S. Shaw, S. M. Clark, and C. M. B. Henderson, "Hydrothermal formation of the calcium silicate hydrates, tobermorite (Ca₅Si₆O₁₆(OH)₂ · 4H₂O) and xonotlite (Ca₆Si₆O₁₇(OH)₂): an in situ synchrotron study," *Chemical Geology*, vol. 167, no. 1–2, pp. 129–140, 2000.
 - [12] M. Li and H. Liang, "Formation of micro-porous spherical particles of Calcium Silicate (Xonotlite) in dynamic hydrothermal process," *China Particuology*, vol. 2, no. 3, pp. 124–127, 2004.
 - [13] A. A. P. Mansur and H. S. Mansur, "Preparation, characterization and cytocompatibility of bioactive coatings on porous calcium-silicate-hydrate scaffolds," *Materials Science and Engineering C*, vol. 30, no. 2, pp. 288–294, 2010.
 - [14] T. T. H. Bach, C. Cau Dit Coumes, I. Pochard, C. Mercierc, B. Revel, and A. Nonatb, "Influence of temperature on the hydration products of low pH cements," *Cement and Concrete Research*, vol. 42, pp. 805–817, 2012.
 - [15] M. Sinirkaya, A. K. Özer, and M. S. Gülaboglu, "Investigation of the changes of P₂O₅ content of phosphate rock during simultaneous calcination/sulfation," *Powder Technology*, vol. 211, no. 1, pp. 72–76, 2011.
 - [16] Y. Geng, X. Wang, W. Chen, Q. Cai, C. Nan, and H. Li, "Synthesis, characterization and application of novel bicontinuous mesoporous silica with hierarchical pore structure," *Materials Chemistry and Physics*, vol. 116, no. 1, pp. 254–260, 2009.
 - [17] N. Demirkiran and A. Künkül, "Dissolution kinetics of ulexite in perchloric acid solutions," *International Journal of Mineral Processing*, vol. 83, no. 1–2, pp. 76–80, 2007.
 - [18] Y. Liu, X. Sheng, Y. H. Dong, and Y. J. Ma, "Removal of high-concentration phosphate by calcite: effect of sulfate and pH," *Desalination*, vol. 289, pp. 66–71, 2012.
 - [19] M. Felipe-sese, D. Eliche-Quesada, and F. A. Corpas-Iglesias, "The use of solid residues derived from different industrial activities to obtain calcium silicates for use as insulating construction materials," *Ceramics International*, vol. 37, no. 8, pp. 3019–3028, 2011.

Research Article

Characterization of Porous WO₃ Electrochromic Device by Electrochemical Impedance Spectroscopy

Chien Chon Chen

Department of Energy Engineering, National United University, Miaoli 36003, Taiwan

Correspondence should be addressed to Chien Chon Chen; chentexas@gmail.com

Received 4 October 2012; Accepted 22 December 2012

Academic Editor: Wen Zeng

Copyright © 2013 Chien Chon Chen. This is an open access article distributed under the Creative Commons Attribution License, which permits unrestricted use, distribution, and reproduction in any medium, provided the original work is properly cited.

This paper concerns the microstructure of the anodic tungsten oxide (WO₃) and its use in an electrochromic (EC) glass device. When voltages between 100 V and 160 V were applied to tungsten film for 1 h under 0.4 wt. % NaF electrolyte, porous WO₃ film was formed. The film, which had a large surface area, was used as electrochromic film for EC glass. The average transmittance in a visible region of the spectrum for a 144 cm² EC device was above 75% in the bleached state and below 40% in the colored state, respectively. Repeatability using of the colored/bleached cycles was tested good by a cyclic voltammograms method. The internal impedance values under colored and bleached states were detected and simulated using an electrical impedance spectra (EIS) technique. The EC glass impedance characteristics were simulated using resistors, capacitors, and Warburg impedance. The ITO/WO₃, WO₃/electrolyte, electrolyte/NiO, and NiO/ITO interfaces can be simulated using a resistance capacitance (RC) parallel circuits, and bulk materials such as the indium tin oxide (ITO) and conducting wire can be simulated by using a series of resistors.

1. Introduction

In recent years, the nanometer technological progress has led to the creation of many special new materials. Therefore now, information photoelectricity, catalysis, and magnetism have broader application domains because of nanotechnology. For example, the tungsten oxide (WO₃), which has rich special physics and chemical properties, is widely treated as electrochromic (EC) [1, 2].

According to a 2012 US department of energy (DOE) report, windows contribute to about 40 percent of overall building heating and cooling load with annual impact of about 4.4 quads, and there is a potential to reduce lighting impact by 1 quad through day lighting. The Environmental Protection Agency says an average household spends over 40 percent of its annual energy budget on heating and cooling costs. By 2020, industry leaders believe that windows will become active parts of building climate, engineering, information, and structural systems. Advanced electrochromic (EC) technologies such as EC windows will darken in sunlight without the use of an external control circuit. Such windows would be ideal for applications such as car sunroofs. According to the National Renewable Energy Laboratory (NREL), by

allowing control of daylighting and solar gain, electrochromic windows have the potential to reduce annual US energy consumption by several quadrillion (10¹⁵) Btus (quads). The United States currently consumes a total of about 94 quads of energy per year [3–5].

EC glass—also known as smart windows or switchable windows—changes its light transmission properties when voltage is applied. This type of window has “memory” and does not need constant voltage once the change has been initiated [6, 7]. The use of smart glass can allow control of the amount of light and heat passing through and thus save heating, air conditioning, and lighting costs. An EC device is comprised of five layers: the working electrode, the ion conducting layer, and the counter electrode are sandwiched between two electronically conductive transparent electrodes coated on glass. Critical aspects of smart glass include installation costs, the use of electricity, durability, as well as functional features such as the speed of control, possibilities for dimming, and the degree of transparency of the glass [8–10].

Tungsten trioxide (WO₃) has been the most widely used material in EC glass since its electrochromism was

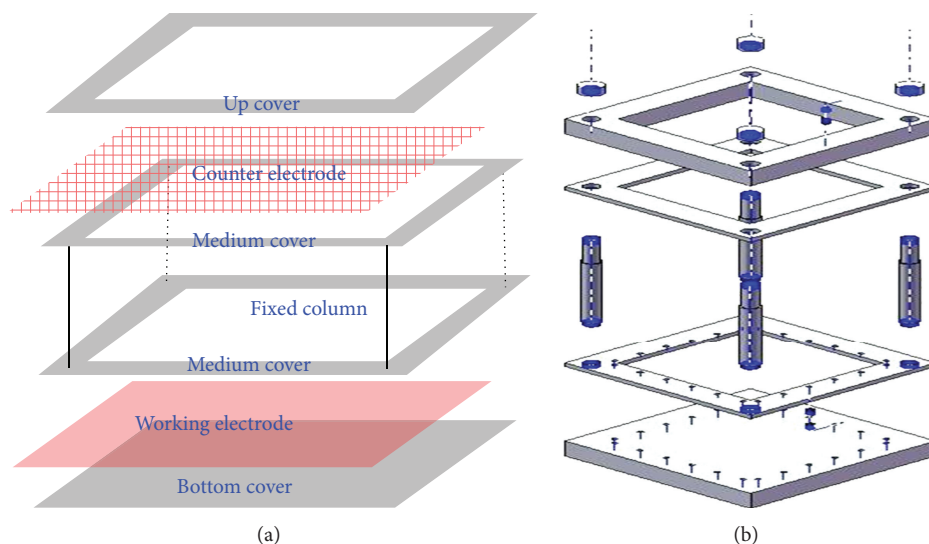


FIGURE 1: Schematic diagram of anodization mold: (a) counter electrode is fixed between top and middle cover, working electrode is between middle and bottom cover, and the counter-working electrodes distance is adjusted by using a fixed column and (b) three-dimensional diagram.

first reported in 1969 [11, 12]. Tungsten oxide has a large number of interstitial sites where guest ions can be inserted. Tungsten trioxide in its fully occupied state is transparent, but electrochemical reduction caused it to enter the EC state [13]. Much work on improving the performance of EC glass has been published. For example, Nagai et al. [14] published a study about the durability of the EC glazing. An all-solid-state structure can enhance the durability of EC glazing by reducing thermal effect. Reisfeld [15] published an EC glass fabrication technique involving mixing metal oxide from sol-gel using colloidal solutions of tungstic acid. The needed operational voltage was about ± 1.3 V, and the number of cycles based on theoretical estimates was about $10^5 \sim 10^6$ cycles. They noted that the rate of color change can be accelerated by increasing the conductivity of the tin-doped indium oxide (ITO) supporting glass. The blue coloration of the mixed valence tungsten in the EC film prevents the entry of solar light mainly in the UV and in a large part of the visible spectrum. They also mentioned that the effect of blocking solar radiation can be achieved by adding a fractional amount of MoO_3 . Fang and Eames [16] pointed out the edge effect in EC windows. Even vacuum glazing small sizes ($0.4 \text{ m} \times 0.4 \text{ m}$), leading to the thermal conductance in the central glazing region being 3.1% greater than the result, was calculated using an analytic model that does not consider edge effects. For larger sizes of vacuum glazing (1 m^2), the variation between the central glazing heat transmittance was calculated using finite volume and analytic models is 0.4%. Also, they mentioned that high temperatures will both damage the glazing system and make the indoor environment unbearable. The glass pane with the electrochromic layer must in all installations face the outdoor environment [17–21].

Transition metal oxides of WO_3 have transparent and semiconducting physical characteristics that make them usable for electrochromic film in electrochromic glass. In

recent years WO_3 thin film has been manufactured by using an anodic oxidation process, purely using chemical solutions and parameters as objects of study [22, 23]. Nanoporous WO_3 thin film should be able to cause hydrogen (H^+) or lithium (Li^+) ions to be more rapid in the reaction process that carries on the proliferation, thereby increasing the color/bleach rate. Large-scale development of electrochromic glass based on porous films can potentially result in tremendous increase color/bleach rate, extended durability, insulated heat transfer, and energy savings. In addition, the production process will be relatively environmentally friendly. The knowledge generated by this research will significantly advance research in the area of the WO_3 film fabrication and use film as insulator and electrochromic film in electrochromic glass applications.

In principle, electrochemical impedance spectroscopy (EIS) measures a broad frequency range that can provide information on the interfaces of electron transport and charge transfer characteristics [24–29]. An analysis of electrochemical devices that describes electron transport and charge recombination in nanoparticle and nanotube film has been presented based on a transmission line model [30–33]. Kern et al. [34] indicated that Nyquist plot characteristics in the low-frequency range correspond to the electrolyte, while the middle-frequency range reflects the anode, and the high-frequency range corresponds to the cathode. Hoshikawa [35] also reported that the ω_1 , ω_2 , ω_3 , and ω_4 semicircles were attributable to electron transfer at the transparent conduction oxide (TCO)/electron transport oxide (TiO_2) interface, TiO_2 , TiO_2 /electrolyte interface, and the diffusion impedance of ions in the electrolyte, respectively. Labidi et al. [36] discussed the EIS properties of surface morphology of WO_3 thin films which were prepared by RF sputtered, and, indicated that The AC impedance spectroscopy is a powerful method to understand the nature of conduction processes and the mechanism of gas/solid interactions. The Nyquist response

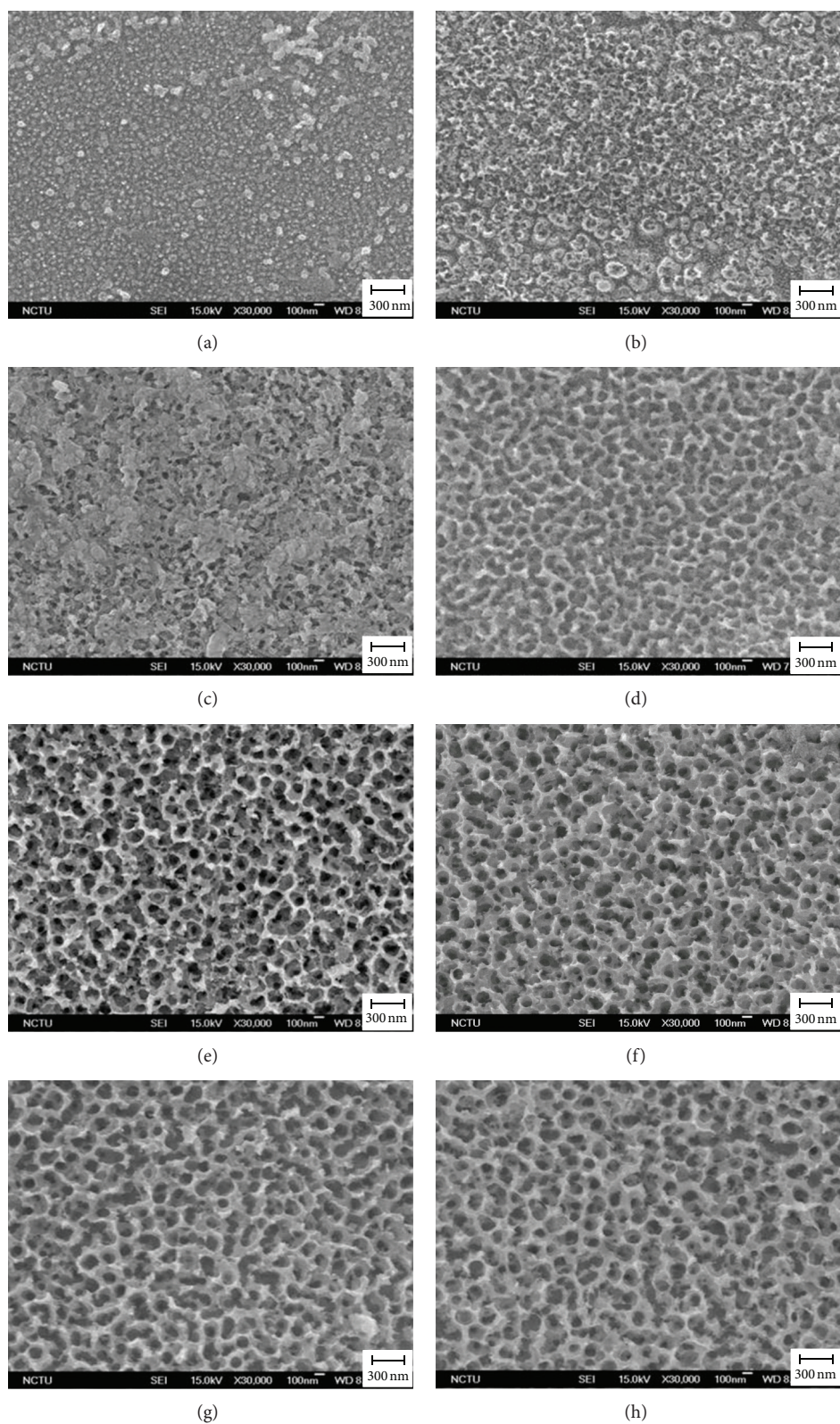


FIGURE 2: SEM images showing the porous structure on anodic tungsten oxide when tungsten was anodized in 0.4 wt.% NaF electrolyte, at 25°C for 1 hr and voltages of (a) 20 V, (b) 40 V, (c) 60 V, (d) 80 V, (e) 100 V, (f) 120 V, (g) 140 V, and (h) 160 V were applied.

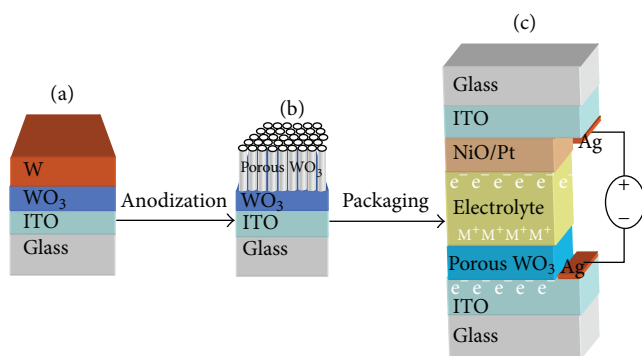


FIGURE 3: Schematic diagram of electrochromic glass based on porous WO₃ and multilayered structure. (a) An under layer of WO₃ was first deposited on the ITO glass and then a metal W film on the WO₃, (b) metal W film was used to form a porous WO₃ of electrochromic film by anodization, and (c) the 144 cm² electrochromic device includes a working electrode (ITO, WO₃), ion conductor (electrolyte), and counter (Pt, NiO₂, ITO).

dry air O₃ decomposed, and the adsorption of oxygen mainly affects the characteristics of the space charge region at the WO₃ grain boundaries.

Electrochromic glass has been developed since the 1970s and especially since the 1990s. However, there are still some aspects that could be improved such as the rate of color change and the lifetime of the EC glasses. In this paper, we use anodic porous WO₃ as EC film. We also report results from an EIS analysis that describes ohmic resistance, electron transfer resistance, diffusion resistance, charge-transfer resistance, contact capacitance, chemical capacitance, electrolysis capacitance, and double-layer capacitance in porous WO₃ EC glass.

2. Experimental Procedures

2.1. WO₃, W, NiO, and Pt Films Deposition. Porous WO₃ EC glass was fabricated on ITO glass as follows. (1) The WO₃ thin film was deposited by RF magnetron sputtering using a 4-inch tungsten metal target with a purity of 99.99%. A mixture of argon and oxygen gases with an Ar/O₂ ratio of 3 was used for the deposition. Working pressure was set to 5×10^{-3} Torr and sputtering power during deposition was 100 W, while the thickness of the film was about 50 nm. (2) Tungsten (W) film was deposited by DC magnetron sputtering on WO₃. Working pressure (without O₂) was set to 5×10^{-3} Torr and sputtering power during deposition was 150 W, while the thickness of the film was about 100 nm. (3) NiO thin film was deposited by RF magnetron sputtering using a 4-inch nickel metal target with a purity of 99.99%. A mixture of argon and oxygen gases with an Ar/O₂ ratio of 1 was used for the deposition. Working pressure was set to 5×10^{-3} Torr and sputtering power during deposition was 100 W, while the thickness of the film was about 50 nm. (4) Platinum (Pt) particles were deposited by DC magnetron sputtering on NiO. Working pressure (without O₂) was set to 5×10^{-3} Torr and sputtering power during deposition was 10 W for 14 sec.

2.2. Porous WO₃ Fabrication. The WO₃ porous film was made by anodization of tungsten film. According to the tungsten Pourbaix diagram [37] when tungsten in an ionic containing electrolyte, for example, sodium fluoride (NaF) solution and applied a voltage, the tungsten (W) can oxidize to a porous tungsten oxide (WO₃). The specific surface area value of WO₃ can further be tested by BET (Brunauer, Emmett, Teller). Porous anodic tungsten oxide was fabricated by anodizing tungsten film in an anodization mold (Figure 1). A Ti counter-electrode net was fixed between a top cover and a middle cover, working tungsten film electrodes were fixed between the middle cover and a bottom cover, and the counter-working electrode distance was adjusted using a fixed column. At the same time, the working electrode and counter-electrode served, respectively, as the positive and negative terminal for a DC power supply. A sample of working and counter-electrodes was sandwiched in the mold, and a silicon rubber sheet was used to prevent electrolytic leaking into the mold. The top, middle, and bottom covers were fastened using threaded Teflon screws. Pressure was applied to the Teflon tubes to keep the top cover and bottom substrate in close contact. Finally, the working electrode in the mold was anodized in 0.4 wt.% NaF electrolyte, and voltage of 20 V to 160 V was applied for 1 h at 25°C. However, when the applied voltage is up to 160 V, the partial of porous WO₃ film was destroyed.

2.3. Electrochromic Device. Electrochromic devices with a configuration consisting of glass/ITO/WO₃/1 M LiClO₄-PC/Pt-NiO/ITO/glass and a size of 144 cm² were obtained by assembling two pieces of coated glass as follows. The two electrodes were assembled into a sandwich type cell and sealed with a hot-melt film (SX1170, Solaronix, thickness 0.1 mm) between electrodes interface. Electrolyte was injected into the space between the two electrodes with a syringe to fabricate an EC glass device. The device was then sealed with vacuum glue (Torr Seal) around electrodes and the electrolyte injecting hole.

2.4. Characterization of Electrochromic Glass. The micro-morphology of the porous WO₃ film was examined using a scanning electron microscope (SEM, JEOL 6500). The optical transmission and reflection spectra were recorded using a UV-VIS-NIR optical photometer (JASCO V570) with an integrating sphere (JASCO ISN-470) in the range from 200 to 800 nm. The electrochromic properties were characterized using cyclic voltammetry (CV) method with a Zahner Impedance Measuring Unit (IM 6). Two electrodes were used to perform electrochemical tests in 1 M LiClO₄ electrolyte in propylene carbonate solution. The internal impedance was evaluated using electrochemical impedance spectroscopy (EIS). The EIS measurements were carried out with a Zahner Impedance Measuring Unit (IM 6). Electrochemical measurements were carried out using two electrode configurations: the glass/ITO/WO₃/porous WO₃ as working electrode and Pt-NiO/ITO electrode as counter-electrode. Cell impedance measurements were recorded over a frequency range of 3 M to 5 m Hz with AC amplitude of

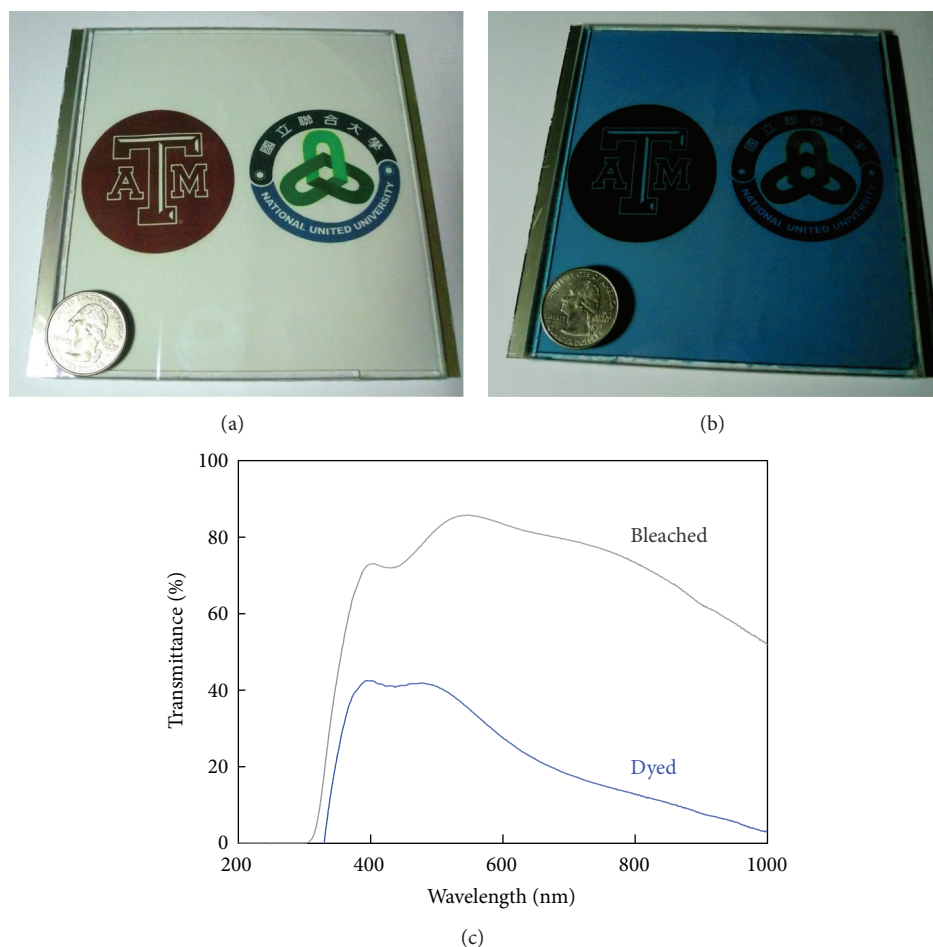


FIGURE 4: Images of electrochromic glass devices and optical transmittance spectrum: (a) electrochromic glass with transparent characteristics in a bleached state, (b) electrochromic glass with blue translucent characteristic in a dyed state, and (c) the glass has transparency of 82% and 21.1% in bleached and dyed states.

10 mV. The EIS data was analyzed by the equilibrium circuit mold and fitted by Microsoft Excel programs.

3. Results and Discussion

3.1. Structure and Characterization of EC Device. Figure 2 shows SEM images of the porous structure on the anodic tungsten oxide when tungsten was anodized in 0.4 wt.% NaF electrolyte at 25°C for 1 h and the following voltages were applied: (a) 20 V, (b) 40 V, (c) 60 V, (d) 80 V, (e) 100 V, (f) 120 V, (g) 140 V, and (h) 160 V. The WO₃ pore sizes increased with the amount of voltage applied. When 20 V was applied, the WO₃ film had an island structure but no pores formed. When voltage was increased to between 40 and 80 V, the WO₃ film was etched by fluorine ions (F⁻) to form partially random porous WO₃ film. Furthermore, when voltages were increased to 100 V~160 V, the pores in the WO₃ widened to form a more regular porous WO₃ film.

Figure 3 shows a schematic diagram of EC glass using porous WO₃ and a multilayer structure. (a) An underlayer of WO₃ (50 nm) was first deposited on the ITO glass and then metal W film was deposited on the WO₃ (100 nm), (b) metal

W film was used to form porous WO₃ electrochromic film by anodization, and (c) the 144 cm² electrochromic device including a working electrode (ITO (200 nm), WO₃), ion conductor (electrolyte), and counter (Pt, NiO (50 nm), ITO). Porous WO₃ is transparent before absorbing hydroxylated or lithiated materials. After voltage (−) is applied to WO₃ electrochromic film, its color changes to blue. WO₃ electrochromic film can serve as an intercalation host for H⁺ and Li⁺. Porous WO₃ film causes hydrogen (H⁺) and lithium (Li⁺) ions to be more rapid in the reaction process that carries on the proliferation, increasing the color/bleach rate. The reactions describing the intercalation/deintercalation of ionic species can be represented as

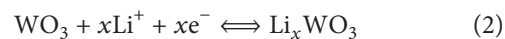
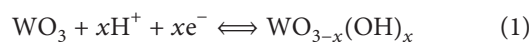


Figure 4 shows a photograph of the 144 cm² EC glass device. Figure 4(a) shows the as-prepared state and the transparent state. When a voltage is applied to the device, the active layer changes from transparent to the translucent

TABLE 1: Equilibrium circuits and mathematical results of real (Z_{RE}) and imaginary value (Z_{IM}) in porous WO_3 EC glass.

Equilibrium circuit	Z_{RE}	Z_{IM}
$R_0 + L_0$	R_0	ωL_0
$\{C_1 // [R_1 + (C_2 // R_2)]\}$	$\frac{[(R_2 + R_1) \times (1 - \omega^2 C_1 C_2 R_1 R_2) + (\omega C_2 R_1 R_2) \times (\omega C_2 R_2 + \omega C_1 R_2 + \omega C_1 R_1)]}{(1 - \omega^2 C_1 C_2 R_1 R_2)^2 + (\omega C_2 R_2 + \omega C_1 R_2 + \omega C_1 R_1)^2}$	$\frac{[(\omega C_2 R_1 R_2) \times (1 - \omega^2 C_1 C_2 R_1 R_2) - (R_2 + R_1) \times (\omega C_2 R_2 + \omega C_1 R_2 + \omega C_1 R_1)]}{(1 - \omega^2 C_1 C_2 R_1 R_2)^2 + (\omega C_2 R_2 + \omega C_1 R_2 + \omega C_1 R_1)^2}$
$[C_3 // (W + R_3)]$	$\frac{\sigma + R_3 \sqrt{\omega}}{\sqrt{\omega} \times (1 + 2\sigma C_3 \sqrt{\omega} + 2\sigma^2 \omega C_3^2 + 2\sigma \omega^{1.5} C_3^2 R_3 + \omega^2 C_3^2 R_3^2)}$	$\frac{-\sigma - 2\sigma^2 \sqrt{\omega} C_3 - 2\sigma \omega C_3 R_3 - \omega^{1.5} C_3^2 R_3^2}{\sqrt{\omega} \times (1 + 2\sigma C_3 \sqrt{\omega} + 2\sigma^2 \omega C_3^2 + 2\sigma \omega^{1.5} C_3^2 R_3 + \omega^2 C_3^2 R_3^2)}$
$(C_4 // R_4)$	$\frac{R_4}{1 + (\omega R_4 C_4)^2}$	$\frac{-\omega R_4^2 C_4}{1 + (\omega R_4 C_4)^2}$
$(C_5 // R_5)$	$\frac{R_5}{1 + (\omega R_5 C_5)^2}$	$\frac{-\omega R_5^2 C_5}{1 + (\omega R_5 C_5)^2}$

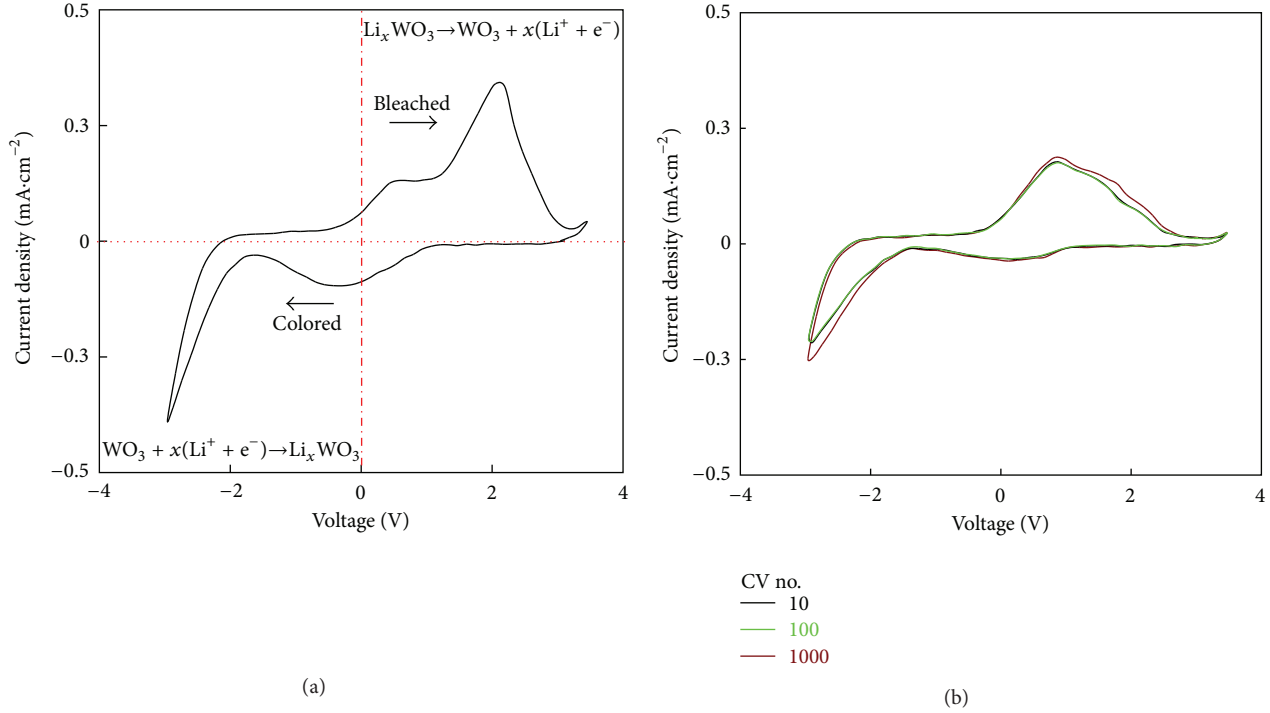


FIGURE 5: Cyclic voltammetry of porous WO_3 electrode performed between -3 V and $+3\text{ V}$ with a scan rate of 50 mV in $0.1\text{ M HClO}_4\text{-PC}$ electrolyte: (a) 1 cycle and (b) 10, 100, and 1000 cycles.

TABLE 2: Parameters determined by fitting the EIS experimental data to the equivalent circuit shown in Figure 8.

Elements	Bleached	Dyed
R_0 (ohm)	6.29	6.25
R_1 (ohm)	1.2	1.1
R_2 (ohm)	0.5	0.65
R_3 (ohm)	110000	120000
R_4 (ohm)	1	1.7
R_5 (ohm)	7	45
C_1 (μF)	80	350
C_2 (μF)	900	420
C_3 (μF)	1200	3000
C_4 (μF)	1500	3800
C_5 (μF)	1100	2800

blue color associated with WO_3 reduction and simultaneous Li^+ insertion, as shown in Figure 4(b). Inversion of the applied voltage results in WO_3 oxidation and the device returns to its initial transparent state. The coloring voltage used in the EC glass was $\pm 1.5\text{ V}$ over 30 sec. The optical transmittance characterization of the device in the wavelength range $400\text{--}800\text{ nm}$ is shown in Figure 4(c). The average transmittance in the visible region of the spectrum was above 75% in the bleached state and below 40% in the colored state, respectively. The cyclic voltammograms of porous WO_3 film are shown in Figure 5(a). The scan rate of measurements was 50 mV/s in the -4 V and $+4\text{ V}$ ranges. It is known that electrochromic film is colored by charge injection ($\text{WO}_3 + x(\text{Li}^+ +$

$\text{e}^-) \rightarrow \text{Li}_x\text{WO}_3$), and a part of this charge was extracted ($\text{Li}_x\text{WO}_3 \rightarrow \text{WO}_3 + x(\text{Li}^+ + \text{e}^-)$) during the subsequent bleaching process. Repeating the colored/bleached cycles, as shown in Figure 5(b), demonstrated good electrochemical stability as Li^+ ion can be almost inserted and extracted reversibly in the 10, 100, and 1000 cycle tests.

3.2. Internal Impedance Detection Using EIS Modeling and Fitting. Figure 6(a) shows the EIS measured data of EC glass under dyed (\blacksquare) and bleached (\square) states. The Bode plot curves show that both bleached and dyed EC glasses have impedance values between 10^0 and 10^1 ohms in high-frequency ranges (from 10^2 to 10^6 Hz). Furthermore, they have impedance values between 10^1 and 10^5 ohms in low-frequency ranges (from 10^2 to 10^{-4} Hz). Because the working and counter-electrodes consist of ITO, Pt particles, and WO_3 , and NiO semiconductor films, the electrodes have low impedance. On the other hand, the electrolyte is composed of 1 M LiClO_4 in propylene carbonate, which has high impedance. Therefore, the impedance in high- and low- frequency ranges is represented by the electrodes and electrolyte characterizations in the Bode plot. The Nyquist plots also show that the EC glass had higher impedance in a bleached state than in a dyed state in wide frequency ranges, as shown in Figure 6(b), and in high- frequency ranges, as shown in Figure 6(c).

An EC glass circuit, shown in Figure 7(a), was constructed based on the EC glass structure. In this circuit, the ohmic impedance includes ITO resistance (R_{01} , R_{03}) and transport wire resistance (R_{02}). The working parts

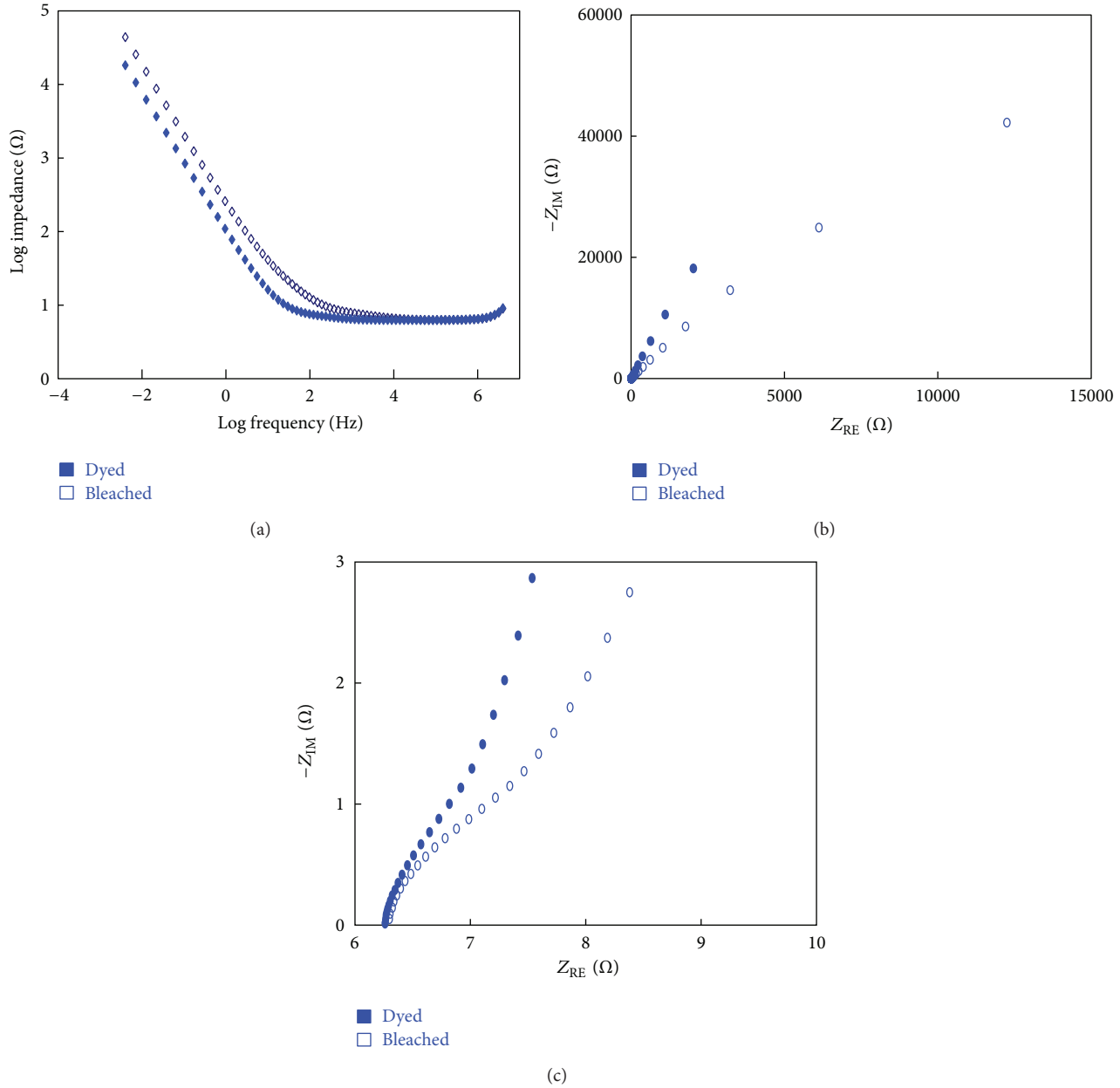
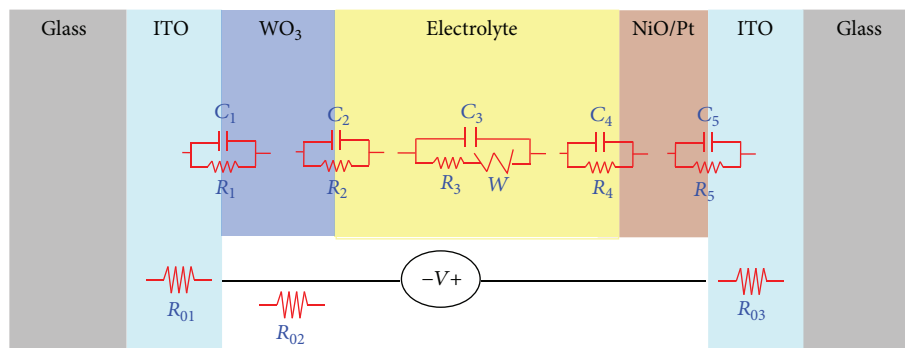


FIGURE 6: AC impedance curves of porous WO_3 electrode from electrochromic glass under dyed (■) and bleached (□) states: (a) bode plot, (b) Nyquist plot, and (c) Nyquist plot in a high-frequency range.

of the ITO/ WO_3 and WO_3 /electrolyte interfaces are presented as $C_1//R_1$ and $C_2//R_2$. The electrolyte is presented as $C_3/(R_3 + W)$. The counterparts of the NiO/electrolyte and ITO/NiO interfaces are presented as $C_4//R_4$ and $C_5//R_5$. The equilibrium circuit, including a series circuit of working electrode, electrolyte, and counter electrode are shown in Figure 7(b). In order to present semicircles and simplify the mathematical operations analysis in each working, electrolyte, and counterpart, the equivalent circuit is portrayed separately in Figure 7(c). Figure 8 shows the experimental (O) and fitted (—) data for the EG glass impedance under (a) dyed and (b) bleached conditions; the inset figures are the Nyquist plots in high-frequency ranges. Figure 9 shows

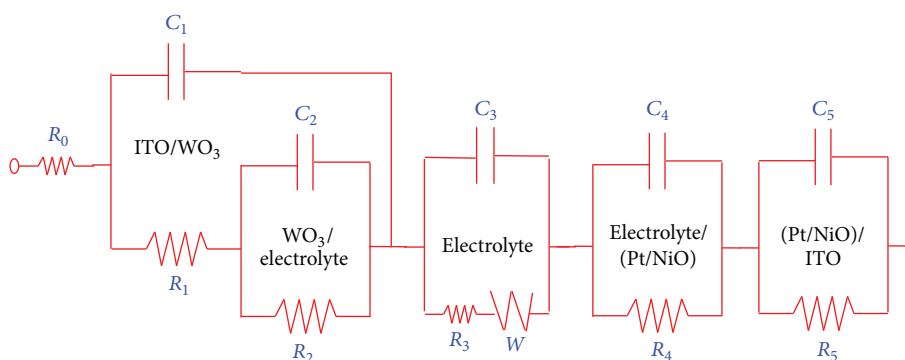
the equilibrium circuit and simulation plot of EG glass (a) working ($C_1//R_1 + (C_2//R_2)$), (b) electrolyte ($C_3/(R_3 + W)$), (c) electrolyte/counter ($C_4//R_4$), and (d) counter ($C_4//R_4$) impedances in the bleached state. Also, (e), (f), (g), and (h) show the EG glass impedances in the dyed state. The detail equilibrium circuits and mathematical results were in Table 1 and the appendix.

Based on the equilibrium circuit model in Figure 7, the EIS data in Figure 8, and the speared circuit model in Figure 9, the fitted results are in Table 2. The ohmic resistance (R_0) is independent of dyed/bleached states. The values of R_0 (6.25 to 6.29 Ω) can be observed at the start point on the Nyquist plot. The resistance between ITO and WO_3 is called the contact



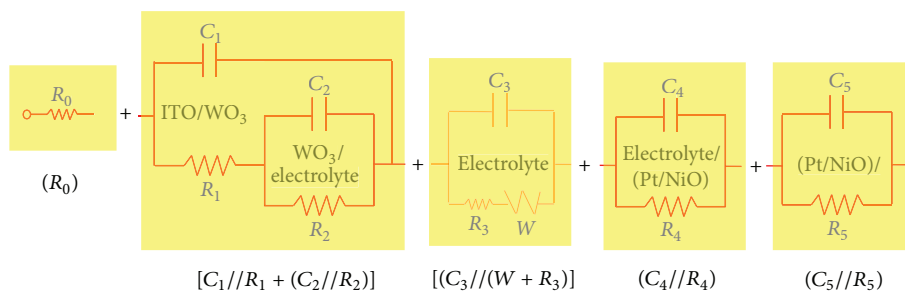
$$R_0 = R_{01} + R_{02} + R_{03}$$

(a)



$$(R_0) + \{C_1 // [R_1 + (C_2 // R_2)]\} + [C_3 // (R_3 + W)] + (C_4 // R_4) + (C_5 // R_5)$$

(b)



$$[C_1 // R_1 + (C_2 // R_2)]$$

$$[(C_3 // (W + R_3))]$$

$$(C_4 // R_4)$$

$$(C_5 // R_5)$$

(c)

FIGURE 7: Schematic diagram of (a) porous WO_3 EC glass structure that can be simulated by using resistor, capacitor, and Warburg impedance. Each interface of ITO/ WO_3 , WO_3 /electrolyte, electrolyte/NiO, and NiO/ITO can be simulated using a RC parallel circuit, and bulk material such as ITO and conducting wire can be simulated by a series of resistors. (b) and (c) Equivalent circuit used for modeling the EIS of EC glass. The impedance of the bulk matter is simulated by $R_0 = R_{01} + R_{02} + R_{03}$, the impedance of working electrode is simulated by $(C_1 // R_1 + (C_2 // R_2))$, the electrolyte is simulated by $C_3 // (R_3 + W)$, and the counter electrode is simulated by $(C_4 // R_4) + (C_5 // R_5)$.

resistance (R_1). Lower R_1 (1.2 and 1.1 Ω) was observed in the presence of a good contact between the ITO and WO_3 . The other resistances—electron transfer resistance (R_2), diffusion resistance (R_3), charge-transfer resistance (R_4), and contact resistance (R_5)—reflect the working, electrolyte, and

counter resistances. When the EC glass is dyed, the Li^+ and H^+ ions dope to WO_3 film and the concentrations of Li^+ and H^+ ions in the electrolyte are reduced. Therefore, the electrodes/electrolyte and bulk electrolyte interfaces of R_2 , R_4 , and R_3 have higher resistances in the dyed (0.65, 1.7, and

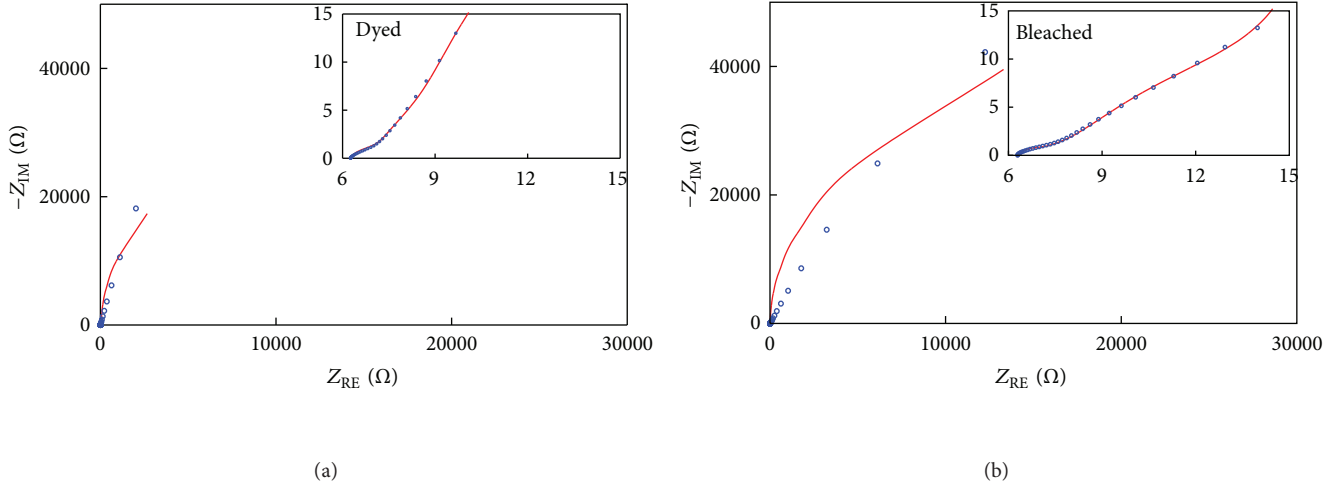


FIGURE 8: Experimental (O) and fitted (—) data for EC glass under (a) dyed and (b) bleached states; inset figures are Nyquist plots in high frequency ranges.

120000 Ω) than in the bleached (0.5, 1.0, and 110000 Ω) state. In contrast, when Li^+ ions move back to the electrolyte and dope to NiO film, R_5 has higher resistance in bleached (45 Ω) than in dyed (7 Ω) states.

The capacitance reflects the characteristic of charge quantity on matter interface. Since a resistance and capacitor parallel (R/C) circuit can present a semicircle on a Nyquist plot, expressed mathematically, the imaginary value is $[\omega R^2 C / (1 + (\omega RC)^2)]$, where ω is angular frequency, R is resistance, and C is capacitor. When $1 + (\omega RC)^2$ tends to zero, the imaginary has a larger value; therefore the highest point on the semicircle can be evaluated as $\omega = 1/RC$. There are clear semicircles of electrolysis impedance shown in the simulation results in Figure 9, except in Figures 9(b) and 9(c). Because the resistances refer to the length of the diameter of the semicircle, the electrolysis capacitances can be calculated by $C = 1/\omega_{\text{peak}} R$, where ω_{peak} is the angular frequency at the top of the semicircle.

The contact capacitance (C_1) reflects the charge transfer between the ITO and WO_3 interface. Charges (Li^+) transferring from WO_3 to ITO in EC glass have a higher C_1 in the colored (350 μF) than that in the bleached (80 μF) state. The chemical capacitance (C_2) reflects the charges in the WO_3 and electrolyte interface. EC glass has a lower C_2 in the colored (900 μF) than in the bleached (420 μF) state. When EC glass is bleached, most of the charges move back to the bulk electrolyte and there is a greater quantity of charges on the WO_3 /electrolyte interface than that in the colored state. Because the electrolyte (1 M $\text{LiClO}_4 + \text{PC}$) used in the EC glass has low conductivity, a Warburg impedance characteristic can be observed in Nyquist plot. A Warburg impedance element can be used to model semi-infinite linear diffusion. The equilibrium circuit of a low conductivity electrolyte includes a capacitor (C_3) series to parallel elements (R_3/W) where W is Warburg impedance ($2\sigma^2/j\omega$; σ is Warburg constant). The electrolyte capacitance (C_3) reflects the capacitance effect in electrolyte. Because charges move back to the electrolyte, the

EC glass has a lower C_3 in the colored (1200 μF) than in the bleached (3000 μF) state.

The double-layer capacitance (C_4) reflects the electrolyte/counter interface and also reflects the surface area of Pt on the NiO. It is expected that Pt sputter deposition on the counter electrode increases the surface area of the counter and, consequently, promotes the separated LiClO_4 into Li^+ and ClO_4^- . Because ClO_4^- moves to the counter surface in the colored state, the EC glass has a higher C_4 in the colored (3800 μF) than in the bleached (1500 μF) state. The contact capacitance (C_5) reflects charge transfer at the ITO and NiO interface. Because charges (ClO_4^-) transfer from NiO to ITO, the EC glass has a higher C_5 in the colored (2800 μF) than in the bleached (1100 μF) state.

The impedance spectra of the porous WO_3 EC glass showed internal resistance consisting of at least thirteen components. It was found that the resistances of the ITO (R_{01} and R_{03}) and the transport wire (R_{02}) appeared as ohmic impedance. The ohmic impedance value was not affected by colored/bleached states. The other resistances—electron transfer resistance (R_1 , R_2 , and R_5), diffusion resistance (R_3), and charge-transfer resistance (R_4)—as the internal resistances were affected by colored/bleached states that are determinative in the performance of EC glass. The interface capacitances of contact capacitance (C_1 and C_5), chemical capacitance (C_2), electrolysis capacitance (C_3), and double-layer capacitance (C_4) are determinative in the performance of charges on the interfaces.

4. Conclusions

A 144 cm^2 electrochromic device was fabricated using ITOs, NiO, porous WO_3 film, and Pt particles. The characteristics of the EC glass were determined using UV-VIS-NIR, CV, and EIS equipments. The average transmittance in the colored and bleached states was 15.7% and 60.2%, respectively. The repeatability of the colored/bleached cycles over 1000 cyclic voltammograms tests was good. In EIS analysis, the

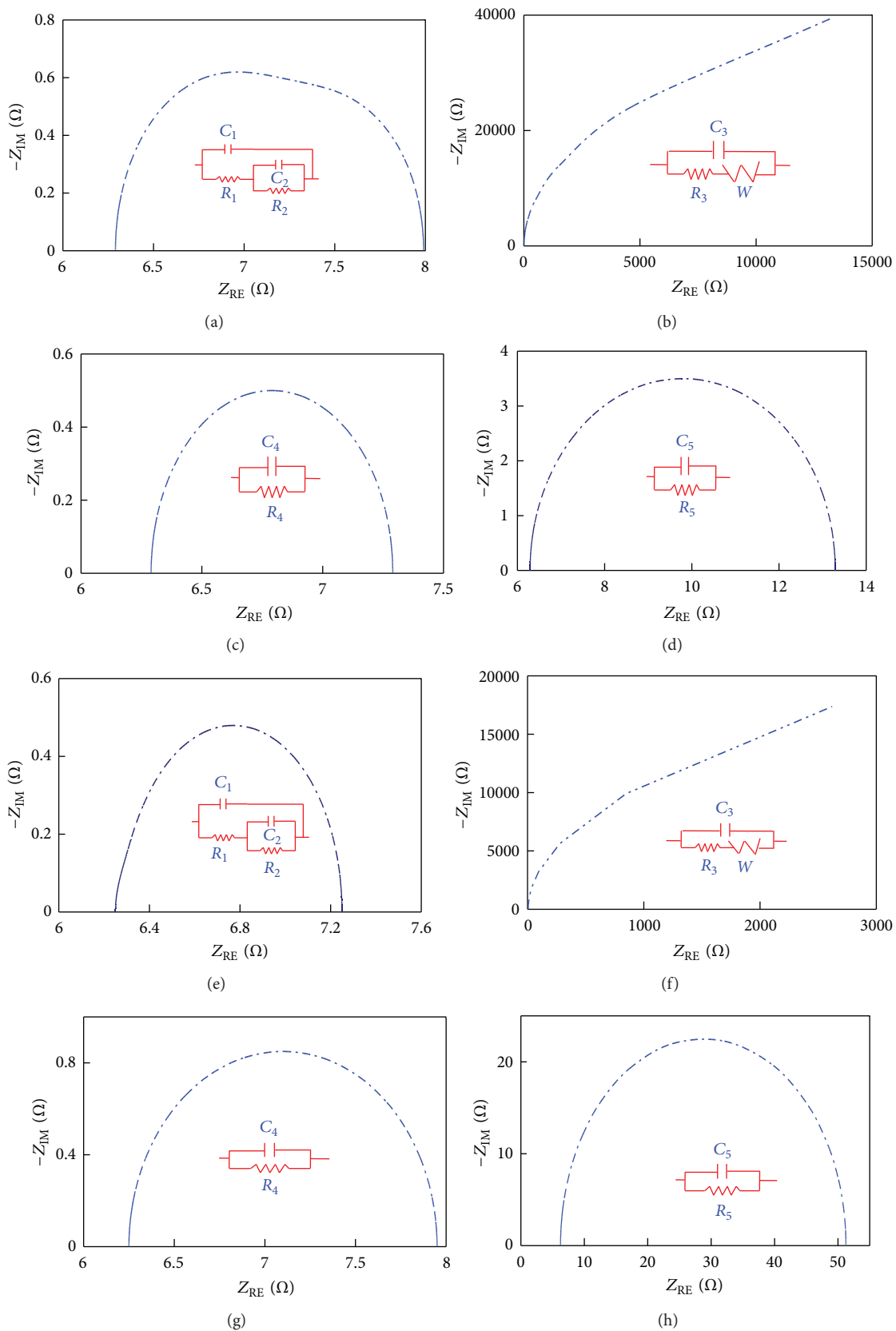


FIGURE 9: Nyquist plots and simulated circuits in EC glass of working electrode (a, e), electrolyte (b, f), and counter electrode (c, d, g, h) under dyed (a, b, c, d) and bleached (e, f, g, h) states.

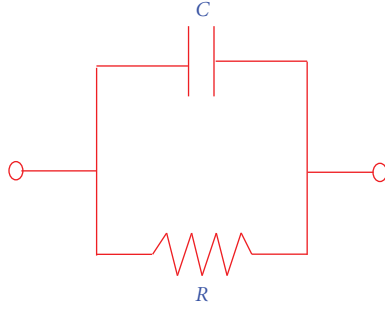


FIGURE 10

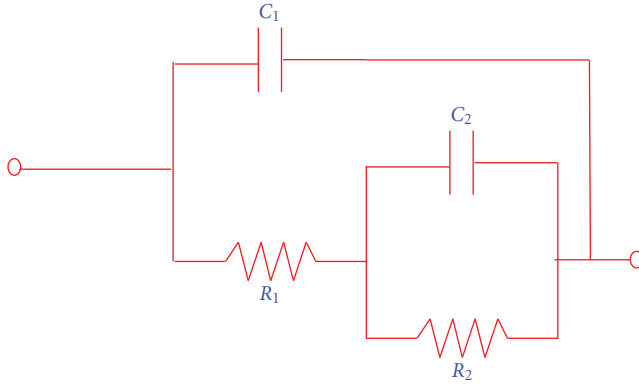


FIGURE 11

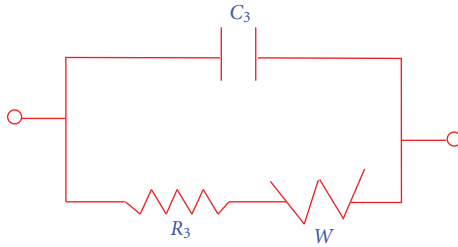


FIGURE 12

ohmic impedance (R_0) value was about 6.3Ω . The other resistances—electrodes/electrolyte and electrolyte interfaces (R_2 , R_4 , and R_3)—have higher resistances in colored (Li^+ ions move to WO_3) than in bleached (Li^+ ions move back to electrolyte and NiO) states. In contrast, R_5 has higher resistance in the bleached than in the dyed state. The contact capacitance (C_1 and C_5), electrolysis capacitance (C_3), and double-layer capacitance (C_4) all have higher values in the colored than in the bleached state, but the chemical capacitance (C_2) is the opposite.

We have shown that anodic WO_3 can be used as electrochromic film in EC glass. The fabrication process can be extended to TiO_2 and Ta_2O_5 , which are electrochromic and solid charge conductive films. A detailed study of porous films used for EC glass using anodization will be described in a future paper.

Appendix

(1) $(C//R)$. See also Figure 10

$$\begin{aligned} \frac{Z_C R}{Z_C + R} &= \frac{R/j\omega C}{(1/j\omega C) + R} \\ &= \frac{R}{1 + j\omega RC} = \frac{R(1 - j\omega RC)}{1 + (\omega RC)^2} \\ &= \frac{R}{1 + (\omega RC)^2} + j \frac{-\omega R^2 C}{1 + (\omega RC)^2} \end{aligned} \quad (\text{A.1})$$

$$Z_{\text{RE}} = \frac{R}{1 + (\omega RC)^2}$$

$$Z_{\text{IM}} = \frac{-\omega R^2 C}{1 + (\omega RC)^2}.$$

(2) $\{C_1/[R_1 + (C_2//R_2)]\}$. See also Figure 11

$$\begin{aligned} &\left(\frac{Z_1 Z_2 R_2 + Z_1 R_1 Z_2 + Z_1 R_1 R_2}{Z_2 + R_2} \right) \\ &\times \left(\frac{Z_2 R_2 + R_1 Z_2 + R_1 R_2 + Z_1 Z_2 + Z_1 R_2}{Z_2 + R_2} \right)^{-1} \\ &= \left(\frac{R_2}{j^2 \omega^2 C_1 C_2} + \frac{R_1}{j^2 \omega^2 C_1 C_2} + \frac{R_1 R_2}{j \omega C_1} \right) \\ &\times \left(\frac{R_2}{j \omega C_2} + \frac{R_1}{j \omega C_2} + R_1 R_2 \right. \\ &\quad \left. + \frac{1}{j^2 \omega^2 C_1 C_2} + \frac{R_2}{j \omega C_1} \right)^{-1} \\ &= \left(\frac{R_2 + R_1 + j \omega C_2 R_1 R_2}{j^2 \omega^2 C_1 C_2} \right) \\ &\times \left((j \omega C_1 R_2 + j \omega C_1 R_1 + j^2 \omega^2 C_1 C_2 R_1 R_2 + 1 \right. \\ &\quad \left. + j \omega C_2 R_2) \times (j^2 \omega^2 C_1 C_2)^{-1} \right)^{-1} \\ &= (R_2 + R_1 + j \omega C_2 R_1 R_2) \\ &\times \left((1 - \omega^2 C_1 C_2 R_1 R_2) \right. \\ &\quad \left. + j(\omega C_2 R_2 + \omega C_1 R_2 + \omega C_1 R_1) \right)^{-1} \\ &= ((R_2 + R_1 + j \omega C_2 R_1 R_2) \\ &\quad \times [(1 - \omega^2 C_1 C_2 R_1 R_2) \\ &\quad - j(\omega C_2 R_2 + \omega C_1 R_2 + \omega C_1 R_1)]) \\ &\times \left((1 - \omega^2 C_1 C_2 R_1 R_2)^2 \right. \\ &\quad \left. + (\omega C_2 R_2 + \omega C_1 R_2 + \omega C_1 R_1)^2 \right)^{-1} \end{aligned}$$

$$\begin{aligned}
&= \left([(R_2 + R_1) + (j\omega C_2 R_1 R_2)] \right. \\
&\quad \times \left[(1 - \omega^2 C_1 C_2 R_1 R_2) \right. \\
&\quad \left. \left. - j(\omega C_2 R_2 + \omega C_1 R_2 + \omega C_1 R_1) \right] \right) \\
&\quad \times \left((1 - \omega^2 C_1 C_2 R_1 R_2)^2 \right. \\
&\quad \left. + (\omega C_2 R_2 + \omega C_1 R_2 + \omega C_1 R_1)^2 \right)^{-1} \\
&= \left([(R_2 + R_1) \times (1 - \omega^2 C_1 C_2 R_1 R_2) \right. \\
&\quad \left. + (\omega C_2 R_1 R_2) \times (\omega C_2 R_2 + \omega C_1 R_2 + \omega C_1 R_1)] \right) \\
&\quad \times \left((1 - \omega^2 C_1 C_2 R_1 R_2)^2 \right. \\
&\quad \left. + (\omega C_2 R_2 + \omega C_1 R_2 + \omega C_1 R_1)^2 \right)^{-1} \\
&\quad + (j[-(R_2 + R_1) \times (\omega C_2 R_2 + \omega C_1 R_2 + \omega C_1 R_1) \\
&\quad + (\omega C_2 R_1 R_2) \times (1 - \omega^2 C_1 C_2 R_1 R_2)]) \\
&\quad \times \left((1 - \omega^2 C_1 C_2 R_1 R_2)^2 \right. \\
&\quad \left. + (\omega C_2 R_2 + \omega C_1 R_2 + \omega C_1 R_1)^2 \right)^{-1} \\
Z_{RE} &= \left([(R_2 + R_1) \times (1 - \omega^2 C_1 C_2 R_1 R_2) + (\omega C_2 R_1 R_2) \right. \\
&\quad \times (\omega C_2 R_2 + \omega C_1 R_2 + \omega C_1 R_1)] \\
&\quad \times \left((1 - \omega^2 C_1 C_2 R_1 R_2)^2 \right. \\
&\quad \left. + (\omega C_2 R_2 + \omega C_1 R_2 + \omega C_1 R_1)^2 \right)^{-1} \\
Z_{IM} &= \left([(\omega C_2 R_1 R_2) \times (1 - \omega^2 C_1 C_2 R_1 R_2) \right. \\
&\quad \left. - (R_2 + R_1) \times (\omega C_2 R_2 + \omega C_1 R_2 + \omega C_1 R_1)] \right) \\
&\quad \times \left((1 - \omega^2 C_1 C_2 R_1 R_2)^2 \right. \\
&\quad \left. + (\omega C_2 R_2 + \omega C_1 R_2 + \omega C_1 R_1)^2 \right)^{-1}.
\end{aligned} \tag{A.2}$$

(3) $[C_3/(W + R_3)]$. See also Figure 12

$$\begin{aligned}
&\left(\frac{1}{j\omega C_3} \times \left(R_3 + \frac{2\sigma^2}{j\omega} \right) \right) \\
&\quad \times \left(\frac{1}{j\omega C_3} + \left(R_3 + \frac{2\sigma^2}{j\omega} \right) \right)^{-1} \\
&= \left(\frac{1}{j\omega C_3} \times \frac{j\omega R_3 + 2\sigma^2}{j\omega} \right)
\end{aligned}$$

$$\begin{aligned}
&\times \left(\frac{1}{j\omega C_3} + \frac{j\omega R_3 + 2\sigma^2}{j\omega} \right)^{-1} \\
&= \left(\frac{j\omega R_3 + 2\sigma^2}{\omega^2 C_3} \right) \\
&\quad \times \left(\frac{j\omega - \omega^2 C_3 R_3 + 2j\omega C_3 \sigma^2}{\omega^2 C_3} \right)^{-1} \\
&= -((j\omega R_3 + 2\sigma^2) \times [\omega^2 C_3 R_3 + j(\omega + 2\omega C_3 \sigma^2)]) \\
&\quad \times ([\omega^2 C_3 R_3 - j(\omega + 2\omega C_3 \sigma^2)] \\
&\quad \times [\omega^2 C_3 R_3 + j(\omega + 2\omega C_3 \sigma^2)])^{-1} \\
&= -(j\omega^3 R_3^2 C_3 - \omega^2 R_3 + j2\omega^2 R_3 C_3 \sigma^2 \\
&\quad + 2\sigma^2 \omega^2 C_3 R_3 + j2\omega \sigma^2 + j4\omega C_3 \sigma^4) \\
&\quad \times (\omega^4 C_3^2 R_3^2 + \omega^2 + 4\omega^2 C_3^2 \sigma^4 + 4\omega^2 C_3 \sigma^2)^{-1} \\
Z_{RE} &= \frac{\omega^2 R_3 - 2\sigma^2 \omega^2 C_3 R_3}{\omega^4 C_3^2 R_3^2 + \omega^2 + 4\omega^2 C_3^2 \sigma^4 + 4\omega^2 C_3 \sigma^2} \\
Z_{IM} &= -\frac{\omega^3 R_3^2 C_3 + 2\omega^2 R_3 C_3 \sigma^2 + 2\omega \sigma^2 + 4\omega C_3 \sigma^4}{\omega^4 C_3^2 R_3^2 + \omega^2 + 4\omega^2 C_3^2 \sigma^4 + 4\omega^2 C_3 \sigma^2}.
\end{aligned} \tag{A.3}$$

Acknowledgment

The authors gratefully appreciate the financial support of the National Science Council of ROC under the contract no. (101-2627-M-239-001-).

References

- [1] Y. Djaoued, S. Balaji, and R. Brünig, "Electrochromic devices based on porous tungsten oxide thin films," *Journal of Nanomaterials*, vol. 2012, Article ID 674168, 9 pages, 2012.
- [2] N. N. Dinh, D. H. Ninh, T. T. Thao, and T. V. Van, "Mixed nanostructured Ti-W oxides films for efficient electrochromic windows," *Journal of Nanomaterials*, vol. 2012, Article ID 781236, 7 pages, 2012.
- [3] G. B. Smith, S. Dligatch, R. Sullivan, and M. G. Hutchins, "Thin film angular selective glazing," *Solar Energy*, vol. 62, no. 3, pp. 229–244, 1998.
- [4] J. Mohelnikova, "Materials for reflective coatings of window glass applications," *Construction and Building Materials*, vol. 23, no. 5, pp. 1993–1998, 2009.
- [5] NREL, <http://www.nrel.gov/>.
- [6] X. Sun, Z. Liu, and H. Cao, "Effects of film density on electrochromic tungsten oxide thin films deposited by reactive dc-pulsed magnetron sputtering," *Journal of Alloys and Compounds*, vol. 504, no. 1, pp. S418–S421, 2010.
- [7] P. M. Kadam, N. L. Tarwal, P. S. Shinde et al., "Enhanced optical modulation due to SPR in gold nanoparticles embedded WO₃ thin films," *Journal of Alloys and Compounds*, vol. 509, no. 5, pp. 1729–1733, 2011.

- [8] C. M. Lampert, "Heat mirror coatings for energy conserving windows," *Solar Energy Materials*, vol. 6, no. 1, pp. 1–41, 1981.
- [9] R. E. Collins and T. M. Simko, "Current status of the science and technology of vacuum glazing," *Solar Energy*, vol. 62, no. 3, pp. 189–213, 1998.
- [10] T. S. Eriksson, C. G. Granqvist, and J. Karlsson, "Transparent thermal insulation with infrared-absorbing gases," *Solar Energy Materials*, vol. 16, no. 1–3, pp. 243–253, 1987.
- [11] H. Byker, in *Proceedings of the Symposium on Electrochromic Materials II*, K. C. Ho and D. A. MacArthur, Eds., vol. PV 94-2 of *Electrochemical Society Proceeding Series*, Pennington, NJ, USA, 1994.
- [12] S. Supothina, P. Seeharaj, S. Yoriya, and M. Sriyudthsak, "Synthesis of tungsten oxide nanoparticles by acid precipitation method," *Ceramics International*, vol. 33, no. 6, pp. 931–936, 2007.
- [13] P. R. Somani and S. Radhakrishnan, "Electrochromic materials and devices: present and future," *Materials Chemistry and Physics*, vol. 77, no. 1, pp. 117–133, 2003.
- [14] J. Nagai, G. D. McMeeking, and Y. Saitoh, "Durability of electrochromic glazing," *Solar Energy Materials and Solar Cells*, vol. 56, no. 3–4, pp. 309–319, 1999.
- [15] R. Reisfeld, M. Zayat, H. Minti, and A. Zastrow, "Electrochromic glasses prepared by the sol-gel method," *Solar Energy Materials and Solar Cells*, vol. 54, no. 1–4, pp. 109–120, 1998.
- [16] Y. Fang and P. C. Eames, "The effect of glass coating emittance and frame rebate on heat transfer through vacuum and electrochromic vacuum glazed windows," *Solar Energy Materials and Solar Cells*, vol. 90, no. 16, pp. 2683–2695, 2006.
- [17] Y. C. Nah, A. Ghicov, D. Kim, S. Berger, and P. Schmuki, "TiO₂-WO₃ composite nanotubes by alloy anodization: growth and enhanced electrochromic properties," *Journal of the American Chemical Society*, vol. 130, no. 48, pp. 16154–16155, 2008.
- [18] A. B. Powell, C. W. Bielawski, and A. H. Cowley, "Design, synthesis, and study of main chain poly(N-heterocyclic carbene) complexes: applications in electrochromic devices," *Journal of the American Chemical Society*, vol. 132, no. 29, pp. 10184–10194, 2010.
- [19] M. S. Burdis and D. G. Weir, Sage Electrochromics, Electrochromic devices and methods, Patent US 2006/0209383A1, 2006.
- [20] S. S. Kalagi, D. S. Dalavi, R. C. Pawar, N. L. Tarwal, S. S. Mali, and P. S. Patil, "Polymer assisted deposition of electrochromic tungsten oxide thin films," *Journal of Alloys and Compounds*, vol. 493, no. 1–2, pp. 335–339, 2010.
- [21] C. Santato, M. Odziemkowski, M. Ulmann, and J. Augustynski, "Crystallographically oriented mesoporous WO₃ films: synthesis, characterization, and applications," *Journal of the American Chemical Society*, vol. 123, no. 43, pp. 10639–10649, 2001.
- [22] C. Cai, D. Guan, and Y. Wang, "Solution processing of V₂O₅-WO₃ composite films for enhanced Li-ion intercalation properties," *Journal of Alloys and Compounds*, vol. 509, no. 3, pp. 909–915, 2010.
- [23] V. Karastoyanov and M. Bojinov, "Anodic oxidation of tungsten in sulphuric acid solution-Influence of hydrofluoric acid addition," *Materials Chemistry and Physics*, vol. 112, no. 2, pp. 702–710, 2008.
- [24] G. Kron, T. Egerter, J. H. Werner, and U. Rau, "Electronic transport in dye-sensitized nanoporous TiO₂ solar cells-Comparison of electrolyte and solid-state devices," *Journal of Physical Chemistry B*, vol. 107, no. 15, pp. 3556–3564, 2003.
- [25] K. Schwarzburg and F. Willig, "Diffusion impedance and space charge capacitance in the nanoporous dye-sensitized electrochemical solar cell," *Journal of Physical Chemistry B*, vol. 107, no. 15, pp. 3552–3555, 2003.
- [26] G. He, L. Zhao, Z. Zheng, and F. Lu, "Determination of electron diffusion coefficient and lifetime in dye-sensitized solar cells by electrochemical impedance spectroscopy at high fermi level conditions," *Journal of Physical Chemistry C*, vol. 112, no. 48, pp. 18730–18733, 2008.
- [27] C. C. Chen, D. Fang, and Z. Luo, "Fabrication and characterization of highly-ordered valve-metal oxide nanotubes and their derivative nanostructures: a review," *Reviews in Nanoscience and Nanotechnology*, vol. 1, no. 4, pp. 229–256, 2012.
- [28] S. R. Biaggio, R. C. Rocha-Filho, J. R. Vilche, F. E. Varela, and L. M. Gassa, "A study of thin anodic WO₃ films by electrochemical impedance spectroscopy," *Electrochimica Acta*, vol. 42, no. 11, pp. 1751–1758, 1997.
- [29] J. J. Kim, D. A. Tryk, T. Amemiya, K. Hashimoto, and A. Fujishima, "Color impedance and electrochemical impedance studies of WO₃ thin films: behavior of thinner films in non-aqueous electrolyte," *Journal of Electroanalytical Chemistry*, vol. 433, no. 1–2, pp. 9–17, 1997.
- [30] L. Andrade, S. M. Zakeeruddin, M. K. Nazeeruddin, H. A. Ribeiro, A. Mendes, and M. Gratzel, "Influence of sodium cations of N3 dye on the photovoltaic performance and stability of dye-sensitized solar cells," *ChemPhysChem*, vol. 10, no. 7, pp. 1117–1124, 2009.
- [31] J. Bisquert, M. Grätzel, Q. Wang, and F. Fabregat-Santiago, "Three-channel transmission line impedance model for mesoscopic oxide electrodes functionalized with a conductive coating," *Journal of Physical Chemistry B*, vol. 110, no. 23, pp. 11284–11290, 2006.
- [32] G. Franco, J. Gehring, L. M. Peter, E. A. Ponomarev, and I. Uhlenndorf, "Frequency-resolved optical detection of photojected electrons in dye-sensitized nanocrystalline photovoltaic cells," *Journal of Physical Chemistry B*, vol. 103, no. 4, pp. 692–698, 1999.
- [33] F. Fabregat-Santiago, E. M. Barea, J. Bisquert, G. K. Mor, K. Shankar, and C. A. Grimes, "High carrier density and capacitance in TiO₂ nanotube arrays induced by electrochemical doping," *Journal of the American Chemical Society*, vol. 130, no. 34, pp. 11312–11316, 2008.
- [34] R. Kern, R. Sastrawan, J. Ferber, R. Stangl, and J. Luther, "Modeling and interpretation of electrical impedance spectra of dye solar cells operated under open-circuit conditions," *Electrochimica Acta*, vol. 47, no. 26, pp. 4213–4225, 2002.
- [35] T. Hoshikawa, M. Yamada, R. Kikuchi, and K. Eguchi, "Impedance analysis of internal resistance affecting the photoelectrochemical performance of dye-sensitized solar cells," *Journal of the Electrochemical Society*, vol. 152, no. 2, pp. E68–E73, 2005.
- [36] A. Labidi, C. Jacolin, M. Bendahan et al., "Impedance spectroscopy on WO₃ gas sensor," *Sensors and Actuators B*, vol. 106, no. 2, pp. 713–718, 2005.
- [37] M. Pourbaix, *Atlas of Electrochemical Equilibria in Aqueous Solutions*, vol. 282, National Association of Corrosion Engineers, Houston, Tex, USA, 1974.

Research Article

Facile Synthesis of Fe-Doped Titanate Nanotubes with Enhanced Photocatalytic Activity for Castor Oil Oxidation

Guozhu Fu, Gang Wei, Yanqiu Yang, WeiCheng Xiang, and Ning Qiao

State Key Laboratory of Chemical Resource Engineering, Beijing University of Chemical Technology, Beijing 100029, China

Correspondence should be addressed to Ning Qiao; qiaoning@mail.buct.edu.cn

Received 13 December 2012; Accepted 31 December 2012

Academic Editor: Shao-Wen Cao

Copyright © 2013 Guozhu Fu et al. This is an open access article distributed under the Creative Commons Attribution License, which permits unrestricted use, distribution, and reproduction in any medium, provided the original work is properly cited.

Iron-doped titanate nanotubes were synthesized by hydrothermal method, and the photocatalytic activity was greatly enhanced by iron doping.

Followed by the discovery of carbon nanotubes, synthesis of one-dimensional (1D) nanomaterials has attracted great interest because of their exceptional electrical and mechanical properties [1–4]. Some inorganic 1D nanomaterials including ZnO, VO_x , and TiO_2 have been synthesized in recent years [5–8]. Among these materials, titanic compound nanotubes have stimulated particular interest. Titanic nanocrystals have been extensively studied in photocatalytic or photoelectrochemical systems and so forth [9–12], and fabrication of tubular structures offers an effective approach to adjust their properties, which are crucial in practical applications. For example, the photocatalytic activity of TiO_2 could be enhanced by the tubular structures because of their large specific surface, which leads to a higher potential of applications in environmental purification and generation of hydrogen gas and so forth [13].

Recently, particular interest is devoted to obtain $\text{H}_2\text{Ti}_3\text{O}_7$ -type nanotubes synthesized by hydrothermal method [14–16], and these nanotubes show excellent ion-exchange ability and photocatalytic activities and may be applied to photocatalysis, photoluminescence, and dye-sensitized solar cells [3]. However, their structures are still not well understood. The photocatalytic property is originated from the charge carriers produced by the excitation process on the particle surface, and the photocatalytic efficiency is determined by the transfer rate and recombination rate of carriers [17]. However, the carriers are usually unstable and easy to recombine. To improve the photocatalytic efficiency, the transfer rate must be enhanced and recombination rate

should be reduced. Introducing other elements especially the transition metal ions into the matrix has been proved to be an effective method to improve the photocatalytic efficiency, and many reports on the doped TiO_2 and their properties have been published [17–19]. More recently, followed by the development of researches on one-dimensional materials, fabrication of doped nanorods and nanowires with transition metal ions has stimulated much interest due to their exclusive properties and potential applications [20–22]. However, doped tubelike nanostructures have never been reported. Since the tube channel has potential advantage to provide direct conduction paths for the electrons [23], it is reasonable to believe that doped tubelike structures will induce some excellent properties for their applications.

In this communication we reported that the Fe-doped titanated nanotubes (TiNTs) can be easily synthesized via a hydrothermal process. Commercial anatase TiO_2 powders (2 g) and $\text{FeCl}_2 \cdot 4\text{H}_2\text{O}$ (0.05 g, 0.15 g, and 0.25 g) were dispersed into an aqueous solution of NaOH (10 mol dm^{-3}) and then moved into a Teflon-lined autoclave. The autoclave was heated in an oven at 130°C for 72 h. The precipitate was filtrated and washed with diluted HCl until $\text{pH} = 7$. Final products were obtained by air-drying.

The structure analysis of obtained products was investigated by an X-ray diffraction (Philips X'Pert PRO MPD) operated at 40 kV and 30 mA using Cu $K\alpha$ radiation through the 2θ -range from 5 to 70 degrees. The typical XRD pattern of products with various levels of iron doping is presented in Figure 1. In all cases, several weak and broad diffraction

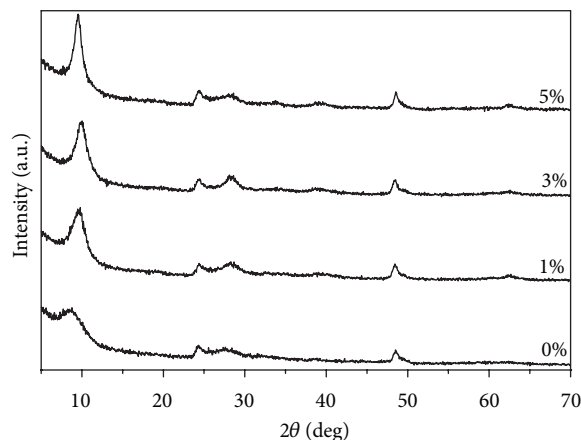


FIGURE 1: XRD pattern of synthesized sample.

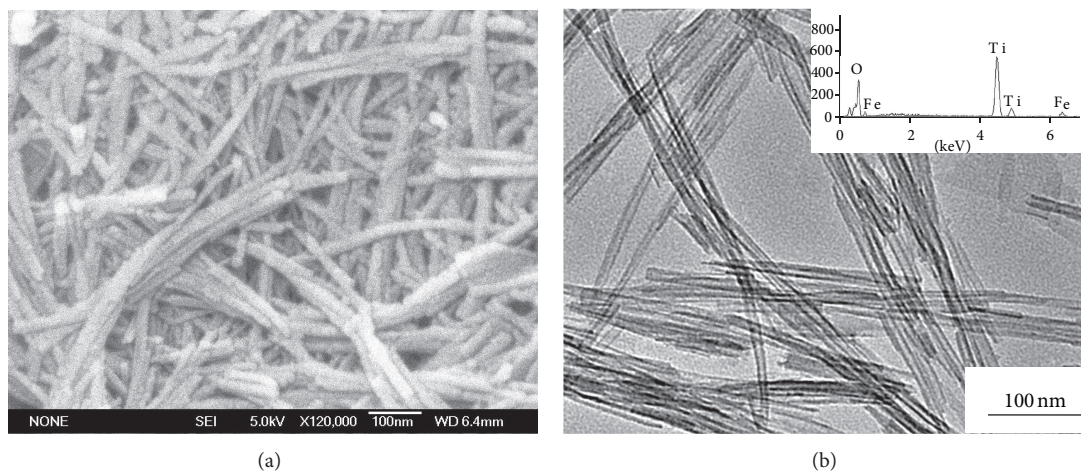


FIGURE 2: (a) SEM and (b) TEM images of synthesized products.

peaks exist (positioned at $2\theta = 9.9, 24, 28$, and 48°), which could be assigned to the diffraction peaks of titanates such as $\text{H}_2\text{Ti}_3\text{O}_7$ structure (monoclinic unit cell with $a = 1.603$, $b = 0.375$, $c = 0.919$ nm, and $\beta = 101.45^\circ$) [13]. No crystalline anatase TiO_2 or ferric oxide was detected in the pattern. In addition, the height of diffraction peaks is increased by the iron doping, which illustrates that the iron doping gives rise to the increase of the crystallization. Wang et al. [17] have reported that iron doping promotes the formation of rutile phase in TiO_2 particles, while the influence of iron on the crystallization of titanate has never been reported.

Morphology of synthesized products was characterized by both field-emission scanning electron microscope (SEM, JSM-6700F) and transmission electron microscope (TEM, Hitachi H-800). Figure 2 gives the typical images of titanates with $R_{\text{Fe/Ti}} = 3\%$. From the SEM micrograph shown in Figure 2(a) we can see that needle-shaped products with uniform morphology are obtained. The typical diameter and length are about 20 and 300 nm, respectively, and no particles or layered structures were observed from the image. The

TEM image shown in Figure 2(b) reveals the nanotubular structures of synthesized products. A large quantities of tubular nanoparticles with uniform diameter about 20 nm were synthesized, and the length of obtained particles is about several hundred nanometers.

The energy dispersive X-ray spectroscopy (EDX) analysis recorded from the synthesized nanotubes illustrates that the characteristic peaks of Fe, Ti, and O were detected, indicating that Fe ions were successfully doped into the lattice of titanate.

Raman spectrum of synthesized nanotubes with different iron levels is shown in Figure 3. They are almost identical except for the intensity of peaks. The Raman features of synthesized nanotubes could be roughly regarded as a reflection of the six-coordinated layered titanate although the iron was doped into the titanate [3], but the exact assignment of the Raman spectra to specific active modes in layered titanates is still not well understood. In addition, these peaks are broadened and strengthened with increasing the iron levels, which reflects the split of lattice vibration modes caused by the decrease of symmetry. Raman spectroscopy is widely used

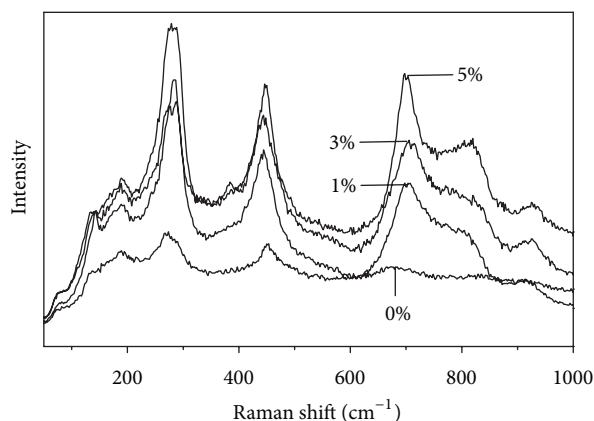


FIGURE 3: Raman spectra of synthesized sample.

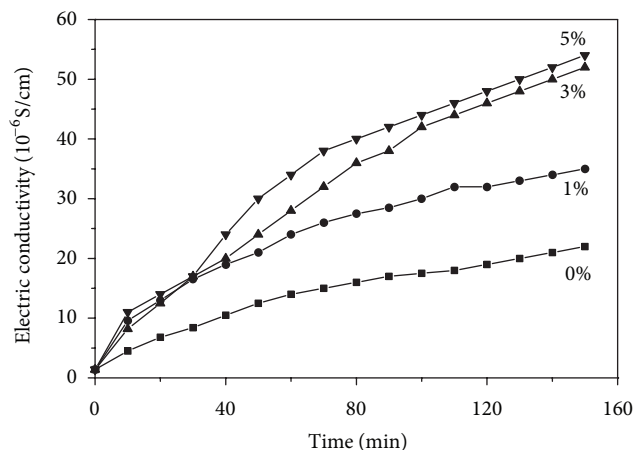


FIGURE 4: Photocatalytic activities of synthesized nanotubes.

to investigate the near-surface defect structure because of its surface sensitiveness, accordingly, the increase of peak height could be attributed to the increase of oxygen vacancies in the titanates. The defects promote charge transfer and efficiently separate the electrons and holes by shallow trapped electrons, which might give rise to remarkable increase of photocatalytic activity.

Photocatalytic activities of synthesized nanotubes were evaluated by the conductometric determination method (CDM) which uses castor oil as probe reactant [24, 25]. It has been confirmed that this method is effective for estimating the catalytic activity of inorganic pigments in oil cosmetics. In the test, 0.2 g of synthesized TiNTs was mixed with 20 mL of castor oil and moved into a quartz tube with UV-light irradiation for 150 min. Air gas was bubbled in and then flowed out and induced into the deionized water placed in an electric conductivity measurement cell. Volatile molecules produced by the oxidation of the castor oil were trapped in the water by the effluent gas leading to the increase of conductivity. The degree of photocatalytic activity was estimated by the extent of conductivity change.

Figure 4 shows the photocatalytic activities of synthesized nanotubes, and we can conclude from the results that the photocatalytic activities are greatly enhanced by the iron doping. The change curve of electric conductivity for undoped TiNTs is very flat while the curve is relatively sharp for the doped ones. After irradiated for 150 min, the electric conductivity for 3% doped TiNTs is 52 $\mu\text{S}/\text{cm}$, which is about 2-fold higher than that of undoped TiNTs. These results obviously indicate that doping with iron ions is very effective in increasing the photocatalytic activity of TiNTs.

The photocatalytic activity originates from the production of excited electron in the conduction band, along with corresponding positive holes in the valence band through the absorption of suitable illumination [17]. By introducing the Fe^{3+} in the matrix, Fe atoms replace the Ti in the crystal lattice, and the oxygen vacancies and defects increase to maintain charge equilibrium. During the process of photocatalytic reaction, oxygen vacancies and defects could become the centers to capture photoinduced electrons so that the recombination of photoinduced electrons and holes was effectively inhibited [26]. Thus, oxygen vacancies and defects were in favor of photocatalytic activity. The oxygen vacancies and defects were increased by the iron doping; consequently, the photocatalytic activity is enhanced by the level of iron doping as shown in Figure 4.

In conclusion, we have firstly reported the synthesis of the iron-doped TiNTs, and this method may be applied to synthesize transition metal ions doped TiNTs and other nanostructures (such as nanobelt). This work provides a facile route to improve the photocatalytic efficiency of materials, and other properties such as magnetic property may also be changed. In addition, existence of Ti-OH on the surface [27] makes the decoration of TiNTs possible, and further assembly may also be achieved. These works are still under research.

Acknowledgment

Financial support from the National High Technology Research and Development Program of China (863 Program) (Grants 2009AA03Z802 and 2009AA03Z803) is gratefully acknowledged.

References

- [1] P. X. Gao, C. S. Lao, Y. Ding, Z. L. Wang, and Z. L., "Metal/semiconductor core/shell nanodisks and nanotubes," *Advanced Functional Materials*, vol. 16, pp. 53–62, 2006.
- [2] P. Hu, F. Yuan, L. Bai, J. Li, and Y. Chen, "Plasma synthesis of large quantities of zinc oxide nanorods," *Journal of Physical Chemistry C*, vol. 111, no. 1, pp. 194–200, 2007.
- [3] P. Hu, L. Y. Bai, L. J. Yu, J. L. Li, F. L. Yuan, and Y. F. Chen, "Shape-controlled synthesis of ZnS nanostructures: a simple and rapid method for one-dimensional materials by plasma," *Nanoscale Research Letters*, vol. 4, pp. 1047–1053, 2009.
- [4] Z. Zhang, C. Shao, P. Zou et al., "In situ assembly of well-dispersed gold nanoparticles on electrospun silica nanotubes for catalytic reduction of 4-nitrophenol," *Chemical Communications*, vol. 47, no. 13, pp. 3906–3908, 2011.

- [5] P. Hu, N. Han, X. Zhang et al., "Fabrication of ZnO nanorod-assembled multishelled hollow spheres and enhanced performance in gas sensor," *Journal of Materials Chemistry*, vol. 21, no. 37, pp. 14277–14284, 2011.
- [6] H. Yu, Z. Zhang, M. Han, X. Hao, and F. Zhu, "A general low-temperature route for large-scale fabrication of highly oriented ZnO nanorod/nanotube arrays," *Journal of the American Chemical Society*, vol. 127, no. 8, pp. 2378–2379, 2005.
- [7] P. Hu, X. Zhang, N. Han, W. Xiang, Y. Cao, and F. Yuan, "Solution-controlled self-assembly of ZnO nanorods into hollow microspheres," *Crystal Growth & Design*, vol. 11, no. 5, pp. 1520–1526, 2011.
- [8] C. C. Tsai and H. Teng, "Structural features of nanotubes synthesized from naoh treatment on TiO_2 with different post-treatments," *Chemistry of Materials*, vol. 18, pp. 367–373, 2006.
- [9] D. Li and Y. Xia, "Fabrication of titania nanofibers by electrospinning," *Nano Letters*, vol. 3, no. 4, pp. 555–560, 2003.
- [10] M. Zhang, Y. Bando, and K. Wada, "Synthesis of coaxial nanotubes: titanium oxide sheathed with silicon oxide," *Journal of Materials Research*, vol. 16, no. 5, pp. 1408–1412, 2001.
- [11] A. Hagfeldt and M. Gratzel, "Light-induced redox reactions in nanocrystalline systems," *Chemical Reviews*, vol. 95, no. 1, pp. 49–68, 1995.
- [12] S. U. M. Khan, M. Al-Shahry, and W. B. Ingler, "Efficient photochemical water splitting by a chemically modified n-TiO_2 ," *Science*, vol. 297, no. 5590, pp. 2243–2245, 2002.
- [13] Q. Chen, W. Z. Zhou, G. H. Du, and L. M. Peng, "Trititanate nanotubes made via a single alkali treatment," *Advanced Materials*, vol. 14, no. 17, pp. 1208–1211, 2002.
- [14] A. Thorne, A. Kruth, D. Tunstall, J. T. S. Irvine, and W. Zhou, "Formation, structure, and stability of titanate nanotubes and their proton conductivity," *Journal of Physical Chemistry B*, vol. 109, no. 12, pp. 5439–5444, 2005.
- [15] C. C. Tsai and H. Teng, "Regulation of the physical characteristics of titania nanotube aggregates synthesized from hydrothermal treatment," *Chemistry of Materials*, vol. 16, no. 22, pp. 4352–4358, 2004.
- [16] T. Kasuga, M. Hiramatsu, A. Hoson, T. Sekino, and K. Niihara, "Formation of titanium oxide nanotube," *Langmuir*, vol. 14, no. 12, pp. 3160–3163, 1998.
- [17] X. H. Wang, J. G. Li, H. Kamiyama et al., "Pyrogenic iron(III)-doped TiO_2 nanopowders synthesized in RF thermal plasma: phase formation, defect structure, band gap, and magnetic properties," *Journal of the American Chemical Society*, vol. 127, pp. 10982–10990, 2005.
- [18] R. Asahi, T. Morikawa, T. Ohwaki, K. Aoki, and Y. Taga, "Visible-light photocatalysis in nitrogen-doped titanium oxides," *Science*, vol. 293, no. 5528, pp. 269–271, 2001.
- [19] H. Irie, Y. Watanabe, and K. Hashimoto, "Nitrogen-concentration dependence on photocatalytic activity of $\text{TiO}_{2-x}\text{N}_x$ powders," *Journal of Physical Chemistry B*, vol. 107, no. 23, pp. 5483–5486, 2003.
- [20] B. C. Cheng, Y. H. Xiao, G. S. Wu, and L. D. Zhang, "Controlled growth and properties of one-dimensional ZnO nanostructures with Ce as activator/dopant," *Advanced Functional Materials*, vol. 14, no. 9, pp. 913–919, 2004.
- [21] B. D. Yuhas, D. O. Zitoun, P. J. Pauzauskie, R. R. He, and P. D. Yang, "Transition-metal doped zinc oxide nanowires," *Angewandte Chemie International Edition*, vol. 45, no. 3, pp. 420–423, 2006.
- [22] J. H. He, C. S. Lao, L. J. Chen, D. Davidovic, and Z. L. Wang, "Large-scale Ni-doped ZnO nanowire arrays and electrical and optical properties," *Journal of the American Chemical Society*, vol. 127, no. 47, pp. 16376–16377, 2005.
- [23] M. A. Khan, H. T. Jung, and O. B. Yang, "Synthesis and characterization of ultrahigh crystalline TiO_2 nanotubes," *Journal of Physical Chemistry B*, vol. 110, no. 13, pp. 6626–6630, 2006.
- [24] J. Frank, J. V. Geil, and R. Freaso, "Automatic determination of oxidation stability of oil and fatty products [Food quality control, vegetable and animal fats]," *Food Technology*, vol. 36, no. 6, pp. 71–76, 1982.
- [25] M. K. Läubli and P. A. Bruttel, "Determination of the oxidative stability of fats and oils: comparison between the active oxygen method (AOCS Cd 12-57) and the rancimat method," *Journal of the American Oil Chemists' Society*, vol. 63, no. 6, pp. 792–795, 1986.
- [26] L. Q. Jing, X. J. Sun, B. F. Xin, B. Q. Wang, W. M. Cai, and H. G. Fu, "The preparation and characterization of la doped TiO_2 nanoparticles and their photocatalytic activity," *Journal of Solid State Chemistry*, vol. 177, no. 10, pp. 3375–3382, 2004.
- [27] X. T. Zhang, Y. M. Wang, C. M. Zhang et al., "Chemical modified titanate nanotubes and their stable luminescent properties," *Science in China Series B*, vol. 35, pp. 1–6, 2005.

Research Article

Application of Flower-Like ZnO Nanorods Gas Sensor Detecting SF₆ Decomposition Products

Shudi Peng, Gaolin Wu, Wei Song, and Qian Wang

Chongqing Electric Power Research Institute, Chongqing 401123, China

Correspondence should be addressed to Shudi Peng; psdzq@yahoo.cn

Received 21 November 2012; Accepted 3 January 2013

Academic Editor: Wen Zeng

Copyright © 2013 Shudi Peng et al. This is an open access article distributed under the Creative Commons Attribution License, which permits unrestricted use, distribution, and reproduction in any medium, provided the original work is properly cited.

Gas insulated switchgear (GIS) is an important electric power equipment in a substation, and its running state has a significant relationship with stability, security, and reliability of the whole electric power system. Detecting and analyzing the decomposition byproducts of sulfur hexafluoride gas (SF₆) is an effective method for GIS state assessment and fault diagnosis. This paper proposes a novel gas sensor based on flower-like ZnO nanorods to detect typical SF₆ decompositions. Flower-like ZnO nanoparticles were synthesized via a simple hydrothermal method and characterized by X-ray powder diffraction and field-emission scanning electron microscopy, respectively. The gas sensor was fabricated with a planar-type structure and applied to detect SF₆ decomposition products. It shows excellent sensing properties to SO₂, SOF₂, and SO₂F₂ with rapid response and recovery time and long-term stability and repeatability. Moreover, the sensor shows a remarkable discrimination among SO₂, SOF₂, and SO₂F₂ with high linearity, which makes the prepared sensor a good candidate and a wide application prospect detecting SF₆ decomposition products in the future.

1. Introduction

Gas insulated switchgear (GIS) filled with pressurized sulfur hexafluoride gas (SF₆) is widely used in electric power system in recent decades with the advantages of small floor space, high stability and reliability, high-strength insulation, none smeary oil, lower maintenance cost, and so on [1–6]. Sulfur hexafluoride gas has excellent insulating performance and arc extinction function, and it can dramatically improve the insulation intensity when used as an insulating medium. So it is widely applied to GIS and other gas insulation equipments [1, 3]. However, there exist some unavoidable insulating defects in the process of GIS design, manufacture, installation, and operation [4].

As an inert gas, pure SF₆ is colorless, tasteless, nontoxic, and nonflammable, and its decomposition temperature is as high as 500°C [7]. Although SF₆ is of great chemical inertness and the reliability of GIS is very high, inevitable insulating faults based on arc discharge, spark discharge, or partial discharge may occur due to the internal insulating defects. Researches both at home and abroad demonstrate that such internal insulation faults would cause SF₆ gas to

decompose, and generate several kinds of low-fluorine sulfides, such as SF₄, SF₃, and SF₂ [2, 4, 5, 8, 9]. If the SF₆ in GIS is pure, the decomposed low-fluorine sulfides will reduce to SF₆ fast with the decrease of operating temperature. Actually, it always contains a certain amount of impurities, such as air and water. Some low-fluorine sulfides are very active to react with trace moisture and oxygen and generate the compounds of SOF₄, SOF₂, SO₂F₂, SO₂, HF, and so on. As the GIS insulating defects vary, the decomposed gas mixtures will be different. And the composition contents and decomposition rates are also various. Therefore, detecting and analyzing the decomposed chemical byproducts accurately can efficiently identify and diagnose fault type occurred in GIS.

At present, many methods [10–13] are used to detect the SF₆ decomposition components in GIS, for instance, gas chromatography, gas detection tube, infrared absorption spectrometry, and semiconductor gas sensor. Gas chromatography [10] is mainly used for offline testing and it takes a quite long time. Gas detection tube [11] has no response to some decomposition components and its stability depends on environment condition. Infrared absorption spectrometry [12, 13] has cross-response on SF₆ and cannot quantitatively

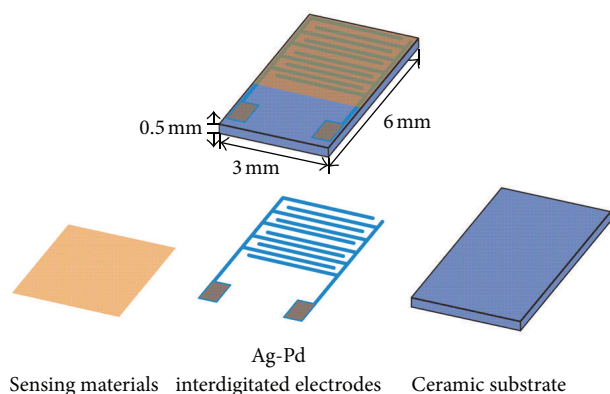


FIGURE 1: Schematic representation of planar ZnO gas sensor structure.

detect the decomposition components. In recent years, metal oxide semiconductor gas sensor based on ZnO [14], SnO₂ [15], TiO₂ [16], Fe₂O₃ [17], WO₃ [18], or In₂O₃ [19] has been widely used for detecting and online monitoring target gas, owing to advantages of simple fabrication process, rapid response and recovery time, low maintenance cost, long service life, long-term stability and repeatability, and so on. With the development of nanotechnology, various gas sensors have been fabricated with small particle size and high surface-to-volume ratio [20]. However, most of these gas sensors mainly focus on toxic gas [21, 22], organic gas [23, 24], carbon dioxide [25], hydrogen [26], and rare studies concerning the SF₆ decompositions. Meanwhile, the cross-sensitivity among the decomposition components is tough, so investigating sensing properties especially selectivity is the most crucial issue for online monitoring SF₆ decompositions.

In this work, we proposed a simple and effective hydrothermal synthesis route to prepare flower-like ZnO nanorods. X-ray powder diffraction (XRD) and field-emission scanning electron microscopy (FESEM) were used to characterize the microstructures and morphologies of the prepared samples. Then a gas sensor based on the flower-like ZnO nanorods was fabricated, and its gas sensing properties against SF₆ decompositions were investigated. Particularly, the study mainly focused on the sensing behaviors of the prepared sensor against SOF₂, SO₂F₂, and SO₂, and its cross-sensitivity was also demonstrated. The prepared sensor exhibited excellent gas response to different SF₆ decompositions at different working temperature with high linearity, rapid response-recovery, and long-time stability and repeatability.

2. Experimental

2.1. Preparation and Characterization of ZnO Nanorods. Flower-like zinc oxide nanorods samples were successfully synthesized through a hydrothermal method using ammonium hydroxide (NH₄OH, 28 wt% NH₃ in H₂O) as the base source and zinc nitrate hexahydrate (Zn(NO₃)₂·6H₂O) as the source of Zn²⁺ ions. All chemicals were of analytical reagent grade and purchased from Beijing Chemicals Co., Ltd. In a typical synthesis process, an adequate amount of

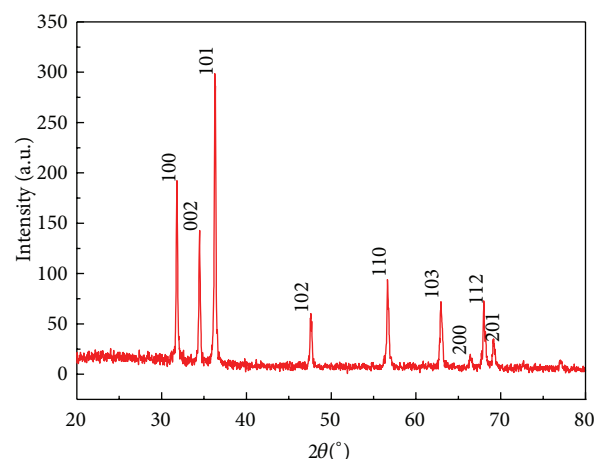


FIGURE 2: XRD patterns of the ZnO nanorods.

Zn(NO₃)₂·6H₂O was dissolved in deionized water (DI water) with a large beaker, and NH₄OH was added slowly to the solution under intense magnetic stirring. The mixed solution was stirred for 30 min and then transferred into a sealed Teflon autoclave with 100 mL of inner volume and 80% of fill ratio. After 24 h reaction at 180°C, the reactor was cooled to room temperature naturally. Subsequently, the prepared white products were centrifuged, washed two or three times with DI water and ethanol alternately, and dried at 80°C in air for further use.

XRD analysis was conducted on a Rigaku D/max-2500 X-ray diffractometer with the 2θ range of 20–80°C at room temperature, and Cu K_{α1} as the source of X-ray at 40 kV, 40 mA, and λ = 1.5418 Å. FESEM images were performed on a JEOL JEM-6700F microscope operating at 3 and 5 kV, respectively.

2.2. Fabrication and Measurement of ZnO Sensor. ZnO nanorods gas sensor was fabricated based on a planar construction with a simple and convenient fabrication procedure. The scheme of the planar ZnO gas sensor structure was shown in Figure 1, where prepared planar ZnO nanorods gas sensor is constituted of planar ceramic substrate, Ag-Pd interdigitated electrodes, and sensing material. The length, width, and height of the planar ceramic substrate are suggested to be about 6, 3, and 0.5 mm, respectively. There are five pairs of Ag-Pd interdigitated electrodes on planar ceramic substrate with both width and distance about 0.15 mm. As-prepared samples were further ground into fine powder and mixed with diethanolamine and ethanol to form a paste with a weight ratio of 100 : 10 : 10. It was subsequently screen printed onto the planar ceramic substrate to form a sensing film and the thickness was about 10 μm and then dried in air at 60°C for 5 h. Finally, the sensor was further aged at an aging test chamber for 240 h.

Gas sensing properties of the prepared planar ZnO gas sensor to SF₆ decomposition byproducts were investigated using an intelligent gas detecting system. Targeted gases were

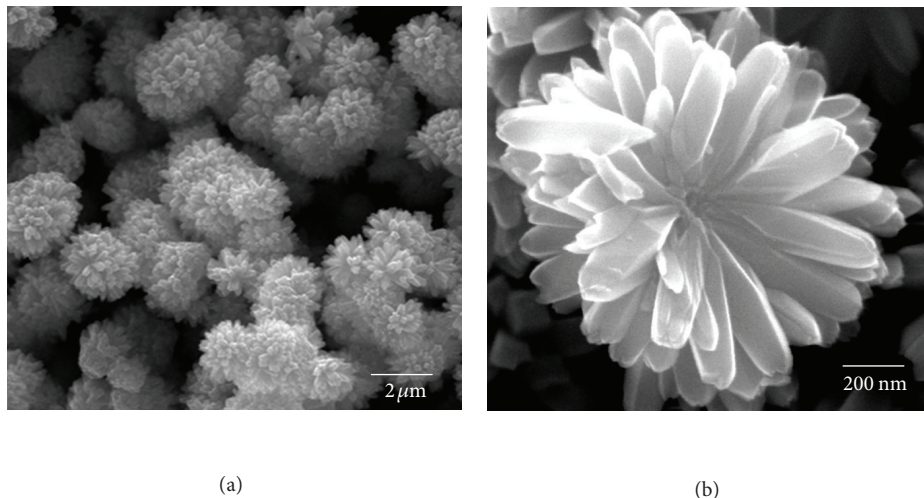


FIGURE 3: (a) Low-resolution FESEM image and (b) high-resolution FESEM image of the ZnO nanorods.

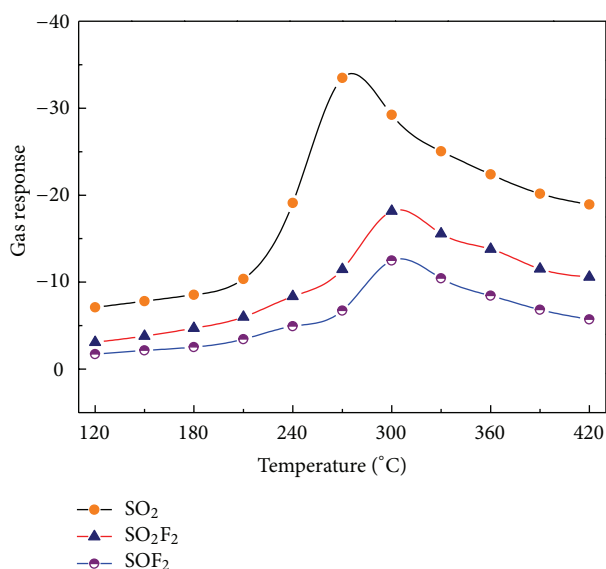


FIGURE 4: Gas response versus temperature curves to 50 $\mu\text{L/L}$ of SO_2 , SOF_2 , and SO_2F_2 .

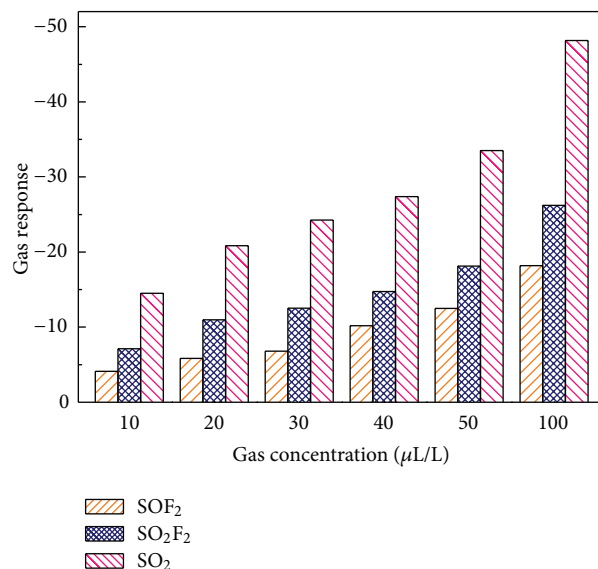


FIGURE 5: Gas response versus concentrations curves to SO_2 , SOF_2 , and SO_2F_2 .

mixed with N_2 by a dynamic gas distributing system which worked with high accuracy mass flow controllers and then injected into the gas sensing chamber. The concentration of detecting gas was controlled and detected by gas mass flow meter. The operating temperature of the gas sensor was controlled by varying current flow of the heater. And the surface temperature of the planar sensor was measured by a thermocouple in real time. When the testing sensor was preheated at 300°C for some time in air and the baseline of resistance was smooth and stable, we could start our gas sensing properties test.

Gas response was defined as the relative variation of the electrical resistance of the gas sensor: $S\% = (R - R_0)/R_0 \times 100\%$. R is the resistance of flower-like ZnO nanorods gas sensor in target gas environment and R_0 being in pure air. The

response time was defined as the time taken by the sensor to achieve 90% of the total resistance change in the case of gas in or the recovery time in the case of gas out. All experiments were repeated several times to ensure the reproducibility and stability of the sensor.

3. Results and Discussion

3.1. Structure and Morphology. Figure 2 shows the XRD patterns of the as-prepared ZnO nanorods. All the diffraction peaks are consistent with the values in the standard card (JCPDS 36-1451) and can be indexed as typical wurtzite hexagonal ZnO crystal structure with lattice constants $a = 3.249 \text{ \AA}$ and $c = 5.206 \text{ \AA}$. No other diffraction peaks from any impurities are detected.

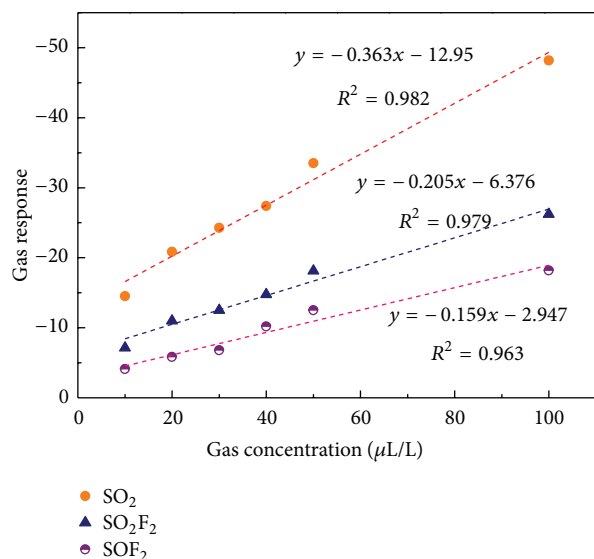


FIGURE 6: The linear calibration curves of SO₂, SOF₂, and SO₂F₂.

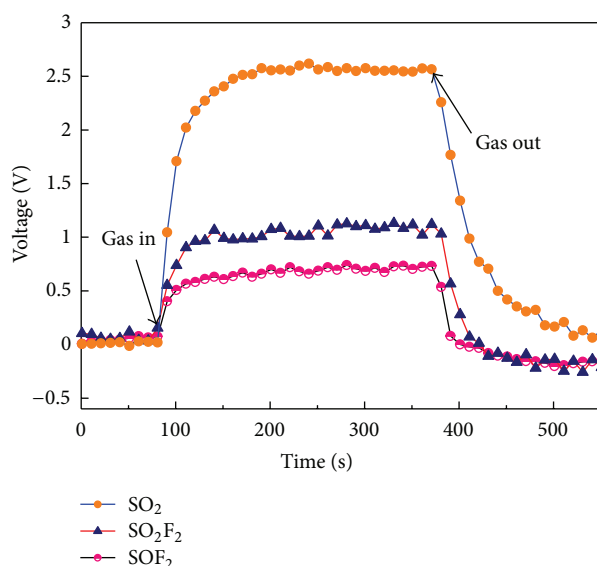


FIGURE 7: The response and recovery behaviors of the sensor to 10 μL/L of SO₂, SOF₂, and SO₂F₂.

Figures 3(a) and 3(b) are typical low-resolution and high-resolution FESEM images of the prepared flower-like ZnO nanorods samples synthesized with the hydrothermal method. The nanoparticles have a high uniform flower-like bundle structure and self-assemble into flowers. The average length of ZnO nanorods is about 400 nm with an aspect ratio of 4:1.

3.2. Gas Sensing Properties and Sensing Mechanism. The gas sensing performances of metal oxide semiconductor gas sensor are dominantly influenced by working condition. Gas

sensing experiments are performed with an intelligent gas detecting system at different operating temperatures to find out the optimum working temperature. Figure 4 shows the gas responses of the prepared flower-like ZnO nanorods gas sensor against 50 μL/L of SF₆ compositions as a function of operating temperature, which ranges from 120°C to 420°C. As seen in Figure 4, the measured gas response curves have a common change trend, in which gas response increases firstly with rising operating temperature and reaches the maximum, and then decreases with an continuous increase of the operating temperature.

This behavior can be understood by a dynamic equilibrium mechanism between gas adsorption and desorption process of gas molecule on the surface of ZnO or other similar semiconducting metal oxides. In the beginning, the rate of gas adsorption is much higher than that of desorption, and the amount of net adsorbed gas increases as the operating temperature rises. It would reach a saturated adsorption state and maintain a dynamic balance at the constant operating temperature. With a sequential increase of the operating temperature, the balance will be broken and it changes to a net desorption process, which ultimately results in a decreasing gas response. As shown in Figure 4, the optimal operating temperatures of the sensor to 50 μL/L of SO₂, SOF₂, and SO₂F₂ are 250, 300, and 300°C with gas response of -33.44, -12.47, and -18.06, respectively, which are applied in all the following investigations in this paper.

At their optimal operating temperatures, we performed the gas responses of the prepared plane flower-like ZnO gas sensor against different concentrations of SO₂, SOF₂, and SO₂F₂. Figure 5 shows the relationship between gas responses and 10, 20, 30, 40, 50, and 100 μL/L of SO₂, SOF₂, and SO₂F₂, respectively. The gas response measured is manifested to persistently increase with a rising gas concentration. At the same level of gas concentration, the gas response values of the sensor to the three targeted gases decrease in the order of SO₂, SO₂F₂, and SOF₂.

If the gas response curve is linear or quasilinear, the sensor can be applied to engineering application in practice. Therefore, based on the linear fitting tool in Origin software, linear characteristics of the prepared sensor to SO₂, SO₂F₂, and SOF₂ were discussed. Figure 6 shows the linear calibration curves of the sensor to SO₂, SO₂F₂, and SOF₂ with gas concentrations in the range of 10–100 μL/L. As seen in Figure 6, all the three gas response curves meet highly linear with gas concentration, and the linear correlation coefficient R^2 for SO₂, SO₂F₂, and SOF₂ is suggested to be about 0.982, 0.979, and 0.963, respectively. Such a higher linear dependence indicates that our prepared flower-like ZnO gas sensor can be used as promising materials for detecting SF₆ decompositions such as SO₂, SO₂F₂, and SOF₂.

Response time and recovery time are other two key indicators to evaluate gas sensor performances. Figure 7 shows the response and recovery characteristic of the prepared sensor to 10 μL/L of SO₂, SO₂F₂, and SOF₂ with the sensor working at its optimum operating temperature. As shown in Figure 7, the response times for 10 μL/L of SO₂, SO₂F₂, and SOF₂ are about 21, 13, and 10 s, and correspondingly the recovery times are about 45, 32, and 17 s, respectively.

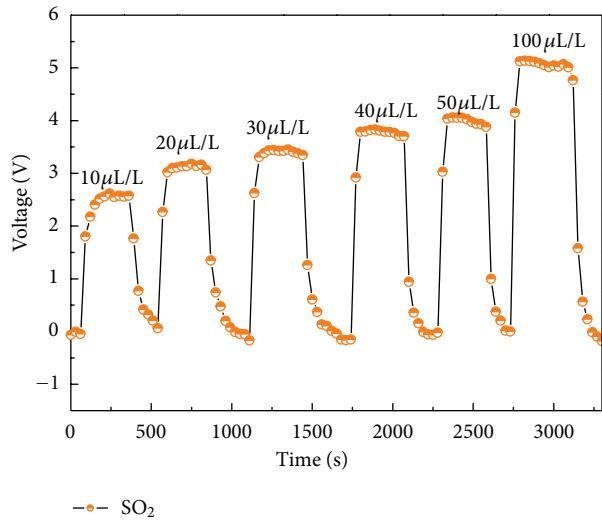


FIGURE 8: The response and recovery behaviors of the sensor to SO_2 .

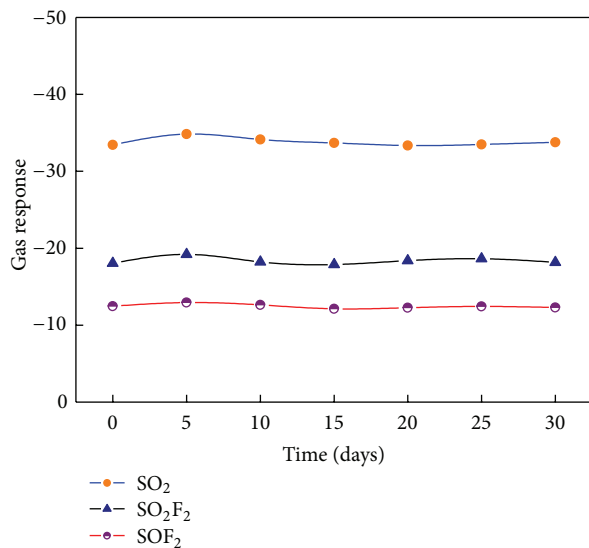


FIGURE 9: The stability and repeatability of the sensor against $50 \mu\text{L/L}$ of SO_2 , SO_2F_2 , and SOF_2 .

Such rapid response and recovery characteristic could be ascribed to the structure of the prepared flower-like sensor, which has a much bigger specific surface area than other conventional sensing structures, provides a larger adsorption area, and increases the amount of gas molecules adsorbed on the surface. Those advantages increase the rate of charge carriers and facilitate the movement of carriers through the barriers, consequently fast response and response property are observed.

The response and recovery behaviors versus SO_2 with concentration at 10, 20, 30, 40, 50, and $100 \mu\text{L/L}$ are shown in Figure 8. With the concentration of detected gas increasing,

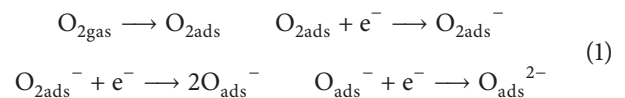
the gas response amplitude increases apparently, nevertheless the response and recovery property changes slightly which indicates a very good and satisfying reproducibility of prepared sensor against the decompositions. Figure 9 shows the long-term stability and repeatability of the sensor against $50 \mu\text{L/L}$ of SO_2 , SO_2F_2 , and SOF_2 . One can clearly see in Figure 9 that the gas response changes slightly and keeps at a nearly constant value during the long experimental cycles, which confirms the excellent longtime stability and repeatability of the prepared flower-like ZnO nanorods gas sensor for detecting SO_2 , SO_2F_2 , and SOF_2 .

For most metal oxide semiconductor gas sensors such as zinc oxide, tin oxide, titanium oxide, ferric oxide, and indium oxide, the sensing properties are dominantly controlled by the change of electrical resistance [27], which is fundamentally attributed to the chemical adsorption and desorption process of gas molecules on sensing surface of the sensor.

It is well known to all that zinc oxide is a typical n-type semiconducting material and there exist many oxygen vacancies in the crystal lattices [28–30], where various kinds of oxygen could be adsorbed. The species of adsorbed oxygen are closely related to the ambient temperature [31]. At room temperature, oxygen is likely to be adsorbed on ZnO surface or grain boundaries with a typical physical adsorption mode. And it would turn into chemical adsorption by thermal excitation or electric excitation with certain energy.

As shown in Figure 10(a), oxygen would capture electrons and form a depletion region on the surface area, which results in a decrease in the concentration of charge carrier and electron mobility, thus gas sensor shows a higher electrical resistance. Figure 10(b) illustrates the gas sensing process of SO_2 as an example exploring the gas sensing mechanism of the prepared sensor detecting SF_6 decompositions. When flower-like ZnO nanorods are reducing gas ambient at moderate temperature (such as in certain concentration of SO_2 , SO_2F_2 , and SOF_2), the reducing gas reacts with chemical adsorbed oxygen, and then trapped electrons would be released back into ZnO surface. Electrons released from chemical adsorbed oxygen would reduce the height of barriers in the depletion region and increase the number of charge carriers [32, 33], which promotes the movements of charge carriers between conduction band and valence band and eventually increases the electrical conductivity of the sensor [34, 35].

With temperature rising, chemical adsorbed oxygen exists in various forms, namely, $\text{O}_{2\text{ads}}^-$, O_{ads}^- , and $\text{O}_{\text{ads}}^{2-}$, as shown in the following reaction equations:



As mentioned above the state of adsorbed oxygen is mainly determined by the ambient temperature. At lower experimental temperatures, oxygen dominantly exists in the form of a “molecular ion” $\text{O}_{2\text{ads}}^-$ and transfers into “atomic ion” O_{ads}^- and $\text{O}_{\text{ads}}^{2-}$ with a further rising operating temperature. Experimental results indicate that the transition temperature for oxygen from “molecular ion” to “atomic ion” is about 450–500 K. As performed in Figure 4, the optimum

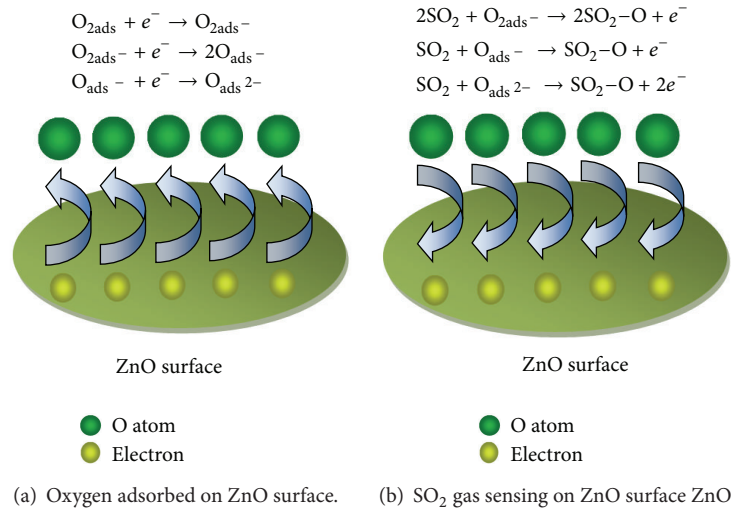


FIGURE 10: Schematic plot illustrating the sensing mechanism of prepared sensor to SO₂.

working temperatures for SO₂, SO₂F₂, and SOF₂ are about 250, 300, and 300°C, respectively. Thus, we draw a conclusion that the sensing behavior of the prepared sensor to SO₂ gas may belong to the “molecular ion” reaction pattern, while it is an “atomic ion” gas response mode for SO₂F₂ and SOF₂.

4. Conclusions

In summary, Flower-like ZnO nanorods have been successfully synthesized and characterized by XRD and FESEM. The optimum operating temperatures of the prepared sensor to SO₂, SO₂F₂, and SOF₂ are about 250, 300, and 300°C. The response (recovery) time of the sensor to 10 μL/L of SO₂, SO₂F₂, and SOF₂ is 21 (45), 13 (32), and 10 (17) s, respectively. Especially, the flower-like ZnO nanorods gas sensor shows high linearity to SO₂, SO₂F₂, and SOF₂ at the range of 10–100 μL/L with excellent linear correlation coefficient R^2 at 0.982, 0.979, and 0.963, separately. These findings demonstrate that our prepared flower-like ZnO nanorods have some excellent potential advantages for using as gas sensors to detect and online monitor the SF₆ decompositions such as SO₂, SOF₂, and SO₂F₂ in practice, although further studies are still needed.

References

- [1] J. Tang, F. Liu, X. X. Zhang, Q. H. Meng, and J. B. Zhou, “Partial discharge recognition through an analysis of SF₆ decomposition products Part I: decomposition characteristics of SF₆ under four different partial discharges,” *IEEE Transactions on Dielectrics and Electrical Insulation*, vol. 19, no. 1, pp. 29–36, 2012.
- [2] M. Shih, W. J. Lee, and C. Y. Chen, “Decomposition of SF₆ and H₂S mixture in radio frequency plasma environment,” *Industrial and Engineering Chemistry Research*, vol. 42, no. 13, pp. 2906–2912, 2003.
- [3] J. Tang, F. Liu, X. X. Zhang, Q. H. Meng, and J. G. Tao, “Partial discharge recognition through an analysis of SF₆ decomposition products part 2: feature extraction and decision tree-based pattern recognition,” *IEEE Transactions on Dielectrics and Electrical Insulation*, vol. 19, no. 1, pp. 37–44, 2012.
- [4] R. J. Van Brunt and J. T. Herron, “Fundamental processes of SF₆ decomposition and oxidation in glow and corona discharges,” *IEEE Transactions on Electrical Insulation*, vol. 25, no. 1, pp. 75–94, 1990.
- [5] M. Shih, W. J. Lee, C. H. Tsai, P. J. Tsai, and C. Y. Chen, “Decomposition of SF₆ in an RF plasma environment,” *Journal of the Air and Waste Management Association*, vol. 52, no. 11, pp. 1274–1280, 2002.
- [6] I. Sauers, H. W. Ellis, and L. G. Christophorou, “Neutral decomposition products in spark breakdown of SF₆,” *IEEE Transactions on Electrical Insulation*, vol. EI-21, no. 2, pp. 111–120, 1986.
- [7] W. T. Tsai, “The decomposition products of sulfur hexafluoride (SF₆): reviews of environmental and health risk analysis,” *Journal of Fluorine Chemistry*, vol. 128, no. 11, pp. 1345–1352, 2007.
- [8] L. Vial, A. M. Casanovas, I. Coll, and J. Casanovas, “Decomposition products from negative and 50 Hz ac corona discharges in compressed SF₆ and SF₆/N₂ (10 : 90) mixtures. Effect of water vapour added to the gas,” *Journal of Physics D*, vol. 32, no. 14, pp. 1681–1692, 1999.
- [9] C. T. Dervos and P. Vassiliou, “Sulfur hexafluoride (SF₆): Global environmental effects and toxic byproduct formation,” *Journal of the Air and Waste Management Association*, vol. 50, no. 1, pp. 137–141, 2000.
- [10] E. Duffour, “Molecular dynamic simulations of the collision between copper ions, SF₆ molecules and a polyethylene surface: a study of decomposition products and an evaluation of the self-diffusion coefficients,” *Macromolecular Theory and Simulations*, vol. 19, no. 2-3, pp. 88–99, 2010.
- [11] J. I. Baumbach, P. Pilzecker, and E. Trindade, “Monitoring of circuit breakers using ion mobility spectrometry to detect SF₆-decomposition,” *International Journal for Ion Mobility Spectrometry*, vol. 2, no. 1, pp. 35–39, 1999.
- [12] R. Kurte, C. Beyer, H. M. Heise, and D. Klockow, “Application of infrared spectroscopy to monitoring gas insulated high-voltage equipment: electrode material-dependent SF₆ decomposition,”

- Analytical and Bioanalytical Chemistry*, vol. 373, no. 7, pp. 639–646, 2002.
- [13] W. Ding, R. Hayashi, K. Ochi et al., “Analysis of PD-generated SF₆ decomposition gases adsorbed on carbon nanotubes,” *IEEE Transactions on Dielectrics and Electrical Insulation*, vol. 13, no. 6, pp. 1200–1207, 2006.
- [14] J. Singh, A. Mukherjee, S. K. Sengupta, J. Im, G. W. Peterson, and J. E. Whitten, “Sulfur dioxide and nitrogen dioxide adsorption on zinc oxide and zirconium hydroxide nanoparticles and the effect on photoluminescence,” *Applied Surface Science*, vol. 258, no. 15, pp. 5778–5785, 2012.
- [15] B. Wang, L. F. Zhu, Y. H. Yang, N. S. Xu, and G. W. Yang, “Fabrication of a SnO₂ nanowire gas sensor and sensor performance for hydrogen,” *Journal of Physical Chemistry C*, vol. 112, no. 17, pp. 6643–6647, 2008.
- [16] J. Gong, Y. Li, Z. Hu, Z. Zhou, and Y. Deng, “Ultrasensitive NH₃ gas sensor from polyaniline nanograin enashed TiO₂ fibers,” *Journal of Physical Chemistry C*, vol. 114, no. 21, pp. 9970–9974, 2010.
- [17] X. Liu, J. Zhang, X. Guo, S. Wu, and S. Wang, “Porous α -Fe₂O₃ decorated by Au nanoparticles and their enhanced sensor performance,” *Nanotechnology*, vol. 21, no. 9, Article ID 095501, 2010.
- [18] B. Cao, J. Chen, X. Tang, and W. Zhou, “Growth of monoclinic WO₃ nanowire array for highly sensitive NO₂ detection,” *Journal of Materials Chemistry*, vol. 19, no. 16, pp. 2323–2327, 2009.
- [19] S. E. Moon, H. Y. Lee, J. Park et al., “Low power consumption and high sensitivity carbon monoxide gas sensor using indium oxide nanowire,” *Journal of Nanoscience and Nanotechnology*, vol. 10, no. 5, pp. 3189–3192, 2010.
- [20] W. Zeng, T. Liu, Z. Wang, S. Tsukimoto, M. Saito, and Y. Ikuhara, “Selective detection of formaldehyde gas using a Cd-Doped TiO₂-SnO₂ sensor,” *Sensors*, vol. 9, no. 11, pp. 9029–9038, 2009.
- [21] M. Chen, Z. Wang, D. Han, F. Gu, and G. Guo, “Porous ZnO polygonal nanoflakes: synthesis, use in high-sensitivity NO₂ gas sensor, and proposed mechanism of gas sensing,” *Journal of Physical Chemistry C*, vol. 115, no. 26, pp. 12763–12773, 2011.
- [22] E. Oh, H. Y. Choi, S. H. Jung et al., “High-performance NO₂ gas sensor based on ZnO nanorod grown by ultrasonic irradiation,” *Sensors and Actuators B*, vol. 141, no. 1, pp. 239–243, 2009.
- [23] K. Zheng, L. Gu, D. Sun, X. Mo, and G. Chen, “The properties of ethanol gas sensor based on Ti doped ZnO nanotetrapods,” *Materials Science and Engineering B*, vol. 166, no. 1, pp. 104–107, 2010.
- [24] A. Wei, L.-H. Pan, X.-C. Dong, and W. Huang, “Room-temperature NH₃ gas sensor based on hydrothermally grown ZnO nanorods,” *Chinese Physics Letters*, vol. 28, no. 8, pp. 702–706, 2011.
- [25] C. Wen, Y. Ju, W. Li et al., “Carbon dioxide gas sensor using SAW device based on ZnO film,” *Applied Mechanics and Materials*, vol. 135–136, pp. 347–352, 2012.
- [26] O. Lupan, G. Chai, and L. Chow, “Novel hydrogen gas sensor based on single ZnO nanorod,” *Microelectronic Engineering*, vol. 85, no. 11, pp. 2220–2225, 2008.
- [27] W. Zeng, T. Liu, and Z. Wang, “Enhanced gas sensing properties by SnO₂ nanosphere functionalized TiO₂ nanobelts,” *Journal of Materials Chemistry*, vol. 22, no. 8, pp. 3544–3548, 2012.
- [28] J. Kim and K. Yong, “Mechanism study of ZnO nanorod-bundle sensors for H₂S gas sensing,” *Journal of Physical Chemistry C*, vol. 115, no. 15, pp. 7218–7224, 2011.
- [29] D. Velasco-Arias, D. Díaz, P. Santiago-Jacinto, G. Rodríguez-Gattorno, A. Vázquez-Olmos, and S. E. Castillo-Blum, “Direct interaction of colloidal nanostructured ZnO and SnO₂ with NO and SO₂,” *Journal of Nanoscience and Nanotechnology*, vol. 8, no. 12, pp. 6389–6397, 2008.
- [30] Q. Qi, T. Zhang, Q. Yu et al., “Properties of humidity sensing ZnO nanorods-base sensor fabricated by screen-printing,” *Sensors and Actuators B*, vol. 133, no. 2, pp. 638–643, 2008.
- [31] M.-W. Ahn, K.-S. Park, J.-H. Heo et al., “Gas sensing properties of defect-controlled ZnO-nanowire gas sensor,” *Applied Physics Letters*, vol. 93, no. 26, Article ID 263103, 2008.
- [32] M. W. Ahn, K. S. Park, J. H. Heo, D. W. Kim, K. J. Choi, and J. G. Park, “On-chip fabrication of ZnO-nanowire gas sensor with high gas sensitivity,” *Sensors and Actuators B*, vol. 138, no. 1, pp. 168–173, 2009.
- [33] J. Zhang, S. Wang, M. Xu et al., “Hierarchically porous ZnO architectures for gas sensor application,” *Crystal Growth and Design*, vol. 9, no. 8, pp. 3532–3537, 2009.
- [34] Z. Yuan, X. Jiaqiang, X. Qun, L. Hui, P. Qingyi, and X. Pengcheng, “Brush-like hierarchical zno nanostructures: synthesis, photoluminescence and gas sensor properties,” *Journal of Physical Chemistry C*, vol. 113, no. 9, pp. 3430–3435, 2009.
- [35] J. Zhang, X. Liu, S. Wu, B. Cao, and S. Zheng, “One-pot synthesis of Au-supported ZnO nanoplates with enhanced gas sensor performance,” *Sensors and Actuators B*, vol. 169, pp. 61–66, 2012.

Research Article

Gas Sensing Properties and Mechanism of Nano-SnO₂-Based Sensor for Hydrogen and Carbon Monoxide

Weigen Chen, Qu Zhou, Fu Wan, and Tuoyu Gao

State Key Laboratory of Power Transmission Equipment & System Security and New Technology, Chongqing University, Chongqing 400030, China

Correspondence should be addressed to Qu Zhou, zhouqupsd@yahoo.cn

Received 17 September 2012; Revised 27 October 2012; Accepted 4 November 2012

Academic Editor: Wen Zeng

Copyright © 2012 Weigen Chen et al. This is an open access article distributed under the Creative Commons Attribution License, which permits unrestricted use, distribution, and reproduction in any medium, provided the original work is properly cited.

Nano-SnO₂ powder was prepared by the hydrothermal method in this paper. X-ray powder diffraction (XRD) and scanning electron microscopy (SEM) were used to characterize the composition of the crystalline phase and the morphology of the prepared gas-sensitive materials, respectively. In particular, the study focused on the sensing behaviors of nano-SnO₂-based sensor towards power transformer fault gases such as hydrogen and carbon monoxide. The optimum working temperature for hydrogen and carbon monoxide is about 400°C and 360°C, separately. Further investigations into the adsorption process of gas molecule on SnO₂ (110) surface based on the first principles were conducted. The calculations indicated that 1σ orbits of H₂ split into several new electronic peaks and 5σ orbits of CO almost degenerated completely in the adsorption process, which promoted charge transfer between gas molecule and SnO₂ (110) surface. It provides a qualitative explanation for the prepared nano-SnO₂-based sensor exhibiting different gas sensing properties towards H₂ and CO.

1. Introduction

Power transformer is one of the most important apparatus in power transmission. The safety and reliability of the power system are directly affected by the operation conditions. Once faults happen on power transformer, it will cause great damage to the national economy [1–4]. At present, most of the large power transformers are still oil-immersed transformers, when the transformer internal paper-oil insulation faults occur due to overheating or partial discharge [2, 3], they may cause gaseous compounds such as hydrogen, carbon oxides, and some low molecular hydrocarbons, and most of those fault gases would dissolve in transformer oil [5–8]. Dissolved gas-in-oil analysis (DGA) and online monitoring of the dissolved gases in transformer oil are two important technologies for power transformer conditional maintenance.

At present, we mainly use gas chromatography, fourier transform infrared spectroscopy, Raman spectrometry, and photoacoustic spectrometry to detect the dissolved gases in transformer oil. With the development of nanotechnology,

there is a new trend to use gas sensor based on nanometric materials detecting the dissolved gases. With many advantages such as simple manufacture technique, low cost, rapid response and recovery time, and long life and stability, semiconductor metal oxides such as SnO₂ is promising for online monitoring the fault gases in power transformer [9–16]. However, due to the similar element compositions and molecular structures of transformer fault gases, it is difficult to understand the sensing behaviors of SnO₂ to those gases [17, 18]. Although many relevant researches have been carried out, an atomic level understanding of SnO₂-based materials sensing properties toward transformer fault gases is crucial [19–22]. As both H₂ and CO are the effective fault gases in power transformers, the sensing properties of nano-SnO₂-based gas sensor to H₂ and CO were investigated in this paper.

In this paper, the nano-SnO₂ sensing materials were prepared by the hydrothermal method; its microstructure and gas sensing properties towards H₂ and CO were investigated. Furthermore, an atomic level understanding of the sensing properties based on the first principles calculations

was carried out. The main purpose is to make clear the gas response properties of nano-SnO₂ towards H₂ and CO. This study promises a new feasible way to explore new gas sensors for the on-line monitoring of fault gases dissolved in power transformers.

2. Experiment Process

2.1. Synthesis of Nano-SnO₂ Sensing Materials. Nano-SnO₂ powder was synthesized via hydrothermal method. Firstly, 1.753 g SnCl₄·5H₂O (A.R.) was dissolved in a beaker with 20 mL deionized water and 20 mL absolute ethanol; NH₃·H₂O (A.R.) was dropped into the mixed solution until the pH reached 9 under intense magnetic stirring. After magnetic stirring for about 30 min at 70°C, the mixture solution was transferred into a Teflon-lined autoclave with capacity of 50 mL, which was heated at 180°C for 24 h. Then the autoclave was cooled at room temperature naturally. Finally, the as-obtained powder was washed with deionized water and ethanol several times, respectively, until Cl⁻ could not be examined by 0.1 mol/L AgNO₃ aqueous solution and dried in air for the further characterizations.

2.2. Fabrication of Nano-SnO₂ Gas Sensor. Nano-SnO₂ based gas sensor was fabricated through traditional side heating preparation process. The powder was mixed with diethanolamine and ethanol to obtain a homogenous paste. It was subsequently brushed onto an alumina tube substrate, and dried at 100°C for 2 h in air. Then, a Ni-Cr heating wire was inserted into the alumina tube substrate. Finally, the tube was welded on the pedestal of the sensor. Figure 1(a) shows the schematic drawing of the as-fabricated gas sensor. As illustrated in Figure 1(b), there are Au electrodes placed at the two sides of the alumina tube to read the electrical resistance of gas sensor. The distance between the two electrodes is estimated to be 6 mm, and the diameter of the tube is 1.2 mm. Then the gas sensor is aged at 120°C for 240 h to improve its stability and repeatability.

2.3. Characterization of Structure and Gas Sensing Property. X-ray powder diffraction (XRD) was taken to identify the crystalline phase composition of the prepared nano-SnO₂ samples at the range of 20–80° with Cu K_{α1} radiation ($\lambda = 1.5406 \text{ \AA}$) at 40 kV and 40 mA. The morphology of SnO₂ nanostructures was characterized by scanning electron microscopy (SEM).

The static measuring system was used to test gas sensing properties. The operating temperature of the gas sensor was controlled by varying the current of Ni-Cr heating wire. Gas sensing properties were studied under laboratory condition with room temperature at 30°C and humidity as 50%. The relative variation of the gas sensor resistance (gas response) in this paper was defined as $S = (R_o - R)/R_o$, where R_o and R represent the resistances of the sensor in N₂ and in targeted gas, respectively. All measurements were repeated several times in order to ensure the reproducibility of the gas sensing response.

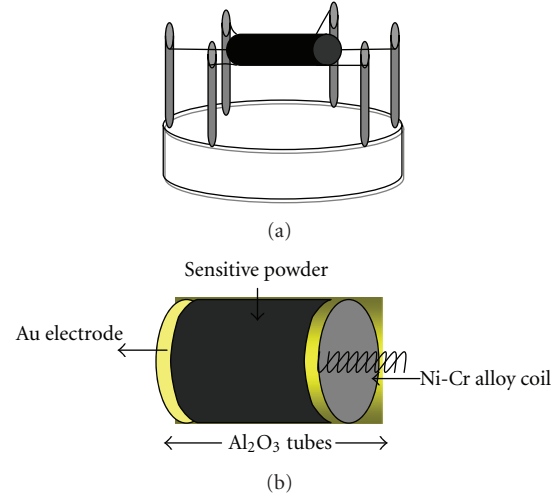


FIGURE 1: The structure of gas sensor ((a) base structure; (b) tube structure).

2.4. First Principles Calculation. Based on the density functional theory (DFT) [23–25], the first principles calculations were performed with the assistant of Cambridge Sequential Total Energy Package (CASTEP) program in this paper [26, 27]. Exchange-correlation function between electrons was described by the Revised Perdew-Burke-Ernzerhof (RPBE) form of generalized gradient approximation (GGA). Interaction between nuclei and electrons was approximated with ultrasoft pseudopotential to treat the valence electrons, and the valence electron configurations for H, C, O, and Sn atoms were chosen as 1s, 2s 2p, 2s 2p, and 5s 5p, respectively. The cutoff energy of the plane-wave was set at 380 eV to ensure energy convergence within 1–2 meV/atom. The maximum root mean square convergent tolerance was 1.0×10^{-6} eV/atom. In the whole process of geometry optimization and energy calculation, all atoms were allowed to relax in all directions freely [28–31].

3. Results and Discussion

3.1. Characteristic of Sensing Material. To determine the crystalline phase composition of the prepared SnO₂ powder, the X-ray diffraction pattern of the sample is shown in Figure 2. One can clearly see that the main characteristic peaks (110), (101), and (211) appeared in 27.9°, 34.3°, and 52.4° respectively, perfectly corresponding to the tetragonal rutile phase of SnO₂ with the lattice constants of $a = 4.738 \text{ \AA}$ and $c = 3.188 \text{ \AA}$ (JCPDS21-1250). The average particle size of the sample is calculated from the XRD peaks based on the Scherrer formula as follows:

$$D = \frac{0.89\gamma}{(\beta \cos \theta)}, \quad (1)$$

where D is the mean particle size of the powder, γ is the X-ray wavelength, β is the half peak width, and θ is the Bragg angle. According to the broadening of the (110) diffraction line, the calculated average particle size is about 20 nm.

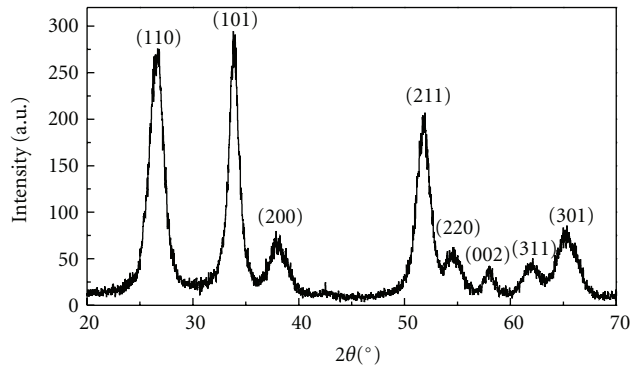
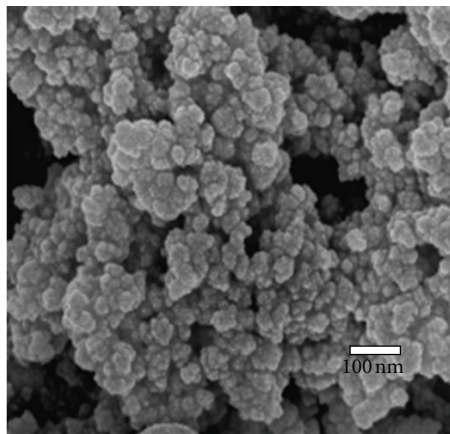
FIGURE 2: XRD spectra of the nano-SnO₂ powder.FIGURE 3: EM micrograph of the nano-SnO₂ powder.

Figure 3 shows the SEM image of the prepared nano-SnO₂ sample, which is disperse, and the particles are uniform in shape and particle size. They are nearly spherical with the diameters about 25–30 nm.

3.2. Gas Sensing Properties

3.2.1. Optimum Operating Temperature Property. The operating temperature is one of the most important properties of the as-prepared gas sensor. The optimum operating temperature is closely related to not only nature property of the material itself, but also the gas-sensing process of the gas towards the surface of materials. To investigate the operating temperature property of the prepared nano-SnO₂-based gas sensor, the gas response to transformer fault gases at different temperatures was measured.

Figure 4 shows the response of nano-SnO₂-based gas sensor to hydrogen and carbon monoxide as a function of the operating temperature, with the gas concentration as 50 ul/L, environmental temperature at 30°C and humidity as 50%. As shown in Figure 4, the gas responses increase firstly and then decrease with the rise of operating temperature, which can be explained by a dynamic equilibrium state of adsorption and desorption. With the operating temperature increasing, the adsorption amount of the gas would reach to a balance

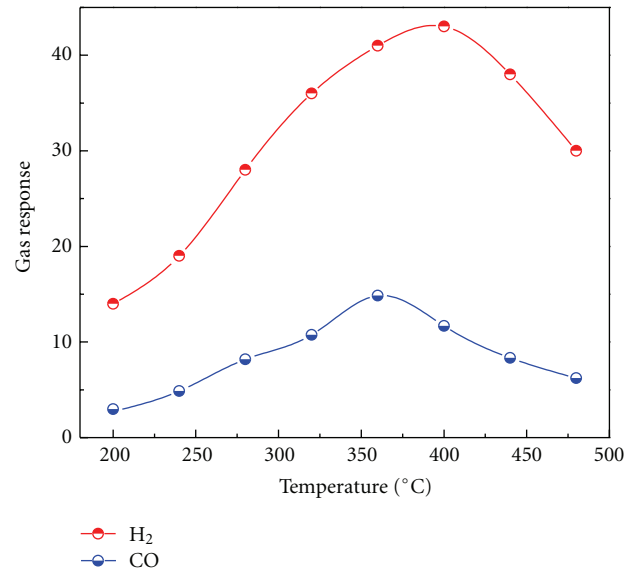


FIGURE 4: Gas response of the sensor to different operating temperatures.

at a suitable temperature firstly. And then the balance of desorption is broken which is followed by the decrease of gas response. The gas response to 50 ul/L hydrogen and carbon monoxide at different operating temperatures can be seen clearly from Figure 4. The optimum operating temperature for carbon monoxide and hydrogen are revealed to be about 360°C and 400°C, respectively, indicating that the sensor shows the maximum gas response at these temperatures.

3.2.2. Gas Response Property. If gas response of the prepared gas sensor presents a linear or quasilinear relationship with the concentration of the measured gas, the gas sensor can be used in the on-line monitoring of the fault gases dissolved in power transformer oil. The gas sensor responses were tested with the concentration of the target gas in the range of 5–100 ul/L, environmental temperature at 30°C, and humidity as 50%.

Figure 5 shows the gas response to hydrogen and carbon monoxide as a function of the gas concentration at their optimum operating temperatures. From Figure 5, it can be demonstrated that the gas responses have the trend of increasing at different degrees with rising of gas concentration. The gas response curves meet the quasi-linear relationship with the concentrations of the detected gases, satisfying the requirements of engineering application for on-line monitoring.

3.2.3. Response-Recovery Property. The response time and recovery time are the other two key properties for gas sensor, which are defined as the required time for reaching 90% of the maximum response when gas in and 10% when gas out, respectively. Figure 6 shows the response-recovery property of the sensor working at their optimum operating temperatures, with gas concentration of 50 ul/L, environmental temperature at 30°C and humidity as 40%. From the curves,

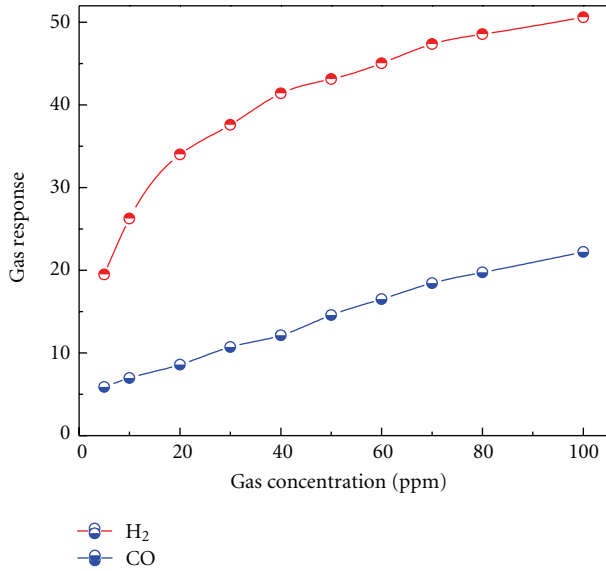


FIGURE 5: Gas response of the sensor to different gas concentrations.

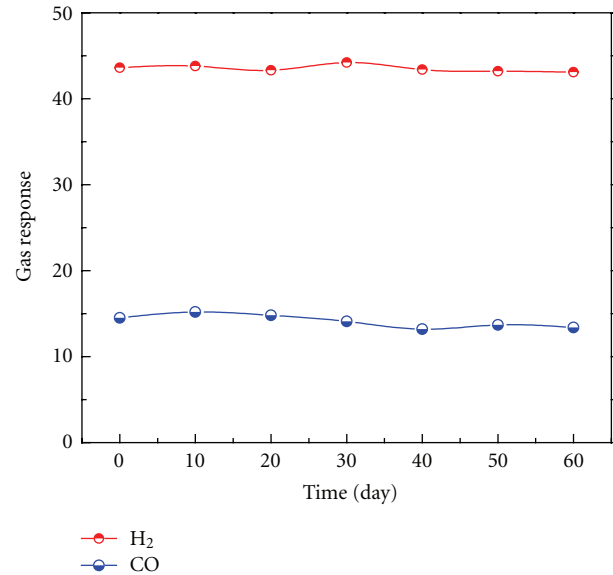


FIGURE 7: The long-term stability and repeatability of the sensor.

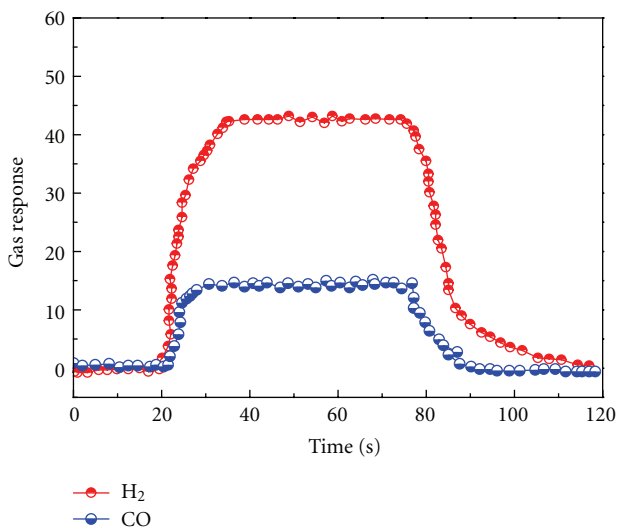


FIGURE 6: Response and recovery time of the gas sensor.

it can be known that the gas response increases sharply with gas in and returns to its original state while gas out. According to the definition above, the response and recovery time for hydrogen as shown in Figure 6 is about 12 s and 25 s, for carbon monoxide about 8 s and 15 s, respectively.

3.2.4. Stability and Repeatability. Finally, the stability of the sensor to 50 ul/L fault gases was investigated with their optimum operating temperatures, environmental temperature at 30°C, and humidity as 40%. As shown in Figure 7, the gas response changes slightly for two months, which indicates that the prepared gas sensor presents excellent long-term stability and repeatability.

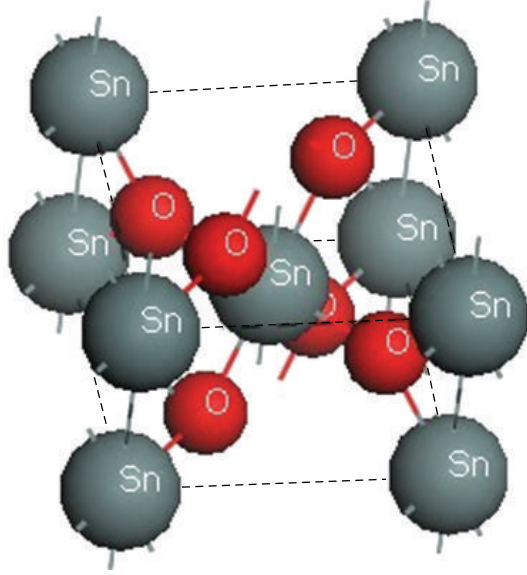
3.3. Gas Sensing Mechanism. According to the researches above, it can be concluded that even at the same experiment

conditions, the prepared gas sensor exhibits different sensing properties such as the optimum operating temperature property and gas response property. The previous studies about gas sensing mechanism mainly concentrated on the grain size [33], grain growth direction [34], specific surface area [35–38], and so forth. But they could not have given a reasonable explanation for sensing variances of gas sensor to different gases [39]. So it is needed to further study the gas sensing reaction process in atomic level to figure out more accurate mechanism [40–42].

At present researchers mainly consider the sensing behaviors of semiconductor metal oxides through a trial-and-error experiment method, which wastes a lot of unnecessary manpower, materials, finance, and time [43]. With the development of computer technology, they can be studied by theoretical calculation method. Although many works have been conducted on nano-SnO₂-based sensor, its gas sensing mechanism remains controversial.

SnO₂ is a typical n-type semiconductor as reported, and its gas sensing property was mainly determined by the surface. When placed in a gas with certain concentration, it would be adsorbed by gas molecule on its surface firstly, and then the resistance and conductance of the surface would be modified. In order to reveal the different gas responses against hydrogen and carbon monoxide, the adsorption process between the gas molecule and sensing surface should be investigated deeply to gain an insight into the gas sensing mechanism.

It is well known that the sensing property of SnO₂ is dominantly controlled by surface, and that SnO₂ crystal has four major low-index surfaces (110), (101), (100), and (001) [23, 38], respectively. In particular, the (110) surface is of the most thermodynamically stable surface among the four low-index surfaces [19, 26, 27], and it has been widely used to investigate the surface properties of SnO₂ through the first principles method. To understand the sensing mechanism of

FIGURE 8: The unit cell model of rutile SnO_2 .

SnO_2 -based gas sensors, the first principles calculations were performed to investigate the interactions of H_2 and CO with SnO_2 (110) surface to reveal the sensing mechanism of SnO_2 .

Firstly, we built the rutile SnO_2 unit cell model with lattice parameters $a = 4.737$ and $c = 3.186$ Å. As shown in Figure 8, each Sn atom is bonded with six O atoms nearby, and each O with three Sn. To preserve symmetry, the top and bottom layers of the slab were taken to be identical, and a surface vacuum slab of 10 Å was added to the (110) surface to avoid unnecessary interactions between the slabs. A super cell consisted of a 1×1 surface unit cell was employed, which was composed of a finite number of layers but of infinite extent. As shown in Figure 9, the SnO_2 (110) surface as a single slab consisted of several atomic layers, which was cut from the optimized bulk structure. The central five layers were constrained at their sites, while the surface and subsurface layers on either side of the slab were allowed to relax freely for all the calculations. There are four kinds of surface atoms: O_{2c} , O_{3c} , Sn_{5c} , and Sn_{6c} , respectively, as shown in Figure 9. The outermost atomic layer is composed of two coordinate oxygen anions O_{2c} (bridging oxygen), which occupy bridging positions between fully coordinated tin atoms Sn_{6c} located in the second layer. Five coordinated tin atoms Sn_{5c} (5-fold Sn^{4+}) and fully coordinated tin atoms Sn_{6c} (6-fold Sn^{4+}) as well as fully coordinated oxygen anions O_{3c} (plane oxygen) occupy the second layer. And the third atomic layer is constituted of subbridging oxygen atoms.

Table 1 listed the outermost atoms displacement of the rutile SnO_2 (110) surface with geometry optimization calculation by the CASTEP program module. The O_{2c} , O_{3c} , and Sn_{6c} atoms at the top layer move out of the surface by 0.04 Å, 0.16 Å, and 0.18 Å, respectively. While Sn_{5c} atom relaxes inwards 0.10 Å, which has the same tendency with the results reported in other literatures [23, 26, 32].

As mentioned above, the surface layer of SnO_2 (110) surface has four different characteristic atoms O_{2c} , O_{3c} , Sn_{5c} ,

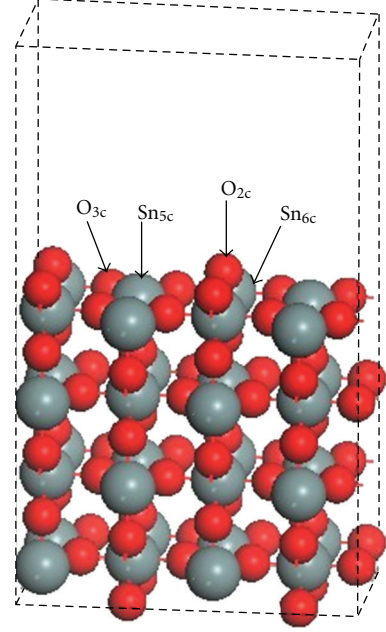
FIGURE 9: The atomic model of SnO_2 (110) surface.

TABLE 1: Displacement of surface atoms along the (110) direction.

	O_{2c}	O_{3c}	Sn_{5c}	Sn_{6c}
DFT (GGA-RPBE)	0.04	0.16	-0.10	0.18
DFT (GGA-PBE) [32]	0.03	0.135	-0.092	0.15
DFT (GGA-PBE) [26]	0.09	0.18	-0.11	0.22
DFT (B3LYP) [23]	0.02	0.14	-0.12	0.26

and Sn_{6c} . Different from nonpolar molecules such as H_2 , CO molecule is likely to be adsorbed on the surface layer atoms with its carbon end or oxygen end. In consideration of this, we initially imported CO gas molecule perpendicularly onto the surface layer atoms with carbon end to O_{2c} and O_{3c} sites and oxygen end to Sn_{5c} and Sn_{6c} sites, respectively. The initial vertical CO was placed at the sites that C atom could be bonded with Sn or O atom of SnO_2 (110) surface layer, and O atom could provide typical bond with Sn atom. Simultaneously, H_2 gas molecule was imported perpendicularly onto the surface layer atoms with the initial vertical heights that H atom could provide typical bond with surface layer atoms. The bond length and angle of adsorbed characteristic gas molecular models built in this work are in consistent with the theoretical data.

In order to examine which adsorption position is the most energetically stable, we firstly calculated the adsorption energy (ΔE_{ads}) [18, 32, 44]. As a key parameter of the adhesive property of adsorption system, the adsorption energy is defined in the following equation [18, 32, 44]:

$$\Delta E_{\text{ads}} = E_{\text{surf}} + E_{\text{gas}} - E_{\text{gas+surf}}, \quad (2)$$

where E_{surf} is the energy of SnO_2 (110) surface before adsorption, E_{gas} is the energy of free gas molecule, and $E_{\text{gas+surf}}$ is the total energy of the system after adsorption. In general, a positive ΔE_{ads} indicates that the molecule adsorption process

TABLE 2: Adsorption energy on SnO₂ (110) surface.

Gas	Adsorption energy $\Delta E_{\text{ads}}/\text{eV}$			
	O _{2c}	O _{3c}	Sn _{5c}	Sn _{6c}
H ₂	0.031	0.018	0.024	0.027
CO (O end)			0.032	0.017
CO (C end)	0.021	0.029	0.042	0.024

is exothermic, and the adsorption system is energetically stable [18, 32]. For the purpose of comparison, all the energies are calculated with the supercell of identical size.

The calculated adsorption energies for detected gases adsorbed on SnO₂ (110) surface are represented in Table 2. According to the definition of adsorption energy, a positive value demonstrates an exothermic reaction, which means a stable adsorption process. The bigger the adsorption energy is, the greater the excitation chance of the gas molecule electrons is.

Table 2 shows that the ΔE_{ads} of hydrogen adsorbed on O_{2c} atom site is relatively higher than that of other adsorption sites, indicating that hydrogen adsorption on O_{2c} atom site is the most thermodynamically favored process. Therefore, it is considered as the most energetically stable adsorption geometry, and in our calculation results the corresponding ΔE_{ads} for hydrogen on O_{2c}, O_{3c}, Sn_{5c}, and Sn_{6c} is 0.031 eV, 0.018 eV, 0.024 eV, and 0.027 eV, respectively. Simultaneously, ΔE_{ads} for carbon monoxide with C end to O_{2c}, O_{3c}, Sn_{5c}, and Sn_{6c} is 0.021 eV, 0.029 eV, 0.042 eV, and 0.024 eV, respectively and O end to Sn_{5c} and Sn_{6c} is 0.032 eV, and 0.017 eV. The ΔE_{ads} of carbon monoxide with C end on Sn_{5c} (Sn_{6c}) atom site is somewhat higher than that with O end, meaning that carbon monoxide is favored to be adsorbed on Sn_{5c} (Sn_{6c}) atom site with C end. And the ΔE_{ads} of carbon monoxide with C end on Sn_{5c} atom site is relatively higher than that of other adsorption site; therefore, we can conclude that carbon monoxide adsorbed on SnO₂ (110) surface with C end on Sn_{5c} atom site is the most energetically stable adsorption position.

Further research on the difference of sensing properties can be performed by analyzing the total density of states (DOSs) and partial density of states (PDOSs) of gas molecule and atoms in the adsorption system. The DOSs and PDOS of O_{2c} and Sn_{5c} on SnO₂ (110) surface are demonstrated in Figure 10, the DOS of hydrogen and carbon monoxide before and after adsorption are shown in Figure 12. For a deeply understanding of the adsorption process, the DOS and PDOS of free CO molecule are also demonstrated in Figure 11.

From Figure 10, it can be seen that the lower valence band of O_{2c} is mainly contributed by the 2s orbits, and the upper valence band results from the 2p orbits. For Sn_{5c} atoms, the 5s and 5p orbits compose the valence band and conductance band together.

As seen in Figure 11, the DOS of free carbon monoxide is composed of 4 σ , 1 π , 5 σ , and 2 π orbits and the occupied 5 σ orbit is at the Fermi level. The 4 σ is mainly contributed by the 2p, 2s of O, and 2s of C, 1 π mainly from the 2p of C and 2p of O, 5 σ mainly from the 2s and 2p orbits of C, and 2 π

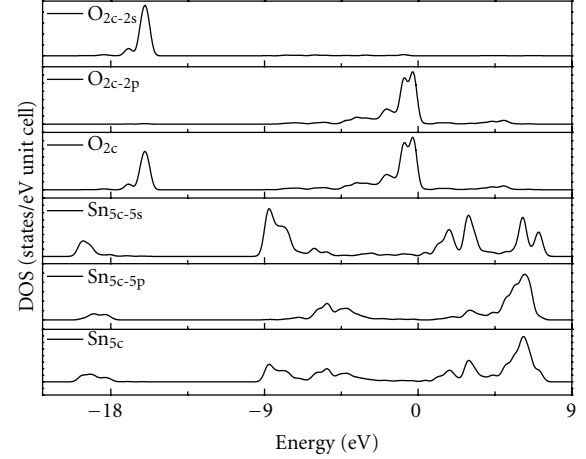
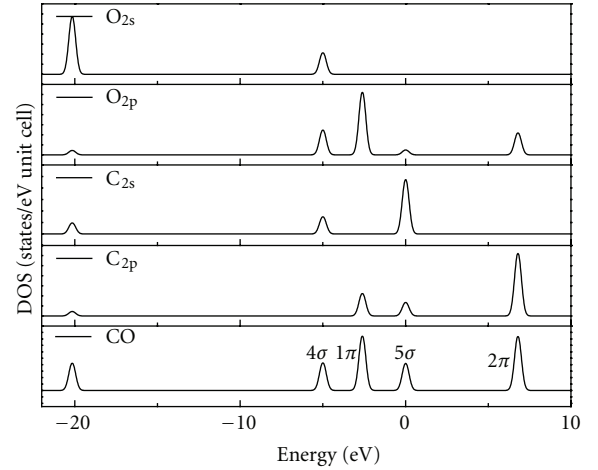
FIGURE 10: DOS and PDOS of O_{2c} and Sn_{5c} from SnO₂ (110) surface.

FIGURE 11: DOS and PDOS of free CO molecule.

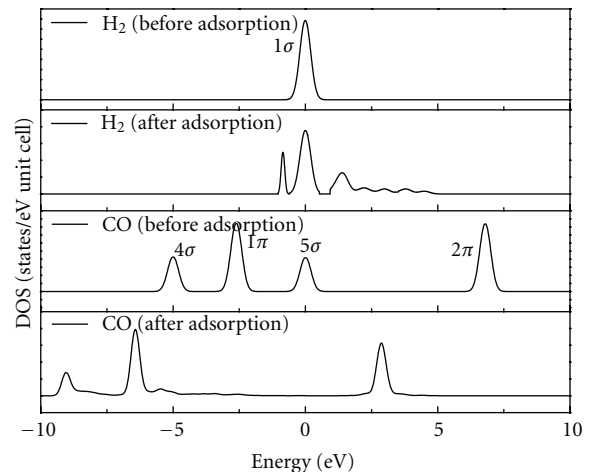
FIGURE 12: DOS of H₂ and CO before and after adsorption.

TABLE 3: The Mulliken charge and population of H₂ and CO.

		Before adsorption		After adsorption	
		s	p	s	p
H ₂	H	0.62	0.03	0.60	0.01
	H	0.62	0.03	0.60	0.01
CO	C	1.68	1.90	1.51	2.16
	O	1.84	4.58	1.83	4.44

mainly from the 2p of C and 2p of O. After carbon monoxide adsorbed on Sn_{5c} site with C end on (110) surface, the DOS of adsorbed carbon monoxide decreases slightly and the 5 σ orbits are almost completely degenerated. It implies a strong interaction between the 5 σ orbits of CO molecule and 5s 5p orbits of Sn_{5c}.

For free hydrogen whose occupied 1 σ orbital is at the Fermi level, the DOS of hydrogen changes slightly and obviously separates into several peaks after hydrogen adsorption on O_{2c} site. The change of DOS peaks indicates an interaction between the 1s orbital of adsorbed hydrogen and the 2p orbital of O_{2c} atoms, which may increase the probability of electron transfer from valence band to conductance band if intrinsic electrons are activated thermally or electronically.

The Mulliken population and charge transfer [18, 32, 44] between the gas molecule and adsorption surface was further investigated to illustrate the sensing mechanism of the rutile tin oxide to hydrogen and carbon monoxide. Table 3 demonstrates the Mulliken population of hydrogen and carbon monoxide before and after the adsorption on the (110) surface.

As shown in Table 3, the charge transfers of H₂ and CO gas molecule on (110) surface have the common tendency. The total number of electrons decreases at different degrees after being adsorbed on the surface. The number of the lost electrons from H₂ and CO is 0.08 e and 0.06 e, respectively. Accordingly, the lost electrons from adsorbed gas molecule are received by the (110) surface. It will decrease the height of barrier in the depletion region, increase the conductance of the sensor, and result in an increasing of output voltage which was generally observed in the on-line monitoring stage.

It should be noted that it is controversial to quantitatively interpret the gas sensing mechanism, due to the possible deviations between experimental conditions and ideal theoretical models. However, a qualitative comparison on different gas molecules adsorbed in the same adsorption system to investigate their different of sensing properties should be reliable [32].

4. Conclusions

This study has prepared nano-SnO₂ powder via hydrothermal method and investigated its morphology and microstructure. In particular, it focused on the gas sensing properties of the prepared sensor against power transformer fault gases such as hydrogen and carbon monoxide. Experiments showed that the optimum operating temperatures for 50 μ L

H₂ and CO were about 400°C and 360°C, with the gas response being 43.15 and 14.86, respectively.

Based on the first principles method the gas adsorption process was further investigated at the atomic level. Calculations results indicated that H₂ was favored to adsorb on O_{2c} site, and Sn_{5c} was the energetically stable adsorption position for CO with C end. After the adsorption of H₂ on O_{2c} site of (110) surface, there appeared new electronic peaks at the Fermi level. And the 5 σ orbits of CO almost completely degenerated after CO adsorbed on Sn_{5c} position of (110) surface with C end. From the Mulliken population analysis, the lost electron number of H₂ and CO is 0.08 e and 0.06 e, respectively, and this will increase the conductance of the sensor.

The differences gas sensing properties of nano-SnO₂-based sensor towards H₂ and CO were qualitatively explained by the theoretical calculations. They will present a new feasible way on exploring new nano-SnO₂-based gas sensor and other sensing materials for on-line monitoring of fault gases dissolved in power transformers.

Acknowledgments

The authors acknowledge the support of the National Natural Science Foundation of China (51277185) and the Funds for Innovative Research Groups of China (51021005).

References

- [1] H. Xiong, C. X. Sun, R. J. Liao, J. Li, and L. Du, "Study on kernel-based possibilistic clustering and dissolved gas analysis for fault diagnosis of power transformer," *Proceedings of the Chinese Society of Electrical Engineering*, vol. 25, no. 20, pp. 162–166, 2005.
- [2] N. Y. Peng, X. S. Wen, Y. Wang, J. B. Chen, and X. Z. Chai, "Potential fault diagnosis method based on linear classifier for oil-immersed transformer," *Proceedings of the Chinese Society of Electrical Engineering*, vol. 24, no. 6, pp. 147–151, 2004.
- [3] W. G. Chen, Y. X. Yun, C. Pan, and C. X. Sun, "Analysis of infrared absorption properties of dissolved gases in transformer oil," *Proceedings of the Chinese Society of Electrical Engineering*, vol. 28, no. 16, pp. 148–153, 2008.
- [4] L. J. Zhou, G. N. Wu, P. Tang, H. L. Wang, and C. Su, "Model of semiconductor gas sensor for monitoring dissolved gases in insulation oil," *Automation of Electric Power Systems*, vol. 30, no. 10, pp. 75–79, 2006.
- [5] A. Cirera, A. Cabot, A. Cornet, and J. R. Morante, "CO-CH₄ selectivity enhancement by in situ Pd-catalysed microwave SnO₂ nanoparticles for gas detectors using active filter," *Sensors and Actuators B*, vol. 78, no. 1–3, pp. 151–160, 2001.
- [6] R. Ionescu, A. Vancu, C. Moise, and A. Tomescu, "Role of water vapour in the interaction of SnO₂ gas sensors with CO and CH₄," *Sensors and Actuators B*, vol. 61, no. 1, pp. 39–42, 1999.
- [7] Y. Shimizu, T. Maekawa, Y. Nakamura, and M. Egashira, "Effects of gas diffusivity and reactivity on sensing properties of thick film SnO₂-based sensors," *Sensors and Actuators B*, vol. B46, no. 3, pp. 163–168, 1998.

- [8] S. D. Choi and D. D. Lee, "CH₄ sensing characteristics of K-, Ca-, Mg impregnated SnO₂ sensors," *Sensors and Actuators B*, vol. 77, no. 1-2, pp. 335–338, 2001.
- [9] J. Huang, N. Matsunaga, K. Shimanoe, N. Yamazoe, and T. Kunitake, "Nanotubular SnO₂ templated by cellulose fibers: synthesis and gas sensing," *Chemistry of Materials*, vol. 17, no. 13, pp. 3513–3518, 2005.
- [10] M. R. Cássia-Santos, V. C. Sousa, M. M. Oliveira et al., "Recent research developments in SnO₂-based varistors," *Materials Chemistry and Physics*, vol. 90, no. 1, pp. 1–9, 2005.
- [11] M. E. Franke, T. J. Koplin, and U. Simon, "Metal and metal oxide nanoparticles in chemiresistors: does the nanoscale matter?" *Small*, vol. 2, no. 1, pp. 36–50, 2006.
- [12] M. Sauvan and C. Pijolat, "Selectivity improvement of SnO₂ films by superficial metallic films," *Sensors and Actuators B*, vol. 58, no. 1–3, pp. 295–301, 1999.
- [13] R. M. Prasad, A. Gurlo, R. Riedel, M. Hübner, N. Barsan, and U. Weimar, "Microporous ceramic coated SnO₂ sensors for hydrogen and carbon monoxide sensing in harsh reducing conditions," *Sensors and Actuators B*, vol. 149, no. 1, pp. 105–109, 2010.
- [14] A. Köck, A. Tischner, T. Maier et al., "Atmospheric pressure fabrication of SnO₂-nanowires for highly sensitive CO and CH₄ detection," *Sensors and Actuators B*, vol. 138, no. 1, pp. 160–167, 2009.
- [15] T. Zhang, L. Liu, Q. Qi, S. Li, and G. Lu, "Development of microstructure In/Pd-doped SnO₂ sensor for low-level CO detection," *Sensors and Actuators B*, vol. 139, no. 2, pp. 287–291, 2009.
- [16] Q. Qi, T. Zhang, X. Zheng et al., "Electrical response of Sm₂O₃-doped SnO₂ to C₂H₂ and effect of humidity interference," *Sensors and Actuators B*, vol. 134, no. 1, pp. 36–42, 2008.
- [17] F. Quaranta, R. Rella, P. Siciliano et al., "Novel gas sensor based on SnO₂/Os thin film for the detection of methane at low temperature," *Sensors and Actuators B*, vol. 58, no. 1–, pp. 350–355, 1999.
- [18] W. Zeng, T. M. Liu, D. J. Liu, and E. J. Han, "Hydrogen sensing and mechanism of M-doped SnO₂ (M = Cr³⁺, Cu²⁺ and Pd²⁺) nanocomposite," *Sensors and Actuators B*, vol. 160, no. 1, pp. 455–462, 2011.
- [19] C. W. Zhang, P. J. Wang, and F. Li, "First-principles study on surface magnetism in Co-doped (110) SnO₂ thin film," *Solid State Sciences*, vol. 13, no. 8, pp. 1608–1611, 2011.
- [20] M. Hübner, R. G. Pavelko, N. Barsan, and U. Weimar, "Influence of oxygen backgrounds on hydrogen sensing with SnO₂ nanomaterials," *Sensors and Actuators B*, vol. 154, no. 2, pp. 264–269, 2011.
- [21] H. Zhang, Z. Li, L. Liu et al., "Enhancement of hydrogen monitoring properties based on Pd-SnO₂ composite nanofibers," *Sensors and Actuators B*, vol. 147, no. 1, pp. 111–115, 2010.
- [22] Y. Wang, Q. Mu, G. Wang, and Z. Zhou, "Sensing characterization to NH₃ of nanocrystalline Sb-doped SnO₂ synthesized by a nonaqueous sol-gel route," *Sensors and Actuators B*, vol. 145, no. 2, pp. 847–853, 2010.
- [23] J. Oviedo and M. J. Gillan, "Energetics and structure of stoichiometric SnO₂ surfaces studied by first-principles calculations," *Surface Science*, vol. 463, no. 2, pp. 93–101, 2000.
- [24] J. B. L. Martins, E. Longo, J. Andrés, and C. A. Taft, "Theoretical study of cluster models and molecular hydrogen interaction with SnO₂ [110] surface," *Journal of Molecular Structure: THEOCHEM*, vol. 335, no. 1–3, pp. 167–174, 1995.
- [25] M. Calatayud, J. Andrés, and A. Beltrán, "Theoretical analysis of adsorption and dissociation of CH₃OH on the stoichiometric SnO₂(110) surface," *Surface Science*, vol. 430, no. 1, pp. 213–222, 1999.
- [26] J. Oviedo and M. J. Gillan, "First-principles study of the interaction of oxygen with the SnO₂ (110) surface," *Surface Science*, vol. 490, no. 3, pp. 221–236, 2001.
- [27] J. Oviedo and M. J. Gillan, "Reconstructions of strongly reduced SnO₂ (110) studied by first-principles methods," *Surface Science*, vol. 513, no. 1, pp. 26–36, 2002.
- [28] F. Ciriaco, L. Cassidei, M. Cacciatore, and G. Petrella, "First principle study of processes modifying the conductivity of substoichiometric SnO₂ based materials upon adsorption of CO from atmosphere," *Chemical Physics*, vol. 303, no. 1-2, pp. 55–61, 2004.
- [29] M. A. Mäki-Jaskari, T. T. Rantala, and V. V. Golovanov, "Computational study of charge accumulation at SnO₂ (110) surface," *Surface Science*, vol. 577, no. 2-3, pp. 127–138, 2005.
- [30] C. W. Zhang, P. J. Wang, and F. Li, "First-principles study on surface magnetism in Co-doped (110) SnO₂ thin film," *Solid State Sciences*, vol. 13, no. 8, pp. 1608–1611, 2011.
- [31] T. T. Rantala, T. S. Rantala, and V. Lantto, "Electronic structure of SnO₂ (110) surface," *Materials Science in Semiconductor Processing*, vol. 3, no. 1-2, pp. 103–107, 2000.
- [32] Z. Wen, L. Tian-Mo, and L. Xiao-Fei, "Hydrogen sensing properties of low-index surfaces of SnO₂ from first-principles," *Physica B*, vol. 405, no. 16, pp. 3458–3462, 2010.
- [33] V. N. Mishra and R. P. Agarwal, "Sensitivity, response and recovery time of SnO₂ based thick-film sensor array for H₂, CO, CH₄ and LPG," *Microelectronics Journal*, vol. 29, no. 11, pp. 861–874, 1998.
- [34] N. Yamazoe, G. Sakai, and K. Shimanoe, "Oxide semiconductor gas sensors," *Catalysis Surveys from Asia*, vol. 7, no. 1, pp. 63–75, 2003.
- [35] I. J. Kim, S. D. Han, I. Singh, H. D. Lee, and J. S. Wang, "Sensitivity enhancement for CO gas detection using a SnO₂-CeO₂-PdO_x system," *Sensors and Actuators B*, vol. 107, no. 2, pp. 825–830, 2005.
- [36] H. Lu, W. Ma, J. Gao, and J. Li, "Diffusion-reaction theory for conductance response in metal oxide gas sensing thin films," *Sensors and Actuators B*, vol. 66, no. 1–3, pp. 228–231, 2000.
- [37] Y. Shen, T. Yamazaki, Z. Liu, D. Meng, and T. Kikuta, "Hydrogen sensors made of undoped and Pt-doped SnO₂ nanowires," *Journal of Alloys and Compounds*, vol. 488, no. 1, pp. L21–L25, 2009.
- [38] B. Wang, L. F. Zhu, Y. H. Yang, N. S. Xu, and G. W. Yang, "Fabrication of a SnO₂ nanowire gas sensor and sensor performance for hydrogen," *Journal of Physical Chemistry C*, vol. 112, no. 17, pp. 6643–6647, 2008.
- [39] A. Srivastava and K. Jain, "Study on ZnO-doped tin oxide thick film gas sensors," *Materials Chemistry and Physics*, vol. 105, no. 2-3, pp. 385–390, 2007.
- [40] Y. B. Xue and Z. A. Tang, "Density functional study of the interaction of CO with undoped and Pd doped SnO₂ (110) surface," *Sensors and Actuators B*, vol. 138, no. 1, pp. 108–112, 2009.
- [41] G. Wu, J. Zhang, Y. Wu, Q. Li, K. Chou, and X. Bao, "Adsorption and dissociation of hydrogen on MgO surface: a first-principles study," *Journal of Alloys and Compounds*, vol. 480, no. 2, pp. 788–793, 2009.
- [42] F. Trani, M. Causà, D. Ninno, G. Cantele, and V. Barone, "Density functional study of oxygen vacancies at the SnO₂ surface and subsurface sites," *Physical Review B*, vol. 77, no. 24, Article ID 245410, pp. 245–252, 2008.

- [43] Y. C. Lee, H. Huang, O. K. Tan, and M. S. Tse, "Semiconductor gas sensor based on Pd-doped SnO₂ nanorod thin films," *Sensors and Actuators B*, vol. 132, no. 1, pp. 239–242, 2008.
- [44] J. D. Prades, A. Cirera, J. R. Morante, J. M. Pruneda, and P. Ordejón, "Ab initio study of NO_x compounds adsorption on SnO₂ surface," *Sensors and Actuators B*, vol. 126, no. 1, pp. 62–67, 2007.

Research Article

Mineral Phase and Physical Properties of Red Mud Calcined at Different Temperatures

Chuan-sheng Wu^{1,2,3} and Dong-yan Liu^{1,3}

¹ College of Civil Engineering, Chongqing University, Chongqing 400044, China

² College of Civil Engineering, Chongqing Vocational Institute of Engineering, Chongqing 400037, China

³ Laboratory of New Technology for Construction of Cities in Mountain Area, Chongqing University and Ministry of Education, Chongqing 400045, China

Correspondence should be addressed to Dong-yan Liu, cqdyliu@yahoo.com.cn

Received 9 August 2012; Revised 20 September 2012; Accepted 24 September 2012

Academic Editor: Ming-Guo Ma

Copyright © 2012 C.-s. Wu and D.-y. Liu. This is an open access article distributed under the Creative Commons Attribution License, which permits unrestricted use, distribution, and reproduction in any medium, provided the original work is properly cited.

Different characterizations were carried out on red mud uncalcined and samples calcined in the range of 100°C–1400°C. In the present paper, the phase composition and structural transition of red mud heated from room temperature are indicated by XRD, TG-DTA, and SEM techniques. The mean particle diameter, density, and bond strength of these samples also have been investigated. The results indicate the decomposition of gibbsite into Al_2O_3 and H_2O between 300°C and 550°C and calcite into CaO and CO_2 in the interval of 600–800°C. Tricalcium aluminate and gehlenite are formed in the range of 800–900°C. Combined with the SEM images, the results of physical property testing show that the particle size and the strength each has a continuous rise during the heat treatment from 150°C to 1350°C. But the value of density will undergo a little drop before 450°C and then increases to a higher value at the temperature of 1200°C. These obtained results provide an important base for the further studies of comprehensive utilization of red mud.

1. Introduction

Red mud is a reddish brown coloured solid waste produced during the physical and chemical processing of bauxite. Bauxite is composed of aluminum hydroxide minerals, including primarily gibbsite ($\text{Al}(\text{OH})_3$), boehmite ($\gamma\text{-AlO}(\text{OH})$), diaspor ($\alpha\text{-AlO}(\text{OH})$), hematite (Fe_2O_3) and goethite ($\text{FeO}(\text{OH})$) [1]. The red mud, according to the production process of the aluminum, can be divided into Bayer process red mud, sintering progress red mud, and combined process red mud. It was reported that there is 0.8~1.5 t of red mud produced by each 1 t alumina produced. Globally, the total amount of red mud produced every year is between 60 and 120 million tons, [2] about 30 million tons of which is produced in China, and the accumulated quantity can reach to 200 million tons in China.

As to the treatment of red mud, stockpiling it in the open yard may lead to serious pollution of the surrounding soil,

air, and groundwater. The dike breach at the Ajakai Tim-foldgyar Zrt alumina plant in Hungary [3] is warning us to pay enough attention to the comprehensive treatment of the red mud. The comprehensive utilization of red mud can be divided into the following aspects. First, recovery of Fe, Al, Na [4–6], and rare earth elements like Sc, Y, La, Ti, V [6–10] in red mud. Second, reuse of red mud as cement production [11–14] and other construction materials like brick [15, 16], glass [17, 18], and aerated concrete block [19]. Third, utilization of red mud as road base material and filling material in mining [20, 21] and plastic [22]. Forth, application of red mud to absorb heavy metal ions like Cu^{2+} , Zn^{2+} , Ni^{2+} , Cd^{2+} [23–25], and nonmetallic ions and molecules like NO_3^- [26–28] in the wastewater. Fifth, application of red mud can absorb heavy metal ions in the soil [29, 30] and SO_2 in the wastegas [31, 32].

For the purpose of better comprehension utilization of red mud, several studies [33–38] have been carried out on

the physical and chemical properties of red mud under heat treatment. However, most of the above reports on the characterization of red mud have not detailedly research the physical properties from room temperature to an extreme high temperature. The research of SEM diagrams of red mud calcined at different temperature also has not been reported before. In the present paper, the mean particle diameter, density, and bond strength of red mud calcined within the interval 150–1350°C have been investigated. These tests were aimed to correlate phase composition and structural transition of red mud heated from room temperature, which are indicated by XRD, TG-DTA, and SEM techniques. This research is part of a long-term project on the exploitation of the comprehensive utilization of red mud and provides an important base for the further studies of comprehensive utilization of red mud.

2. Materials and Experimental Procedure

2.1. Materials. Red mud samples were collected from an alumina refining plant, in Guizhou, China, the process of which is bauxite-calcination method. Approximately 3–5 kg of red mud samples were collected from six different sites which have been stocked for 3 years. Samples were dried to constant weight at a temperature of $105 \pm 5^\circ\text{C}$ for 24 h. Powder batches of about 500 g were calcined for 6 h in at 150, 300, 450, 600, 900, 1050, 1200, 1350°C. Then the samples were removed from the furnace and cooled to room temperature in air. A powder batch of about 500 g was prepared without heat treatment for the use in comparison experiment and TG-DT analysis.

The chemical composition of the uncalcined red mud determined by X-ray fluorescence (XRF-1800X) analyzer is given in Table 1.

2.2. Experimental Methods. X-ray diffraction (XRD) analysis was carried out on a Rigaku (Japan) D/MAX 2500C diffractometer using $\text{CuK}\alpha$ radiation, voltage 40 kV, current 200 mA, equipped with a graphite monochromator in the diffracted beam. Crystalline phases were identified using the database of the International Center for Diffraction Data-JCPDS for inorganic substances. (JCPDS, International Centre for Diffraction Data, 1601 Park Line, Swarthmore, PA, 1987).

Thermal analysis was performed on a Netzsch (Germany) STA 449 simultaneous analyzer. Thermogravimetric (TG) and differential thermal (DT) analysis were performed in the range of 50–1450°C (stripping gas: dry N_2 , helium flow = 100 mL/min, heating rate: $10^\circ\text{C}/\text{min}$). Measurement were carried out in 0.3 cm^3 volume alumina crucibles using α -alumina as reference, analyzing $\approx 100\text{ mg}$ of dry sample.

The volume frequency of particle diameter is characterized by a Winner2008A (Chinese) laser particle size analyzer, whose measuring range is $0.05\text{--}2000\text{ }\mu\text{m}$. The density measurements were performed with a helium pycnometer (Micromeritics, Model 1305, USA). And the strength

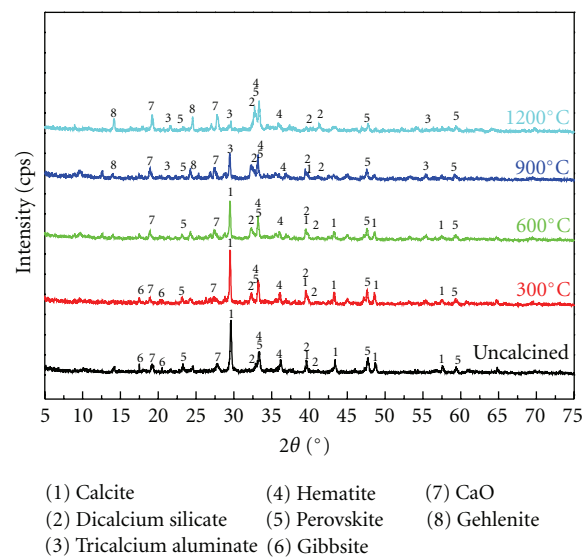


FIGURE 1: XRD patterns of uncalcined red mud and samples heated at 300°C, 600°C, 900°C, and 1200°C.

performance of red mud calcined at different temperature is tested on a Trautwein DigiShearTM (Chinese) multi-functional direct shear test systems with the following testing condition: the shear rate is 0.03 mm/minute, the maximum shear displacement is 6.5 mm.

SEM observation was performed on TESCAN VEGA II scanning electron microscope for the characterization of the micromorphology of red mud calcined at different temperatures.

3. Results and Discussions

3.1. XRD Analysis. The element analysis and phase characterization of red mud have been reported several times [33, 34, 37, 38]. However, the analysis data of the composition of red mud is not uniform. The XRD patterns of the red mud uncalcined and calcined at the temperatures of 300°C, 600°C, 900°C, 1200°C are shown in Figure 1.

From Figure 1, it can be seen that the main phases in the uncalcined red mud are calcite (CaCO_3), dicalcium silicate (Ca_2SiO_4), hematite (Fe_2O_3), perovskite (CaTiO_3), gibbsite ($\text{Al}(\text{OH})_3$), and CaO. Among these mineral phases, gibbsite cannot be detected in the sample treated over 600°C for the reason of pyrolysis. Calcite is the fundamental phase up to 900°C. Above this temperature, calcite (CaCO_3) decrease parallels the increase of CaO and the occurrence of minor components, such as tricalcium aluminate ($\text{Ca}_3\text{Al}_2\text{O}_6$) and gehlenite ($\text{Ca}_2\text{Al}_2\text{SiO}_7$). This indicated the transform of calcite to tricalcium aluminate and Gehlenite and the decomposition of Calcite to CaO in the interval of 600–900°C. Dicalcium silicate (Ca_2SiO_4), hematite (Fe_2O_3), perovskite (CaTiO_3), and CaO are not affected by temperature through the process of heating.

TABLE 1: The main chemical constituents of red mud (%) [38].

Chemical constituent	Fe ₂ O ₃	Al ₂ O ₃	SiO ₂	CaO	Na ₂ O	TiO ₂	Sc ₂ O ₃	Nb ₂ O ₅	TREO	Loss
Sintering process	6.66	9.18	18.1	38.09	4	6.72	0.02	0.02	0.25	16.96

3.2. TG-DT Analysis. The TG-DTA diagram (Figure 2) shows a continuous weight loss distributed in the range of 50–1450°C. The figure shows two main portions of mass loss as the rise of temperature. The first one is during the heating temperature interval of 50–550°C when the physically absorbed water and chemically bound water is off. Before the firing temperature is up to 550°C, the sample loses 8.26% total of its weight. The proportion of physically absorbed water is small. Combined with the results of XRD analysis, it can be known that the lost chemically bound water is mainly from the decomposition of gibbsite (Al(OH)₃), which is shown as following equation: $\text{Al(OH)}_3 \rightarrow \text{Al}_2\text{O}_3 + \text{H}_2\text{O}$. But if there are no Al₂O₃ phases detected along with the decrease of Al(OH)₃, then Al₂O₃ is believed to have been combined with the CaO (discussed as following) to form tricalcium aluminate or Gehlenite.

Then the mass of the sample undertakes a more rapid decline in the range of 550–900°C with a mass change of 21.81%. As the report [38] says, the main reason is the release of CO₂, which can also be indicated by the XRD pattern in Figure 1. The decrease of Calcite (CaCO₃) and the increase of CaO around the temperature of 900°C can prove that the decomposition of CaCO₃ is the main source of released CO₂. The chemical equations during this progress are as following: $\text{CaCO}_3 \rightarrow \text{CaO} + \text{CO}_2$, $3\text{CaO} + \text{Al}_2\text{O}_3 \rightarrow \text{Ca}_3\text{Al}_2\text{O}_6$, $2\text{CaO} + 2\text{Al}_2\text{O}_3 + \text{SiO}_2 \rightarrow 2\text{Ca}_2\text{Al}_2\text{SiO}_7$. Besides, when the sample is heated at the temperature over 900°C, there is not an obvious mass change.

There are three main endothermic peaks in the DT diagram of red mud. It can be known that the decomposition temperatures of gibbsite to Al₂O₃ and calcite are separately 300–550°C and 600–800°C. And the main reaction temperature of CaO and Al₂O₃ to prepared ricalcium aluminate (Ca₃Al₂O₆) is 850–900°C.

Combined the results of XRD analysis and the TG-DT analysis, the phase transition during the heat treatment can be indicated as the following: (1) the main mineral phases of dried red mud at room temperature are calcite (CaCO₃), dicalcium Silicate (Ca₂SiO₄), hematite (Fe₂O₃), perovskite (CaTiO₃), gibbsite (Al(OH)₃), and CaO; (2) in the range of 300–550°C, the gibbsite decomposes into Al₂O₃ and H₂O; (3) at the temperature of 600–800°C, the calcite decomposes into CaO and CO₂; (4) the phases of tricalcium aluminate (Ca₃Al₂O₆) and gehlenite (Ca₂Al₂SiO₇) start to emerge in the 800–900°C interval; (5) there is no obvious mass change or phase change above 900°C.

3.3. Physical Properties Testing. The physical properties such as particle size, density and strength change as the increase of the calcined temperature of red mud. The particles size

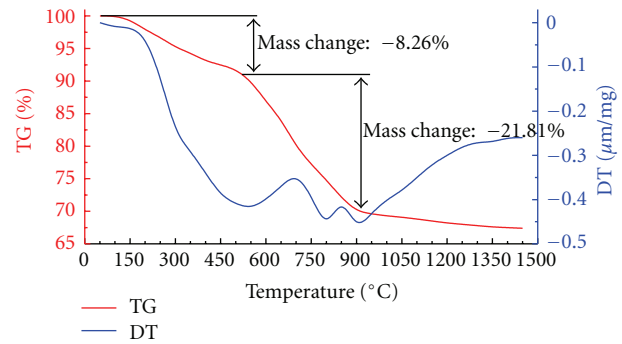


FIGURE 2: Thermogravimetric (TG) and differential thermal (DT) analysis diagram of dried red mud.

distribution of the uncalcined red mud is shown in Figure 3(a). It can be seen that the ground red mud particles are mostly in the range of 1–80 μm with a mean value of 26.7 μm. But it will be different as the change of calcined temperature, which can be indicated from the Figure 2(b). With the firing temperature from 150°C to 1350°C, the average particle diameter of red mud rises from 26.7 μm to 38.2 μm. The increase of the particle size may influenced the improvement of crystallization. From the XRD pattern (Figure 1), it can be known that, except the vanishing phases like calcite and gibbsite, the crystallinities of the majority of phases of red mud are improved by heat treatment. This will promote the rising of the mean particle diameter value.

The density of red mud at room temperature is 3.26 g/cm³, which will change as the red mud is under heat treatment. The bond strength of uncalcined red mud tested by the direct shear test systems is 322 kPa. The values of density and bond strength change as the functions of temperature are shown in Figure 4. From the diagram we can know the following aspects. The value of density decrease until the temperature is 450°C, which is in contrast to the change of bond strength. Then they both increase obviously from 450°C to 1200°C and decline a little when the temperature is higher than 1200°C. The maximum values of density and bond strength are 3.41 cm³ and 452 kPa at 1200°C.

These phenomena can also be explained by the XRD analysis result like the change of mean particle diameter value. The enhancement of strength properties may result from the improvement of crystallinities of major phases and the appearance of high strength phases like tricalcium aluminate and gehlenite. While as to the change of density, the decline before 450°C is determined by the emission of water and the decomposition of gibbsite (Al(OH)₃),

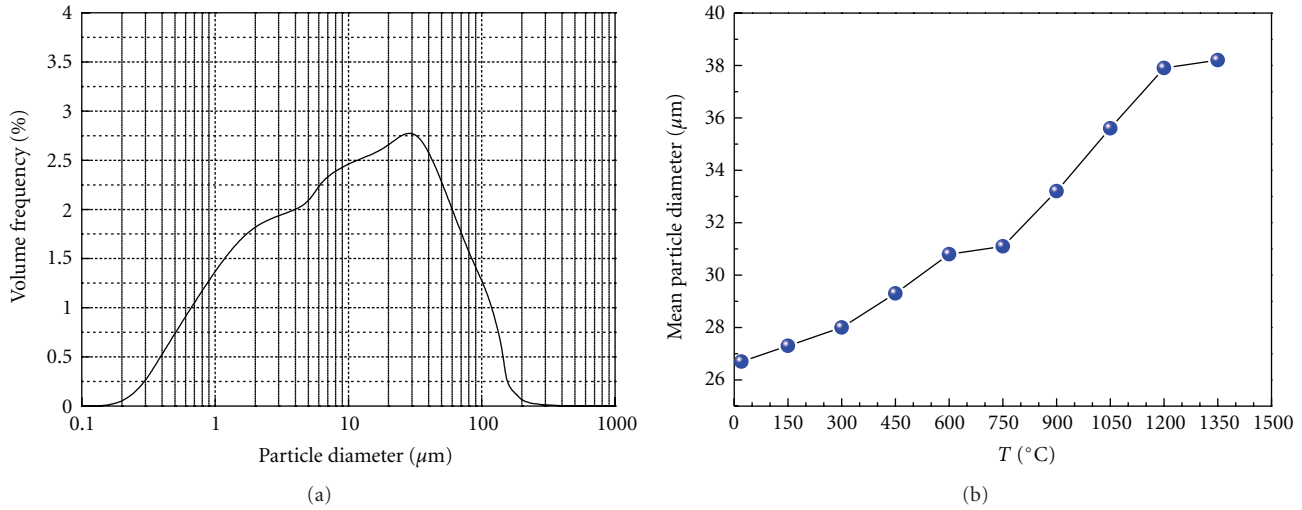


FIGURE 3: (a) Particle size distribution of red mud at room temperature; (b) mean particle size at different calcined temperatures.

2.42 g/cm³) to Al₂O₃ (3.97 g/cm³) and calcite (CaCO₃, 2.60~2.80 g/cm³) to CaO (3.25~3.38 g/cm³).

3.4. SEM Analysis. For the purpose of further comprehension the phase change progress of red mud during heat treatment, red mud uncalcined, and samples calcined at 150°C, 450°C, 600°C, 900°C, and 1200°C are dispersed in anhydrous alcohol and grinded by ultrasonic vibration for the same time (24 h). Then the samples were observed by scanning electron microscope to obtain the micromorphology maps of these samples. The SEM images of red mud uncalcined and calcined are showed in Figure 5.

From Figure 5(a) it can be known that the microscopic structure of uncalcined red mud is relatively loose, with high porosity and small particle size. On the contrary, the diagrams of red mud calcined at a series of temperatures (Figures 5(b)–5(e)) indicate that the heat treatment can improve the value of particle diameter and make the particles easy to gather with each other. The increasing tendency of particle size is consistent to the values measured by laser particle size analyzer as shown in Figure 3(b).

Different microstructures result from different physical and chemical progresses. With the influence of heating at 150°C, red mud loses the majority of its physically absorbed water and part of chemically bound water. So Figure 5(b) presents large particles and a high porosity, corresponding to a low density as shown in Figure 4. When calcined at 450°C, with the decomposition of phases like gibbsite, red mud has lost almost all the chemically bound water. So it can have larger particle and higher porosity (also lower density) than calcined at 150°C (Figure 5(c)). Density of red mud is determined by two main different factors: porosity and particle size. When firing at 600°C, 900°C, and 1200°C, there is no water emission that leads to the variation of porosity. But the phase transition and improvement of crystalline degree can make the increase of particle diagram significant (Figures

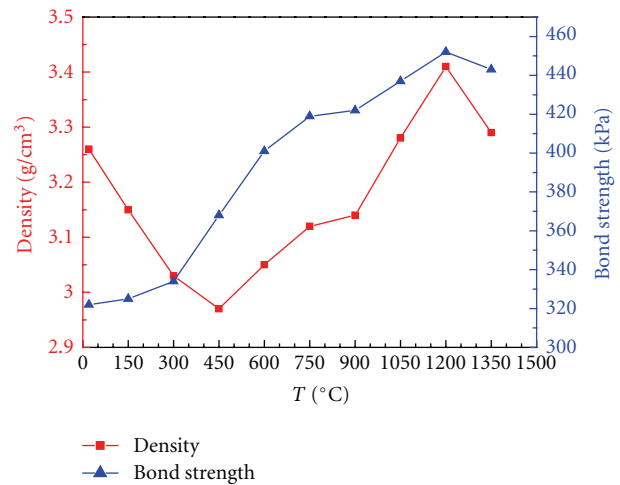


FIGURE 4: Changes of density and bond strength as the functions of calcined temperature.

5(e)–5(f)). Therefore red mud can have a gradually increasing value of density.

4. Conclusion

In this paper, through the XRD and TG-DT analysis, the phase transition during the heat treatment contained the following several progresses: (1) gibbsite decomposes into Al₂O₃ and H₂O (300–550°C); (2) calcite decomposes into CaO and CO₂ (600–800°C); (3) the emergence of Tricalcium aluminate (Ca₃Al₂O₆) and gehlenite (Ca₂Al₂SiO₇) (800–900°C). From the results of physical property testing and SEM analysis, it can be indicated that the physical properties of red mud have the obvious variations during the progress of firing of red mud. The particle size and the strength each has a continuous rise during the heat treatment from 150°C

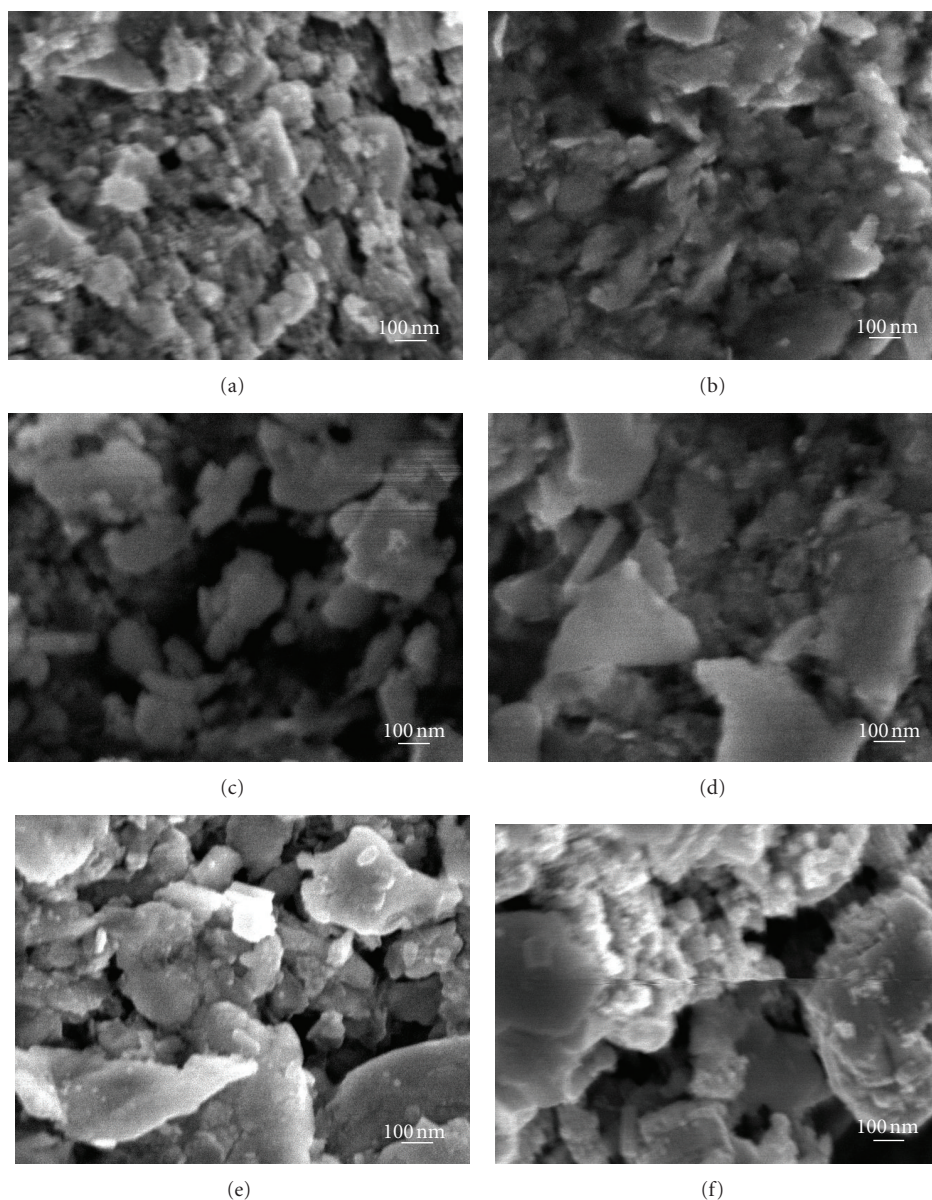


FIGURE 5: The SEM images of red mud (a) uncalcined and calcined at (b) 150°C, (c) 450°C, (d) 600°C, (e) 900°C, and (f) 1200°C.

to 1350°C, because of the improvement of crystallinities of major phases and the appearance of high strength phases like tricalcium aluminate and gehlenite. But as to the value of density, it will undergo a little drop before 450°C as an effect of the increase of porosity, and then increases to a new high value at the temperature of 1200°C. All the obtained results will provide an important base for the further studies of comprehensive utilization of red mud.

References

- [1] Mineral Photos—Aluminum & Bauxite Homepage, 2012, <http://www.mii.org/Minerals/photoal.html>.
- [2] P. Renforth, W. M. Mayes, A. P. Jarvis, I. T. Burd, D. C. Manning, and K. GruzeScience, "Contaminant mobility and carbon sequestration downstream of the Ajka (Hungary) red mud spill: the effects of gypsum dosing," *Science of the Total Environment*, vol. 421-422, pp. 253–259, 2012.
- [3] H. J. Reeves, G. Wealthall, and P. L. Younger, "Advisory Visit to the Bauxite Processing Tailings Dam near Ajka, Veszprems County, Western Hungary," Open Report OR/11/006, British Geological Survey, Keyworth, UK, 2011.
- [4] Y. F. Sun, F. Z. Dong, and J. T. Liu, "Technology for recovering iron from red mud by Bayer process," *Metal Mine*, vol. 9, pp. 176–178, 2009 (Chinese).
- [5] L. Zhong and Y. F. Zhang, "Sub molten salt method recycling red mud," *The Chinese Journal of Nonferrous Metals*, vol. 18, pp. 70–73, 2008.
- [6] X. F. Zheng, "Recycling technology of aluminum and sodium from low temperature bayer process red mud," *Shandong Metallurgy*, vol. 32, pp. 16–17, 2010.

- [7] P. M. Orhsekkiihn, T. Lybempudu, and K. M. Ochsenkiihn, "Recovery of lanthanides and yttrium from red mud by selective leaching," *Analytica Chimica Acta*, vol. 319, pp. 249–254, 1996.
- [8] M. Ochsenkühn-Petropulu, T. Lyberopulu, and G. Parissakis, "Selective separation and determination of scandium from yttrium and lanthanides in red mud by a combined ion exchange/solvent extraction method," *Analytica Chimica Acta*, vol. 315, no. 1–2, pp. 231–237, 1995.
- [9] D. I. Smirnov and T. V. Molchanova, "The investigation of sulphuric acid sorption recovery of scandium and uranium from the red mud of alumina production," *Hydrometallurgy*, vol. 45, no. 3, pp. 249–259, 1997.
- [10] X. H. Chen, Y. Chen, M. Gan, and K. X. Xu, "Precipitation and separation of vanadium from bayer process sodium aluminate solution," *The Chinese Journal of Process Engineering*, vol. 10, pp. 24–38, 2010.
- [11] X. R. Qiu and Y. Y. Qi, "The reasonable utilization of red mud in cement production," *Cement Technology*, vol. 6, pp. 103–105, 2011.
- [12] E. Kalkan, "Utilization of red mud as a stabilization material for the preparation of clay liners," *Engineering Geology*, vol. 87, no. 3–4, pp. 220–229, 2006.
- [13] A. A. Barsheri, *New Cement*, Edited by Y. Y. Qian, China Building Industry Press, Beijing, China, 1983.
- [14] I. Vangelatos, G. N. Angelopoulos, and D. Boufounos, "Utilization of ferroalumina as raw material in the production of Ordinary Portland Cement," *Journal of Hazardous Materials*, vol. 168, no. 1, pp. 473–478, 2009.
- [15] A. P. Yang, "The development of brick made of red mud and fly ash," *Light Metals*, vol. 12, pp. 17–18, 1996.
- [16] N. Yalçın and V. Sevinç, "Utilization of bauxite waste in ceramic glazes," *Ceramics International*, vol. 26, no. 5, pp. 485–493, 2000.
- [17] J. K. Yang, D. D. Zhang, and B. Xiao, "Study on glass-ceramics mostly made from red mud and fly ash," *Glass & Enamel*, vol. 32, pp. 9–11, 2004 (Chinese).
- [18] Z. Y. Liang, "The research on black glass decorative materials made from red mud," *Environmental Protection of Chemical Industry*, vol. 18, pp. 50–51, 1998.
- [19] B. Wu, D. C. Zhang, and Z. Z. Zhang, "The study of producing aerated-concrete blocks from red-mud," *China Resources Comprehensive Utilization*, vol. 6, pp. 29–31, 2005.
- [20] L. G. Yang, Z. L. Yao, and D. S. Bao, "Pumped and cemented red mud slurry filling mining method," *Mining Research and Development*, vol. 16, pp. 18–22, 1996.
- [21] H. M. Wang, "The comprehensive utilization of red mud," *Shanxi Energy and Conservation*, vol. 11, pp. 58–61, 2011.
- [22] X. L. Nan, T. A. Zhang, Y. Liu, and Z. H. Dou, "Analysis of comprehensive utilization of red mud in China," *The Chinese Journal of Process Engineering*, vol. 10, no. 1, pp. 264–270, 2010.
- [23] M. Vaclavikova, P. Misaelides, G. Gallios, S. Jakabsky, and S. Hredzak, "Removal of cadmium, zinc, copper and lead by red mud, an iron oxides containing hydrometallurgical waste," *Studies in Surface Science and Catalysis*, vol. 155, pp. 517–525, 2005.
- [24] M. Erdem, H. S. Altundoğan, and F. Tümen, "Removal of hexavalent chromium by using heat-activated bauxite," *Minerals Engineering*, vol. 17, no. 9–10, pp. 1045–1052, 2004.
- [25] L. Santona, P. Castaldi, and P. Melis, "Evaluation of the interaction mechanisms between red muds and heavy metals," *Journal of Hazardous Materials*, vol. 136, no. 2, pp. 324–329, 2006.
- [26] Y. Çengelöğlu, E. Kir, and M. Ersöz, "Removal of fluoride from aqueous solution by using red mud," *Separation and Purification Technology*, vol. 28, no. 1, pp. 81–86, 2002.
- [27] G. Akay, B. Keskinler, A. Çakici, and U. Danis, "Phosphate removal from water by red mud using crossflow microfiltration," *Water Research*, vol. 32, no. 3, pp. 717–726, 1998.
- [28] H. S. Altundoan, S. Altundoan, F. Tümen, and M. Bildik, "Arsenic adsorption from aqueous solutions by activated red mud," *Waste Management*, vol. 22, no. 3, pp. 357–363, 2002.
- [29] R. Ciccu, M. Ghiani, A. Serici, S. Fadda, R. Peretti, and A. Zucca, "Heavy metal immobilization in the mining-contaminated soils using various industrial wastes," *Minerals Engineering*, vol. 16, no. 3, pp. 187–192, 2003.
- [30] E. Lombi, F. J. Zhao, G. Wieshammer, G. Zhang, and S. P. McGrath, "In situ fixation of metals in soils using bauxite residue: biological effects," *Environmental Pollution*, vol. 118, no. 3, pp. 445–452, 2002.
- [31] Z. Bekir, A. Inci, and Y. Hayrettin, "Sorption of SO₂ on metal oxides in a fluidized bed," *Industrial and Engineering Chemistry Research*, vol. 27, no. 3, pp. 434–439, 1988.
- [32] G. Z. Lu, T. A. Zhang, L. Bao, Z. H. Dou, and W. G. Zhang, "Roasting pretreatment of high-sulfur bauxite," *The Chinese Journal of Process Engineering*, vol. 8, no. 5, pp. 892–896, 2008.
- [33] V. M. Sglavo, R. Campostrini, S. Maurina et al., "Bauxite 'red mud' in the ceramic industry—part 1: thermal behaviour," *Journal of the European Ceramic Society*, vol. 20, no. 3, pp. 235–244, 2000.
- [34] Y. Zhang and Z. Pan, "Characterization of red mud thermally treated at different temperatures," *Journal of Jinan University for Science and Technology*, vol. 19, pp. 293–297, 2005 (Chinese).
- [35] V. Jobbágy, J. Somlai, J. Kovács, G. Szeiler, and T. Kovács, "Dependence of radon emanation of red mud bauxite processing wastes on heat treatment," *Journal of Hazardous Materials*, vol. 172, no. 2–3, pp. 1258–1263, 2009.
- [36] S. Srikanth, A. K. Ray, A. Bandopadhyay, B. Ravikumar, and A. Jha, "Phase constitution during sintering of red mud and red mud-fly ash mixtures," *Journal of the American Ceramic Society*, vol. 88, no. 9, pp. 2396–2401, 2005.
- [37] H. Chen, H. Sun, and H. Li, "Effect of heat treatment temperature on cementitious activity of red mud," *Light Metals*, vol. 9, pp. 22–25, 2006 (Chinese).
- [38] X. Liu, N. Zhang, H. Sun, J. Zhang, and L. Li, "Structural investigation relating to the cementitious activity of bauxite residue—red mud," *Cement and Concrete Research*, vol. 41, no. 8, pp. 847–853, 2011.